



ULTRAFAST ELECTROHYDRODYNAMIC 3D PRINTING WITH SUBMICROMETER RESOLUTION

Ievgenii Liashenko

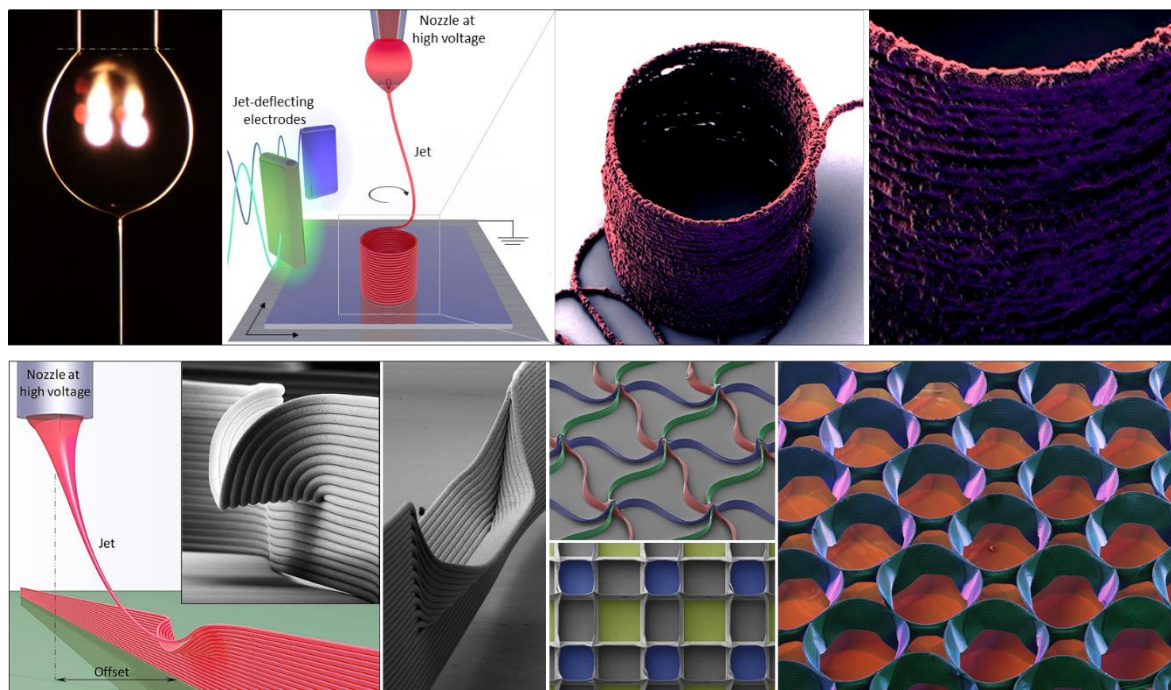
ADVERTIMENT. L'accés als continguts d'aquesta tesi doctoral i la seva utilització ha de respectar els drets de la persona autora. Pot ser utilitzada per a consulta o estudi personal, així com en activitats o materials d'investigació i docència en els termes establerts a l'art. 32 del Text Refós de la Llei de Propietat Intel·lectual (RDL 1/1996). Per altres utilitzacions es requereix l'autorització prèvia i expressa de la persona autora. En qualsevol cas, en la utilització dels seus continguts caldrà indicar de forma clara el nom i cognoms de la persona autora i el títol de la tesi doctoral. No s'autoritza la seva reproducció o altres formes d'explotació efectuades amb finalitats de lucre ni la seva comunicació pública des d'un lloc aliè al servei TDX. Tampoc s'autoritza la presentació del seu contingut en una finestra o marc aliè a TDX (framing). Aquesta reserva de drets afecta tant als continguts de la tesi com als seus resums i índexs.

ADVERTENCIA. El acceso a los contenidos de esta tesis doctoral y su utilización debe respetar los derechos de la persona autora. Puede ser utilizada para consulta o estudio personal, así como en actividades o materiales de investigación y docencia en los términos establecidos en el art. 32 del Texto Refundido de la Ley de Propiedad Intelectual (RDL 1/1996). Para otros usos se requiere la autorización previa y expresa de la persona autora. En cualquier caso, en la utilización de sus contenidos se deberá indicar de forma clara el nombre y apellidos de la persona autora y el título de la tesis doctoral. No se autoriza su reproducción u otras formas de explotación efectuadas con fines lucrativos ni su comunicación pública desde un sitio ajeno al servicio TDR. Tampoco se autoriza la presentación de su contenido en una ventana o marco ajeno a TDR (framing). Esta reserva de derechos afecta tanto al contenido de la tesis como a sus resúmenes e índices.

WARNING. Access to the contents of this doctoral thesis and its use must respect the rights of the author. It can be used for reference or private study, as well as research and learning activities or materials in the terms established by the 32nd article of the Spanish Consolidated Copyright Act (RDL 1/1996). Express and previous authorization of the author is required for any other uses. In any case, when using its content, full name of the author and title of the thesis must be clearly indicated. Reproduction or other forms of for profit use or public communication from outside TDX service is not allowed. Presentation of its content in a window or frame external to TDX (framing) is not authorized either. These rights affect both the content of the thesis and its abstracts and indexes.

Ultrafast electrohydrodynamic 3D printing with submicrometer resolution

IEVGENII LIASHENKO



DOCTORAL THESIS
2020

IEVGENII LIASHENKO

Ultrafast electrohydrodynamic 3D printing with submicrometer resolution

DOCTORAL THESIS

Supervised by **Dr. Joan Rosell-Llompart**
Dr. Andreu Cabot

Department of Chemical Engineering



UNIVERSITAT
ROVIRA i VIRGILI



Institut de Recerca en Energia de Catalunya
Catalonia Institute for Energy Research

Tarragona
2020



UNIVERSITAT
ROVIRA I VIRGILI

Escola Tècnica Superior d'Enginyeria Química
Departament d'Enginyeria Química
Avinguda dels Països Catalans, 26
43007 Tarragona (Spain)
Tel. +34 977 55 96 03
<http://www.etseq.urv.es/deq/>



Jardins de les Dones de Negre 1, 2^a pl.
Catalonia Institute for Energy Research
Sant Adria de Besos
08930 Barcelona (Spain)
T. + 34 933 562 615
www.irec.cat

Tarragona, 29th May, 2020

I STATE that the present study, entitled "Ultrafast electrohydrodynamic 3D printing with submicrometer resolution", presented by Ievgenii Liashenko for the award of the degree of Doctor, has been carried out under my supervision at the Department of Chemical Engineering (DEQ) of University Rovira i Virgili and at Catalonia Institute for Energy Research.

Doctoral Thesis Supervisors:

Dr. Joan Rosell-Llompart

Dr. Andreu Cabot

The work described in the thesis was carried out between May 2015 and May 2020 in the *Functional Nanomaterials* group at Catalonia Institute for Energy Research (IREC) led by Prof. Andreu Cabot and in the *Droplets, intErfaces, and floWs* group at University Rovira i Virgili led by Prof. Joan Rosell-Llompart. Experimental work was conducted in IREC facilities and funded by IREC.

Additional results obtained during the research stay (September 2019 - February 2020) in Prof. Paul Dalton group at Julius-Maximilian-University of Würzburg are presented in the Chapter 6 of the thesis.

Acknowledgements

Last 5 years during my PhD were the most challenging, creative, inspiring and fulfilling times of my life and I greatly appreciate such enriching and transformative experience. In the hindsight, that was definitely the best path I could take.

Foremost, I want to sincerely thank my Mentors: Prof. Joan Rosell-Llompart and Prof. Andreu Cabot for supporting me in any possible way and being a perfect example from which I could learn during all those years. Thanks, Andreu, for hiring me to spearhead our 3D printing efforts, providing everything necessary and supporting me financially through those years when I didn't have scholarship. Thanks to Joan for teaching me a lot about electrohydrodynamics and the encouragement you gave me before I decided to give it a try to this crazy jet-deflection idea. It was great to have two supervisors and to be exposed to two visions, and I thank both of you for giving me enough freedom to explore and pursue other extracurricular activities like InnoEnergy PhD school and research stay at Dalton Lab.

Thanks to many friends from the FN group who constantly provided great company, support, fun and smart conversations: Oleksandr, Taisiia, Michaela, Peter, Anthea, Alberto... and many others! My friends and colleagues from the DEW team, even though we rarely met, played a disproportionately important role and here I want to specially thank Nikolas, Eszter, Antonio, Elena, Laura and Prof. Jordi Grifoll.

I was lucky to learn another 3D printing technique and to work with its inventor Prof. Paul Dalton during a wonderful research stay at Dalton Lab. I want to thank Andrei Hrynevich for our surprisingly creative and fruitful collaboration, and all Biofab members for creating a pleasant working environment where ideas thrive.

I acknowledge great training opportunities provided by EIT KIC InnoEnergy PhD school, which gave yet another dimension to my PhD experience and equipped me with invaluable soft skills and entrepreneurial insights. I've met extraordinary people, took courses in best innovation hubs and business schools, and travelled a lot – nothing could have complimented my PhD experience in a better way!

Importantly, I want to thank all funding sources which made all this possible: grants 2017FI_B_01202 and Llabor-2018-003, SEHTOP ENE-77798-C4-3-R, BOOSTER ENE-46624-C4-3-R, Thermoflex, 2017-SGR-1516, 2017PFR-URV-B2-59, fellowship from EIT KIC InnoEnergy PhD school and Erasmus+ Traineeship Programme. I sincerely thank the European Union for all those opportunities I enjoyed, including my Master's grant from Erasmus Mundus Programme in European Rheology (EURHEO).

Also, I personally thank Sci-Hub for its effort "to remove all barriers in the way of science".

Finally, it all wouldn't be possible without the love and support from my Family. Thanks to Kseniia (and my cat Schweppes) for being an invaluable part of my life and distracting me from work when needed, and keeping me sane. Thanks to my parents for their love and care, and especially to my farther for nurturing my thirst of knowledge from early years.

...to my beloved parents...

“If you want to go deeply into any subject, you need a lot of time, and in particular you need the privilege of wasting time. You need to experiment with unproductive paths, explore dead ends, make space for doubts and boredom, and allow little seeds of insight to slowly grow and blossom. If you cannot afford to waste time, you will never find the truth.”

— Yuval Noah Harari

Contents

Summary	ix
List of publications	xi
Patent applications	xi
List of conferences	xii
Chapter 1 Introduction	1
1.1. Manufacturing.....	2
1.2. Additive manufacturing and its potential.....	3
1.3. Classification of AM technologies.....	6
1.4. Extrusion-based printing: advantages and limitations	8
1.5. Electrohydrodynamic jetting	10
1.5.1. History of invention	11
1.5.2. Electrospray and electrospinning	12
1.5.3. From electrospinning to EHD jet printing.....	14
1.5.4. Printing with continuous fiber vs. droplets	16
1.5.5. Conventional EHD jet printing: setup and control variables	19
1.5.6. Printing regimes and the challenge of positioning fast jets	23
1.6. Thesis aims and structure.....	27
1.7. References.....	29
Chapter 2 XY mechanical stage: a limiting factor for fast and high-resolution EHD jet printing	35
2.1. Introduction.....	37
2.1.1. Fundamentals of motion	38
2.1.2. XY mechanical stages.....	39
2.2. Methods	42
2.2.1. Simulated performance of an ideal XY stage	42
2.2.2. Examined XY stage.....	42
2.2.3. Actual performance of the XY stage	42
2.3. Results and Discussion.....	43
2.3.1. Simulated performance of a theoretical stage	43
2.3.2. XY stage	44
2.3.3. Maximum vs. gradual acceleration ramp	46
2.3.4. Speed while executing complex moves	50
2.3.5. Precision while executing complex moves	54
2.4. Conclusions.....	56

2.5. References	57
Chapter 3 Ultrafast 3D printing with submicrometer features using electrostatic jet deflection.....	59
3.1. Introduction	61
3.2. Methods.....	63
3.2.1. Chemicals	63
3.2.2. Inks formulation	63
3.2.3. Printer set-up and printing process.....	64
3.2.4. Set-up and software for electrostatic jet-deflection.....	65
3.2.5. Optical imaging.....	65
3.2.6. SEM imaging.....	66
3.2.7. Simulation of jet deflection.....	66
3.3. Results and Discussion	67
3.3.1. 3D printer design.....	67
3.3.2. Printing 2D patterns	70
3.3.3. Printing 3D objects	73
3.3.4. Charge dissipation	74
3.3.5. Solvent evaporation	77
3.3.6. Material versatility	80
3.3.7. Technology comparison	80
3.4. Conclusions	82
3.5. References	83
Supporting videos	86
Chapter 4 Parametric analysis and control of electrostatic jet deflection	87
4.1. Introduction	89
4.2. Methods.....	91
4.2.1. Finite element analysis.....	91
4.2.2. Experimental study of jet deflection angle	91
4.2.3. High-speed imaging and analysis	93
4.2.4. Acceleration of the deflecting jet.....	94
4.2.5. Signal generation and amplification.....	94
4.3. Parametric studies of jet deflection	95
4.3.1. Finite element study	95
4.3.2. Experimental study	100
4.4. Control of jet deflection	107
4.4.1. Software for controlling jet-deflection printing	108
4.4.2. Deformation correction	110
4.5. Conclusions	113
4.6. References	115

Chapter 5 In-line fiber speed control for EHD jet-deflection printing.....	117
5.1. Introduction.....	119
5.2. Methods	123
5.2.1. Printing setup description	123
5.2.2. Materials and inks preparation	124
5.2.3. Printing protocol and in situ inspection.....	124
5.2.4. Post-printing fiber inspection	125
5.2.5. Electric field simulation	126
5.3. Results and Discussion.....	127
5.3.1 Jet-deflecting electrodes configurations to control jet position	127
5.3.2 Jet speed from 2D patterns	128
5.3.3 Jet deflection method based on 3D structures	131
5.3.4 Operating regimes for the jet deflection method	134
5.3.5. Case study: Jet speed dependence on nozzle voltage	137
5.3.6. Case study: Jet speed determination in presence of jet instabilities	137
5.3.7. Simulation of in situ inspection system	139
5.4. Conclusions.....	141
5.5. References	142
Chapter 6 Unlocking the geometric freedom of melt electrowriting using microscale layer shifting	145
6.1. Introduction.....	147
6.2. Methods	149
6.2.1. Printer set-up and printing process	149
6.2.2. SEM Imaging	150
6.2.3. Mechanical Testing	150
6.3. Results and Discussion.....	151
6.3.1. Microscale layer shifting.....	151
6.3.2. Adjustable mechanical properties	153
6.3.3. Complex geometries enabled by layer shifting approach	154
6.3.4. Novel scaffold designs	158
6.4. Conclusions.....	163
6.5. References	164
6.6. ANNEX	166
General Conclusions	171
Future aims and Outlook	175

Summary

Additive manufacturing technologies based on layer-by-layer deposition of material ejected from a nozzle provide unmatched versatility but are limited in terms of printing speed and resolution. Electrohydrodynamic (EHD) jetting uniquely allows generating submicrometer jets that can reach speeds above 1 m/s, but such jets cannot be precisely collected by too slow mechanical stages.

Here, we demonstrate that through controlling the voltage applied to electrodes located around the electrified jet, its trajectory can be continuously adjusted to control the jet deposition location, thus allowing to print arbitrary 2D micropatterns. Extensive experimental study revealed that electrostatically deflected EHD jet can reach lateral accelerations up to 10^6 m/s^2 , greatly exceeding accelerations provided by best mechanical stages, which are limited to maximum 30 m/s^2 . The jet was found to be surprisingly resilient and stable even when being deflected at frequencies as high as 10000 Hz. Using high-speed imaging we conducted a parametric analysis, revealing the effect of deflection signal parameters and setup configurations on the deflection angle.

To control the printing and to locate arriving jet into 2D patterns, a custom-made software was developed to generate jet-deflecting signals. Through such electrostatic jet deflection, 3D objects with submicrometer features were printed by stacking nanofibers on top of each other at layer-by-layer frequencies as high as 2000 Hz. The fast jet speed and large layer-by-layer frequencies achieved translate into printing speeds up to 0.5 m/s in-plane and 0.4 mm/s in the vertical direction, which is three to four orders of magnitude faster than other additive manufacturing techniques providing equivalent feature sizes.

Accurate printing entails that the jet speed must be closely matched by the printing speed (i.e. jet-deflection speed). This, however, requires that the EHD jet speed is stable and precisely measured, in the first place. Current methods to identify the jet speed are cumbersome and involve powerful/expensive microscope techniques (such as SEM). Here we address this issue by proposing a novel method to determine the jet speed via jet deflection, which does not rely on resolving individual fibers. Advantageously, simple

optical imaging is enough to implement this method, and we demonstrate that it could be used in-situ to monitor the jet speed through image recognition.

When EHD jet can be made slow, such as in melt-based EHD jetting, XY stages are sufficient for printing structures that don't comprise small curvature radii (sharp corners). While most previous research involved unsophisticated pattern designs based on straight lines and vertical stacking of fiber-layers, here we introduce a novel method enabling to significantly expand the variety of possible printed geometries. By updating the printing path for each deposited layer, we demonstrate prints with complex geometries, such as overhangs produced without support structures, branching and texturing of fiber-walls, as well as nature-inspired designs and tailored scaffolds. We show that this powerful design approach also can be used to control the mechanical properties of the printed structures, which can be beneficial in a spectrum of value-added applications.

List of publications

1. Liashenko, I., Rosell-Llompart, J. & Cabot, A. Ultrafast 3D printing with submicrometer features using electrostatic jet deflection. *Nature Communications* 11, 753 (2020). <https://doi.org/10.1038/s41467-020-14557-w> (Impact factor 11.9)
2. Liashenko, I.*, Hrynevich, A.*, Dalton, P. Designing outside the box: Unlocking the geometric freedom of melt electrowriting using microscale layer shifting. *Advanced Materials*. 2020, 2001874. <https://doi.org/10.1002/adma.202001874> (Impact factor 25.8)
* - equal contribution
3. Liashenko, I., Cabot, A. & Rosell-Llompart, J. 2D and 3D printing with electrohydrodynamic jets with in-line fiber speed control.
To be submitted
4. Hrynevich, A.*, Liashenko, I.*, Dalton, P. The accurate prediction of melt electrowritten patterns from simple geometrical printing pathways.
To be submitted
* - equal contribution

Patent applications

Patents filed at the European Patent Office (EPO)

1. LIASHENKO Ievgenii, CABOT CODINA Andreu, ROSELL LLOMPART Joan.
Printing Device and Method.
(Application # 19382349.9, Priority date May 7th, 2019)
2. LIASHENKO Ievgenii, CABOT CODINA Andreu, ROSELL LLOMPART Joan.
Device and Method for Determining the Speed of Printing of a Fiber and the Length of a Printed Fiber.
(Application # 19382350.7, Priority date May 7th, 2019)

List of conferences

1. Ievgenii Liashenko, Andreu Cabot, Joan Rosell-Llompарт. Ultra-fast submicron resolution electrohydrodynamic additive manufacturing. [Poster and oral presentation] 14th Doctoral Day at University Rovira i Virgili, Tarragona (SPAIN), May 2017. Best poster award.
2. Ievgenii Liashenko, Andreu Cabot, Joan Rosell-Llompарт. Ultra-fast submicron resolution electrohydrodynamic additive manufacturing. [Poster + Abstract in the book of proceedings] Workshop on Fluid Mechanics 2017. Red Nacional para el Desarrollo de la Microfluídica, DPI2015-71901-REDT, Tarragona (SPAIN), July 20-21, 2017.
3. Ievgenii Liashenko, Andreu Cabot, Joan Rosell-Llompарт. Ultra-high resolution electrohydrodynamic AM technique with superior printing speed. [Poster C4-P-THU-P2-6] EUROMAT-2017 (European Congress and Exhibition on Advanced Materials and Processes), Thessaloniki (GREECE), September 17-22, 2017. (Symposium C.4: Additive Manufacturing.). Best poster award.
4. Ievgenii Liashenko, Andreu Cabot, Joan Rosell-Llompарт. Ultra-fast electrohydrodynamic 3D printing with submicron resolution. [Poster and oral presentation] 15th Doctoral Day at University Rovira i Virgili, Tarragona (SPAIN), May 2017. Best poster award.
5. Ievgenii Liashenko, Andreu Cabot, Joan Rosell-Llompарт. Ultra-fast electrohydrodynamic 3D printing with submicron resolution. [Poster] InnoEnergy PhD School Conference, Budapest (HUNGARY), October 3-5, 2018.

Chapter 1

Introduction

1.1. Manufacturing

Improving manufacturing technologies is critical for the production of goods with ever-improving properties, functionalities, economics and form-factors, and goes in lockstep with overall scientific and technological advancement. Any conceivable product must be designed with the capabilities of existing manufacturing methods in mind, otherwise it is doomed to stay in the realm of science-fiction. For this reason, the advancement in fabrication technology can be viewed as an essential driver of innovation and human well-being.

In the last century, manufacturing processes were developed towards increasing automation and miniaturization. Automation triggered the Industrial Revolution, enabling cheaper production methods and better-quality standards. On the other hand, miniaturization and continuous advancement in electronics resulted in the Information Revolution.

Miniaturization was greatly triggered by the Space Race, which had put severe restrictions on the mass and functionality of the payload. At that time, the cost of overcoming the pull of Earth' gravity well and lifting 1 kg of payload to orbit was astronomical¹. Even today, after drastic decrease achieved during the last decade, the cost is at least 2000 \$/kg². Curiously, the processing power and the memory available on the Apollo 11 computer, which successfully landed man on the Moon 50 years ago, is dwarfed by the processing power and memory of current mobile phones by a factor of 100.000 and 1.000.000³. This staggering progress in silicon-based electronics, named *Moore's law*^{4,5}, is possible thanks to photolithography⁶, which currently can manufacture transistors smaller than 10 nm⁷. However, this manufacturing technique also has limitations, especially in the realm of hot research topics, such as: flexible electronics⁸, soft robotics⁹, sensors¹⁰, microfluidics/lab-on-the-chip^{11,12}, tissue engineering¹³, thermoelectrics¹⁴ and energy applications¹⁵, where the use of established silicon-based technology is suboptimal. Its limited applicability can be explained by its high cost, use of aggressive chemistry and need of extremely clean conditions, limitations in manufacturing complex 3D shapes and materials which can be processed using this approach.

From the materials standpoint, the progress in nanotechnology resulted in abundance of functional nanomaterials, developed for any conceivable application. However, the grand and persisting challenge is how those advanced materials can be put into novel devices, and especially into the ones that can be 3D structured and made with high resolution. Low-tech methods like spin-coating or doctor-blade are insufficient for satisfying those challenges and new manufacturing methods must be devised.

1.2. Additive manufacturing and its potential

Contrasting with subtractive manufacturing, which involves removing sections of a material by machining or cutting it away, additive manufacturing is based on adding successive layers of material to create an object. Following ASTM (American Society for Testing and Materials) Standard #52900-15¹⁶, additive manufacturing is a “process of joining materials to make objects from 3D model data, usually layer upon layer”. The term *3D printing* is often used synonymously with additive manufacturing.

To print a desired part, it must first be designed using Computer-Aided Design (CAD). Alternatively, a CAD model can be obtained by scanning the existing part which has to be replicated or modified. Then, the CAD model is typically converted in stereo-lithography format (STL) where the shape is transformed and stored as triangulated surface. Then, depending on AM technique and printing parameters (such as preset layer height), such STL model is “sliced”, thus generating printing trajectories for each layer, which are often expressed as a G-code.

Additive manufacturing has become the new paradigm of distributed production of customized products and a motor of innovation, providing multiple advantages over traditional manufacturing techniques. AM allows geometric freedom of design leading to more complex and optimized products, improved material versatility and its economic utilization/reduced waste¹⁷⁻¹⁹. AM also enables facile product customization, rapid prototyping and shorter product-to-market time. Another advantage is a significant reduction in the number of manufacturing process steps, as different materials and components can be seamlessly integrated during AM. As a result, AM challenges existing business models and supply chains due to its disruptive nature, as it allows printing-on-

demand and printing at point-of-use, while product design can be easily shared electronically²⁰⁻²².

However, existing additive manufacturing approaches still have important technological limitations, especially on production speed, availability and combination of materials, and control over their microstructure and thus functionality. Additionally, the cost and complexity of manufacturing equipment that enables producing at high resolution are prohibitive for a true distributed production¹⁷⁻²². Also, due to the rapid progress and diversity of AM technologies, it currently lacks proper standardization/certification and sometimes reliable software, which may result in poor properties and reproducibility. Increasing the palette of available materials, printing speed and resolution are still important challenges to overcome before AM can become a ubiquitous tool, and this thesis contributes in this direction.

AM and 3D printing have been a focal point for much of scientific research and undergone rapid increase in the number of scientific publications, as shown on Figure 1a. Electrohydrodynamic (EHD) printing, which is at the topic of this thesis, is an AM technology with a potential to print at submicron scale with high speed a wide range of materials, and is discussed later in this chapter. As can be seen from Figure 1, both 3D printing and EHD printing, in particular, have received a lot of attention by the research community over last two decades. Over a 19-year period, compound growth in scientific output was 900% for AM/3D printing and 1500% for EHD printing, representing average annual growth of about 12% and 15.5%, correspondingly.

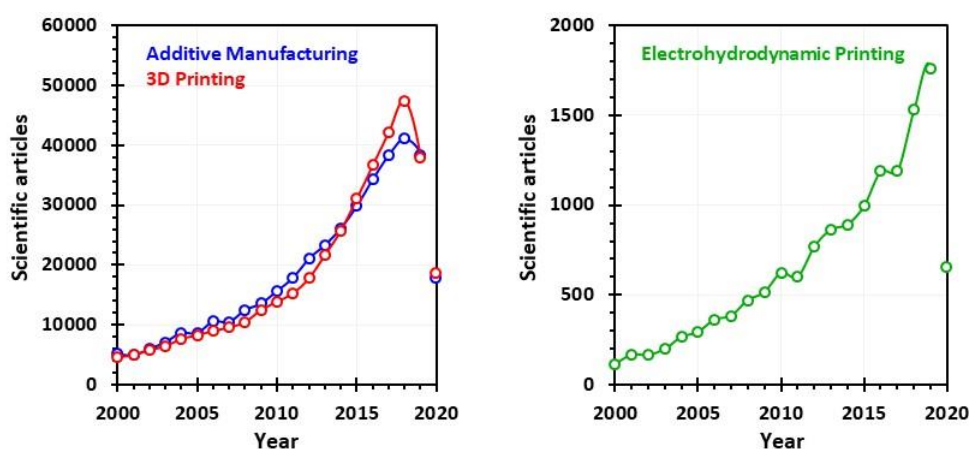


Figure 1. Impact of Additive Manufacturing on scientific research. Annual number of scientific publications from 2000 till 2020 in: **a** AM/3D printing and **b** EHD printing. Search

was performed in Google Scholar on May 2020, using keywords “additive manufacturing”, “3D printing” and “electrohydrodynamic printing” and represents the number of articles having keywords in title or in the text.

Beyond quantifiable measure of conducted research, 3D printing has also had a significant societal impact, and is often seen from the perspective of science-fiction. While such widespread interest and inspiration can be advantageous for overall technology advancement, for example by increasing its research funding, it also must be treated with care to objectively assess the state-of-the-art. One useful tool to decipher the maturity level of any particular technology is to observe its *hype cycle*. Gartner’s Hype Cycle is a graphical depiction of a common pattern that arises with each new technology or other innovation and is used to track technology maturity and future potential. The five phases in the Hype Cycle are Technology Trigger, Peak of Inflated Expectations, Trough of Disillusionment, Slope of Enlightenment and Plateau of Productivity. Figure 2 plots different technologies and applications of 3D printing and their current state on the hype cycle. Novel conceptual research ideas result in the appearance of new technologies, but their consolidation and maturation (Slope of Enlightenment) always requires thorough technological study. Note that different technologies may progress with various speeds towards their maturation and adoption, while some may fail before they can reach the market.

EHD printing is not mentioned in Figure 2 probably because it classifies 3D printing by the area of application, and not by the printing principle. In our opinion, EHD printing could be placed into Innovation trigger phase. Closest technologies which appear on the shown Gartner’s Hype Cycle are Nanoscale 3D printing, 3D printed wearables and 3D bioprinted organ transplants. All of them appear in the 1st phase, confirming our view.

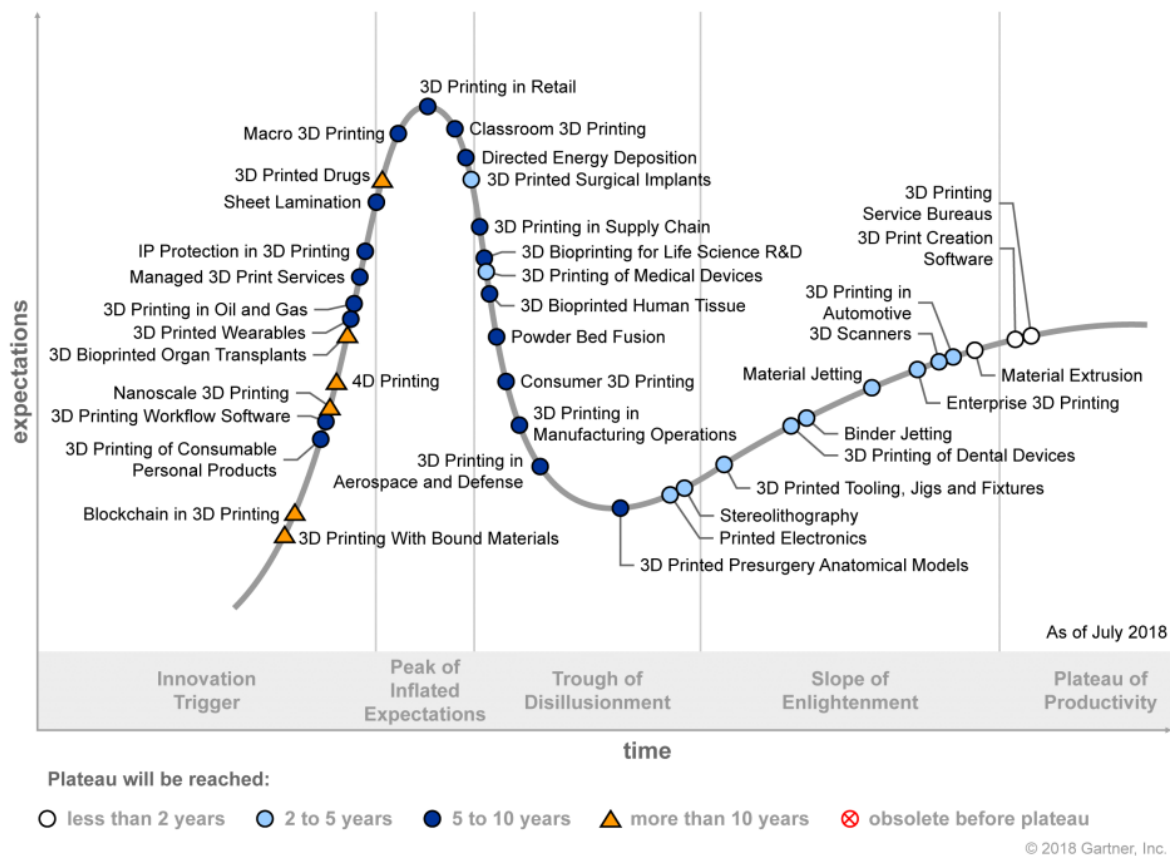


Figure 2. Gartner’s Hype Cycle for 3D printing technologies showing their relative maturity and ascend through the hype cycle. Adopted from <https://www.gartner.com/en>.

1.3. Classification of AM technologies

Additive manufacturing is an umbrella term uniting handful of technologies, which could be classified in a couple of ways to shed the light on their main concepts, used materials and operating principles. One classification of AM techniques is provided by ASTM standard #52900-15¹⁶, which distinguishes seven families of AM:

Table 1. Classification of AM technologies.

AM family	Operating principle	Technologies
VAT Photo-polymerization	A vat of liquid photopolymer resin is cured through selective exposure to light (via a laser or projector) which then initiates polymerization and converts the exposed areas to a solid part.	SLA™ - Stereolithography Apparatus DLP™ - Digital Light Processing 3SP™ - Scan, Spin, and Selectively Photocure CLIP™ - Continuous Liquid Interface Production
Powder Bed Fusion	Powdered material is selectively consolidated by melting it together using a heat source such as a laser or electron beam. The powder surrounding the consolidated part acts as support material for overhanging features.	SLS™- Selective Laser Sintering; DMLS™- Direct Metal Laser Sintering; SLM™- Selective Laser Melting; EBM™- Electron Beam Melting; SHS™- Selective Heat Sintering; MJF™- Multi-Jet Fusion
Binder Jetting	Liquid bonding agents are selectively applied onto thin layers of powdered material to build up parts layer by layer. Metal or ceramic powdered parts are typically fired in a furnace after they are printed.	3DP™- 3D Printing ExOne Voxeljet
Material Jetting	Droplets of material are deposited layer by layer to make parts. Common varieties include jetting a photocurable resin and curing it with UV light, as well as jetting thermally molten materials that then solidify in ambient temperatures.	Polyjet™ SCP™- Smooth Curvatures Printing MJM - Multi-Jet Modeling Projet™
Directed Energy Deposition	Powder or wire is fed into a melt pool which has been generated on the surface of the part where it adheres to the underlying part or layers by using an energy source such as a laser or electron beam. This is essentially a form of automated build-up welding.	LMD - Laser Metal Deposition LENS™- Laser Engineered Net Shaping DMD™- Direct Metal Deposition LENS™ – Laser Engineered Net Shaping
Sheet Lamination	Sheets of material are stacked and laminated together to form an object. The lamination method can be adhesives or chemical (paper/ plastics), ultrasonic welding, or brazing (metals).	LOM - Laminated Object Manufacture SDL - Selective Deposition Lamination UAM - Ultrasonic Additive Manufacturing
Material Extrusion	Material is extruded through a nozzle or orifice in tracks or beads, which are then combined into multi-layer models. Common varieties include heated thermo-plastic extrusion and syringe dispensing.	FFF - Fused Filament Fabrication FDM™- Fused Deposition Modeling

Another classification by the material form is possible, where separate classes are: *resin*-based, *powder*-based, *extrusion*-based and *droplet*-based systems. Yet another possibility is to distinguish AM methods between: *light*-based, *nozzle*-based and *particle/binder*-based. In either case, any classification includes a family of technologies where a material is extruded through a nozzle, which is of particular interest due to its material versatility.

1.4. Extrusion-based printing: advantages and limitations

Extrusion-based printing is based on material extrusion from a nozzle or orifice onto a printing substrate, thus forming a printed structure. The printed material is extruded by applying a pressure (also called back-pressure) to push the material through the nozzle, selectively deposited layer-by-layer as a continuous extruded filament. Curiously, there is at least one example of extrusion-based printing in Nature: spiders. Spiders weave complex 3D structures by ejecting a low-viscosity protein solution²³ from their “nozzles”, which undergoes rapid solidification and forms silk filaments. Depending on the spider species, the diameter of such silk threads ranges from 10 nm to 10 μm . There have been attempts to mimic the Nature and engineer similar solutions to print at microscale, but it has been challenging to use concentrated inks with thin nozzles²⁴.

Besides low cost and simplicity, the main advantage of nozzle-based 3D printing strategies is that they allow the manufacture of items made of virtually any substance, ranging from polymers²⁵, to metals²⁶, to ceramics²⁷, to wood²⁸, and even to biological tissues²⁹. Such unmatched material versatility stems from the use of metal or polymer melts or solvent-based inks, which can be formulated to contain any component in the form of ions, molecules, nanoparticles, or even living cells³⁰.

The drawbacks of extrusion-based techniques stem from the need to push the printed material through the nozzle. The inner diameter of the nozzle strongly influences the volumetric flow rate at the same applied pressure. For example, for viscous Newtonian fluid, this dependence is governed by the Hagen-Poiseuille equation³¹, which shows that the volumetric flow rate is inversely proportional to the nozzle' inner diameter to the power of four. This explains the drastic increase in pressure drop and the decrease in the ink flow rate as nozzle width is reduced. Therefore, using progressively thinner nozzles to print smaller features becomes unfeasible.

Another aspect of direct writing^{16,25,31} is that the printed material must be sufficiently solid once deposited, allowing to build a 3D structure with high fidelity. When printing with melts, this can be achieved via rapid cooling and solidification of the printed material. In the case of solutions, sufficiently fast solidification through evaporation is usually challenging, requiring the use of inks with tailored rheological properties to limit their

subsequent flow after deposition. For example, an ink can be formulated to contain large fraction of polymer or particles, thus increasing its storage modulus (elasticity) or exhibiting a yield stress. The use of materials having a yield stress is convenient, as material can be designed to not reflow when low stress is applied (when deposited on the surface), but to readily flow when the stress exceeds its yield stress (when it is pushed through the nozzle). Additionally, shear thinning non-Newtonian fluids can be used to decrease the pressure drop when the ink is forced through the nozzle. In general, controlling the rheological properties of the ink, and thus its printing fidelity, requires a lot of trial and error to achieve desired ink performance.

Additionally, known rheological effects from non-Newtonian fluids may occur, causing further challenges. For example, polymeric melts or concentrated solutions frequently exhibit *die swelling*, also known as the Barus effect (Figure 3b). When a polymeric stream is forced through a nozzle, polymeric chains get stretched, temporarily storing this mechanical stress. Once the polymer exits the nozzle and the force is removed, the stretched polymeric chains bounce back to their normal conformation, and the jet swells. From a processing perspective, the extruded jet becomes thicker, sometimes much thicker, than the inner diameter of the nozzle, which impacts printing resolution. While it can be accounted by using smaller nozzle, it will require drastic increase in pressure requirements.

Recently, attempts were made to bypass some of the abovementioned challenges. One such strategy is based on using low-viscosity ink which gets crosslinked as it travels through a transparent nozzle and is irradiated to trigger crosslinking³². This allows to increase the ink flow rate (and jet speed) while improving printing fidelity and resolution, as well as avoiding Barus effect³³. Such creative approach hints that the extrusion-based approach can be further improved in the future.

Despite of the recent progress in extrusion-based printing, main challenges persist and seem insurmountable for printing using nozzle apertures smaller than several tens of micrometers. Thinner nozzles not only drastically increase viscous losses, but are also prone to clogging, which obviously limits possible ink compositions. To make matters worse, the smaller the nozzle and the jet thickness get, the slower the printing process.

1.5. Electrohydrodynamic jetting

To effectively reduce the width of the printed lines, instead of forcing the extrusion of material through very thin nozzles, the melt or ink can be pulled by means of an electric field applied between the nozzle and the printing substrate (Figure 3c-e). Once the electrical stresses acting on the liquid surface overcome the surface tension stress, the liquid meniscus deforms into a Taylor cone (Figure 3c) wherefrom a thin and fast jet of ink is propelled electrostatically towards the printing substrate³⁴. This structure is often called cone-jet. Such EHD jetting strategy is uniquely suited for high resolution 3D printing compared to other nozzle-based 3D printing method. EHD jetting allows printing submicrometer features with no risk of nozzle clogging, as it enables the generation of nanometer-sized jets from wide nozzle apertures using a great variety of inks, with viscosities ranging over several orders of magnitude³⁵.

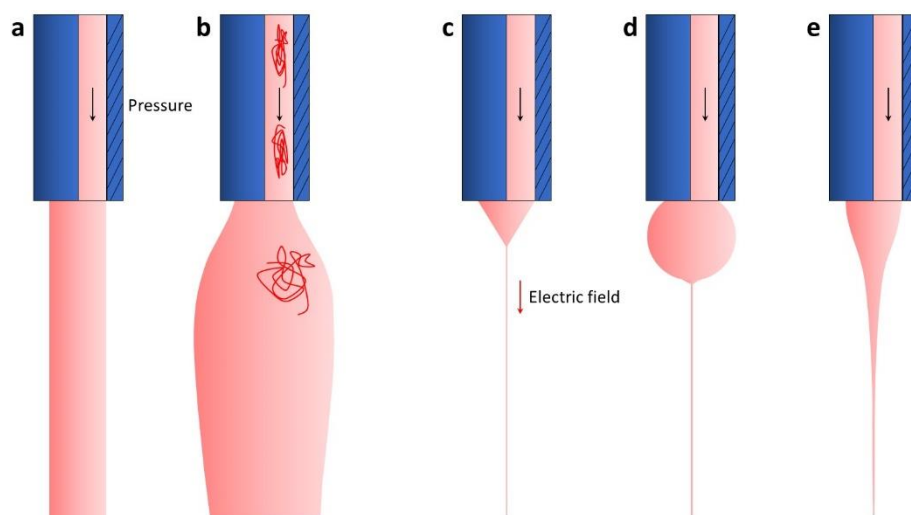


Figure 3. Pressure-driven extrusion vs. EHD jetting of printing material. **a** Ideal case of pressure-driven extrusion when the jet diameter is the same as the inner diameter of a nozzle. **b** Die swelling (the Barus effect) of polymer melts due to the relaxation of stretched molecules. Application of strong electric field pulls the material into a fine and fast EHD jet (**c-e**). **c** Classical shape of the Taylor cone observed for low-viscosity liquids. **d** Typical shape of EHD jet for liquids with medium viscosity, such as used in solvent-based EHD jetting. **e** Gradual cone elongation typical for high-viscosity liquids, such as polymeric melts.

1.5.1. History of invention

The EHD phenomenon was first observed as EHD atomization or *electrospray*, and recorded by William Gilbert in as early as 1600^{36,37}. He observed that when electrically charged piece of amber was brought close to a droplet of water, the drop formed a cone shape and small droplets were ejected from the tip of that cone. Later, in 1750, Jean-Antoine Nollet demonstrated that water stream under high voltage aerosolizes when brought to the Earth-ground vicinity³⁸. Another fundamental work was conducted Lord Rayleigh, who theoretically evaluated the maximum charge that a spherical liquid drop can carry, also known as the “Rayleigh limit”³⁹⁻⁴⁰. The cone-jet was first photographed by John Zeleny in 1914⁴¹ and its conical part was later mathematically described by Sir Geoffrey Taylor⁴² and was subsequently known as “Taylor cone” in honor of his contribution. In the 1980’s John B. Fenn showed how electrospray atomization can be used for introducing large non-volatile molecules into the gas phase, which revolutionized electrospray ionization mass spectroscopy of biological macromolecules⁴³. John Fenn won the Nobel Prize in Chemistry in 2002 and gave a Nobel lecture titled “Electrospray Wings for Molecular Elephants”⁴⁴.

Interestingly, EHD was first used for printing in 1867 when William Thomson, 1st Baron Kelvin, patented *The Siphon Recorder*⁴⁵. In that device an ink was printed on a moving paper tape via electrospraying the ink just above its surface. This printer automatically recorded incoming telegraph messages as a wavy line printed on the paper tape, as shown in Figure 4, predating ink-jet printing by at least 100 years! This was a breakthrough at a time, because previously message recording had to be done continuously in-situ by two operators, thus the process was greatly simplified by reading the printed message. Curiously, the printing principle was based on the oscillation of the nozzle, where Morse code of a received signal (dots and dashes) was used to actuate the coil, which pulled and deflected the nozzle through a silk thread, thus resulting in printing wavy line. Such wavy line then was decoded by the operator into a readable message.

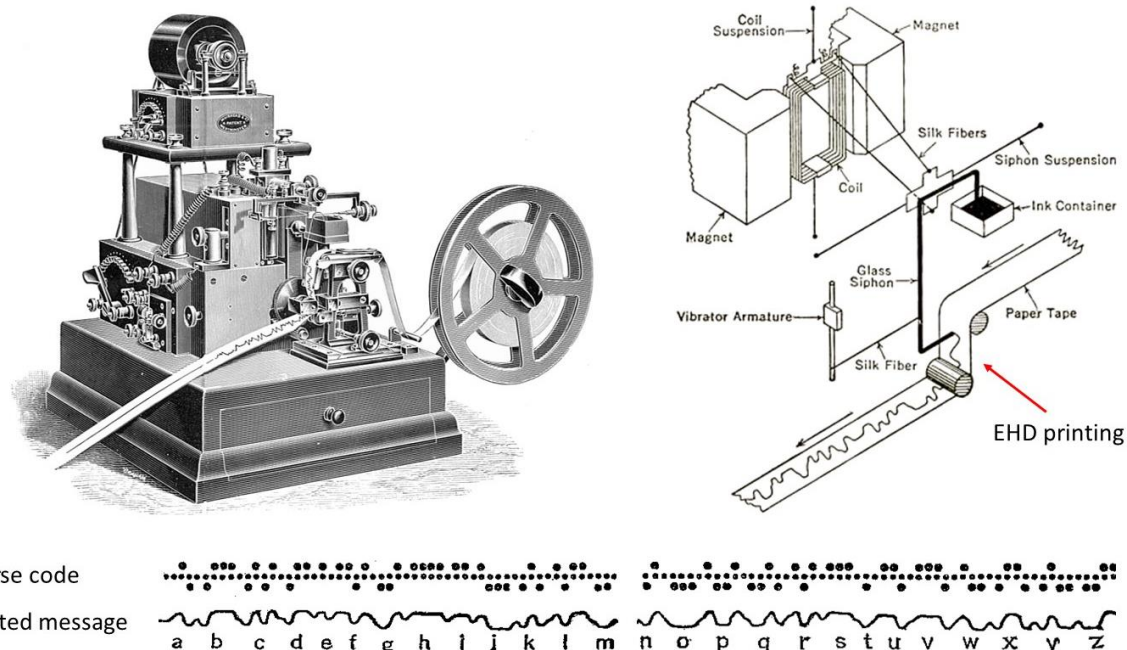


Figure 4. Siphon recorder for an automatic recording of incoming telegraph messages.

Contrary to electrospay, viscous liquids can be electrospun into continuous filaments or fibers, which was first described in 1887 by Sir Charles Vernon Boys⁴⁶. The process of electrospinning was patented in 1902 by J.F. Cooley⁴⁷ and W.J. Morton⁴⁸. In 1938 Nathalie Rozenblum and Igor Petryanov-Sokolov first used electrospun fibers for filtering applications⁴⁹. Later, the new resurgence of the EHD field was triggered by the work of Darrell Reneker in the 1990's.

1.5.2. Electrospay and electrospinning

Both electrospay and electrospinning have been known for many decades and have found numerous applications. While electrospay and electrospinning has provoked a lot of interest from the research community and became well-established techniques, still much remains unknown about them. The underlying physics of EHD jetting is notoriously complex, involving numerous electrical effects, fluid mechanics, rheology, chemistry, polymer science, heat and mass transfer, etc., which explains the challenge of developing a complete and accurate model for such multifaceted phenomena. On the other hand, in last decades, extensive experimental studies shed light on many underlying phenomena occurring during EHD jetting. Partially this became possible thanks to the use of powerful microscope techniques, such as scanning electron microscope (SEM) and transmission

electron microscope (TEM), which allowed to examine both the shape and size of produced particles/fibers, as well as the use of X-ray diffraction (XRD) to reveal their chemical composition. Additionally, extremely high speed of EHD jetting and jet breakup posed further challenges toward studying the underlying physics. In this regard, high-speed imaging, which became more available in this last decade, greatly helped in those endeavors.

In general, the key feature inherent to EHD jetting techniques (i.e. electrospray and electrospinning) is the ability to generate large surface area from small amount of material (large specific surface area). Such capability of overcoming surface tension forces and increasing the surface area of a free liquid interfaces is hard to match using any other approach.

When using low-viscosity liquids, EHD jet experiences periodic varicose instabilities and further breaks up into the train of droplets, typically having bimodal size distribution: the main droplets and the, smaller, satellite droplets. Those droplets repel each other due to their electric charges, which results in the separation of their trajectories and forms the electrospray plume. As the airborne droplets travel towards the collector, they may evaporate and shrink to the point when their charge-to-volume ratio exceeds the Rayleigh limit. The same forces that resulted in the Taylor cone formation, now act to create a secondary in-flight jet emission from the droplet itself, known as “coulombic explosion”⁵⁰. The progeny droplets generated by the Coulombic explosion are much smaller than the primary droplet. Micro- and nanoparticles form upon drying of those airborne droplets and get deposited on the collector. The effect of electrospray parameters on jet breakup and Coulombic explosion was previously studied⁵¹, allowing to engineer the size, size distribution and surface morphology of the collected particles⁵². The electrospray is used for generating tailored particles for pharmaceutical, food and cosmetic applications⁵³⁻⁵⁵. Furthermore, the production rate can be increased via setting an array of nozzles and particles can be loaded with a drug or bio-sensitive molecules⁵⁶. Such advances will ultimately bring electrospray closer to commercial viability, allowing to produce micro- and nanostructured materials with controlled composition and performance.

When using high-viscosity liquids, the viscosity of the jet inhibits the varicose instability that leads to jet breakup³⁴. The airborne continuous jet is further stretched by the electrical

stresses and is further accelerated towards the collector. Such persistent elongation of the jet may result in a very fine and fast jet, with jet diameter as small as c.a. 100 nm and speed as high as c.a. 10 m/s⁵⁷. The whipping motion of an electrospun fiber caused by the kink instability, also known as bending instability⁵⁸, as it flies toward the collector, is a characteristic of electrospinning, which leads to the deposition of fiber in random orientations, forming a non-woven fiber mat⁵⁷. Various functional materials can be electrospun, such as polymers, polymer blends, precursors, nanoparticles, etc. Electrospinning provides a powerful route to producing inorganic nanofibers for a plethora of applications, as active elements in sensing, as membranes for separation and purification, as substrates in catalysis, as components for composite reinforced materials, and as electrodes in energy conversion or storage devices that include batteries, solar cells, and actuators⁵⁹. Hollow nanofibers were also produced and are particularly useful for nanofluidics and hydrogen storage. Highly porous nanofibers allow to further increase the surface area, which is especially beneficial for applications like filtration and absorption, fuel cells and solar cells, catalysis and batteries, as well as tissue engineering.

Even though electrospun mats with random fiber orientation have already found use in many applications, the random nature of collected fibers is detrimental for many other potential applications. For example, electronic and photonic devices, as well as fiber-based reinforcement require well-aligned fibers, where fiber orientation is essential for controlling electrical, optical or mechanical properties. In response to this need, simple methods to collect aligned fibers were developed. One such method is based on fast-rotating cylinders or frames, which elongate the fiber and collect it in aligned manner⁶⁰. Another approach is to use a pair of split electrodes as a collector, thus forcing the whipping fiber to be attracted by one or another electrode, thus spanning the distance between them as aligned fibers⁶¹. Yet another possibility is to control the fiber whipping direction by placing two insulating blocks around the jet⁶².

1.5.3. From electrospinning to EHD jet printing

As electrospinning became widely used for various materials and applications, and even allowed the collection of aligned fiber mats, it became apparent that it can be further developed for the precise microfabrication applications, such as for electronic components,

flexible electronics and bioengineering. For such applications, single electrospun fibers must be printed in a controlled manner, following a preset 2D trajectory. Traditional electrospinning techniques, both solvent-based and melt-based, were not suited for the task of direct writing fibers, and thus were substantially modified to meet this requirement.

The primary challenge which had to be addressed for the controlled fiber deposition was to eliminate or inhibit the bending instability inherent to electrospinning. In electrospinning, the EHD jet is straight for some distance before it develops kink instabilities⁶³, caused due to the stretching of the jet and the repulsion between the charged parts or the jet. The simplest and the most effective approach was to decrease the nozzle-to-collector separation, from more than 10 cm typically used in electrospinning, to less than 1 cm. This modification, often called *near-field electrospinning* (NFES), allowed the production of a straight and stable jet, depositing at a predictable location on the collector⁶⁴. Furthermore, this drastic decrease in the separation distance also allowed to use much smaller voltages to produce the EHD jet, which had an additional benefit of decreasing its speed. Such improvements opened an interesting perspective for the realization of position-controlled deposition and precise integration of individual fibers within devices, which greatly expanded the application field of NFES ranging from nano-generators, microbatteries, wearable sensors, nanodevices and microelectromechanical systems, to tissue engineering applications.

Further information on the invention of NFES, an overview of printed materials and applications, as well as a summary of remaining challenges and development directions can be found in excellent review on the topic: “Near-field electrospinning: progress and applications”⁶⁵. As well, the breathtaking progress in *melt electrowriting* (MEW) was recently summarized in “The Next Frontier in Melt Electrospinning: Taming the Jet” by its inventors Prof. Paul Dalton and Prof. Dietmar Hutmacher⁶⁶.

It must be pointed out, that in this work we generally refer to near-field electrospinning and melt electrowriting as *EHD jet printing*. We believe that *EHD jet printing* is a more universal terminology which has printing as its goal, rather than emphasizing the fact that this technology was historically derived from electrospinning. Furthermore, we believe that the term EHD jet printing allows a better generalization of the research challenges, which are fundamental to both solvent-based and melt-based EHD jet printing (commonly termed

near-field electrospinning and *melt electrowriting*). The objective of this doctoral thesis is thus to contribute to the fascinating field of EHD jet printing by solving some of its persistent challenges. Next, we describe the advantages of printing with fiber vs. droplets, discuss the common setup design and printing parameters, and differentiate various printing regimes.

1.5.4. Printing with continuous fiber vs. droplets

In continuous EHD jet printing a thin jet is ejected and propelled toward the printing substrate, where it is deposited as a continuous fiber having no breaks. This feature differentiates EHD jet printing from drop-on-demand (DoD) printing, where a multitude of droplets are generated and propelled towards a printing substrate. While DoD printing can reproducibly create electrically charged microdroplets or even nanodroplets which are readily collected on the substrate, the ink flow rate at which the production of droplets can be stabilized is very low, and it decreases as the droplet size is decreased (thus increasing printing resolution)⁶⁷. Another reason behind using very low flow rates is the necessity to accurately position the drops onto the moving substrate. To evaluate the printing rate of transparent electrodes by the DoD method⁶⁷ we estimated that printing 1 mm² of such electrodes would require ≈30 years of uninterrupted printing. Therefore, although the DoD technique has demonstrated outstanding printing resolution and positioning control, its inherent slow printing rate renders it impractical for industrial applications. To overcome this problem of slow printing, the use of continuous EHD jets deposited as lines is a better option⁶⁸.

While continuous jet must be generated in a continuous fashion, a multitude of droplets can be generated either continuously or intermittently (“on demand”), depending on the ejection mechanism:

1. Intermittent droplet generation (DoD) can be actuated by applying bursts of energy to liquid interface, overcoming the surface tension, thus ejecting a portion of liquid ink and propelling it away from the liquid interface. Such intermittent or “on demand” droplet formation is based on creating a pressure wave strong enough to overcome surface tension and to separate a portion of ink from the liquid interface. Multiple phenomena can be used

to trigger such pressure wave, such as: piezoelectric, thermal, acoustic, etc., and were extensively studied and applied in ink-jet printing.

2. Continuous droplet generation is achieved by first forming a continuous jet of ink, which subsequently undergoes Plateau–Rayleigh instability, where the surface tension forces develop swells on the jet which grow in time, eventually breaking off into separate ink portions or droplets. Such jet breakup is spontaneous, but can also be controlled/triggered by feeding sound waves to the jet.

Liquid breakup happens by the action of surface tension forces (working towards minimizing the surface area), and is retarded by the action of viscoelastic forces. The relative importance of these forces, thus the jet breakup behavior, strongly depends on ink composition. For some inks, such as polymer melts, jet breakup typically does not occur due to high viscosity of polymeric melts, as well as elasticity (tension stresses) which builds up when such inks are stretched.

In this thesis, a continuous jet is used for printing of 2D patterns and 3D structures, where resolution and the speed of printing are essential advantages over previously known methods. To increase the throughput of solid material deposited on the printing substrate, inks with high content of solid constituents are favored. Advantageously, such inks tend to be very viscous (many orders of magnitude over the inks used for printing in using droplets formed from jet breakup) and thus effectively prohibit the jet breakup by the Plateau–Rayleigh instability. Furthermore, certain ink components, such as polymers with high molecular weight or with branched molecular chains, significantly increase ink viscosity (even when added in small concentrations) and thus either preclude droplet formation, or must be present in minimal concentrations, which has the disadvantage of drastically decreasing the printing speed.

Furthermore, at equal resolution or width of the printing line, continuous jetting is advantageous because it can carry more volume of ink compared with intermittent jetting of droplets, where the jet is effectively interrupted between ejecting ink portions (switched on and off, where no material is ejected for large portion of pulsing period). Additionally, continuous droplet generation has the disadvantage that droplet diameter is always larger than the jet diameter, which is detrimental to the printing resolution, or requires smaller

jets for the same printing resolution than printing based on continuous-fiber deposition. This situation becomes even worse when droplets impact on the printing substrate and splash, increasing the contact area and further decreasing printing resolution. On the other hand, sufficiently solid fiber typically keeps its shape when deposited, resulting both in smaller voxel size and much higher aspect ratio, which is essential for microscopic 3D printing.

Continuous fiber deposition has yet another benefit for 3D printing of continuous features, such as lines and walls obtained by stacking of multiple fiber-layers. Such continuous features are useful in applications such as electronics, for creating conducting paths/electrodes, and scaffolds for tissue engineering, for example. On the other hand, to obtain such features by printing of droplets, multiple droplets must be carefully positioned next to each other, which is a disadvantage which only gets more persistent as the printed pattern becomes more complex (for example, as a wall becomes taller). This is due to the “autofocusing effect”⁶⁹ which attracts electrically charged droplets to places such as the crossing of 2 walls and results in printing defects such as pillars located on those crossings. Such challenges in the fidelity of the printed structure can be overcome by printing with a continuous fiber.

An additional benefit of fiber vs. droplet printing is the possibility to fabricate composite fibers from multiple materials, either by varying the fiber composition along the fiber length (switching printing materials) or by creating multiple material fibers (such as core-shell or empty tubes) by simultaneously feeding multiple materials through the nozzle, forming a compound jet⁷⁰. Yet another benefit of fiber printing is that a sufficiently solid fiber can be suspended between two contact points in three dimensions, which can be hardly achieved by droplet-based printing.

Concluding, multiple benefits of printing with continuous fibers over printing using droplets are higher printing speed, higher resolution, higher freedom in ink formulation, and better 3D printing fidelity especially when 3D printing continuous features. Motivated by these advantages, in this work we have focused on continuous EHD jet to print in 3D.

1.5.5. Conventional EHD jet printing: setup and control variables

Electrohydrodynamic (EHD) jet printing, sometimes referred to as e-jet printing, is a high-resolution printing technology where an ink jet is driven by an electrostatic field to print predefined designs. EHD jetting has been used with mechanical translation of the substrate or the nozzle to position the jet at predefined locations on a substrate, thus enabling the printing of solid items from predefined designs²⁴. We refer to conventional or stage-driven EHD jet printing as the creation of such items by using a translation stage to position the EHD jet on the substrate. Figure 5 schematically shows the elements of such a printer, while the EHD 3D printing setup used in this study with unconventional elements is presented on Figure 6.

The EHD jetting phenomenon generates a fast moving and fine ink jet, which is collected on a substrate. The ink flows out of a channel through a small opening, referred to as nozzle. We refer to a collected jet as fiber. Virtually any liquid may be used for EHD jetting, which we will refer as ink. This ink may typically comprise any suitable combination of solvents, polymers, inorganic precursors, particles, and living cells.

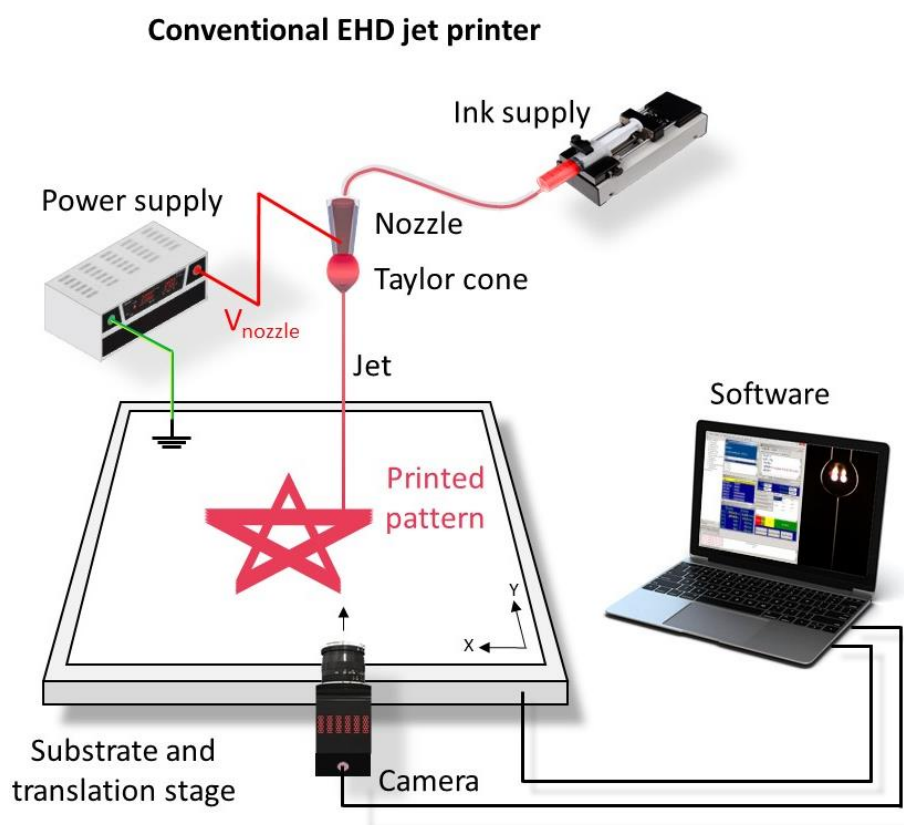


Figure 5. Schematic of conventional EHD jet printer.

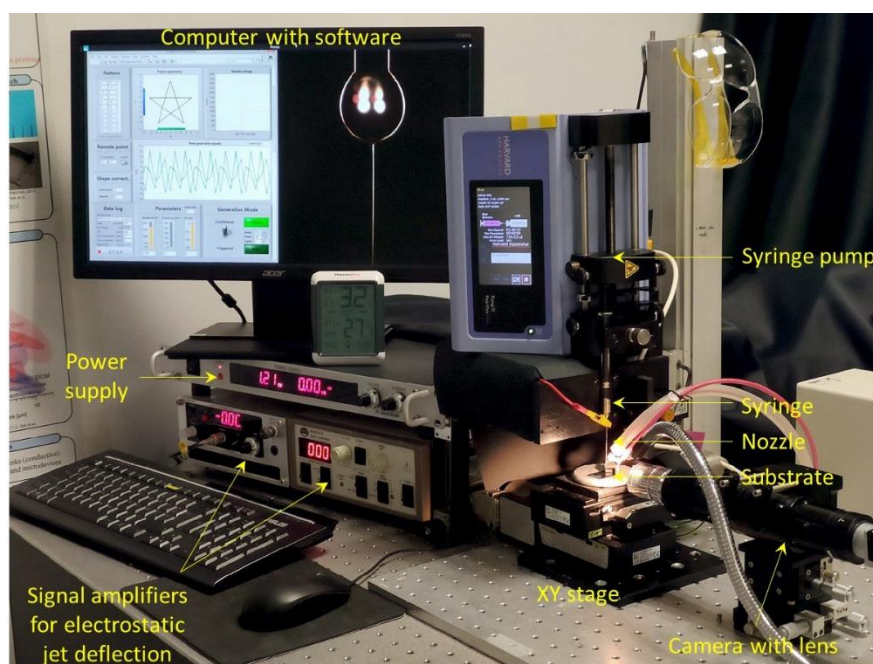


Figure 6. EHD printer setup used in this study with solvent-based inks (Chapters 3-5).

The ink flow rate is the volumetric rate at which liquid ink is supplied from a reservoir to the exit of the nozzle, and usually it is independently controlled. In the case when the ink is a melt (from a room temperature solid, for example a molten polymer), a heating system is incorporated to the reservoir and the nozzle to maintain the ink in a molten state. The nozzle is a thin tube which can be made of conductive material (e.g. stainless steel) or insulating material (e.g. glass) and typically is square cut (blunt ending) at the drop end. The pendant drop is formed by the ink accumulated at the exit of the nozzle. Electrical contact between power supply and pendant drop of liquid ink is necessary. This is typically done by either a wire connected to a power supply on one end, and to the ink or electrically conductive nozzle on the other end. An insulating nozzle can be made conductive by covering with an electrically conducting material, such as gold or platinum, where the electrical path to the liquid drop is ensured at the tip.

The diameter of the opening of the nozzle influences the electrostatic field around the pendant drop. Faster and thinner EHD jets are typically obtained using nozzles of smaller diameters, which concentrate electrical stresses at the Taylor cone.

The range of ink flow rates is different depending if the jet is produced from a solution or a melt. Melts typically solidify on-the-fly due to the cooling of the jet. Heating temperature,

melt flow rate, ambient temperature and the nozzle-to-substrate separation all influence the rate of melt solidification. Arriving fiber can have different degrees of solidification, which is useful to control its adhesion to the previously deposited fiber. Sufficiently solid fibers can be easily suspended spanning considerable gaps. The ability to generate fibers of varying diameters was demonstrated via drastic change in melt flow rate, ranging from 0.8 to 50 μm^{71} . Such wide range of ink flow rates and obtainable fiber diameters is an advantage of MEW over solvent-based EHD jetting. Another advantage of MEW is the high stability of the printing process, which is probably due to high melt viscosity and simpler physics of solidification by cooling compared to the complex phenomena associated with the solvent-based electrified jets.

For solvent-based EHD jets, solvent evaporation from the pendant drop and the airborne jet is a critical for controlling the stability of the jet and the fidelity of a printed structure. Solvent evaporation is a complex phenomenon depending of plethora of factors. One factor is the size of the pendant drop influences the surface area of ink/gas interface and thus defines the evaporation rate of any volatile solvent present in the ink from the pendant drop. Still ambient air typically surrounds the liquid drop. However, better control over evaporation rate can be achieved by supplying a gentle stream of another gas (such as synthetic air, nitrogen, carbon dioxide) which does not perturb the jet trajectory. Additionally, evaporation rate is influenced by the pendant drop's temperature, the surrounding gas temperature, the solvent vapor concentration in the gas phase (relative humidity, when the solvent is water), and by ink composition. To control (increase or reduce or suppress) the rate of solvent evaporation, a gas stream containing a controlled amount of solvent vapor can be introduced around (coaxially) or in the vicinity of the jet. In addition, a gas stream can be introduced coaxially to the pendant drop at the exit of the nozzle, to shield the ink from ambient moisture. This is useful to prevent that ambient moisture gets absorbed by the ink, when it causes unwanted effects such as the precipitation of one of its solutes, or the separation into different phases⁷². On the other hand, such precipitation or separation may be a desired effect.

The gas composition can also be important to prevent electrical discharges. When using high surface tension inks (such as, for example, water-based suspensions) electrical gas discharges can sometimes take place when creating strong enough electrostatic fields in

the ink's vicinity between the nozzle and the substrate. Such discharges can be arrested (prevented) by using a high breakdown potential gas, such as carbon dioxide (CO₂) or sulfur hexafluoride (SF₆). However, to our knowledge, gases other than air have not been used in EHD printing experiments.

For continuous jet generation, ink composition needs to satisfy rheological requirements: the ink should be viscoelastic enough to prevent the breakup of the jet into fragments or droplets; and the ink should dry fast enough during its flight, to get deposited as an effectively solid (vitreous jet or rubbery jet with sufficient firmness and stability), which we refer to as fiber. When the deposited jet is substantially liquid (lacking enough viscoelasticity and still able to flow after deposition), the jet will typically accumulate forming undesired deposits such as big droplets on the substrate⁷³.

To generate the jet from the pendant drop, an electrostatic field is established between electrically charged nozzle and electrically grounded substrate. The jet is generated and accelerated towards the substrate by the electrostatic field set between the nozzle and the substrate. Alternatively, the same effect can be reached by electrically grounding the nozzle and applying a voltage to the substrate. These configurations for applying the voltage, as well as its polarity are not strictly equivalent and were shown to influence the EHD jetting⁷⁴. Another possibility is to apply a voltage between the nozzle and a ring extractor electrode, which could be placed near the pendant drop⁷⁵.

The nozzle-to-substrate separation should be large enough to allow sufficient solidification of the jet before it gets deposited on the substrate, but it should be small enough to prevent jet whipping (see section 1.5.3.). The nozzle-to-substrate separation is usually under 10 mm in EHD jet printing and typically between 3-5 mm (hence the name *near-field* electrospinning).

Power supply applies voltage to the nozzle/pendant drop. If the voltage is sufficiently high, the pendant drop gets deformed to a pointed tip called Taylor cone wherefrom a single jet is ejected towards the substrate. The shape of the Taylor cone varies greatly depending on ink properties, typically adopting a nearly-conical shape for low-viscosity inks (Figure 3c) and a pendant drop shape for solutions with medium viscosity (Figure 3d), while polymeric melts usually result in a profile with gradual transition from the nozzle diameter to the

diameter of deposited fiber (Figure 3e). The jet flies from the jet-ejection point on the pendant drop to the substrate. As the jet is accelerated due to the pulling by the electrical stresses, its cross-sectional area decreases.

The diameter of the collected jet (i.e. fiber diameter) is influenced by various factors, most importantly by the ink composition, evaporation rate of its volatile components, and the stretch rate caused by electrical stresses. Solution-based and melt-based EHD jet printing have different ranges of fiber diameters⁶⁵. Fibers formed from polymer melts range in diameter between 0.5 μm and 200 μm , more typically in the range between 1 μm and 30 μm . Fiber diameters from solvent-based inks range between 0.010 μm , and 10 μm , more typically between 0.05 μm and 2 μm .

The fiber collection speed, namely the length of the jet that arrives to the substrate per unit time, depends on several parameters: ink composition and rheological properties, ink flow rate, evaporation rate (or solidification rate in case of melt), electrostatic field strength and nozzle-to-substrate separation.

1.5.6. Printing regimes and the challenge of positioning fast jets

One of the greatest current challenges of material jetting technologies (Table 1) is to controllably deposit materials as very small 2D (two-dimensional) and 3D (three-dimensional) items at high speed. Currently EHD jetting is combined with mechanical translation of the substrate or the nozzle, to print patterns on a substrate. To print a preset design with proper accuracy by this method, the EHD jet speed as it approaches the substrate and the speed of stage translation must be matched, because when the jet is generated faster than it is properly positioned on the substrate, it accumulates on the substrate in an uncontrolled manner. EHD jets can be generated to move at speeds in the range between 0.5 and 5000 mm/s, but conventional EHD jet printing systems cannot utilize this entire range because they do not provide enough acceleration, limiting the speed and resolution in both 2D and 3D printing. Very accurate printing can be done by proper mechanical translation stages when the jet speed is low enough, but the accurate deposition of small items using a translation stage is then too slow to be industrially relevant.

The intended printing speed is the preset speed at which the predefined design (e.g. a motif) is intended to be produced forming the printed item. In the prior art, to print a predefined design, typically the substrate is translated in the XY plane using a mechanical translation stage while the nozzle is fixed. In this case, the maximum allowed printing speed (thus the maximum allowed intended speed) equals the actual speed of substrate translation in the XY plane, caused by the translation stage.

To ensure high quality printing by the present invention, the intended printing speed needs to sufficiently match the fiber collection speed. If the intended printing speed is larger than the fiber collection speed, stretching and even breaking of the fiber can take place. If the intended printing speed is lower than the fiber collection speed, then undesired fiber accumulation or buckling takes place. The requirement of matching the intended printing speed and fiber collection speed cannot be satisfied by conventional EHD jet printing using mechanical translation stages, because of their insufficient acceleration.

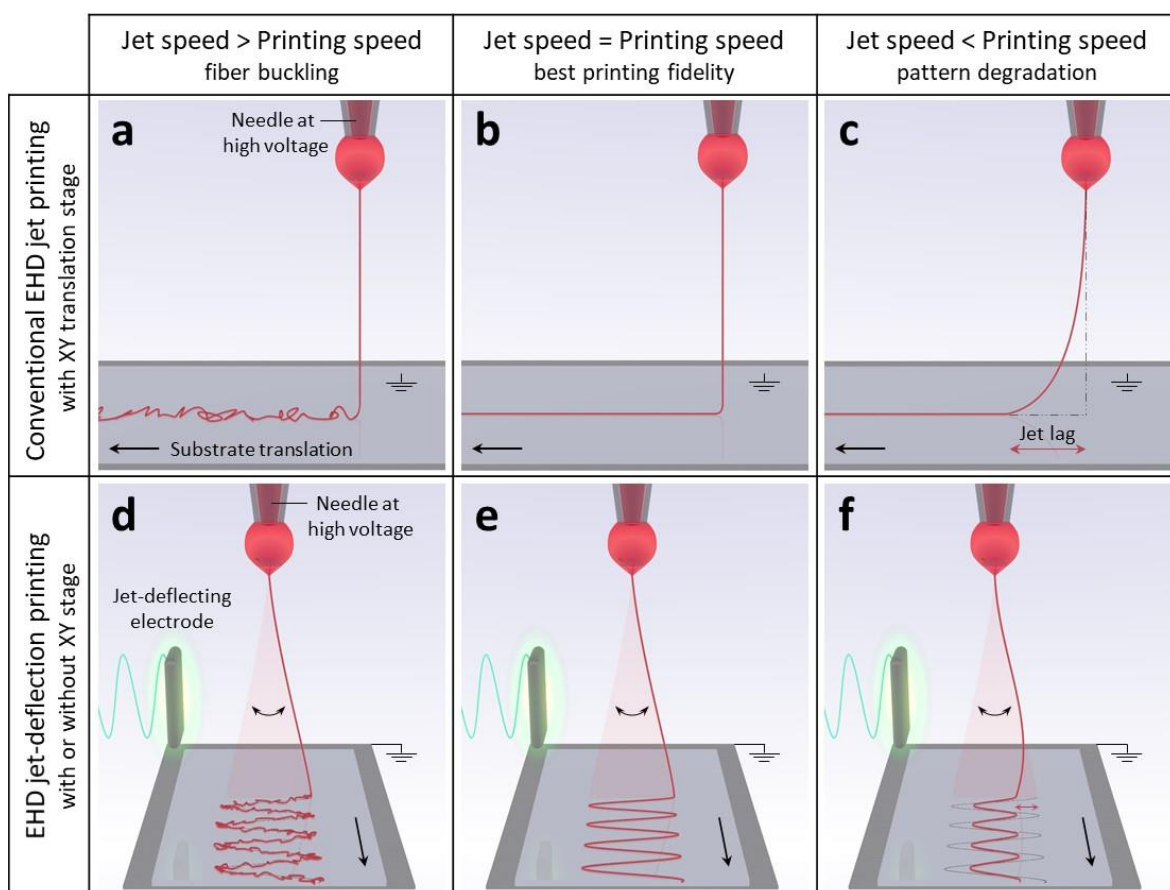


Figure 7. EHD jet printing regimes depending on the speeds ratio. **a-c** show conventional stage-driven printing and **d-f** show the electrostatic jet deflection EHD jet printing.

Figure 7a,d show the situation when the fiber collection speed is higher than the intended printing speed. For substantially viscous jet (which is unable to collect into a puddle of liquid), jet buckling or coiling can happen due to mechanical interaction between the jet and the substrate, resulting in irregular fiber deposition and poor XY resolution of printed item. For substantially liquid jet (which lacks viscoelasticity, so it is still able to flow after deposition), the jet may form a puddle of liquid on the substrate (not shown in the figure).

When the fiber speed equals the collection speed (Figure 7b,e), straight lines are printed following preset printing design, allowing to print 2D items with high XY resolution. The difference between stage-driven EHD jet printing and jet-deflection printing is that much higher collection speeds and accelerations are possible (see Chapters 2-5).

When the fiber speed is lower than the collection speed, this results in shortage of available fiber length for printing the intended design. In conventional EHD jet printing (Figure 7c) the fiber already adhered on the substrate exerts additional extensional force on the jet at its contact with the substrate. Such extensional force stretches the jet, and may result in its breaking (not shown). Even though the stretched jet does not break under the mechanical pull from substrate translation, the length of the collected fiber will be always smaller than the intended length (translated by the translation stage), which will result in “cutting” corners and degrading item geometry compared to the preset design.

In the case of jet deflection (Figure 7d-f) jet stretching and breaking are also possible. If the jet is substantially fluid upon its deposition on the substrate, the ink may accumulate on the substrate unpredictably. Such accumulation of ink may firmly fix the contact point between the jet and the substrate, while the jet in the space between the nozzle and the substrate will continue to deflect under the action of electrostatic field.

The printing regimes described above assume that both the fiber collection speed and the intended printing speed are constant (independent of time), which is not necessarily true during printing, but is rather used here for the sake of comparison and simplicity. In reality, the speed of the substrate translation is not constant and can deviate significantly from the preset speed, especially when attempting to execute complex trajectories at high speed.

1.6. Thesis aims and structure

The scope of the present thesis is to address some current limitations of electrohydrodynamic (EHD) jet printing by developing new methods for the accurate printing of fast EHD jets (with speeds $\gg 10$ mm/s, up to 500 mm/s) with submicrometer resolution. The main challenge which this thesis aims to resolve is to match the high speed of EHD jet by the printing speed, which is required for fast and precise printing. To achieve this goal and to overcome the current speed limitations of XY stages, we have developed an electrostatic jet deflection method, which allows decoupling the printing speed from that of the substrate, where the former can greatly exceed the latter. A second challenge addressed in this thesis is the fine control of printing of EHD jets made of polymer melts. For printing such slow EHD jets (with speeds < 10 mm/s) we use XY stages, and identify the printing defects and establish a method to correct them, with a goal of achieving novel printed geometries with controlled mechanical performance of the printed structures.

This thesis is built around six chapters that comprise an introductory chapter and five chapters reporting the obtained results. Each of the results chapters contains an introduction to the specific work described therein, experimental and results sections, as well as conclusions and references. To conclude this work, general conclusions of the present thesis are given together with future aims and outlook.

The scope and the structure of this thesis:

- **Chapter 1. Introduction.** This chapter provides the insight into the micromanufacturing techniques, introduces EHD jet printing with its unique advantages and limitations, and describes the conventional printing setup and relevant processing parameters.
- **Chapter 2. XY mechanical stage: a limiting factor for fast and high-resolution EHD jet printing.** The aim of this work is to provide a detailed analysis of a high-performance mechanical stage available on the market by experimentally evaluating its precision and dynamic characteristics. This chapter shows why even the best XY stages are not adequate for direct-write printing with fast EHD jets. Overcoming this problem is the main goal of this thesis.

- **Chapter 3. Ultrafast 3D printing with submicrometer features using electrostatic jet deflection.** This chapter introduces a new strategy to control EHD jet deposition location through electrostatic jet deflection. It aims to describe this printing method in detail, showing the main printing results and highlighting its advantages and flexibility.
- **Chapter 4. Parametric analysis and control of electrostatic jet deflection.** Here we aim to study the relevant setup and process parameters affecting the jet deflection printing we devised. In particular, we describe how jet-deflecting signals are generated in our custom-made software, based on preset pattern design and printing parameters. The developed software was essential for controlling the printing process and embodies a critical methodological improvement over previous research in electrostatic jet deflection.
- **Chapter 5. In-line fiber speed control for EHD jet-deflection printing.** The goal of this chapter is to devise a simple and automatable method to determine the speed of EHD jet. We show how this can be done using our jet deflection approach and propose that this method can be used for in-situ control of EHD jet printing.
- **Chapter 6. Unlocking the geometric freedom of melt electrowriting using microscale layer shifting.** The last chapter complements this thesis by showing our findings on stage-driven EHD jet printing of polymer melts, where much thicker and slower jets than were discussed in the previous chapters are precisely collected into 3D structures. Here we demonstrate that through deliberate microscale shifting of printing paths fiber-layers can be stacked with controlled offsets to print geometrically complex structures with adjustable mechanical properties.

1.7. References

1. https://en.wikipedia.org/wiki/Saturn_V
2. <https://theconversation.com/how-spacex-lowered-costs-and-reduced-barriers-to-space-112586>
3. <https://www.independent.co.uk/news/science/apollo-11-moon-landing-mobile-phones-smartphone-iphone-a8988351.html>
4. Moore, G. E. (1965). Cramming More Components Onto Integrated Circuits, *Electronics*, April 19, 1965. *Electronics*, 38(8), 82–85.
5. Khan, H.N., Hounshell, D.A. & Fuchs, E.R.H. Science and research policy at the end of Moore’s law. *Nat Electron* 1, 14–21 (2018).
6. Leuschner, R., & Pawlowski, G. (2008). Photolithography. In *Handbook of Semiconductor Technology Set* (pp. 253–263). Wiley.
7. <https://venturebeat.com/2020/01/07/a-bright-future-for-moores-law>
8. Nathan, A., Ahnood, A., Cole, M. T., Lee, S., Suzuki, Y., Hiralal, P., ... Milne, W. I. (2012). Flexible electronics: The next ubiquitous platform. In *Proceedings of the IEEE* (Vol. 100, pp. 1486–1517). Institute of Electrical and Electronics Engineers Inc.
9. Rus, D., & Tolley, M. T. (2015, May 27). Design, fabrication and control of soft robots. *Nature*. Nature Publishing Group.
10. Jayathilaka, W. A. D. M., Qi, K., Qin, Y., Chinnappan, A., Serrano-García, W., Baskar, C., ... Ramakrishna, S. (2019, February 15). Significance of Nanomaterials in Wearables: A Review on Wearable Actuators and Sensors. *Advanced Materials*, 31. Wiley-VCH Verlag.
11. Zhang, J., Yan, S., Yuan, D., Alici, G., Nguyen, N. T., Ebrahimi Warkiani, M., & Li, W. (2016). Fundamentals and applications of inertial microfluidics: A review. *Lab on a Chip*. Royal Society of Chemistry.
12. Huh, D., Matthews, B. D., Mammoto, A., Montoya-Zavala, M., Yuan Hsin, H., & Ingber, D. E. (2010). Reconstituting organ-level lung functions on a chip. *Science*, 328(5986), 1662–1668.
13. Sears, N. A., Seshadri, D. R., Dhavalikar, P. S., & Cosgriff-Hernandez, E. (2016, August 1). A Review of Three-Dimensional Printing in Tissue Engineering. *Tissue Engineering - Part B: Reviews*. Mary Ann Liebert Inc.
14. Ibáñez, M., Luo, Z., Genç, A. et al. High-performance thermoelectric nanocomposites from nanocrystal building blocks. *Nat Commun* 7, 10766 (2016).
15. Ahmadi, M. H., Ghazvini, M., Nazari, M. A., Ahmadi, M. A., Pourfayaz, F., Lorenzini, G., & Ming, T. (2019). Renewable energy harvesting with the application of nanotechnology: A review. *International Journal of Energy Research*. John Wiley and Sons Ltd.

16. ISO / ASTM 52900-15, Standard Terminology for Additive Manufacturing – General Principles – Terminology, ASTM International, West Conshohocken, PA, 2015, www.astm.org
17. Gibson, I., Rosen, D. & Stucker, B. Additive manufacturing technologies. 3D Printing, Rapid Prototyping, and Direct Digital Manufacturing. (Springer, 2013).
18. Pei, E., Monzón, M. & Bernard, A. Additive Manufacturing - Developments in Training and Education. (Springer, 2018).
19. Srivatsan, T. S. & Sudarshan, T. S. Additive manufacturing: Innovations, Advances, and Applications. (CRC Press, 2015).
20. J.D. Prince, 3D printing: an industrial revolution, *Journal of Electronic Resources in Medical Libraries* 11(1) (2014) 39-45.
21. S.H. Huang, P. Liu, A. Mokasdar, L. Hou, Additive manufacturing and its societal impact: a literature review, *The International Journal of Advanced Manufacturing Technology* 67(5-8) (2013) 1191-1203
22. I.J. Petrick, T.W. Simpson, 3D printing disrupts manufacturing: how economies of one create new rules of competition, *Research-Technology Management* 56(6) (2013) 12-16.
23. Vollrath, F., Knight, D. Liquid crystalline spinning of spider silk. *Nature* 410, 541–548 (2001).
24. Li, Q., & Lewis, J. A. (2003). Nanoparticle Inks for Directed Assembly of Three-Dimensional Periodic Structures. *Advanced Materials*, 15(19), 1639–1643.
25. Gladman, A. S., Matsumoto, E. A., Nuzzo, R. G., Mahadevan, L. & Lewis, J. A. Biomimetic 4D printing. *Nat. Mater.* 15, 413–418 (2016).
26. Duda, T. & Raghavan, L. V. 3D metal printing technology. *IFAC-PapersOnLine* 49, 103–110 (2016)
27. Chen, Z. et al. 3D printing of ceramics: a review. *J. Eur. Ceram. Soc.* 39, 661–687 (2019).
28. Xu, W., Wang, X., Sandler, N., Willför, S. & Xu, C. Three-dimensional printing of wood-derived biopolymers: a review focused on biomedical applications. *ACS Sustain. Chem. Eng.* 6, 5663–5680 (2018)
29. Kolesky, D. B. et al. 3D bioprinting of vascularized, heterogeneous cell-laden tissue constructs. *Adv. Mater.* 26, 3124–3130 (2014).
30. Ringeisen, B. R., Othon, C. M., Barron, J. A., Young, D. & Spargo, B. J. Jet-based methods to print living cells. *Biotechnol. J.* 1, 930–948 (2006).
31. Pfitzner, J. (1976). Poiseuille and his law. *Anaesthesia*, 31(2), 273–275.
32. Ouyang, L., Highley, C. B., Sun, W., & Burdick, J. A. (2017). A Generalizable Strategy for the 3D Bioprinting of Hydrogels from Nonviscous Photo-crosslinkable Inks. *Advanced Materials*, 29(8).

33. Soliman, B. G., Lindberg, G. C. J., Jungst, T., Hooper, G. J., Groll, J., Woodfield, T. B. F., & Lim, K. S. (2020). Stepwise Control of Crosslinking in a One-Pot System for Bioprinting of Low-Density Bioinks. *Advanced Healthcare Materials*.
34. Yarin, A. L., Koombhongse, S. & Reneker, D. H. Taylor cone and jetting from liquid droplets in electrospinning of nanofibers. *J. Appl. Phys.* 90, 4836–4846 (2001).
35. Lewis, J. A. Direct ink writing of 3D functional materials. *Adv. Funct. Mater.* 16, 2193–2204 (2006).
36. Gilbert, W. (1600). *De Magnete, Magneticisque Corporibus, et de Magno Magnete Tellure* (On the Magnet and Magnetic Bodies, and on That Great Magnet the Earth).
37. Xie, J., Jiang, J., Davoodi, P., Srinivasan, M. P., & Wang, C. H. (2015). Electrohydrodynamic atomization: A two-decade effort to produce and process micro-/nanoparticulate materials. *Chemical Engineering Science*, 125, 32–57.
38. Dumont, Q., & Cole, R. B. (2014). Jean-Antoine Nollet: The father of experimental electrospray. *Mass Spectrometry Reviews*, 33(6), 418–423.
39. Smith, J. N., Flagan, R. C., & Beauchamp, J. L. (2002). Droplet evaporation and discharge dynamics in electrospray ionization. *Journal of Physical Chemistry A*, 106(42), 9957–9967.
40. Taylor G. Disintegration of water drops in an electric field. *Proc R Soc Lond A*. 1964;280 (1382):383–397.
41. Zeleny J. Instability of electrified liquid surfaces. *Phys, Rev.* 1917;10 (1):1–6.
42. Taylor G. The force exerted by an electric field on a long cylindrical conductor. *Proc Royal Soc A*. 1966;291 (1452):145–158.
43. J. B. Fenn, M. Mann, C. K. Meng, S. F. Wong, C. M. Whitehouse, Electrospray ionization for mass spectrometry of large biomolecules. *Science*. 246 (1989), pp. 64–71.
44. Fenn, J. B. (2003). Electrospray wings for molecular elephants (Nobel lecture). In *Angewandte Chemie - International Edition* (Vol. 42, pp. 3871–3894).
45. Thompson, Silvanus P. *The Life of Lord Kelvin*, Chelsea Publishing Company, New York, NY, 1976.
46. Boys, C. V. (1887). On the production, properties, and some suggested uses of the finest threads. *Proceedings of the Physical Society of London*, 9(1), 8–19.
47. Cooley, J. F. et al. "Apparatus for electrically dispersing fluids" U.S. Patent 692,631 Issue date: February 4, 1902
48. Morton, W.J. et al. "Method of dispersing fluids" U.S. Patent 0,705,691 Issue date: July 29, 1902
49. Filatov, Y. Budyka, A. Kirichenko, V. (Trans. D. Letterman) (2007) *Electrospinning of micro- and nanofibers: fundamentals and applications in separation and filtration processes*, Begell House Inc., New York, USA

50. Hunter, H. C., & Ray, A. K. (2009). On progeny droplets emitted during Coulombic fission of charged microdrops. *Physical Chemistry Chemical Physics*, 11(29), 6156–6165.
51. Rosell-Llompart, J., Grifoll, J., & Loscertales, I. G. (2018). Electrospays in the cone-jet mode: From Taylor cone formation to spray development. *Journal of Aerosol Science*, 125, 2–31.
52. Bodnár, E., Grifoll, J., & Rosell-Llompart, J. (2018). Polymer solution electrospaying: A tool for engineering particles and films with controlled morphology. *Journal of Aerosol Science*, 125, 93–118.
53. Boda, S. K., Li, X., & Xie, J. (2018). Electrospaying an enabling technology for pharmaceutical and biomedical applications: A review. *Journal of Aerosol Science*, 125, 164–181.
54. Kelder, E. M., Marijnissen, J. C. M., & Karuga, S. W. (2018). EDHA for energy production, storage and conversion devices. *Journal of Aerosol Science*, 125, 119–147.
55. Martin, S., Garcia-Ybarra, P. L., & Castillo, J. L. (2018). Ten-fold reduction from the state-of-the-art platinum loading of electrodes prepared by electrospaying for high temperature proton exchange membrane fuel cells. *Electrochemistry Communications*, 93, 57–61.
56. Sochorakis, N., Grifoll, J., & Rosell-Llompart, J. (2019). Scaling up of extractor-free electrospays in linear arrays. *Chemical Engineering Science*, 195, 281–298.
57. Reneker, D. H. & Yarin, A. L. Electrospinning jets and polymer nanofibers. *Polymer* 49, 2387–2425 (2008).
58. Reneker, D. H., Yarin, A. L., Fong, H., & Koombhongse, S. (2000). Bending instability of electrically charged liquid jets of polymer solutions in electrospinning. *Journal of Applied Physics*, 87(9), 4531–4547.
59. Li, D. & Xia, Y. Electrospinning of nanofibers: Reinventing the wheel? *Advanced Materials* 16, 1151–1170 (2004).
60. Kiselev, P., & Rosell-Llompart, J. (2012). Highly aligned electrospun nanofibers by elimination of the whipping motion. *Journal of Applied Polymer Science*, 125(3), 2433–2441.
61. Li, D., Wang, Y., & Xia, Y. (2004). Electrospinning Nanofibers as Uniaxially Aligned Arrays and Layer-by-Layer Stacked Films. *Advanced Materials*, 16(4), 361–366.
62. Hwang, W., Pang, C., & Chae, H. (2016). Fabrication of aligned nanofibers by electric-field-controlled electrospinning: Insulating-block method. *Nanotechnology*, 27(43).
63. Lei, S., Quan, Z., Zhang, H., Qin, X., Wang, R., & Yu, J. (2019). Stable-jet length controlling electrospun fiber radius: Model and experiment. *Polymer*, 180, 121762.
64. Sun, D., Chang, C., Li, S., & Lin, L. (2006). Near-Field Electrospinning. *Nano Letters*, 6(4), 839–842.

65. He, X. X. et al. Near-field electrospinning: progress and applications. *J. Phys. Chem. C.* 121, 8663–8678 (2017).
66. Robinson, T. M., Hutmacher, D. W., & Dalton, P. D. (2019, November 1). *The Next Frontier in Melt Electrospinning: Taming the Jet.* Advanced Functional Materials. Wiley-VCH Verlag.].
67. Schneider, J., Rohner, P., Thureja, D., Schmid, M., Galliker, P., & Poulidakos, D. (2016). Electrohydrodynamic NanoDrip Printing of High Aspect Ratio Metal Grid Transparent Electrodes. *Advanced Functional Materials*, 26(6), 833–840.
68. Phung, T. H., Kim, S., & Kwon, K.-S. (2017). A high speed electrohydrodynamic (EHD) jet printing method for line printing. *Journal of Micromechanics and Microengineering*, 27(9), 95003.
69. Galliker, P., Schneider, J., Eghlidi, H., Kress, S., Sandoghdar, V., & Poulidakos, D. (2012). Direct printing of nanostructures by electrostatic autofocussing of ink nanodroplets. *Nature Communications*, 3.
70. Skylar-Scott, M. A., Mueller, J., Visser, C. W., & Lewis, J. A. (2019). Voxeled soft matter via multimaterial multinozzle 3D printing. *Nature*, 575(7782), 330–335.
71. Hrynevich, A., Elçi, B., Haigh, J. N., McMaster, R., Youssef, A., Blum, C., ... Dalton, P. D. (2018). Dimension-Based Design of Melt Electrowritten Scaffolds. *Small*, 14(22).
72. Huang, L., Bui, N. N., Manickam, S. S. & McCutcheon, J. R. Controlling electrospun nanofiber morphology and mechanical properties using humidity. *J. Polym. Sci. Pol. Phys.* 49, 1734–1744 (2011).
73. Martinez-Prieto, N., Fratta, G., Cao, J., & Ehmann, K. F. (2018). Deposition of variable bead diameter arrays by self- focusing electrohydrodynamic jets. *Journal of Micro and Nano-Manufacturing*, 6(3).
74. Busolo, T., Ura, D. P., Kim, S. K., Marzec, M. M., Bernasik, A., Stachewicz, U., & Kar-Narayan, S. (2019). Surface potential tailoring of PMMA fibers by electrospinning for enhanced triboelectric performance. *Nano Energy*, 57, 500–506.
75. Han, Y., & Dong, J. (2016). Design of Integrated Ring Extractor for High Resolution Electrohydrodynamic (EHD) 3D Printing. *Procedia Manufacturing*, 5, 1031–1042.

Chapter 2

XY mechanical stage:

a limiting factor for fast and high-resolution

EHD jet printing

Abstract

Additive manufacturing technologies based on layer-by-layer deposition of material ejected from a nozzle provide unmatched versatility but are limited in terms of printing speed and resolution. EHD jetting uniquely allows generating submicrometer jets that can reach speeds above 1 m/s. Unfortunately, such fast jets cannot be precisely collected and positioned onto the substrate by too slow mechanical stages. This limitation posed by the mechanical stages prohibits fast printing of 2D and 3D patterns while providing high resolution. In this chapter, we examine dynamic characteristics of a top-notch mechanical stage and evaluate its performance and limitations for EHD jet printing. We start from the fundamentals of motion and then experimentally assess dynamic characteristics of the XY mechanical stage while performing linear and non-linear moves. Conclusions from this study both characterize the performance of the XY stage, rendering it unsuitable for fast EHD jet printing, and serve as a motivation for developing another means of material positioning to enable faster high-resolution 3D printing.

2.1. Introduction

The most important characteristics of a mechanical stage are velocity, acceleration and precision. Unfortunately, it is not possible to give exact values for velocity, acceleration and precision, which will be true for any type of the setup, the software settings and the motion program. First, the fundamentals of motion are described for constant acceleration, being the simplest and most effective regime of motion. Then we present simulated performance of a theoretical XY stage while performing linear moves, thus outlining what would be expected in an ideal and simplest case. Second, a detailed study is performed to reveal the performance of real high-end XY stage, used in this study, and assess its capabilities comparing to the requirements of EHD jet printing.

An ideal XY mechanical stage for EHD jet printing would possess:

- i) Maximum speed on the order of the maximum speed of the EHD jet, being at least 0.5 m/s.
- ii) Virtually infinite acceleration rate to provide immediate acceleration or deceleration when the move starts or ends, as well as when motion direction is changed (Figure 1a). Infinite acceleration is a critical requirement for keeping the translation speed constant while executing a trajectory with changes in translation direction. The importance of instantaneous translation speed matching the EHD jetting speed is discussed in the Chapter 1, 3 and 5.
- iii) Positioning precision of the XY stage while following complex trajectory at high speed. Considering that typical fiber diameter for solution-based EHD jet printing is around 200 nm (ranging from 20 nm to 5 μm in extreme cases), positioning precision on the order of 1 μm would be desirable.

It is obvious that virtually infinite acceleration is not feasible for any mechanical stage, primarily because of the fact that mechanical stage has considerable mass m (and inertia). Thus, it would require an infinite force F to reach very high accelerations a ($F = m * a$), which is not practical.

NB: Chapter 3 demonstrates how this challenge can be bypassed by electrostatic deflection of the EHD jet.

2.1.1. Fundamentals of motion

The simplest form of motion is the one with constant acceleration, and such case will be used as an example. Figure 1b shows the governing equations of motion for the case of constant acceleration.

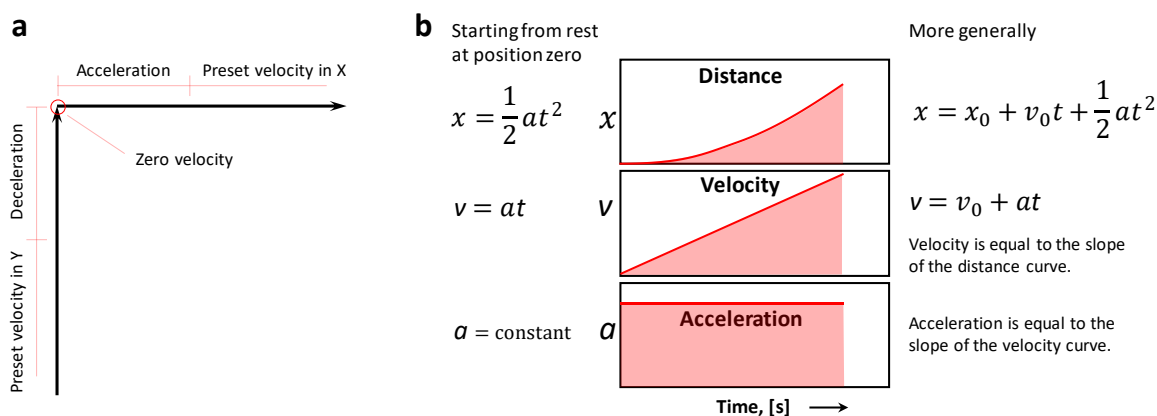


Figure 1. Fundamentals of motion with constant acceleration. Schematic on **a** shows that for any motion trajectory having a change in moving direction there must be a deceleration interval where translation velocity drops from the preset value down to zero, and then accelerates back to the preset value. **b** Governing formulas for motion with constant acceleration, linking distance, velocity and acceleration.

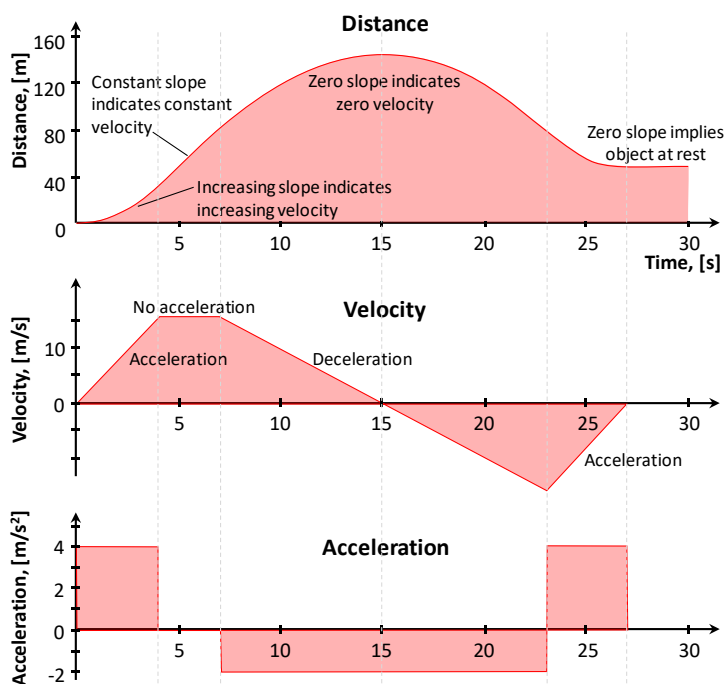


Figure 2. Sample motion with constant acceleration.

A considerable amount of information about the motion can be obtained by examining the slope of the various graphs. The slope of the graph of distance as a function of time equals to the velocity at that time, and the slope of the velocity equals to the acceleration.

In this example shown on Figure 2, where the initial position (distance) and velocity were zero, the height of the position curve is a measure of the area under the velocity curve. The height of the position curve will increase as long as the velocity is positive. As the velocity becomes negative, the position curve drops as the net positive area under the velocity curve decreases. Likewise, the height of the velocity curve is a measure of the area under the acceleration curve. The fact that the final velocity is zero is an indication that the positive and negative contributions were equal.

2.1.2. XY mechanical stages

XY mechanical stages are widely used in the area of 3D printing, and especially in the extrusion-based methods¹⁻², where molten polymer tracks are laid to produce stacked cross-sections comprising a 3D model. Among the mainstream extrusion-based 3D printing techniques, Fused Deposition Modelling (FDM) or Fused Filament Fabrication (FFF) is the most widely used and the most versatile technique, where the printhead assembly is typically mounted atop a gantry and moves in horizontal plane while the build substrate is stationary.

Given the popularity of the FDM/FFF 3D printing and plethora of available printers on the market, their limitations were rigorously studied and are well understood. For example, the main limitations toward higher printing speeds were identified to be in the printhead system and in the XY stage dynamics³. First, a plastic filament must be pushed into a melting compartment and then extruded from a nozzle, which puts certain limitations on the speed of melting of the solid filament, as well as on the maximum exerted force to push a melt through a fine nozzle opening. Second, the extrusion speed must be matched by the printhead translation speed, which is limited depending on the used XY stage system. For FDM/FFF 3D printing, it was shown that addressing and optimizing the performance of all those subsystems can result in faster printing speeds⁴, even though it was achieved on the expense of the printing resolution and positioning precision.

The XY stage positions the printhead relative to the build platform in 3D space. In the most common printer configuration, the mechanical stage comprises three linear actuators each responsible for a Cartesian vector (X, Y, Z). Horizontal (XY) motion of the nozzle is achieved by converting rotary motion of DC motors to linear motion using either a belt drive⁵ or a lead screw⁶ and putting two such linear stages orthogonally⁷⁻⁸. Vertical (Z) motion of the build surface is achieved using a linear actuator oriented vertically.

XY stages are classified by the drive (motor) type, which greatly defines the dynamic performance and the precision of motion. Table 1 generally summarizes various characteristics of drive types. It must be noted that while Piezo motors have the highest accelerations among different motor types, its translation speed is slow. Additionally, piezo drives have very short travel ranges, reaching only 0.3-0.5 mm. These characteristics exclude piezo-driven XY stages from the options available for fast 3D printing applications.

Table 1. Characteristics of XY stages for various drive types. Table adopted from⁹.

Drive Type	Travel range	Speed	Resolution	Repeatability	Load	Price
Linear motor	Long	Fast	High	High	High	\$\$\$
Brushless DC	Medium	Medium	Medium	High	High	\$\$\$
DC motor	Medium	Medium	Medium	Medium	High	\$\$
Stepper motor	Medium	Medium	Medium	Medium	Medium	\$
Piezo motor	Short	Slow	High	Low	High	\$\$

In most printers, stepper motors are used due to their low cost and open-loop angular position control. Angular resolution can be increased using microstepping with the drawback of decreased torque¹⁰. Most desktop 3D printers (e.g., from Makerbot, Printbot and Ultimaker) use a series gantry for the positioning in XY plane, and a lead-screw actuator for Z axis. Such architecture is also found on professional grade printers, including the Stratasys Dimension FDM printers.

Some other architectures, such as the H-frame gantry and the delta architecture are becoming increasingly popular thanks to their higher agility^{10,11}. These architectures provide improved dynamic performance due to the design where motors are fixed on the frame and do not contribute to the inertia of the carriage. The motion is transferred to the carriage through pulleys. Such configuration allows actuators to exert higher force, but the

kinematics and the control of the system becomes more complex due to the elastic elements such as belts or pulleys.

The quality of the XY stage and how well it can execute the printing pattern are critical for high-resolution printing. When motors are commanded beyond their maximum speed/acceleration, the failure of the XY stage occurs, causing it to skip some steps of the commanded pattern, which results to the loss of accuracy. For this reason, there is always a balance between the motion speed and the positioning precision which a particular XY stage can achieve. Such considerations are critical for the fast printing because they imply that the printing is always limited by the precision and speed while executing an arbitrary pattern. Here we are going to analyze a top-notch XY stage to reveal its limitations particularly for the realm of EHD jet printing.

2.2. Methods

2.2.1. Simulated performance of an ideal XY stage

The performance of a theoretical XY stage was performed for the constant acceleration scenario. Simple calculations were conducted in MS Excel from the first principles of motion to simulate the speed evolution when executing linear moves of variable length.

2.2.2. Examined XY stage

The XY translation stage from *PI miCos* is based on two orthogonal linear stages in both X and Y directions. Linear stages PLS-85 VC with servo motors LIA20 have 10 mm nominal travel range and are equipped with RS422 encoders. The movement of the stage is controlled through the *GeoBrick* computational unit which is commanded via the *Pwin32pro* software installed on the computer. Travel trajectories and speeds were expressed as a G-code in *Pwin32pro* software to control the stage motion.

2.2.3. Actual performance of the XY stage

The acceleration characteristics of the X linear stage were altered to study its dynamics while performing straight moves of various lengths, from 5 to 1000 μm . We studied two acceleration regimes: with gradual acceleration ramp (standard regime) and with constant acceleration (provides faster dynamics but is not used due to increased vibrations, loss of positioning precision, and wear). Multiple moves were executed to increase the total translation time, and decrease the error associated with measurement and calculation. Average speed and average acceleration were computed in Excel using known length, number of iterations, and the total translation time. Table 2 and Table 3 present gradual acceleration ramp and maximum acceleration ramp, correspondingly, which are also plotted on Figure 6.

Pwin32pro software allows to access and to record the data from the XY stage encoders, such motors position, speed and acceleration, both the commanded and the actual values, with the temporal resolution of one servo cycle (100 microseconds). Those X and Y positions were recorded from encoders while performing complex trajectory (logo patterns of variable sizes). We used this data to compare the actual speed to the programmed speed (Figures 9-10) and analyzed the positioning precision of the stage (Figure 11).

2.3. Results and Discussion

2.3.1. Simulated performance of a theoretical stage

We've made simple calculations for straight moves in constant acceleration mode, which results are plotted on Figure 3 showing how the velocity and the distance relate to each other while executing a straight move. Acceleration of 20 m/s^2 was chosen, representing the acceleration of best mechanical stages.

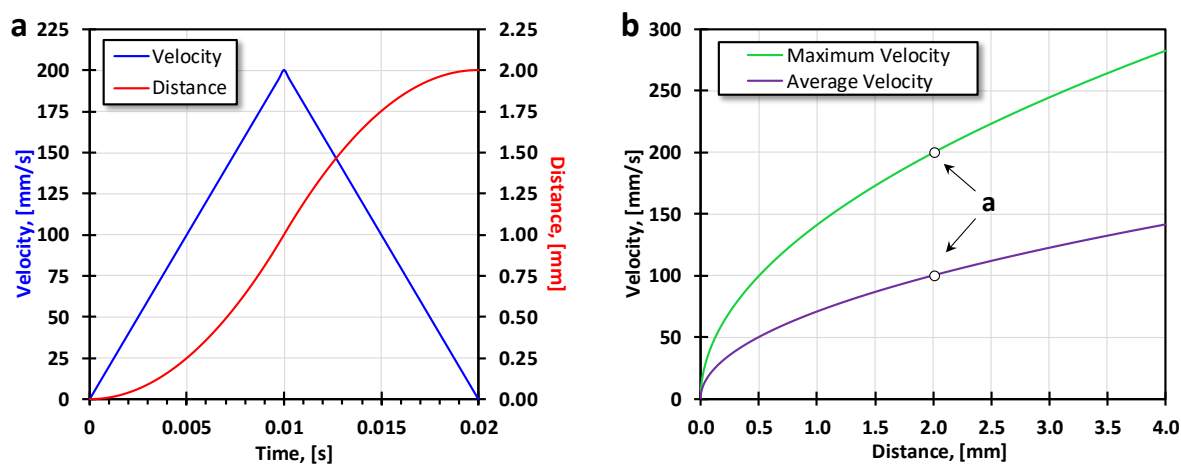


Figure 3. Simulated linear motion with constant acceleration of 20 m/s^2 . **a** shows expected velocity profile as theoretical mechanical stage moves linearly for 2 mm. Similarly, **b** shows the evolution of maximum and average velocities as a function of travelled distance.

Each straight motion has an acceleration part, where velocity increases from zero to some value, and a deceleration part before velocity reaches zero. Depending on distance of straight segment and programmed velocity, three cases are possible. If the segment is too short, programmed velocity will not be reached before deceleration starts, and velocity will have triangular profile. On the other hand, if the segment is long, programmed velocity will be reached and kept constant before deceleration starts, leading to trapezoid velocity profile. Figure 3a shows an intermediate case when deceleration starts immediately after reaching programmed velocity of 200 mm/s, which requires straight segment of 2 mm. Acceleration and deceleration parts take 0.01 s each, and maximum velocity is 200 mm/s, corresponding to the preset velocity. Consequently, mechanical stage needs 0.02 s and 2 mm distance to only reach programmed velocity of 200 mm/s. In this case, average velocity is half of maximum velocity and equals 100 mm/s (not shown on Figure 3a). Similarly, Figure

3b plots maximum and average velocities as a function of the distance, i.e. the length of a straight move. For example, to print with 100 mm/s average speed (marked with a , as on Figure 3a), printed pattern must consist of straight intervals of at least 2 mm average length.

As this chapter we investigate the performance of XY mechanical stage for 3D microprinting applications, more focus is given to short distances. In general, 3D printing technique capable of providing submicron features would be rarely expected to perform straight moves longer than 1 mm side. Such crude approximation already suggests that with a straight segment of 1 mm theoretically expected velocities cannot be higher than $V_{\max}=142$ mm/s and $V_{\text{aver}}=71$ mm/s. Furthermore, any complex pattern of a certain size will have an average segment length much smaller than 1 mm. Average length of a segment depends on the “*intricacy*” of a given printing trajectory and may range from 10 μm to 100 μm . For such small distances, the simulation shown on Figure 3b predicts average velocities c.a. 7.5-22.5 mm/s.

Concluding, the simulation shows that average velocity for small and complex printing trajectories is expected to be below 20 mm/s, much lower than the maximum speed of best stages, typically 200-300 mm/s, and is far from satisfying EHD jet printing velocities of up to 500 mm/s.

2.3.2. XY stage

XY mechanical stage (model *PLS-85 10mm VC LIA20 RS422 HLS*) was purchased from *PI miCos GmbH*. It is a custom-built XY stage, based on PLS (Precision Linear Stage) product line (linear stage *PLS-85* is shown on Figure 4a), but designed to provide maximum dynamic performance and precision available on the market. The maximum velocity of this stage is 300 mm/s, while the maximum velocity of catalog models is 100 mm/s. Its range of travel is 14 mm with an absolute accuracy of $\pm 1 \mu\text{m}$ and resolution of $\pm 0.05 \mu\text{m}$.

XY stage consists of two stacked linear stages, where Y linear stage is placed on top of X linear stage, as on Figure 4b. Black plastic piece (fixed on Y carriage) provides electrical insulation between translation stage and grounded aluminum support, on which printing substrate rests. In this setup printing the substrate is translated in XY plane while the

printhead is stationary. Z motor moves in the vertical direction and controls tip-to-substrate distance.

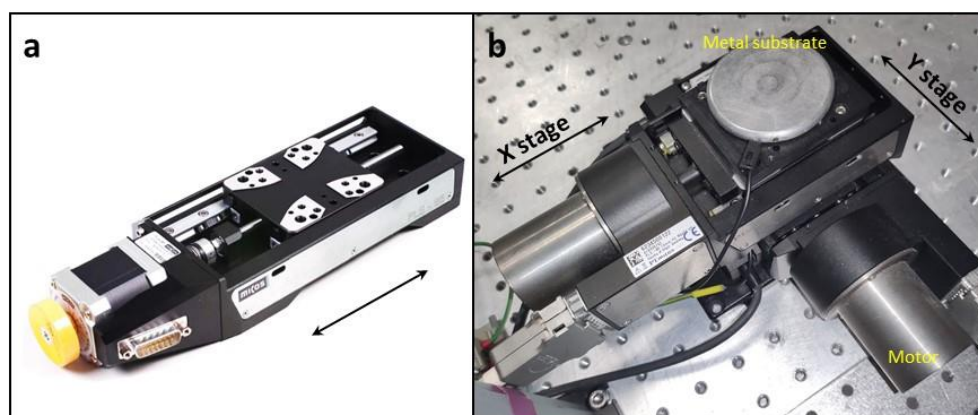


Figure 4. Mechanical stage. **a** Precision Linear Stage PLS-85 from PI miCos. **b** Printing setup with two linear stages in both X and Y axes, used throughout this study. Printing substrate is moved with 10 mm range while the printhead is stationary.

In most extrusion-based 3D printing techniques preset tip-to-substrate distance is reached before translation in XY plane starts, and Z motor rarely has to move during printing. After one layer is printed, subsequent layer is placed on the top of the previous one, and printed structure grows in height. For this reason, Z motion is de facto “decoupled” from XY motion during 3D printing and does not affect printing speed (defined as stage motion in horizontal XY plane). This allows putting much lower requirements (in terms of velocity and acceleration) to Z motor without compromising overall printing performance. Furthermore, in the EHD jet printing the elevation of one printed fiber-layer is very small compared to the tip-to-substrate distance, thus vertical motion of the printhead often can be avoided. For this reason, Z motor capabilities are not investigated in this chapter, as they are not the limiting ones.

The servo motor (*LIA20*) consists of four elements: a normal DC motor, a gear reduction unit, a position-sensing device (encoder), and a control circuit. The function of the servo is to receive a control signal that represents a desired output position of the servo shaft and apply power to its DC motor until its shaft turns to that position. It uses the position-sensing device to determine the rotational position of the shaft, thus providing instructions which way the motor must turn to move the shaft to the commanded position.

Pwin32pro is a software installed on PC where all XYZ stage settings are available. Once motion program (G-code) is set, it is uploaded to *GeoBrick* buffer. *GeoBrick* is a computational unit specially dedicated to controlling XYZ stage. It makes all calculations necessary to interpret uploaded motion program to the stage. Each servo cycle (100 microseconds) *GeoBrick* sends control signals to X, Y and Z servo motors. The control signal is pulse width modulated, where the duration of the positive-going pulse determines the position of the servo shaft. For any servo motor there is a pulse width corresponding to the central position of servo shaft. A longer pulse makes the servo turn to a clockwise-from-center position, and a shorter pulse makes the servo turn to a counter-clockwise-from-center position. In essence, at each moment *GeoBrick* controller commands motors with “go here” instructions, thus controlling overall movement in 3D.

Simple calculations can provide maximum values of acceleration which is limited by XY motor specifications. Acceleration \mathbf{a} can be calculated using formula $\mathbf{F} = \mathbf{m} * \mathbf{a}$, where \mathbf{F} is the force generated by motor of each stage and \mathbf{m} represents the mass being moved by the action of force \mathbf{F} . Particular XY motors can continuously provide 28 N force and 70 N of peak force. Acceleration for each stage will be different because X and Y stages move very different masses. Y stage carries only its slider, plastic piece and aluminum support, which equals approximately $m_Y = 0.4$ kg. On the other hand, X stage additionally moves the Y stage with its slider, which totals to approximately $m_X = 2$ kg. Thus, continuous acceleration for X and Y linear stages are capped to 14 m/s² and 70 m/s², correspondingly.

Summarizing, X and Y stages will have different response. X stage has bigger inertia and lower acceleration, so X stage is a bottleneck which will impede the overall performance of XY mechanical stage.

2.3.3. Maximum vs. gradual acceleration ramp

As discussed previously, the simplest form to reach desired velocity is to apply constant acceleration, resulting in trapezoidal velocity profile. However, at high accelerations mechanical stage may start to vibrate, increasing its wear and decreasing precision.

There are two solutions which allow to avoid severe vibrations. First solution is to decrease maximum permitted acceleration (software limits maximum motor acceleration to allowed

value) in *constant acceleration mode*, to the point when vibrations cease. Second option is to increase acceleration gradually from zero to maximum acceleration a_{max} while accelerating. Typically, such *gradual acceleration mode* is preferred over constant acceleration mode, because it allows to decrease system vibration and permits higher average acceleration compared to the software-limited constant acceleration mode.

When using gradual acceleration mode, which results in S-curve velocity profile, the software allows to adjust and optimize each motor response depending on the application. Optimal parameters depend on the load each stage carries, properties of base on which stage is mounted, and the distance to be moved. Two parameters can be controlled: maximum acceleration a_{max} and acceleration time a_{time} . When maximum acceleration a_{max} is too high and/or acceleration time a_{time} is too small, system begins to oscillate. On the contrary, if a_{max} is too small and/or acceleration time a_{time} is too high, system will require longer time to reach intended (programmed) speed, consequently increasing discrepancy between the programmed and the real speed. Optimal proportion between parameters should be found to keep stage dynamic response as high as possible, while mitigating vibration to an acceptable level.

An obvious disadvantage of gradual acceleration mode is that additional time is lost while ramping up and down acceleration rate at any instance of velocity change. This results in slower average acceleration/deceleration, which means that XY stage will spend more time in any segment where moving direction is changed. Another consequence is that the use of smaller average acceleration rate will require longer straight distance to reach desired velocity (similar to Figure 3b).

Figure 5 shows the velocity vs. distance (position) profile while X linear stage (the one carrying the Y stage atop) executes straight moves with lengths from 50 μm to 4 mm. The stage was moving in a standard regime with gradual acceleration ramp. The data was recorded directly from the mechanical stage encoders. Every servo cycle (100 microsecond) controller reads motors actual positions, compares them to programmed/desired positions, and generates corresponding signals running servo motors. With *Pwin Plot* software it is possible to record all commanded and actual variables from all motors while executing motion program. Among variables are motors' position, velocity, acceleration,

etc. Consequently, any stage motion can be analyzed in great detail. On Figure 5, velocity attenuation and positioning imprecisions are noticeable after fast moves.

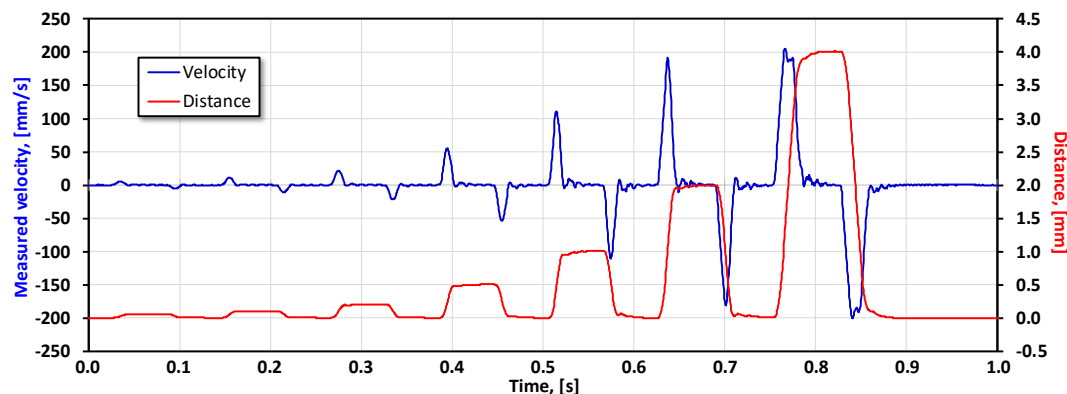


Figure 5. Measured velocity while performing straight moves of increasing length. XY mechanical stage had maximum acceleration of 20 m/s^2 and gradual acceleration ramp while executing moves of $50 \mu\text{m}$, $100 \mu\text{m}$, $200 \mu\text{m}$, $500 \mu\text{m}$, 1 mm , 2 mm and 4 mm .

Complex 2D pattern involves multiple changes in moving direction, where the length of line is small, typically much smaller than 1 mm . Table 2 and Table 3 present the data obtained from measuring the average execution time while the X stage was moved in straight segments of increasing length, from $5 \mu\text{m}$ to $1000 \mu\text{m}$. Maximum acceleration was set to 30 m/s^2 . Multiple moves were executed to increase total translation time, and decrease the error associated with measurement and calculation. Average speed and acceleration experimentally calculated from a PI miCos PLS-85 mechanical stage as it was moved in standard operating conditions executing different lineal trajectory travels. Average speed and average acceleration were computed using known length, number of iterations, and total translation time. Tables 2 and 3 present gradual and maximum acceleration ramps.

Table 2. Dynamic characteristics of mechanical stage with **gradual acceleration** ramp. The acceleration of the stage was software-limited to avoid excessive vibration and wear.

Length of line, [μm]	Number of moves	Total translation time, [s]	Average speed, [mm/s]	Average acceleration, [m/s^2]
5	2000	20.0	0.5	0.2
10	2000	20.0	1.0	0.4
20	2000	20.0	2.0	0.8
50	2000	20.0	5.0	2.0
100	2000	20.0	10.0	4.0
200	2000	20.0	20.0	8.0
500	2000	20.0	50.0	20.0
1000	2000	23.5	85.1	29.0

Table 3. Dynamic characteristics of mechanical stage with **maximum acceleration** ramp. The acceleration of the stage was not limited by the software.

Length of line, [μm]	Number of moves	Total translation time, [s]	Average speed, [mm/s]	Average acceleration, [m/s^2]
5	10000	20.0	2.5	5.0
10	10000	20.0	5.0	10.0
20	10000	20.0	10.0	20.0
50	10000	26.0	19.2	29.6
100	10000	36.5	27.4	30.0
200	2000	10.2	39.2	30.8
500	2000	16.5	60.6	29.4
1000	2000	27.5	72.7	21.2

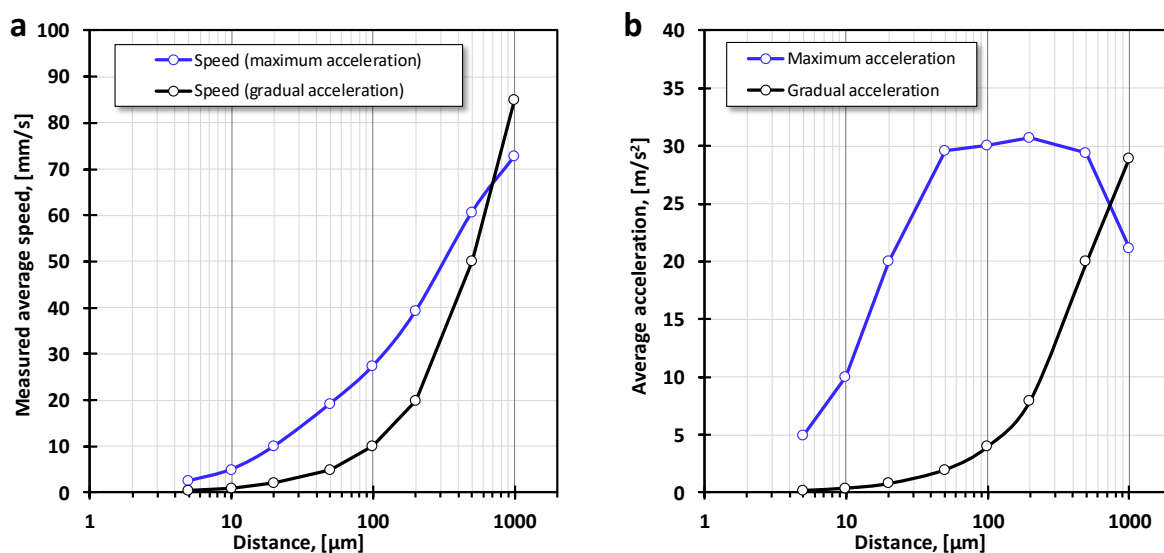


Figure 6. Maximum acceleration vs. gradual acceleration ramp. Graphs show measured average speed (a) and average acceleration (b) of the mechanical stage while executing moves from 5 μm to 1 mm. Different acceleration regimes correspond to the gradual acceleration ramp (software-limited, black, from Table 2) and the maximum acceleration ramp (hardware-limited, highlighted in blue, from Table 3).

Figure 6 plots measured average speed and average acceleration (from Tables 2-3) for both gradual and maximum acceleration regimes. As expected, maximum acceleration regime provides faster speeds, especially for shorter moves, compared to gradual acceleration (5X increase in average speed for short moves of 5-20 μm). From Figure 6b maximum acceleration of 30 m/s^2 can be noted, which is the hardware limit of the XY stage. While for gradual acceleration regime 30 m/s^2 is only reached for 1 mm long moves, in case of maximum acceleration regime it is reached already at 50 μm . It also can be noted that

average acceleration drops for longer moves (200-500 μm) in maximum acceleration regime (blue line). For long distances instantaneous acceleration drops to zero when maximum translation speed is reached, thus driving the average acceleration values down.

While average speed is higher for maximum acceleration ramp, it still cannot meet the requirements of EHD jet printing. Gradual acceleration ramp is a standard and preferred option used to increase movement precision and to avoid excessive vibration and wear of the mechanical stage. For that reason, for further study we use standard gradual acceleration regime.

2.3.4. Speed while executing complex moves

The “*intricacy*” of a pattern can be defined in terms of the number of times when moving direction is changed and the average length of the straight segments composing such pattern. Following this definition, by choosing a pattern geometry and scaling it up and down we are proportionally changing its “*intricacy*” for the XY stage as the average length of a straight segment decreases proportionately. Consequently, the pattern of smaller size is considered as more “*intricate*”.

To demonstrate how XY stage performs while executing complex moves, we chose a logo pattern depicting logos of IREC and URV. Logo consists of straight segments of different directions and lengths, having rounded features, and is used to study stage performance in various conditions. Logo patterns of three sizes: 1 mm, 2 mm and 4 mm (Figure 7) are used in this experiment representing different motion “*intricacy*”. By reducing the logo size, its average straight segment is proportionally reduced, which is expected to affect the average speed of mechanical stage (similar to Figure 3b).

Programmed speed is another parameter used in this experiment, representing desired/commanded speed of motion. For each programmed speed (2-200 mm/s) and pattern size (1-4 mm), velocity data for X and Y motors was recorded directly from encoders. An example of such graph is shown on Figure 8, measured for 2 mm/s programmed speed and 1 mm logo pattern. Instantaneous velocities of X and Y motors are shaded in green and red, while velocity spans from +2 mm/s to -2 mm/s, showing that motors move in different directions depending on the part of the pattern. It is also possible

to precisely define the start and finish of the pattern execution, which can be used to compute the average speed by dividing the total path length by the time of executing one pattern. Similar data was collected for different logo sizes (presented on Figure 7), and for various preset speeds, ranging from 2 to 200 mm/s. Simplified version of those graphs are shown on Figure 9, where motor velocities are converted into the total speed in XY plane.

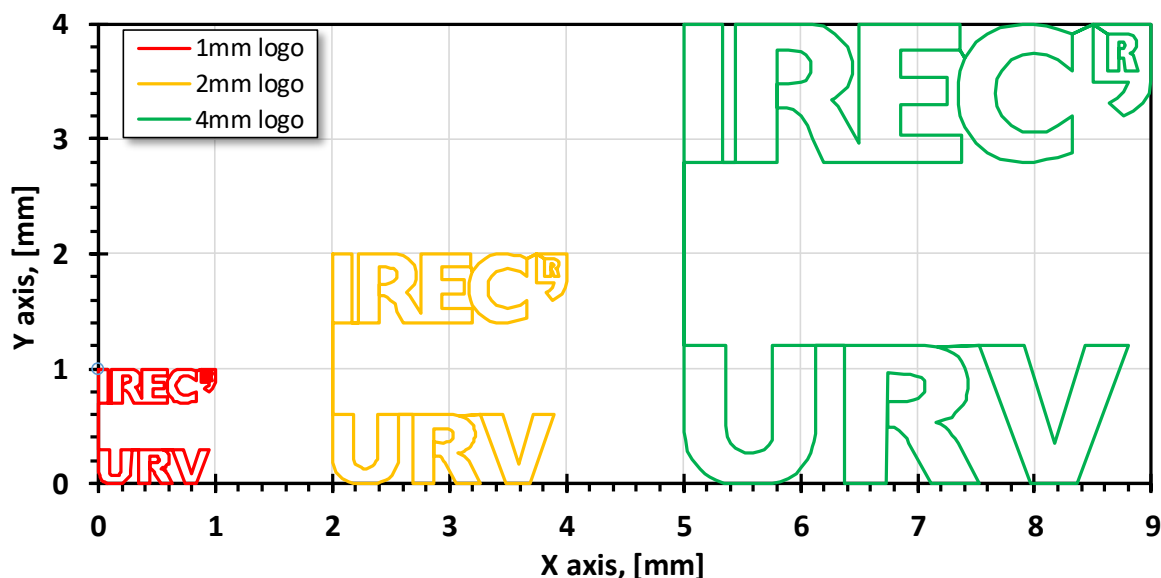


Figure 7. Complex logo pattern of 1, 2, and 4 mm size used to assess the performance of XY mechanical stage.

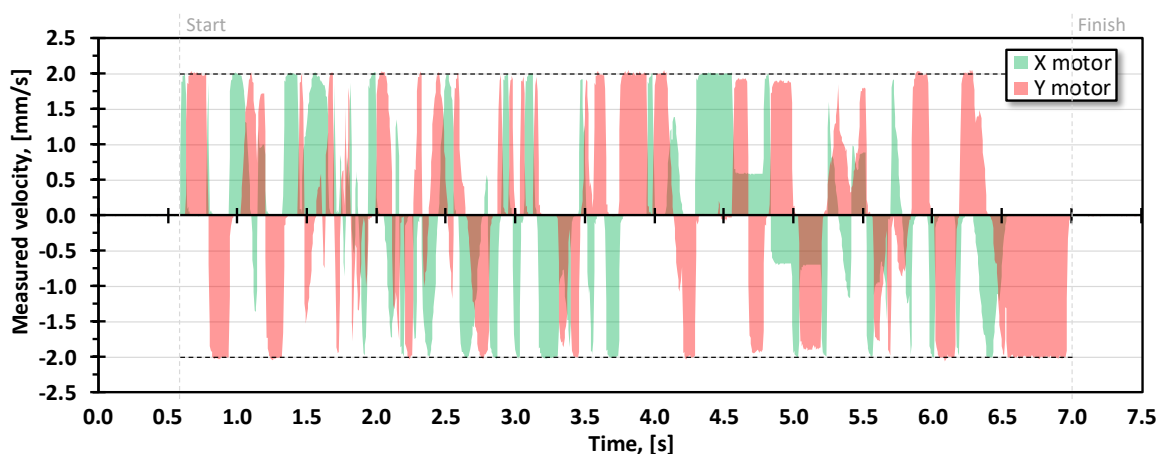


Figure 8. Velocities while executing logo pattern of 1 mm with preset speed of 2 mm/s. Green and red shaded areas correspond to instantaneous velocities of X and Y linear stages, recorded directly from stage encoders.

The same data becomes more informative when presented in terms of **total speed** in XY plane (Figure 9), instead of velocities of separate motors:

$$Total\ speed = \sqrt{(Velocity\ in\ X)^2 + (Velocity\ in\ Y)^2}$$

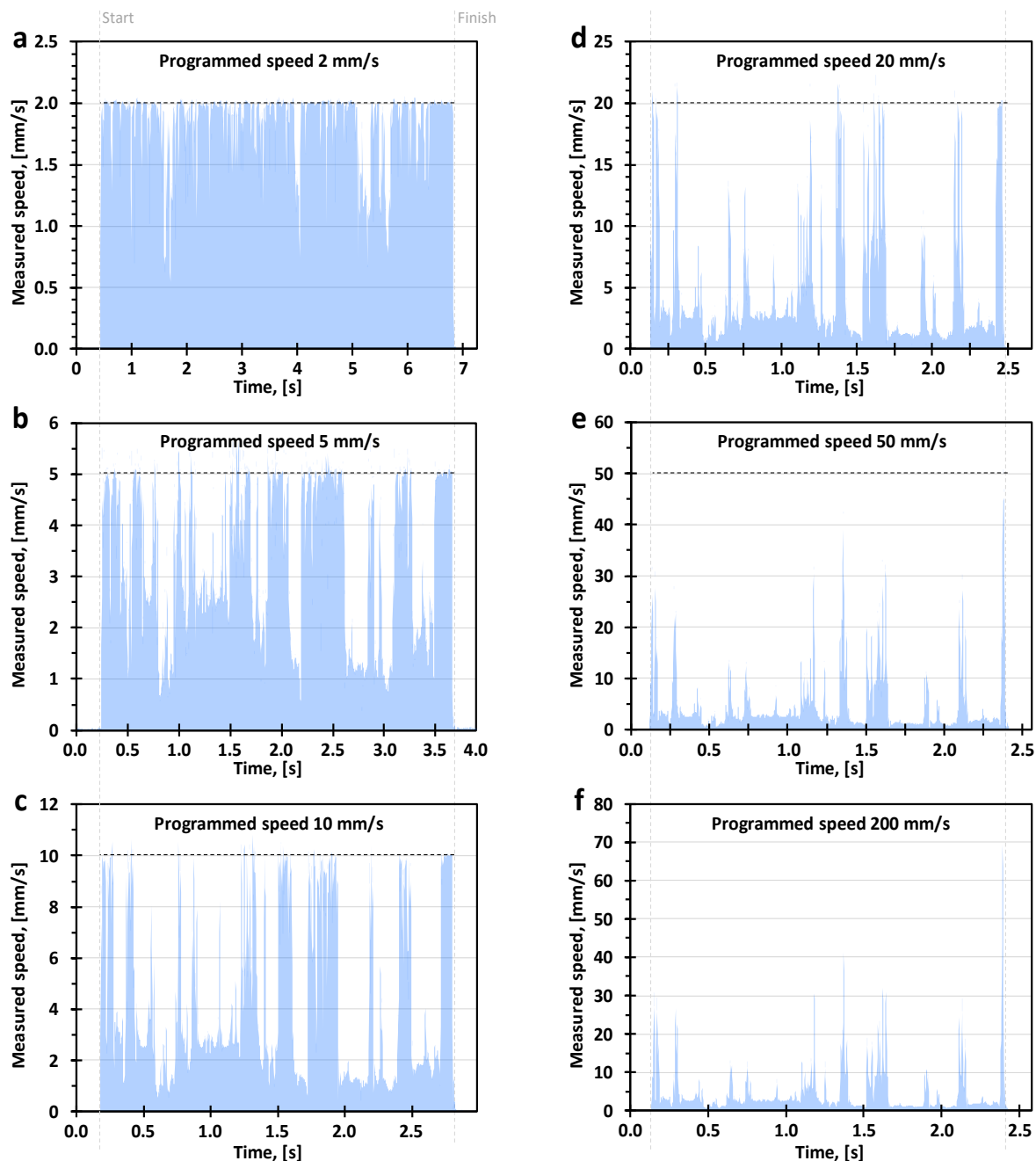


Figure 9. Actual speed vs. Programmed speed while executing logo pattern of 1 mm. Shaded areas represent total instantaneous speed of XY stage, computed from velocities recorded by encoders (Figure 8). Graphs a-f correspond to programmed speeds of 2, 5, 10, 20, 50, and 200 mm/s, where the percent of shaded area visually represents actual performance of XY stage versus the preset speed.

Figure 9 shows the profile of instantaneous speed vs. programmed speed while executing logo pattern of 1 mm, where the proportion of the blue-shaded area visually represents the actual performance of XY stage versus the preset speed. While for 2 mm/s preset speed the performance is still acceptable (Figure 9a), higher speeds result in obvious discrepancy between the programmed speed and actual speed as the XY stage is not able to keep up with the commanded accelerations (Figure 9b-f). The peaks in speed appearing on the speed profile are associated with longer straight segments comprising the logo pattern.

Similar data as on Figure 9 was collected for logo patterns of 2 mm and 4 mm (not shown). Instead, average speeds were computed from such speed profiles. Figure 10a shows actual average speed as a function of both programmed speed and the “intricacy”/(size) of logo pattern. When executing patterns of 1 mm, 2 mm and 4 mm size with maximum programmed speed, XY stage can reach average speeds of only c.a. 5 mm/s, 10 mm/s and 21 mm/s, correspondingly. It can be observed that as logo size is doubled, average speed also doubles. The fact that average speed proportionally scales with logo size confirms the assumption we’ve made during the definition of the trajectory “intricacy”. Figure 10b present the same data in the form of XY stage performance, where performance is an average speed divided by the programmed speed. On both graphs thick black line denotes desirable response of the XY stage, having infinite acceleration.

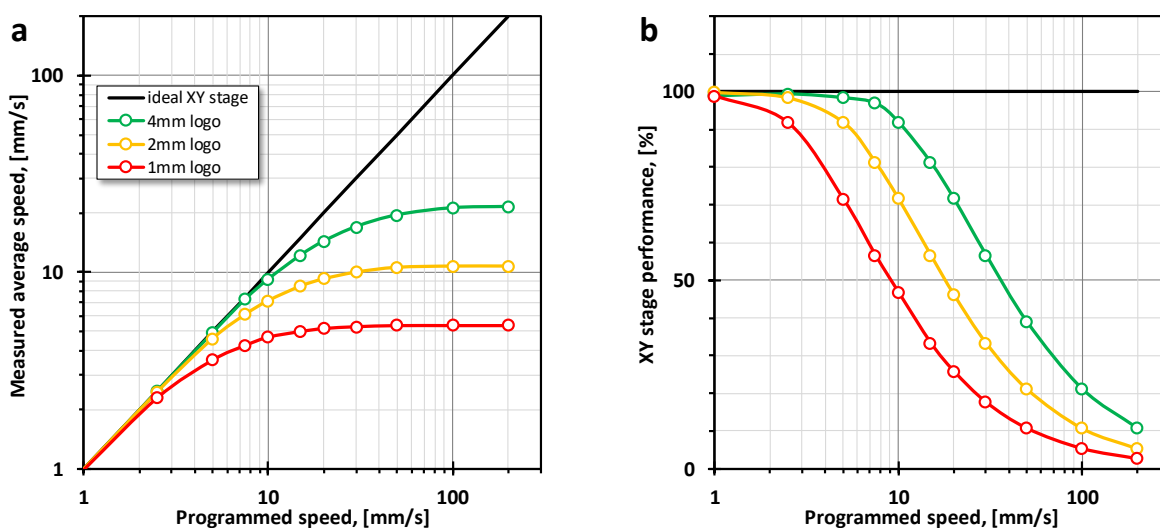


Figure 10. Performance of XY stage. **a** summarizes the data from Figures 8-9, showing Average speed vs. Programmed speed while executing logo patterns of different sizes. Maximum average speed for 1 mm logo was only c.a. 5 mm/s. **b** plots the same data as stage performance, computed as the average speed divided by the programmed speed.

2.3.5. Precision while executing complex moves

Finally, we examine the precision of the XY stage by executing logo pattern of 1 mm size (Figure 7) with different programmed speeds. Instantaneous positions of X and Y linear stages were recorded from XY stage encoders with a fixed interval and plotted in XY coordinate plane to estimate the precision of the executed pattern. For example, red curve on Figure 11a-b represents logo pattern printed with 200 mm/s programmed speed, resulting in actual average speed of only 5 mm/s. Overshooting is apparent on Figure 11b, and positioning error reaches 30 μm , demonstrating that even at such low average speeds positioning precision becomes unacceptable for high-resolution printing. Lower programmed speeds result in a better precision of motion. Note that the stage was operated under standard regime with gradual acceleration ramp, and maximum acceleration ramp would result it much larger inaccuracy.

Red line from Figure 11a-b (200 mm/s programmed speed) is again plotted on Figure 11c, revealing actual positions recorded with 50 ms temporal resolution. Intervals between data points visually represent instantaneous speeds reached by the stage, where severe speed variation is observed, reaching minimum speeds (1-2 mm/s) at curved regions comprising very short straight segments. To further demonstrate the effect of XY stage positioning and instantaneous speed variation, logo pattern of 1 mm was electrohydrodynamically (EHD) printed (standard printing conditions can be found in Chapter 3.2.3.). Heavy fiber accumulation is observed on curved regions (Figure 11d), as translation speed was significantly lower than fiber generation speed, having a perfect agreement with the local speeds shown on the Figure 11c. Furthermore, fiber buckling drastically increased printed line width in those regions. Additionally, same positioning defects are evident from both the recorded XY stage positioning and the printed logo, proving that most imperfections of the printed pattern arise from the speed inconsistency and poor positioning precision while performing complex patterns. This demonstrates that even top-notch mechanical stage cannot provide enough speed and acceleration for printing highly-resolved complex patterns of 1 mm scale and below.

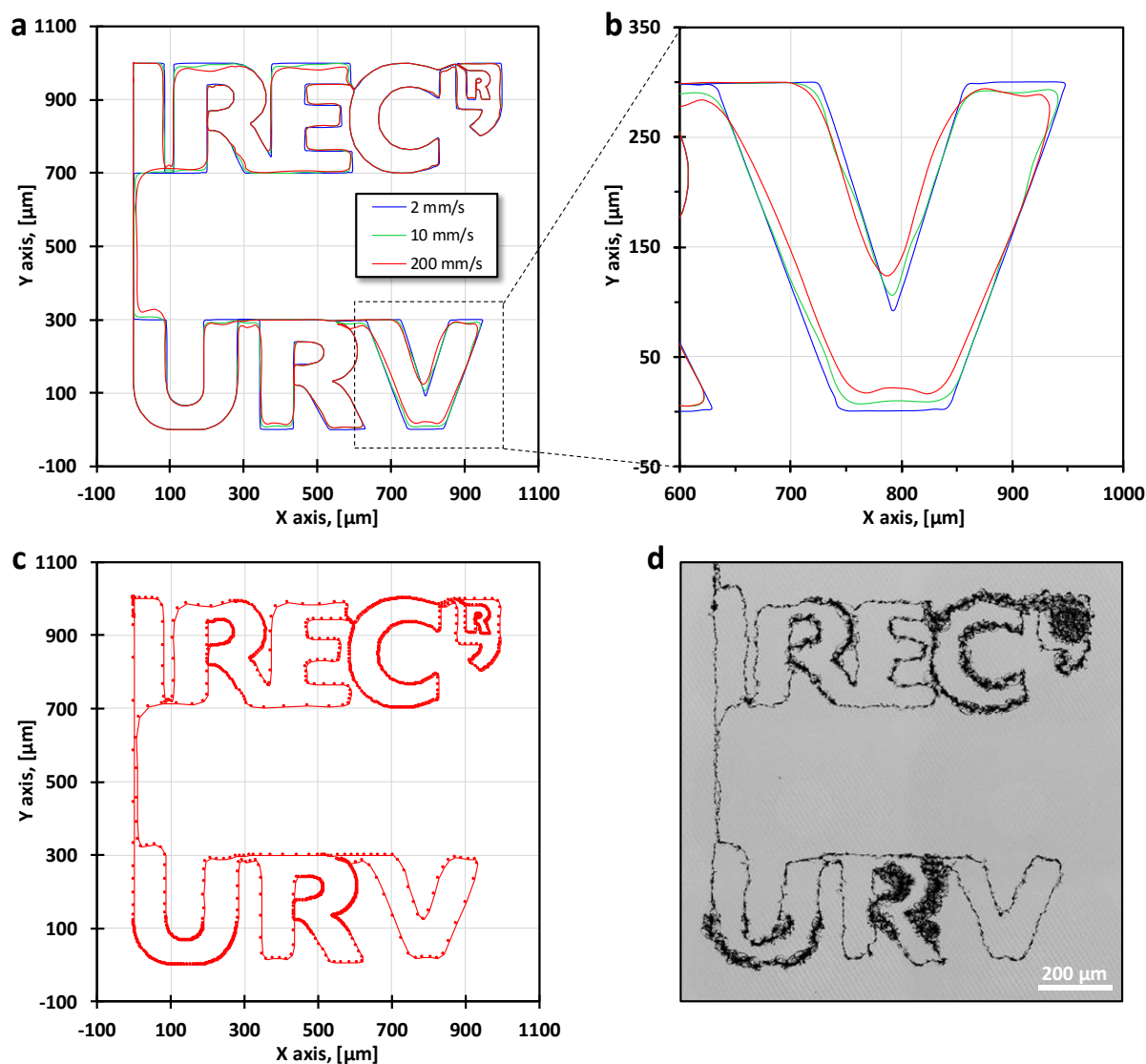


Figure 11. Precision of XY stage while executing logo pattern of 1 mm. X and Y positions of the stage moving at preset speeds of 2, 10, and 200 mm/s (a-b). **b** shows that actual translation path deviates more from the programmed path as the preset speed is increased, resulting in imprecision of c.a. 25-30 μm for 200 mm/s. **c** shows actual path at 200 mm/s preset speed, revealing the data points measured by the encoders with 50 ms resolution. **d** Logo pattern printed by conventional EHD jet printing at 200 mm/s preset speed.

2.4. Conclusions

In summary, this chapter analyzed the performance of XY mechanical stage for EHD jet printing. Ideal XY stage would possess: (i) maximum speed similar to the speed the EHD jet (up to 500 mm/s); (ii) virtually infinite acceleration, necessary to sustain the programmed speed while executing complex patterns; and (iii) high positioning precision, on the order of 1 μm . These requirements cannot be met simultaneously because of the tradeoff between the dynamic performance and the precision of motion. Acceleration of best XY stages is about 1000X smaller than required for fast EHD jet printing at micron resolution. From the maximum acceleration of best XY stages it was simulated that 2 mm long straight segment is necessary to reach the average speed of 100 mm/s. Shorter moves were experimentally executed with gradual vs. maximum acceleration ramp. While maximum acceleration ramp improved the average speed, it is rarely used because it results in excessive vibration/wear of the stage and drastically decreases its precision. Finally, XY stage performance was tested on complex logo patterns while moving at maximum speed. For 1 mm pattern, average speed was only c.a. 5 mm/s while instantaneous speed varied significantly for different parts of the pattern, ranging from 1 mm/s to 70 mm/s. Furthermore, positioning error was as high as 30 μm demonstrating that even at such low average speeds positioning precision becomes unacceptable for high-resolution printing. Concluding, to reach full potential of EHD jet printing, the limitation of too slow XY stage must be overcome by developing another means of material positioning.

2.5. References

1. B. Huang, S.B. Singamneni, Curved Layer Adaptive Slicing (CLAS) for fused deposition modelling, *Rapid Prototyp. J.* 21 (June (no. 4)) (2015) 354–367.
2. G.Q. Zhang, et al., Use of Industrial Robots in Additive Manufacturing ? A Survey and Feasibility Study, in *ISR/Robotik 2014, 41st International Symposium on Robotics (2014)* 1–6.
3. J. Go, S.N. Schiffres, A.G. Stevens & A.J. Hart. Rate limits of additive manufacturing by fused filament fabrication and guidelines for high-throughput system design. *Additive Manufacturing* 16, 1–11 (2017).
4. J. Go, A. J. Hart, Fast Desktop-Scale Extrusion Additive Manufacturing. *Additive Manufacturing*. 18, 276–284 (2017).
5. A. Hace, K. Jezernik & M. Terbuc. VSS motion control for a laser-cutting machine. *Control Engineering Practice* 9, 67–77 (2001).
6. H. Lim, J.W. Seo & C.H. Choi. Position control of XY table in CNC machining center with non-rigid ballscrew. in *Proceedings of the American Control Conference* 3, 1542–1546 (IEEE, 2000).
7. Y. Tomita, K. Makino, M. Sugimine, N. Taniguchi, High-Response X-Y Stage System Driven by In-Parallel Linear Motors. *CIRP Annals - Manufacturing Technology*. 45, 359–362 (1996).
8. K. Itoh, M. Iwasaki & N. Matsui. Robust fast and precise positioning of ball screw-driven table system on machine stand. in *International Workshop on Advanced Motion Control, AMC*.
9. <https://www.newport.com/g/motorized-linear-translation-stage-selection-guide>
10. K.S. Sollmann, M.K. Jouaneh & D. Lavender. Dynamic modeling of a two-axis, parallel, H-frame-type XY positioning system. *IEEE/ASME Transactions on Mechatronics* 15, 280–290 (2010).
11. S. Staicu, D.C. Carp-Ciocardia, Dynamic analysis of Clavel’s Delta parallel robot, 2003 *IEEE International Conference on Robotics and Automation (Cat. No.03CH37422)* 3 (2003) 4116–4121.

Chapter 3

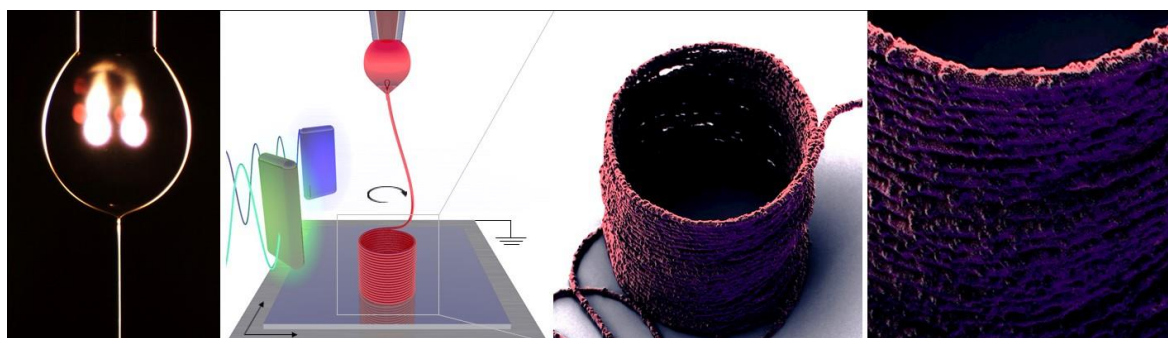
Ultrafast 3D printing with submicrometer features using electrostatic jet deflection

This chapter is based on the results published in:

Liashenko, I., Rosell-Llompart, J. & Cabot, A. Ultrafast 3D printing with submicrometer features using electrostatic jet deflection. *Nature Communications* 11, 753 (Feb. 2020).

Abstract

Additive manufacturing technologies based on layer-by-layer deposition of material ejected from a nozzle provide unmatched versatility but are limited in terms of printing speed and resolution. Electrohydrodynamic jetting uniquely allows generating submicrometer jets that can reach speeds above 1 m s^{-1} , but such jets cannot be precisely collected by too slow mechanical stages. Here, we demonstrate that controlling the voltage applied to electrodes located around the jet, its trajectory can be continuously adjusted with lateral accelerations up to 10^6 m s^{-2} . Through electrostatically deflecting the jet, 3D objects with submicrometer features can be printed by stacking nanofibers on top of each other at layer-by-layer frequencies as high as 2000 Hz. The fast jet speed and large layer-by-layer frequencies achieved translate into printing speeds up to 0.5 m s^{-1} in-plane and 0.4 mm s^{-1} in the vertical direction, three to four orders of magnitude faster than techniques providing equivalent feature sizes.



3.1. Introduction

Additive manufacturing has become the new paradigm of distributed production of customized products, providing advantages in terms of geometric freedom of design, material utilization, and lead time reduction¹⁻³. However, existing additive manufacturing technologies still have important limitations, especially on production speed, availability and combination of materials, and control over their microstructure and thus functionality. Additionally, the cost and complexity of manufacturing equipment that enables producing submicrometer features are prohibitive for a true distributed production.

In additive manufacturing strategies based on ejection of a melt or an ink from a nozzle, material is selectively deposited layer-by-layer either as a continuous extruded filament or jet, or as a train of droplets formed by the actuation of a piezoelectric, a thermal, an ultrasonic or an electrostatic mechanism^{4,5}. Besides cost and simplicity, the main advantage of nozzle-based 3D printing strategies is that they allow the manufacture of items made of virtually any substance, ranging from polymers^{6,7}, to metals^{8,9}, to ceramics¹⁰, to wood^{11,12}, and even to biological tissues¹³. Such unmatched material versatility stems from the use of metal or polymer melts or solvent-based inks, which can be formulated to contain any component in the form of ions, molecules, nanoparticles, or even living cells¹⁴⁻¹⁷.

However, current nozzle-based 3D printing technologies are relatively slow as they rely on the use of a mechanical stage to define the geometry of the printed product. Another drawback is a limited printing resolution because the width of the printed lines correlates with that of the nozzle aperture, typically well above several tens of micrometers. Nozzles with smaller apertures suffer from frequent clogging and high viscous losses, and, consequently, can only be used with low-viscosity inks free of large particles, which obviously limits material versatility. To make matters worse, the smaller the jet thickness gets, the slower the printing process.

To effectively reduce the width of the printed lines, instead of forcing the extrusion of material through very thin nozzles, the melt or ink can be pulled by means of an electric field applied between the nozzle and the printing substrate. Once the electrical stresses acting on the liquid surface overcome the surface tension stress, the liquid meniscus forms

a Taylor cone wherefrom a thin and fast jet of ink is propelled electrostatically towards the printing substrate¹⁸ (Figure 2a). Such electrohydrodynamic (EHD) jetting strategy is uniquely suited for high resolution 3D printing compared to other nozzle-based 3D printing methods^{19–24}. EHD jetting allows printing submicrometer features with no risk of nozzle clogging, as it enables the generation of nanometer-sized jets from wide nozzle apertures using a great variety of inks, with viscosities ranging over several orders of magnitude²⁵.

Despite its advantages, EHD jetting has not been developed to its full potential for 3D printing because of the huge challenge that the precise location of very fast electrified jets, with speeds that can be in excess of 1 m s^{-1} , presents²⁶. Current systems based on EHD jetting use mechanical stages to locate the material on the printing substrate. However, mechanical stages can only match the huge speeds of the electrified jets in long straight lines, but cannot attain the giant accelerations that are needed to sustain such speeds while printing small complex patterns. These unmatched speeds result in uncontrolled jet buckling onto the substrate, degrading the quality of the printed pattern. Whereas buckling has been used to print simple cycloid and wavy patterns along straight lines²¹, the minimum radius of curvature that can be printed without buckling is limited to around 0.5 mm when using high speed electrified jets ($> 0.1 \text{ m s}^{-1}$).

To bypass the challenge of precisely collecting such fast jets, the overall material flow rate has been reduced by pulsing the jet generation²⁷. This strategy, known as EHD drop-on-demand printing, has allowed unprecedented printing resolutions down to 50–80 nm²⁸. However, the severe decrease in printing speed due to the pulsing may make this strategy too slow for industrial implementation.

To unleash the potential of high-speed printing allowed by very fast EHD jetting, here we propose to electrostatically deflect the jet trajectory as a suitable strategy to control the location of a continuous electrified jet when it impacts the substrate. Electrostatic deflection of electrified jets have been previously attempted in simple configurations: (i) patterning the substrate to direct the jet toward specific locations^{29–31}; (ii) manual switching of DC potentials^{32,33}; and (iii) using elementary wavefunctions^{34–41}. But all of them lack the fast control necessary for 3D printing of complex patterns. Here we demonstrate that through high speed amplifiers controlled by software, ultrafast jet deflection can be achieved and used to print 3D objects with submicrometer features.

3.2. Methods

3.2.1. Chemicals

Polyethylene oxide (PEO) of various molecular weights was purchased from Sigma-Aldrich (#182001, viscosity-average molecular weight 300 kDa; #372781, 1000 kDa; #189472, 5000 kDa). Poly(3,4-ethylenedioxythiophene) polystyrene sulfonate (PEDOT:PSS) solutions were purchased from Sigma-Aldrich (#655201, 3-4% in water). Ethanol and ethylene glycol were obtained from different sources. All chemicals were used as received, without further purification. Ag nanoparticles of ca. 50 nm in diameter were synthesized using PVP as ligand⁴⁹. After synthesis, nanoparticles were thoroughly washed by multiple precipitation and redispersion cycles using ethanol as solvent and acetone as antisolvent. Finally, nanoparticles were precipitated for posterior use. Thus obtained Ag nanoparticles could be dispersed in polar solvents such as water and ethanol.

3.2.2. Inks formulation

Deionized water was used as main solvent and some amounts of ethanol or ethylene glycol were added to control surface tension and evaporation rate. All ink compositions are described in Table 1. Electrical conductivity of some inks is provided in Table 2, revealing the dependence of electrical conductivity on PEO concentration and solvent system.

PEO inks were prepared by dissolving the proper mass of PEO (typically 2-10 wt%) in the solvent mixture during 24 hours under magnetic stirring. PEDOT:PSS inks were prepared by adding the proper amount of PEDOT:PSS solution into the dissolved PEO ink and homogenizing the mixture by magnetic stirring. Ag nanoparticle inks were prepared by adding the PEO ink into a flask containing precipitated Ag nanoparticles and dispersing them using ultrasonication and magnetic stirring. All inks were kept in sealed vials, where they could be stored for months and even years without showing signs of degradation. Inks containing PEDOT:PSS were stored in a fridge at 4 °C.

Table 1. Ink compositions used for the printing. Percentages are represented in mass (wt.%) relative to the total mass of the ink. Solvent ratios are also represented in mass.

Ink compositions (wt% and solvent mass ratios)	Figures
10% PEO (300 kDa) in water	6b-d,g; 8a; 9a
8% PEO (300 kDa) in water:ethylene glycol (4:1)	5b-d; 7a-c; 9b
5% PEO (300 kDa) in water:ethanol (1:3)	2d
5% PEO (300 kDa) in water:ethanol (1:1)	3a
2% PEO (5000 kDa) in water:ethanol (1:1)	2a
8.1% PEDOT:PSS dispersion (3-4%) in 2% PEO (5000 kDa) in water:ethanol (1:1).	4a-c; 10b
Solid fiber containing 15% PEDOT:PSS and 85% PEO	

5% Ag NPs in 4.75% PEO (300 kDa) in water:ethanol (1:3)	4d-e; 6e-f; 8b-c; 9c-d
10% Ag NPs in 4.5% PEO (300 kDa) in water:ethanol (1:3)	10a

Table 2. Electrical conductivities measured at 25 °C for inks containing different amounts of PEO, PEO molecular weight, and solvent. Percentages are represented in mass (wt.%) relative to the total mass of the ink. Solvent ratios are also represented in mass.

Ink composition (wt% and solvent mass ratios)	Electrical conductivity [S/cm]
5% PEO (300 kDa) in water:ethanol (1:1)	19.2
5% PEO (1000 kDa) in water:ethanol (1:1)	15.8
2% PEO (1000 kDa) in water:ethanol (1:1)	13.4
10% PEO (300 kDa) in water	99.1
8.1% PEDOT:PSS dispersion (3-4% in water) in 2% PEO (1000 kDa) in water:ethanol (1:1)	19.0

3.2.3. Printer set-up and printing process

Inks were loaded into a glass syringe (Hamilton #81320, 1 ml) and supplied to the nozzle by a syringe pump (Harvard apparatus, Pump 11 Pico Plus Elite 70-4506) with a typical flow rate of 0.05-0.07 $\mu\text{l min}^{-1}$. The pendant drop formed at the nozzle aperture had a diameter of ca. 100-1000 μm . Stainless needles with blunt ending (Hamilton N726S, 26s gauge, 127 μm ID, 474 μm OD) or borosilicate glass tips (c.a. 70-100 μm) were used as nozzle. No surface treatment was applied to the tips before their use. Glass tips were manufactured from borosilicate capillaries (Sutter Instruments, B100-50-15) by a Pipette puller (Sutter Instruments P-97) and the tips were manually broken by scratching two tips against each other, leaving glass tips with an outer diameter of c.a. 70-100 μm . Glass tips were glued atop of a stainless-steel needle with blunt ending (B Braun Sterican, 27 gauge). Silicon wafers (University Wafers #452, p-type, <100>) were used as substrate. Silicon was cleaned with isopropanol to remove organic contamination prior to printing. The nozzle-to-substrate distance ranged 2-5 mm, but typically was 3 mm. A positive potential was applied to the nozzle using a Matsusada AU-20P15, max. 20 kV, 15 mA high voltage supply, while the substrate was positioned on an electrically grounded plate, mounted atop of a XY translation stage (PI miCos linear stages PLS-85 with 10 mm range in both X and Y with RS422 encoders).

Electrohydrodynamic (EHD) jetting was initiated by slowly increasing the nozzle voltage up to 1800-3000 V, until the pendant ink drop elongated and fell on the printing substrate. Jet initiation voltage was lower for inks with lower surface tension (those containing ethanol), and also for nozzles and pendant drops of smaller size. Once the jet was initiated, voltage was lowered to 400-1500 V and the jet was stabilized for 2 minutes before printing. Lowest nozzle voltages in this range were used for inks containing PEO with very high molecular weight (i.e. 5000 kDa), which provided superior jet stability due to their higher viscoelasticity. Jet stability was critical for printing reproducible features and it depended on printing parameters such as the applied voltage, ink properties including viscosity and

volatility, and on ambient parameters that together with the flow rate determined the size and stability of the drop. A proper ink formulation and selection of the printing parameters, including voltages and flow rate at the syringe pump, provided jets that remained stable for over 15 minutes, which was the time period of the longest printing event we studied. Considering that single objects were printed in less than 1 second, 15 minutes allowed printing over 1000 objects.

The printing process was carried out under ambient conditions, with temperature in the range 18-25 °C and 40-80% relative humidity. During printing the substrate was translated relative to the nozzle by the XY translation stage. Translation was either continuous (to produce fiber tracks, as on Figure 4a-c, or long 3D walls, as on Figure 7) or in steps (to print 3D patterns while the substrate was motionless, as on Figures 4d-e, 5-6, and 8).

3.2.4. Set-up and software for electrostatic jet-deflection

The jet was deflected from its default trajectory using jet-deflecting electrodes. For the high-speed video study of the jet deflection and for Figure 3c, two electrodes were positioned on the same axis (left and right on Figure 2d) and the separation between the default jet trajectory and electrodes was 3 mm. A fixed electrodes design (as on Figure 2c) was used for EHD printing, with a nozzle-to-electrodes separation of 10 mm. Electrodes were glued to a plastic holder produced by polymerization of photosensitive resin (Formlabs Form 2 3D printer, FLGPCL04 clear resin).

A LabVIEW software was specifically developed to define and generate the voltage at the different jet-deflecting electrodes from parameters such as the pattern geometry, the number of printed layers, the layer printing frequency and the signal amplitude. A data acquisition card (National Instruments, USB-6259) was used to generate the synchronized analog signals (max. ± 10 V), which were amplified (max. ± 2000 V, Matsusada AMJ-2B10 and Trek 677B) and applied to the jet-deflecting electrodes. The amplitude of the signals applied to jet-deflecting electrodes defined the size of the printed pattern and typically ranged about 1000-2000 V for 10 mm nozzle-to-electrodes separation and 200-400 V for 3 mm nozzle-to-electrodes separation. Printing frequencies typically ranged from 50 to several hundred layers per second, but we could reach layer-by-layer frequencies as high as 2000 Hz.

3.2.5. Optical imaging

The optical microscope used to monitor the printing process consisted of a 12X lens with adjustable zoom and focus (Navitar 1-50486), a 2x lens adaptor (Navitar 1-62136) and a 5X microscope lens (Mitutoyo 1-60226). A high-intensity light source (AmScope HL-250-A) was positioned behind the observed object under ca. 5° angle from the camera optical axis, thus that direct light did not reach the camera sensor (dark-field setting, as on Figures 2a, 2d and 6g). For real time monitoring of the printing process, a paper sheet was put between the light source and the observed object (bright-field setting). Printing process was monitored and recorded using a CMOS camera (Basler acA2040-25gc) mounted on the microscope. High-speed videos (Supplementary Movie 1, captures on Figure 2d, and

Supplementary Movie 2, captures on Figure 6g) were recorded with a high-speed camera (Photron FASTCAM-1024PCI) at 1000 fps.

3.2.6. SEM imaging

Most of printed samples were sputtered with a thin silver layer using a DC magnetron sputter (Emitech K575X, 80 mA, argon, 90 seconds, sample was slowly rotated to obtain uniform thickness) to improve the quality of SEM images and to protect the PEO fiber from degradation/shrinkage caused by the electron beam. Scanning electron microscopy (SEM) micrographs were obtained at 1-2 kV electrons acceleration voltage on AURIGA (FIB-FESEM) from Carl Zeiss using a secondary electrons (SE2) detector. Figure 6e was obtained by superimposing two images taken with SE2 and in-lens detectors and false-coloring the printed object in red and blue respectively.

3.2.7. Simulation of jet deflection

The simulation of the electric potential and field around the jet in the presence of a jet-deflecting electrode (Figure 2b) was done in COMSOL Multiphysics® 5.2a using the following parameters: nozzle potential at +1000 V; substrate and jet-deflecting electrode electrically grounded (0 V); nozzle-to-substrate separation of 3.6 mm; nozzle-to-electrode separation at 2 mm, and electrode size (height, width and thickness): 3.5x3.0x0.5 mm³. Color gradient represents the electric equipotential lines and black arrows represent the electrical field vectors and are proportional to its magnitude. The deflecting electrode, nozzle and ink drop were plotted in white for clarity, but are at the specified potentials. The electric field streamline (also in white) starting at the tip of Taylor cone represented the trajectory of an electrostatically deflected massless jet. Supplementary Movie 3 presents an animation of jet deflection simulation using 2 jet-deflecting electrodes.

3.3. Results and Discussion

3.3.1. 3D printer design

A conventional EHD printer basically comprises a nozzle, a system which supplies the printable material to this nozzle such as a syringe pump, a printing substrate mounted on a XY mechanical stage, and a high voltage power supply connected in between the nozzle and the substrate. The printing substrate is usually placed onto an electrically-grounded electrode and it is preferentially conductive, or it has a conductive surface to dissipate electrostatic charge fast enough. The required charge dissipation time depends on the targeted layer-by-layer printing frequency. Non-conductive substrates can be used when printing at sufficiently low frequencies or when charge dissipation is aided by a local injection of an ion flux or water vapor or by periodically discharging the substrate with a corona discharge needle⁴². Upon application of a voltage difference, typically in the 200-1000 V range, a charged jet is expelled from the ink drop at the exit of the nozzle toward the substrate (Figure 2a). The default trajectory of the jet is a straight line between the drop and the closest substrate point. The jet thickness is independent of the size of the nozzle aperture and it can be below ~ 100 nm depending on the ink properties, the supply rate and the applied voltage⁴³. The viscoelastic properties of the jet need to be properly adjusted for it not to break into droplets. For this purpose, small amounts (2-10 wt%) of a polymer such as polyethylene oxide (PEO) with a high molecular weight, typically 300-5000 kDa, are usually incorporated into solution-based inks⁴³. The separation between the nozzle and the printing substrate is typically in the range from 1 to 5 mm. Longer separations may result in whipping instabilities on the jet, which would hamper its precise localization on the substrate; whereas shorter distances may not allow enough time for the jet to sufficiently solidify or dry up before reaching the printing substrate. As will be shown later, under jet-deflection control shorter nozzle-to-substrate separations also limit the size of the printable area. Patterns are usually printed using a continuous jet. Eventually, this jet could be rapidly interrupted/restarted by electrostatically activating a gutter that collects the jet when its deposition onto the substrate is not desired^{44,45}.

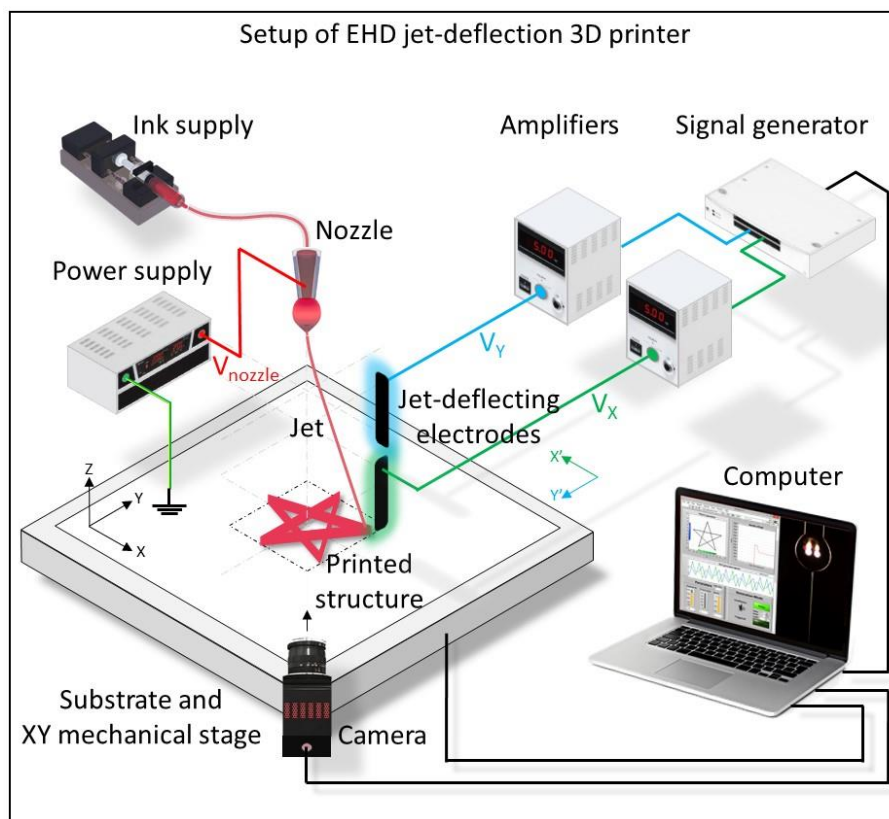


Figure 1. Schematic of an EHD 3D printer with jet-deflecting electrodes.

We modified the conventional EHD printer architecture by setting additional electrodes around the jet (Figures 1, 2c). The purpose of these electrodes was to modify the electric field in the vicinity of the jet to deflect it from its default trajectory and control in this way its point of arrival at the substrate (Figure 2b,d). The voltages at these electrodes were synchronized and produced by amplifying a computer-generated signal in a range from about -2000 V to about 2000 V. The movement and position of the XY mechanical stage supporting the printing substrate was also controlled and synchronized through the same computer. As in conventional 3D printing, the software had full control over the printing process through the parameterization of the layer-by-layer deposition process to print an object with predefined geometry, size and in our approach even microstructure.

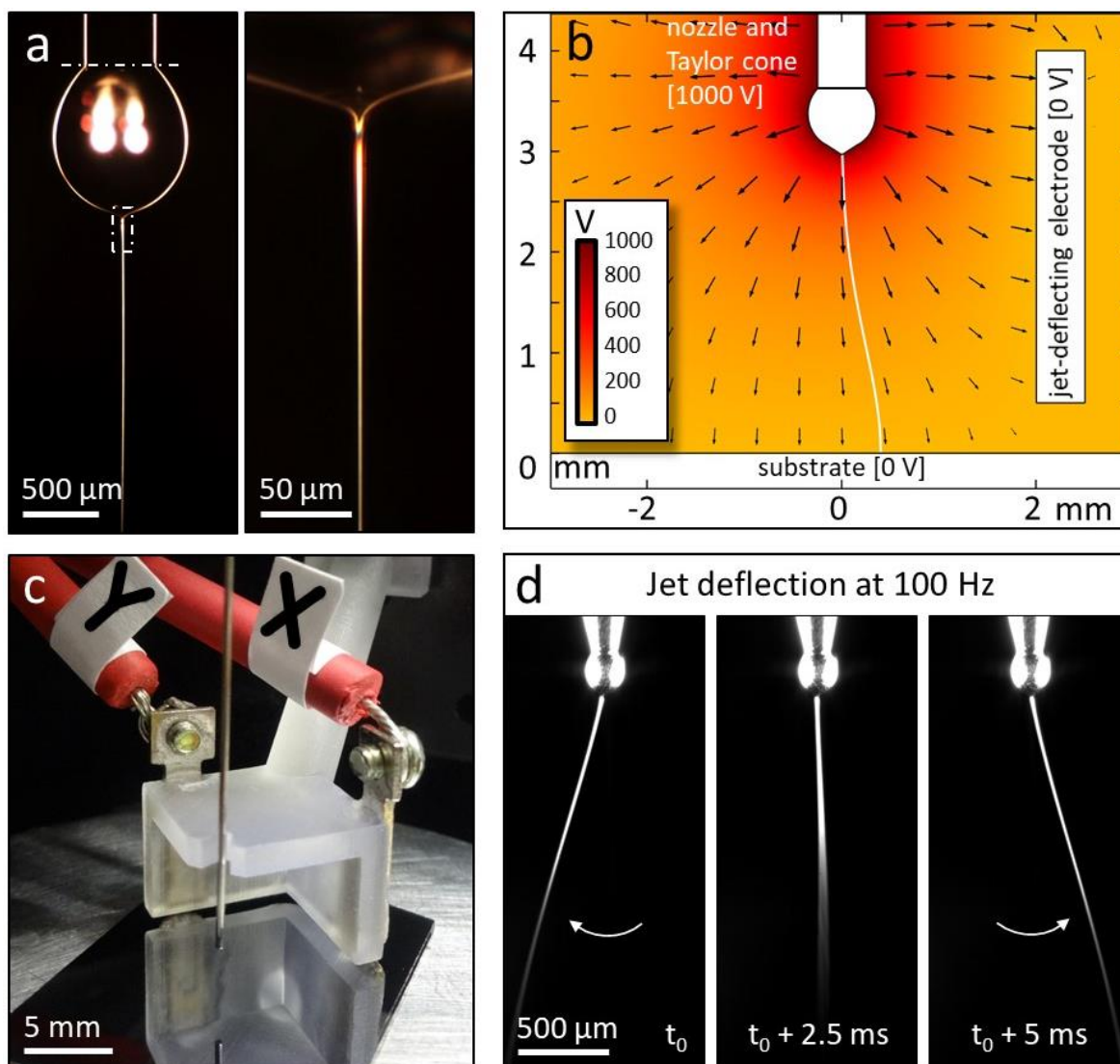


Figure 2. The electrostatic control of the jet trajectory. **a** Optical photographs of the nozzle, ink drop (below dotted line), Taylor cone, and the electrified jet generated by applying 1000 V between the nozzle and a printing substrate (not shown). **b** Simulation of the electric potential and field around the jet in the presence of a jet-deflecting electrode. The deflecting electrode, nozzle and ink drop are shown in white for clarity but are at the specified potentials. The electric field "streamline" (also in white) starting at the tip of Taylor cone represents the theoretical trajectory of a massless jet. Additional simulation results can be found in the Supplementary Movie 3 (as well as in Chapter 4, Fig. 4-5). **c** Set of jet-deflecting electrodes and needle used as nozzle. **d** High-speed video captures of the jet being deflected in 1D with a frequency of 100 Hz (video showing jet deflection at 10, 50 and 100 Hz can be found in the Supplementary Movie 1). Two jet-deflecting electrodes (not shown) were used, positioned on the left and on the right side of the video captures. Video captures show the nozzle, the Taylor cone at the end of the ink drop and the thin jet expelled. The trajectory of this jet and thus its point of arrival to the substrate were modulated by the voltage applied to the jet-deflecting electrodes.

3.3.2. Printing 2D patterns

Figure 1e shows high-speed video captures of a jet produced from an ethanol-water (3:1) ink containing 5% PEO (M_w 300 kDa) being periodically oscillated from the action of a sawtooth wave applied at two opposing jet-deflecting electrodes (Supplementary Movie 1). This electrified jet was remarkably stable under the action of the jet-deflecting field at frequencies as high as 10 kHz. Its deflection angle depended on the amplitude and frequency of variation of the electric field. For small signal amplitudes applied to the jet-deflecting electrodes, small deflection angles ($<15^\circ$) that varied linearly with the voltage amplitude were observed. Higher voltage amplitudes eventually resulted in a non-linear increase in jet deflection angle, which was limited at around 40° before severe jet instabilities started to occur. At a low frequency, small oscillation amplitudes resulted in buckled fibers, while larger amplitudes produced straight fibers (Figure 3a-b). As jet deflection frequency increased, the amplitude range resulting in buckling was decreased (Figure 3c). As a result of this electrostatic jet deflection in one axis, fibers with a thickness down to 100 nm and pattern widths up to 2 mm could be deposited. Using at least two electrodes to deflect the jet in any direction along the substrate plane, 2D structures with any predefined shape could be produced (Figure 4d-e). Placing the printing nozzle at 5 mm from the substrate and using moderate jet deflection angles to ensure a linear dependence with the voltage amplitude, the lateral size of the largest object defined by jet deflection was around 2 mm. Additionally, by coupling and synchronizing the jet deflection system with a mechanical stage, the fast printing of microscopic features could be extended to larger areas (Figures 3a, 4d-e).

As the jet deflection frequency was increased, the jet deflection angle at a given amplitude decreased and the size of the printed pattern/object was reduced (Figure 3c). This result was expected taking into account the finite speed of the electrified jet and the inability of the electrostatic deflection to appreciably stretch the jet. When attempting to print 2D and 3D patterns faster than the jet speed at its arrival to the substrate, the fiber length became insufficient to complete the intended pattern and thus degraded geometries were produced. To avoid this limitation, the jet deflection waveform had to be designed so that the contact point between the jet and the substrate was moving at all times at the same speed of the jet at its point of arrival to the substrate. For the printing speed to match the

jet speed it was required to find the appropriate jet deflection parameters, which could be easily accomplished when using a calibration pattern such as those shown in Figure 4b-c. Detailed discussion on this can be found in Chapters 4 and 5.

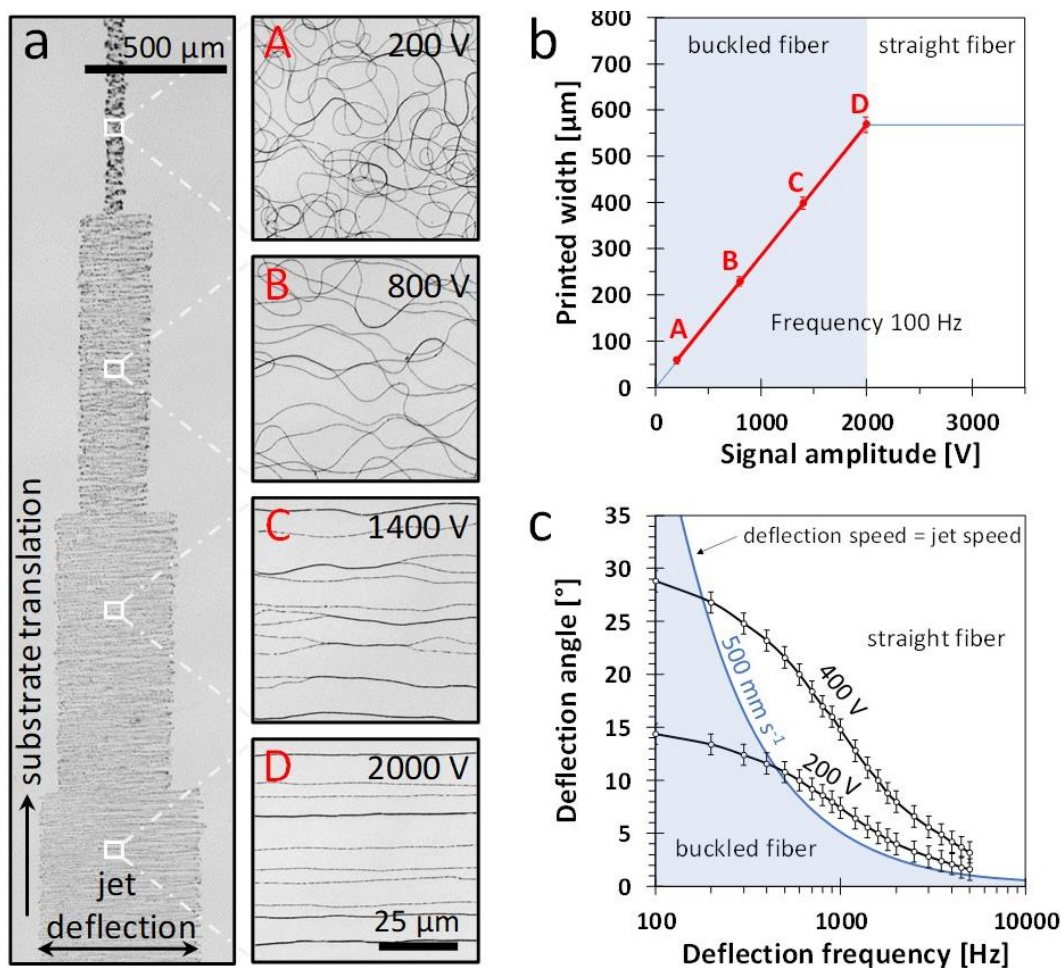


Figure 3. Role of jet deflection parameters. **a** Optical photographs of the PEO fiber collected as the substrate is moved at 1 mm s^{-1} and the jet is deflected with a frequency of 100 Hz . The stepwise increase of amplitude of the jet deflection signal resulted in a stepwise increase of width of the PEO pattern, fiber straightening and alignment. The amplitude of the jet deflection was varied from 200 V to 2000 V as depicted in the micrographs and the two electrodes were located at 10 mm from the default jet trajectory. **b** Dependence of the width of the printed pattern on the signal amplitude at a fixed frequency of 100 Hz . The blue shaded area displays the amplitude range where fiber buckling would be obtained at this fixed frequency. The four points in red correspond to the four amplitudes experimentally tested and presented in (a). At the lowest amplitude that provides straight fibers, the printing speed and the jet speed are matched (point D) and the jet speed can be computed as a product of the fiber length printed in one deflection period times the printing frequency. At this amplitude, the width of the printed pattern reaches a plateau and it cannot be increased by increasing the signal amplitude. **c** Experimental dependence of the jet deflection angle on the jet deflection frequency for two different jet deflection amplitudes, 200 V and 400 V (two opposing electrodes located at 3 mm from the default jet trajectory). A blue line corresponding to a jet deflection speed

of 0.5 m s^{-1} is also plotted. The blue shaded area displays the region providing a jet deflection speed below 0.5 m s^{-1} , thus jets traveling at this speed would result in fiber buckling.

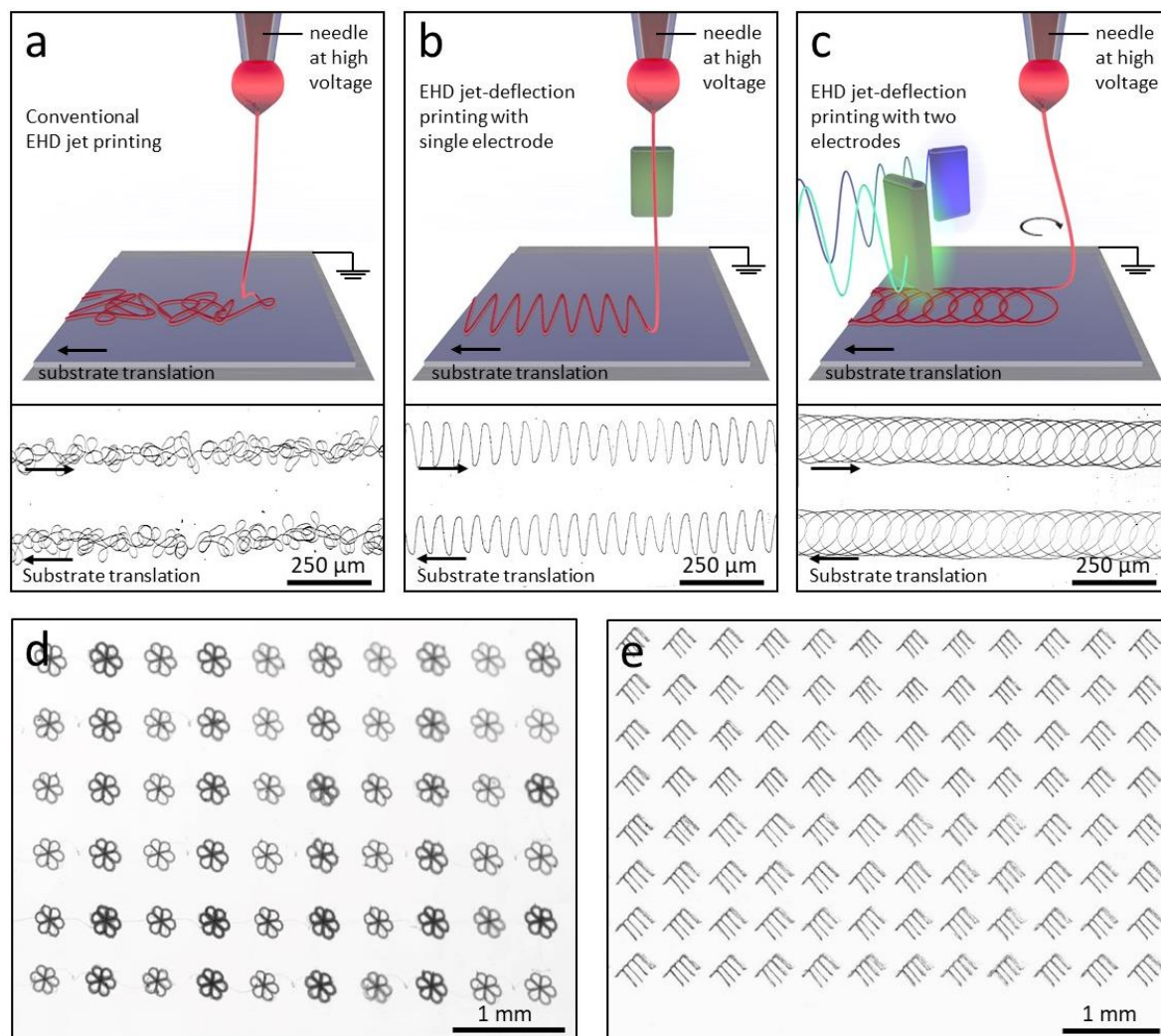


Figure 4. Printing 2D patterns. **a-c** Schematics (top panels) and optical photographs of the experimental PEO-PEDOT:PSS patterns printed as the substrate is continuously moved in a straight line (bottom): **a** fiber buckling obtained with no jet deflection; **b** sawtooth pattern obtained using 1D jet deflection in an axis normal to the translation of the mechanical stage; and **c** circular pattern obtained using 2D jet deflection. **d,e** Optical photographs of more complex 2D patterns printed using two jet-deflecting electrodes to define the pattern and the mechanical stage to translate the substrate between printing events. A 4.7wt% PEO ink containing Ag NPs was used to print these patterns.

3.3.3. Printing 3D objects

3D objects were printed by the successive layer-by-layer deposition of material. Through this procedure, 3D structures with height up to 100 μm and very high aspect ratios, e.g. walls with height-to-thickness ratios well above 1000, were easily printed. Figure 4 displays a schematic diagram of this process, and several SEM micrographs of straight walls printed by stacking up to 150 layers on top of each other. Using PEO inks with relatively low electrical conductivities, we were able to produce 3D structures using layer-by-layer frequencies as high as 2000 Hz. The fast jet and these high layer-by-layer frequencies translated into printing speeds up to 0.5 m s^{-1} in-plane and 0.4 mm s^{-1} off-plane, i.e. in the vertical direction, three to four orders of magnitude faster than achievable by extrusion and drop-on-demand EHD techniques when producing equivalent feature sizes. By either increasing the electrical conductivity of the printed material or using a proper atmosphere to allow faster charge dissipation, 3D printing speeds could be further increased.

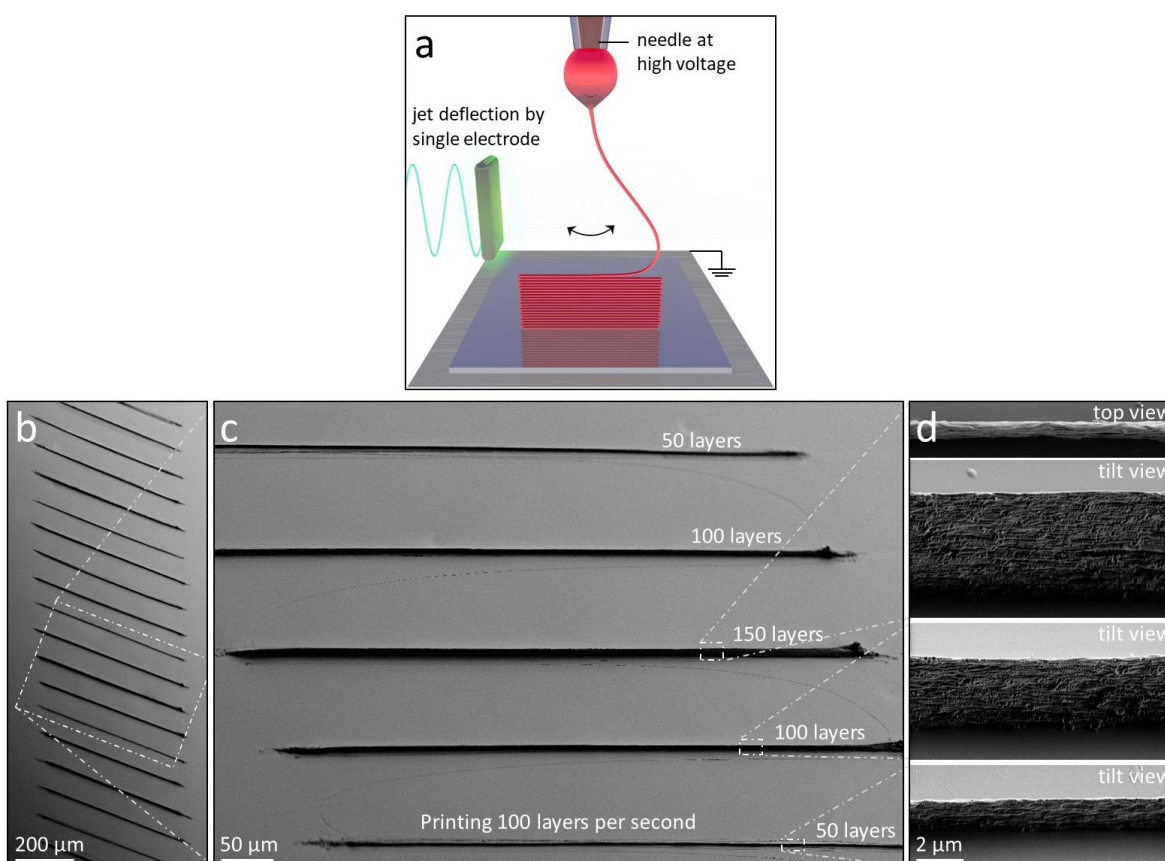


Figure 5. Printing 3D walls. **a** Schematic of the 3D printing of a wall. **b-d** SEM micrographs of PEO walls built by layer-by-layer assembly at a jet oscillation frequency of 50 Hz, thus depositing two layers per period. Each wall was printed using exclusively electrostatic jet deflection to position the material on the substrate. The XY translation stage was moved

only in between walls. The periodic deflection of the jet during 1.5, 1 and 0.5 s resulted in walls of variable height, composed of 150 layers, 100 layers and 50 layers, respectively. SEM micrographs in (d) shows the top view of the wall composed of 150 layers and the 45° tilt view of walls composed of 150, 100 and 50 layers. Scale bars (**b-c**): 200 μm and 50 μm . All SEM micrographs on (d) have the same scale of 2 μm .

3.3.4. Charge dissipation

To achieve efficient layer-by-layer printing, the electric charge carried by the electrified jet and remaining on the printed material must be dissipated fast enough to allow the next layer to assemble on its top. If charge was not dissipated fast enough, the new arriving jet containing charge of equal polarity was repelled, thus falling on random or imprecise locations.

The charge relaxation time (τ) of a material can be computed from its dielectric permittivity (ϵ) and electrical conductivity (σ):

$$\tau = \frac{\epsilon}{\sigma}$$

Considering the electrical conductivities experimentally measured from the inks (Table 2) and the dielectric constant of water, the relaxation time of the ink was 3×10^{-7} s. On the other hand, considering the electrical conductivity of PEO on the order of 10^{-9} S/cm and a dielectric constant on the order of 10 we obtained a PEO relaxation time on the order of 10^{-3} s. When printing PEO patterns, charge dissipates to the high electrical conductivity silicon through wet PEO, which has a higher electrical conductivity than dry PEO, thus the effective relaxation times were lower than 10^{-3} s, in the range from 10^{-7} s to 10^{-3} s. Thus, for conventional inks based on PEO and using a conducting substrate electrically Earth-grounded, charge dissipation sets a limit to the maximum printing frequency at 10^3 - 10^6 layers per second, depending on the wetness of the printed fiber.

After ensuring a fast-enough charge dissipation, the charged nature of the jets was actually highly convenient not only to achieve high printing speeds and accelerations, but also to easily and precisely manufacture 3D objects by self-assembly of the new arriving jet on top of a previously printed structure. Upon reaching the substrate, the electric charge carried by the jet is gradually dissipated by conduction to the substrate, and is replaced by charge

of opposite polarity, as ohmic conduction through the printed fiber lowers its electric potential (towards 0 V, the potential of the earth-grounded substrate). This opposite-polarity charge accumulates at the top-most surface of the printed object, locally enhancing the electric field. Therefore, the newly arriving jet is electrostatically attracted to this charge, tending to self-assemble with high precision on top of the previously deposited layer. This attraction was fundamental to accurately accumulate layers, overcoming limitations associated to the movement-induced vibrations of mechanical stages²⁰. This is the same mechanism termed "electrostatic autofocusing" by Galliker et al.²⁷ underlying the direct-printing of high-aspect-ratio nanostructures using electrically-charged colloidal nanodroplets.

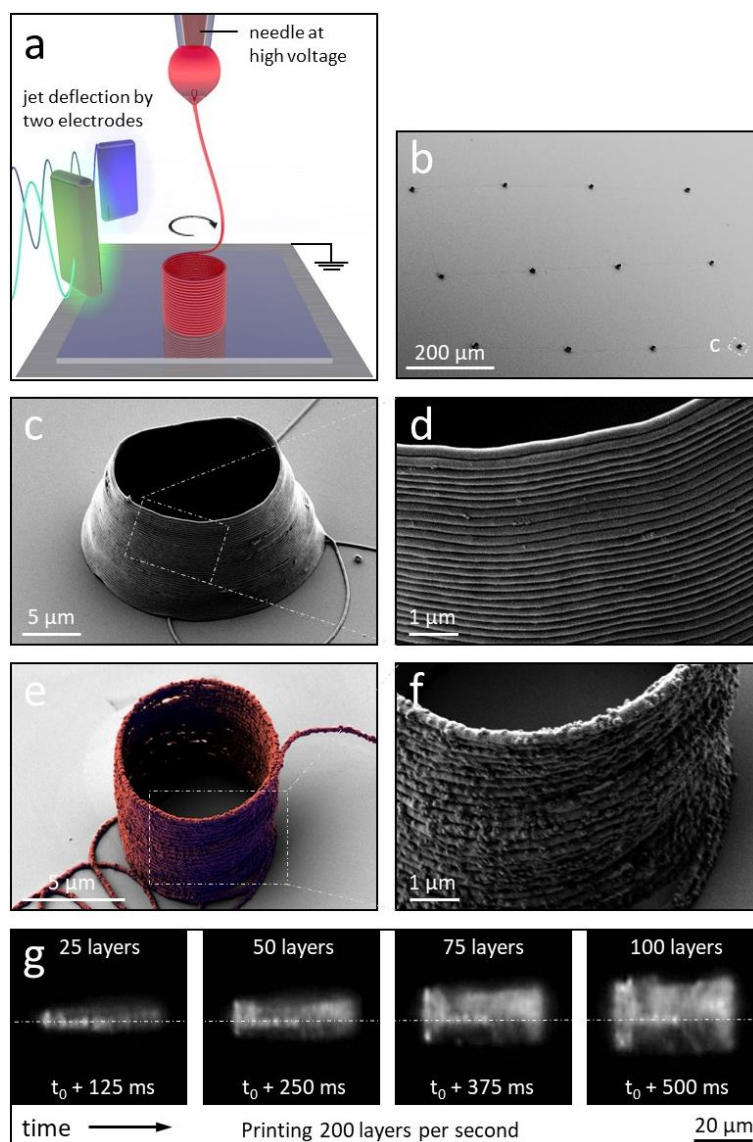


Figure 6. Printing 3D structures. **a** Schematic of the 3D printing of a cylinder. **b-d** SEM micrographs at different magnifications of PEO 3D cylindrical microstructures

manufactured by EHD jet deflection printing. **e-f** SEM micrographs of a PEO-Ag cylindrical structure printed using an ink containing 5 wt% 50 nm Ag nanoparticles. **g** High-speed video captures displaying the growth of a cylindrical structure at a frequency of 200 Hz. The jet of PEO ink had a diameter of ca. 200 nm and it is invisible on these captures (Supplementary Movie 2). SEM micrographs (b-d, f, g) were taken with a 40 degrees tilt. High-speed video captures (g) were taken at a shallow angle to the substrate. Image (e) was obtained by superimposing two images taken with secondary electrons and in-lens detectors, where printed fiber was false-colored in red and blue, respectively.

Considering that the height step of each layer was relatively small, $< 1 \mu\text{m}$, compared to the distance between the nozzle and the substrate, ca. 5 mm, the contribution of the reverse charging to the electric field was extremely local. Thus, while facilitating layer-by-layer assembly, the confined perturbation of the electric field still allowed the printing of complex structures that involved fiber crossovers and line-to-line separations as small as $\sim 1 \mu\text{m}$. Figures 6,8 displays some examples of 3D structures produced from PEO and a combination of PEO and Ag nanoparticles using jet deflection. Even suspended filaments and structures could be produced when the jet was sufficiently dry upon reaching the printing substrate (Figure 8). These examples illustrate that the jet deflection strategy can probably be also used for printing on non-planar substrates such as pillars, meshes and curved surfaces.

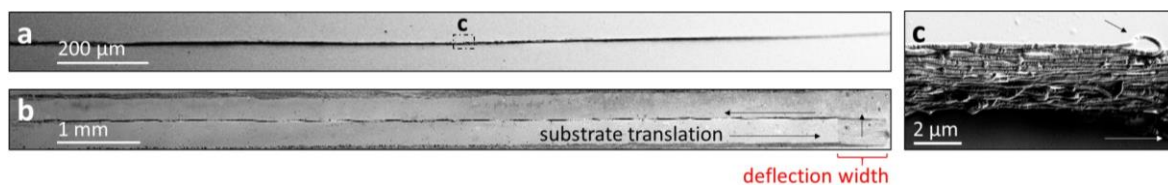


Figure 7. Large 3D wall. Confocal and SEM images of PEO walls produced by combining stage translation and jet deflection. **a** SEM image of a long PEO wall printed by jet deflection in the same direction as for substrate translation. **b** Confocal image of a 10 mm long PEO wall (the maximum translation of the XY stage). **c** SEM image showing a magnified view of a PEO wall printed by simultaneous jet deflection and substrate translation. The black arrow displays a fiber loop formed as the fiber was electrostatically deflected back and forth on top of the wall while the substrate was moving towards the right side of the image.

The jet deflection mode could be combined with the stage translation to produce larger objects. Figure 7 displays SEM images of 10 mm straight walls produced by oscillating the jet in the same direction as the substrate is moved. Large objects with *a priori* any predefined geometry can be potentially obtained by synchronizing the electrostatic jet

deflection with the movement of the substrate on each printed layer, which requires the development of a proper 3D slicing software. The focusing effect may limit the similitude of a newly printed layer with respect to the previous one, *i.e.* very small differences of the printing angle, curvature and location from layer to layer may be prevented by the focusing effect. We estimate this effect to be dominant at a micrometer range distance, thus printing consecutive layer with differences on this order may require a different or additional strategy.

3.3.5. Solvent evaporation

In the additive manufacturing of 3D objects using solvent-based inks, the solvent evaporation rate is a fundamental parameter determining viscoelastic properties of the jet during fly and upon arrival to the substrate. Solvent evaporation rates must be low enough for the nozzle not to clog, but high enough for the jet to arrive sufficiently dry to the printing substrate. Within the wide range of ink viscosities enabling EHD 3D printing, smaller minimum curvature radii on the printed substrate were achieved with jets conserving a low viscosity on their arrival to the substrate (Figure 10b), whereas the printing of fiber bridges required jets reaching the substrate with higher viscosities (Figure 8a). Additionally, once the material is printed, further solvent evaporation and associated volume loss may result in fiber shrinkage, which generally has a negative effect on the geometric fidelity of 3D structures. As an example, Figure 6c shows the truncated cone that resulted from the drying of a straight wall cylinder similar to those shown in the high-speed video captures of Figure 6g (Supplementary Movie 2). By modifying the ink composition and adjusting environmental conditions, shrinking could be controlled and even avoided (Figure 6e).

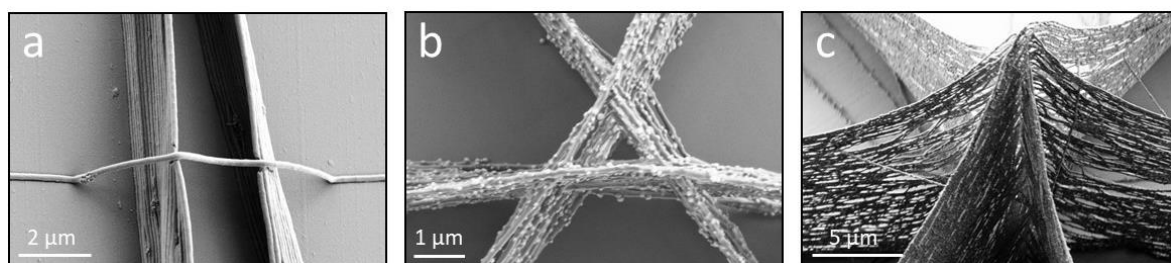


Figure 8. Printing complex 3D structures. **a** SEM micrograph of a single suspended PEO fiber bridging a gap between 2 parallel nanowalls. **b-c** SEM micrographs of the crossing of three walls printed using an ink containing 50 nm Ag nanoparticles, where **b**) is a top view of a crossing having a gap of 1 μm and **c**) is a tilt view of the peak formed by walls crossing

in one point. SEM micrographs (a) were taken with 30 degrees tilt, (b) with no tilt, and (c) with a 40 degrees tilt.

The solvent evaporation rate depends on multiple parameters, mainly the ink composition and particularly the equilibrium vapor pressure of the solvent used, the ambient conditions, the size and speed of the jet, and the diameter of the pendant drop. This last parameter, the diameter of the pendant drop, which depends on the needle size, the flow rate and the solvent evaporation among other parameters, has a strong influence on the printing process and particularly on jet deflection as discussed in Chapter 4.3.1. Besides adjusting the ink composition and tuning the printing parameters, to adjust the rate of solvent evaporation, the printer may be placed within a chamber with a controlled atmosphere or a gas stream containing solvent vapor can be introduced coaxially or near the jet. The control of the gas atmosphere may also be necessary to prevent that ambient moisture or oxygen gets absorbed by sensitive inks, which may cause phase separation or degradation of the ink⁴⁶.

The control of the drying process also allowed tuning the microstructure of the printed object. Smoother and less porous walls were obtained with jets that preserved a relatively low viscosity upon reaching the substrate, while jets arriving much dryer/solid resulted in rougher and highly porous walls (Figure 9). This control of the microstructure opens avenues for applications where surface area and porosity of the printed features are key parameters, such as in catalysis, sensors, nanogenerators, microbatteries, and tissue engineering, to cite a few.

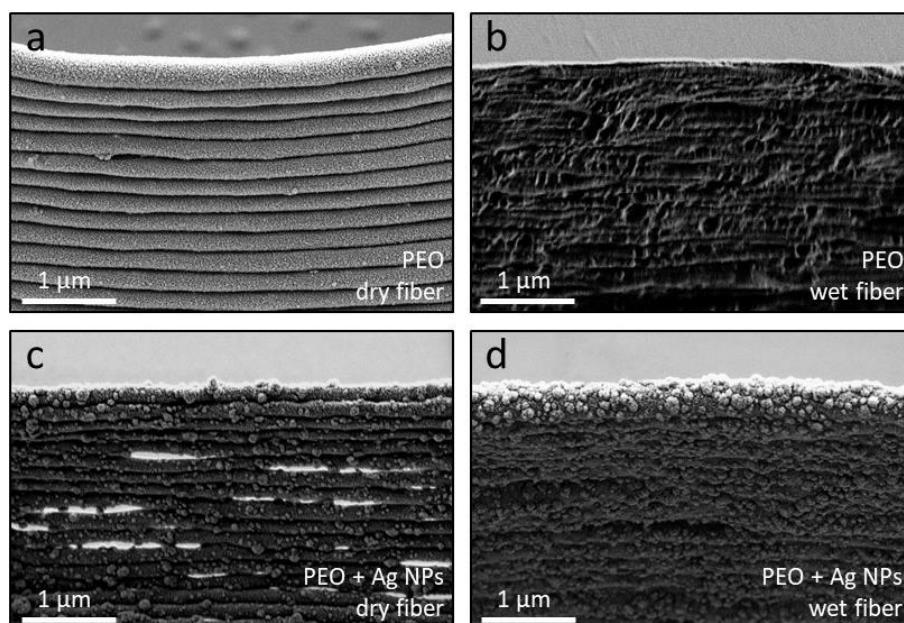


Figure 9. Control of the wall microstructure. SEM micrograph showing the effect of jet wetness/viscosity upon arrival to the substrate on the microstructure of a printed wall: **a** PEO wall obtained by stacking dry-arriving fiber layers, where the different PEO layers are clearly distinguishable. **b** Compact PEO wall obtained by stacking wet-arriving fiber. **c** PEO-Ag wall produced from dry-arriving fiber, where layers and pores between them are clearly visible. **d** Compact PEO-Ag wall produced from wet-arriving fiber.

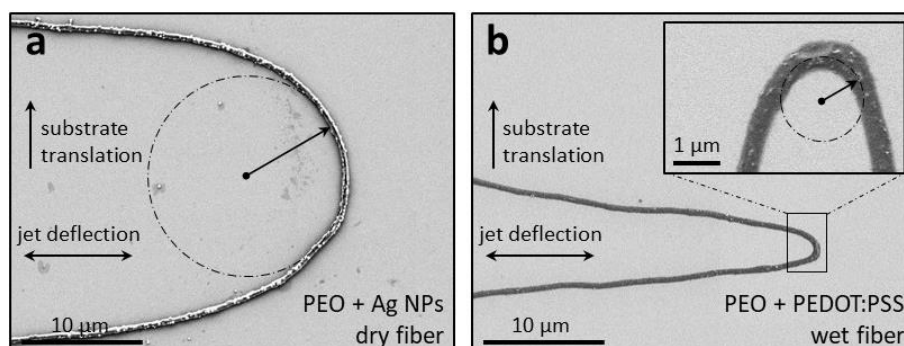


Figure 10. Influence of jet viscosity on minimum curvature radius. SEM micrographs of lines printed by electrostatically deflecting the jet sideways while the substrate was translated at 5 mm s⁻¹. **a** Big curvature radius (ca. 10 μm) resulted from a dry-arriving jet produced from an ink containing 10% Ag NPs in 4.5% PEO (300 kDa) in water:ethanol (1:3) and deflected at 200 Hz using a sawtooth function. **b** Small curvature radius (ca. 1 μm) resulted from a wet-arriving jet produced from a 8.1% PEDOT:PSS dispersion (3-4%) in 2% PEO (5000 kDa) in water:ethanol (1:1) and deflected at 100 Hz using a sawtooth function.

3.3.6. Material versatility

As mentioned before, material versatility is a key advantage of 3D printing based on the layer-by-layer deposition of material ejected from a nozzle over other technologies. While most of the printed structures displayed in the present work were produced from PEO (Figures 3-9, Table 1), structures printed from other polymers could be also produced by proper ink formulation. As an example, patterns displayed in Figures 4a-c were obtained using a combination of PEO and PEDOT-PSS. Additionally, nanoparticles of any material can be incorporated into the ink. As an example, Figures 6e-f and 8b-c display structures produced from an ink containing 5 wt% of Ag nanoparticles and 4.75% in mass of PEO. Besides, inorganic structures can be also produced from the printing of inks containing molecular precursors or metal salts and subsequently annealing them²³. Ultimately, the range of printable materials is only constrained by the requirement that the ink has proper electrical conductivity and viscoelastic properties to flow and prevent its capillary breakup. Therefore, except for minor adjustments in formulation, the electrostatic jet deflection strategy can be extended to produce 3D objects from any of the materials that have already been made into fibers by electrospinning, including biomaterials and even living cells⁴⁷.

3.3.7. Technology comparison

Figure 11 shows a plot of the printing speed ($\mu\text{m}^3 \text{s}^{-1}$) as a function of the feature size (voxel size, μm) for additive manufacturing techniques capable of printing metals with submicron resolution. This plot is an adaptation from Hirt et al.'s⁴⁸. The plot includes data for direct ink writing (DIW), drop-on-demand EHD printing, local electrophoretic deposition, laser-induced forward transfer (LIFT), meniscus-confined electroplating, electroplating of locally dispensed ions in liquid (FluidFM/SICM), laser-induced photoreduction and focused electron/ion beam induced deposition (FEBID/ FIBID)⁴⁸. As a general trend, when manufacturing objects with smaller features the printing speed drastically decreases; each order of magnitude increase in printing resolution results in 4 orders of magnitude slower printing. In this context, the electrostatic jet deflection strategy presented here falls well above the general trend, being capable of printing feature sizes down to 100 nm with unprecedented printing speeds up to $10^5 \mu\text{m}^3 \text{s}^{-1}$.

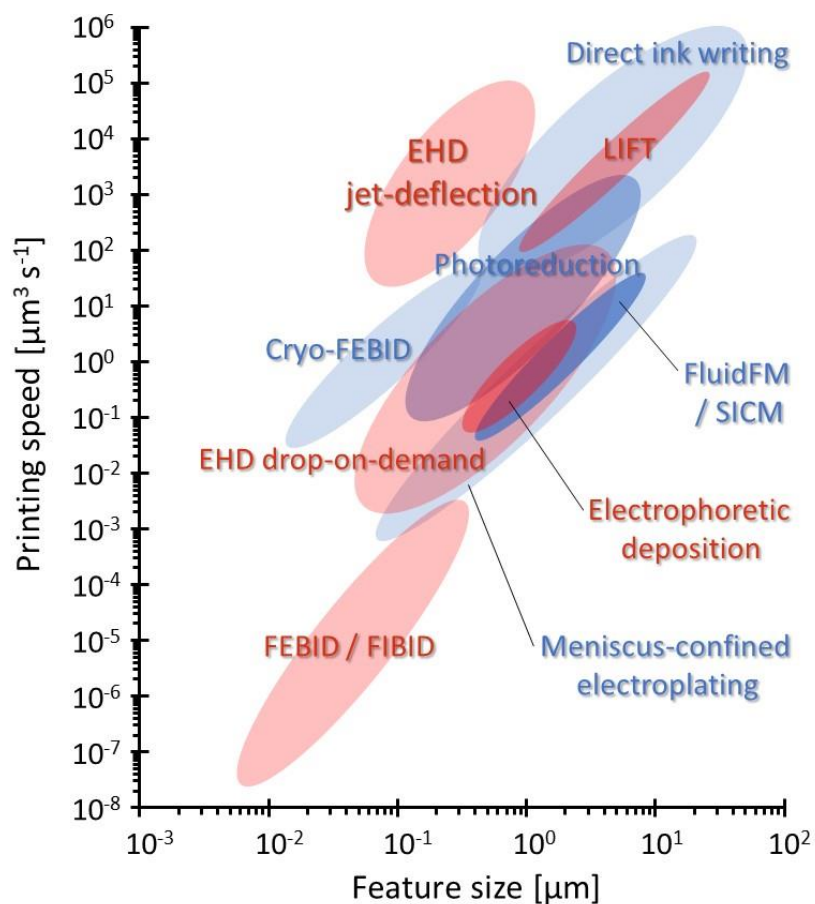


Figure 11. Comparison of additive manufacturing technologies. Map of printing capabilities in terms of printing speed and feature size for manufacturing technologies providing submicron resolution. Adapted from Hirt et al. and extended to include EHD printing based on jet deflection⁴⁸.

3.4. Conclusions

In conclusion, we presented a new and much faster strategy to control the printing process in nozzle-based 3D printing techniques, based on the tuning of the trajectory of an electrified jet by means of the controlled modification of the surrounding electrostatic field through additional electrodes. EHD jetting conveniently allowed producing submicrometer fibers from much thicker nozzles and with a wide range of ink viscosities. By coupling additional electrodes to this system, unprecedented dynamic characteristics were reached. We demonstrated printing speeds up to 0.5 m s^{-1} in-plane and 0.4 mm s^{-1} off-plane, surpassing all known additive manufacturing techniques capable of providing submicron resolution. Additionally, accelerations up to 10^6 m s^{-2} were calculated, four orders of magnitude above those provided by techniques relying on mechanical stages to define the object geometry. Such high accelerations allowed printing patterns with radius of curvature down to $1 \text{ }\mu\text{m}$. Through electrostatic deflection of electrified jets, 3D structures of increasing complexity, including cross overs and bridges, were printed by precise electrostatically-driven layer-by-layer self-assembly at frequencies as high as 2000 layers per second. Besides, controlling the ink viscosity and composition allowed adjusting the microstructure of the printed objects. To sum up, we believe that the unique advantages of EHD jet deflection printing will represent a significant step forward toward ultrafast additive micromanufacturing of 3D objects with virtually any composition and adjusted microstructure and functionality.

3.5. References

1. Gibson, I., Rosen, D. & Stucker, B. Additive Manufacturing Technologies. 3D Printing, Rapid Prototyping, and Direct Digital Manufacturing. (Springer, 2013). doi:10.1520/F2792-12A.2
2. Pei, E., Monzón, M. & Bernard, A. Additive manufacturing - Developments in training and education. Additive Manufacturing - Developments in Training and Education (Springer, 2018). doi:10.1007/978-3-319-76084-1
3. Srivatsan, T. S. & Sudarshan, T. S. Additive Manufacturing: Innovations, Advances, and Applications. Additive manufacturing: Innovations, Advances, and Applications 118, (CRC Press, 2015).
4. Madou, M. J. Fundamentals of Microfabrication and Nanotechnology: Manufacturing Techniques for Microfabrication and Nanotechnology. (CRC Press, 2011).
5. Mao, M. et al. The emerging frontiers and applications of high-resolution 3D printing. Micromachines 8, (2017).
6. Gladman, A. S., Matsumoto, E. A., Nuzzo, R. G., Mahadevan, L. & Lewis, J. A. Biomimetic 4D printing. Nat. Mater. 15, 413–418 (2016).
7. Dalton, P. D. Melt electrowriting with additive manufacturing principles. Curr. Opin. Biomed. Eng. 2, 49–57 (2017).
8. Duda, T. & Raghavan, L. V. 3D Metal Printing Technology. IFAC-PapersOnLine 49, 103–110 (2016).
9. Reiser, A. et al. Multi-metal electrohydrodynamic redox 3D printing at the submicron scale. Nat. Commun. 10, 1–8 (2019).
10. Chen, Z. et al. 3D printing of ceramics: A review. J. Eur. Ceram. Soc. 39, 661–687 (2019).
11. Xu, W., Wang, X., Sandler, N., Willför, S. & Xu, C. Three-Dimensional Printing of Wood-Derived Biopolymers: A Review Focused on Biomedical Applications. ACS Sustain. Chem. Eng. 6, 5663–5680 (2018).
12. Nguyen, N. A., Bowland, C. C. & Naskar, A. K. A general method to improve 3D-printability and inter-layer adhesion in lignin-based composites. Appl. Mater. Today 12, 138–152 (2018).
13. Kolesky, D. B. et al. 3D bioprinting of vascularized, heterogeneous cell-laden tissue constructs. Adv. Mater. 26, 3124–3130 (2014).
14. Han, Y., Wei, C. & Dong, J. Super-resolution electrohydrodynamic (EHD) 3D printing of micro-structures using phase-change inks. Manuf. Lett. 2, 96–99 (2014).
15. Han, Y. & Dong, J. Electrohydrodynamic (EHD) Printing of Molten Metal Ink for Flexible and Stretchable Conductor with Self-Healing Capability. Adv. Mater. Technol. 1700268, 1–8 (2017).

16. Brown, T. D., Dalton, P. D. & Hutmacher, D. W. Direct writing by way of melt electrospinning. *Adv. Mater.* 23, 5651–5657 (2011).
17. Ringeisen, B. R., Othon, C. M., Barron, J. A., Young, D. & Spargo, B. J. Jet-based methods to print living cells. *Biotechnol. J.* 1, 930–948 (2006).
18. Yarin, A. L., Koombhongse, S. & Reneker, D. H. Taylor cone and jetting from liquid droplets in electrospinning of nanofibers. *J. Appl. Phys.* 90, 4836–4846 (2001).
19. He, X. X. et al. Near-Field Electrospinning: Progress and Applications. *J. Phys. Chem. C* 121, 8663–8678 (2017).
20. Zhang, B., He, J., Li, X., Xu, F. & Li, D. Micro/nanoscale electrohydrodynamic printing: from 2D to 3D. *Nanoscale* 8, 15376–15388 (2016).
21. Yin, Z., Huang, Y., Duan, Y. & Zhang, H. Electrohydrodynamic Direct-Writing for Flexible Electronic Manufacturing. *Electrohydrodynamic Direct-Writing for Flexible Electronic Manufacturing* (Springer, 2017). doi:10.1007/978-981-10-4759-6
22. Li, D. & Xia, Y. Electrospinning of Nanofibers : Reinventing the Wheel? 16, 1151–1170 (2004).
23. Reneker, D. H. & Yarin, A. L. Electrospinning jets and polymer nanofibers. *Polymer (Guildf)*. 49, 2387–2425 (2008).
24. Onses, M. S., Sutanto, E., Ferreira, P. M. & Alleyne, A. G. Mechanisms, Capabilities, and Applications of High-Resolution Electrohydrodynamic Jet Printing. *Small* 11, 4237–4266 (2015).
25. Lewis, J. Direct Ink Writing of 3D Functional Materials. 16, 2193–2204 (2006).
26. Kiselev, P. & Rosell-Llompart, J. Highly Aligned Electrospun Nanofibers by Elimination of the Whipping Motion. *J. Appl. Polym. Sci.* 125, 2433–2441 (2012).
27. Galliker, P. et al. Direct printing of nanostructures by electrostatic autofocussing of ink nanodroplets. *Nat. Commun.* 3, 890–899 (2012).
28. Schneider, J. et al. Electrohydrodynamic NanoDrip Printing of High Aspect Ratio Metal Grid Transparent Electrodes. *Adv. Funct. Mater.* 26, 1–8 (2016).
29. Kim, H. Y., Lee, M., Park, K. J., Kim, S. & Mahadevan, L. Nanopottery: Coiling of electrospun polymer nanofibers. *Nano Lett.* 10, 2138–2140 (2010).
30. Lee, M. & Kim, H. Toward Nanoscale Three-Dimensional Printing: Nanowalls Built of Electrospun Nano fibers. *Langmuir* 30, 1210–1214 (2014).
31. Brown, T. D. et al. Melt electrospinning of poly(ϵ -caprolactone) scaffolds: Phenomenological observations associated with collection and direct writing. *Mater. Sci. Eng. C* 45, 698–708 (2014).
32. Bellan, L. M. & Craighead, H. G. Control of an electrospinning jet using electric focusing and jet-steering fields. *J. Vac. Sci. Technol. B* 24(6), 3179 (2006).
33. Martinez-Prieto, N. et al. Feasibility of Fiber-Deposition Control by Secondary Electric Fields in Near-Field Electrospinning. *J. Micro Nano-Manufacturing* 3, 041005 (2016).

34. Fang, F. et al. Controllable Direct-Writing of Serpentine Micro/Nano Structures via Low Voltage Electrospinning. *Polymers (Basel)*. 7, 1577–1586 (2015).
35. Zhu, Z. et al. Fabricated Wavy Micro/Nanofiber via Auxiliary Electrodes in Near-Field Electrospinning. *Mater. Manuf. Process.* 31, 707–712 (2016).
36. Kyselica, R., Enikov, E. T. & Anton, R. One- and two-dimensional electrodynamic steering of electrospun polymer nanofibers. *Appl. Phys. Lett.* 113, (2018).
37. Soldate, P. & Fan, J. Controlled deposition of electrospun nanofibers by electrohydrodynamic deflection. *J. Appl. Phys.* 125, 054901 (2019).
38. Karatay, O., Dogan, M., Uyar, T., Cokeliler, D. & Kocum, I. C. An alternative electrospinning approach with varying electric field for 2-D-aligned nanofibers. *IEEE Trans. Nanotechnol.* 13, 101–108 (2014).
39. Grasl, C., Arras, M. M. L., Stoiber, M., Bergmeister, H. & Schima, H. Electrodynamic control of the nanofiber alignment during electrospinning. *Appl. Phys. Lett.* 102, 7–11 (2013).
40. Rasel, S. M. An Advanced Electrospinning Method of Fabricating Nanofibrous Patterned Architectures with Controlled Deposition and Desired Alignment. (University of Ontario Institute of Technology, 2015).
41. Arras, M. M. L., Grasl, C., Bergmeister, H. & Schima, H. Electrospinning of aligned fibers with adjustable orientation using auxiliary electrodes. *Sci. Technol. Adv. Mater.* 13, 035008 (2012).
42. Bender, F., Wächter, L., Voigt, A. & Rapp, M. Deposition of high quality coatings on SAW sensors using electro spray. *Proc. IEEE Sensors 2*, 115–119 (2003).
43. Bisht, G. S. et al. Controlled continuous patterning of polymeric nanofibers on three-dimensional substrates using low-voltage near-field electrospinning. *Nano Lett.* 11, 1831–1837 (2011).
44. Basaran, O. A. Small-scale free surface flows with breakup: Drop formation and emerging applications. *AIChE J.* 48, 1842–1848 (2002).
45. Derby, B. Additive Manufacture of Ceramics Components by Inkjet Printing. *Engineering* 1, 113–123 (2015).
46. Huang, L., Bui, N. N., Manickam, S. S. & McCutcheon, J. R. Controlling electrospun nanofiber morphology and mechanical properties using humidity. *J. Polym. Sci. Part B Polym. Phys.* 49, 1734–1744 (2011).
47. Zussman, E. Encapsulation of cells within electrospun fibers. *Polym. Adv. Technol.* 22, 366–371 (2011).
48. Hirt, L., Reiser, A., Spolenak, R. & Zambelli, T. Additive Manufacturing of Metal Structures at the Micrometer Scale. *Adv. Mater.* 29, 1–30 (2017).
49. Bastús, N. G., Merkoçi, F., Piella, J. & Puntès, V. Synthesis of highly monodisperse citrate-stabilized silver nanoparticles of up to 200 nm: Kinetic control and catalytic properties. *Chem. Mater.* 26, 2836–2846 (2014).

Supporting videos

Video 1. High speed video study of jet deflection

High-speed video of the jet being deflected in 1D with a frequency of 10, 50, and 100 Hz. The two jet-deflecting electrodes (not shown) were positioned on the left and right sides of the image plane. The video shows the nozzle, the Taylor cone at the end of the ink drop and the thin jet expelled. The trajectory of this jet and thus its point of arrival to the substrate (not shown, positioned 2 mm below the bottom of the image) were modulated by the voltage applied to the jet-deflecting electrodes. The video was recorded with a high-speed camera (Photron FASTCAM-1024PCI) mounted on a microscope and operated at 1000 fps and 1/3000 s shutter speed, under dark-field setting. The video playback speed is 33 times slower than the real video speed.

Video 2. High speed video study of 3D structure printing

High-speed video displaying the printing of a cylindrical structure at a frequency of 200 Hz (200 layers per second). Cylindrical structures comprising 100 layers were printed in 0.5 second intervals while the substrate was not moved. Between consecutive printing events the substrate was rapidly moved by the mechanical stage (PI miCos linear stages PLS-85) at 20 mm s⁻¹. The walls of the resulting structures were vertical during printing, as seen on the video. However, subsequent examination of the same structures on SEM revealed the walls to be a bit tilted (due to drying and shrinking). The PEO-based jet had a diameter of ca. 200 nm and it is invisible on this video. The video was recorded with a high-speed camera (Photron FASTCAM-1024PCI) mounted on microscope at 1000 fps and 1/3000 s shutter speed, under dark-field illumination. Video playback speed is 20 times slower than for the real printing process.

Video 3. Video including results from jet deflection simulation

Compilation of results from finite element analysis of the change of the electric potential and field around the jet in the presence of two jet-deflecting electrodes when the voltage at these electrodes is continuously changed. The electric field "streamline" plotted in white and starting at the tip of Taylor cone represents the theoretical trajectory of a massless jet.

Supporting videos can be found at:

<https://www.nature.com/articles/s41467-020-14557-w>

Chapter 4

Parametric analysis and control of electrostatic jet deflection

Abstract

While the concept of electrostatic jet deflection of EHD jet was proposed multiple times during the last decade, previous research was limited in two major ways. (i) First, the effect of printing parameters on electrostatic jet deflection was only sparsely reported. We performed a rigorous parametric study via both finite element analysis and experimental data obtained with high-speed imaging. Here the effect of setup configuration, control variables and signal parameters on the jet deflection is reported. (ii) Previous methodologies used simplistic signals for electrostatic jet deflection, which had limited control over jet deflection. To address this shortcoming, we have developed a software to control jet-deflection printing. This custom-made software was indispensable for studying jet deflection phenomenon and was a critical stepping stone for obtaining printing results presented in this thesis. Based on the parametric study, we could match the speed of EHD jet by the deflection speed, while printing an arbitrary 2D pattern – the capability which allowed us to bring the old jet-deflection idea to the new level of implementation.

4.1. Introduction

As detailed in Chapter 2, current XY stages have severe limitations in terms of maximum acceleration, speed and positioning precision when assessing their performance from the standpoint of printing at microscale and high speeds. XY stage limitations root from the high mass (2 kg) it has to move in order to displace the substrate relative to the EHD jet.

The possibility of displacing charged EHD jet by auxiliary electrostatic field emerged as an alternative to the traditional use of XY translation stages for EHD printing (as described in Chapter 3). Eliminating the need to move heavy stage and directly deflecting the jet itself (for solvent-based EHD jet, estimated mass <30 micrograms and volume 3000 μm^3) theoretically should allow reaching unprecedentedly high accelerations. Precise control over the jet position and dynamics also entails to the ability to generate electrical signals with very high precision and temporal resolution.

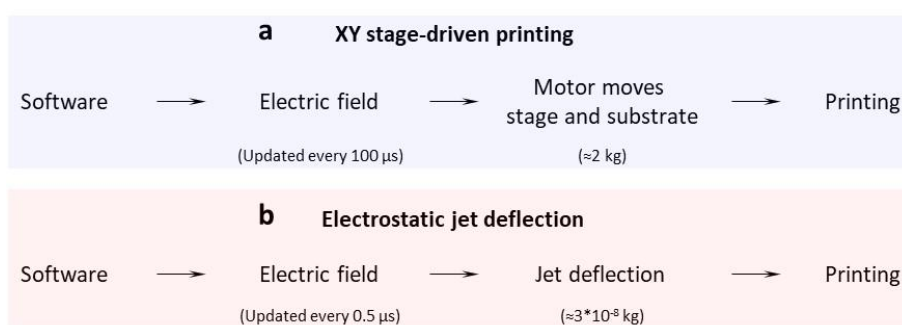


Figure 1. Stage-driven vs. electrostatic jet-deflection EHD jet printing. **a** conventional actuation mechanism for positioning printed material using mechanical stage. **b** electrostatic jet deflection approach, allowing to control jet positioning with higher precision and temporal resolution. Electrostatic force acts directly on the jet, instead of moving heavy mechanical stage, and thus sidesteps dynamic limitations of mechanical stages.

Our development is somewhat connected to crude concepts of electrostatic jet deflection proposed during the last decade, in the fields of electrospinning and EHD jet printing¹⁻¹⁵ (also referred to as: solvent-based near-field electrospinning and melt electrowriting). Despite previous research proved the feasibility of jet deflection, the control was based on primitive configurations: (i) patterning the substrate to direct the jet toward specific locations¹⁻⁵; (ii) manual switching of DC potentials⁶⁻⁷; and (iii) using elementary wavefunctions⁸⁻¹⁵. However, all such previous attempts lacked the capability to generate

complex wavefunctions with high temporal resolution, which is an essential requirement for 3D printing of complex patterns using EHD jets. Furthermore, little effort has been made up to date to study how various parameters affect jet deflection in these systems^{6-9,13,15}. Such knowledge is essential for controlling the printing process to produce accurate 2D patterns and 3D structures. One (previously unresolved) challenge toward accurate printing via jet deflection is the necessity to match the deflection speed to the EHD jet speed (see Chapters 3 and 5), which entails the precise control over electrostatic jet deflection and deep understanding of the effect of control parameters. In this context, this Chapter is fundamental for developing control methodology for accurate printing using fast EHD jets.

Systematic parametric study of electrostatic jet deflection is presented in this chapter. First, relevant parameters, such as electrodes configuration and jet-deflection signal characteristics (amplitude, frequency and bias) are described. Then, finite element analysis is presented, simulating the effect of pendant drop size, electrodes configuration, nozzle voltage and various jet-deflection signal characteristics on the jet deflection. Those simulations are done for stationary conditions, and while important qualitative observations were made, additional experimental study was necessary to provide quantitative data on electrostatic jet deflection under dynamic conditions. We aim to study experimentally the effects from electrodes configuration, as well as signals amplitude, frequency and bias, on the jet deflection angle. This study was performed using high-speed imaging of deflecting jet with subsequent analysis of recorded data, and provides mathematical relationships allowing to predict jet deflection angle from preset parameters. Furthermore, the applicability of obtained graphs is discussed for selecting appropriate printing parameters, while matching jet deflection speed to the EHD jet speed. This chapter does not include printing results as they are shown in Chapters 3 and 5, nevertheless references are made where appropriate.

This chapter also generally describes the custom-made LabView software, specifically designed for controlling EHD jet-deflection printing in all work presented in this thesis. Elements of the user interface and main software functions and parameters are reviewed. The design of the jet-deflection printer used in this parametric study is based on 1-electrode-per-axis configuration. While such configuration has a drawback of printing a

deformed pattern, our LabView software is designed to preventively compensate for such asymmetric electric field when generating the jet-deflection signals, allowing us to obtain an as-desired printed pattern. This software is an essential part of the printer, enabling to print 3D objects with submicrometer features via ultrafast jet deflection.

4.2. Methods

4.2.1. Finite element analysis

The simulations were performed using COMSOL Multiphysics® 5.2a software package with an aim of qualitatively summarizing the effect of printing variables and not to find optimal printing parameters (which was performed empirically). The arrangement used for the simulation is shown on Figure 4. Nozzle-to-substrate separation was ≈ 3.5 mm, resulting in 3 mm separation between the jet-ejection point and the substrate. OD of the conductive nozzle was 0.5 mm. Jet-deflecting electrodes measured 0.5 mm in thickness, 3.5 mm in height, and 2 mm in depth (not visible). Sufficiently large cylinder (with 5 mm radius) and printing substrate were used as boundary conditions at the edges of simulation volume, with potentials of 0 V. Nozzle was set to 1000 V, while the potentials of electrodes were varied to study the length of the jet deflection. Note that the images of the simulation shown on Figure 4a,c are mere cross-sections of the simulated volume.

The trajectory of a massless jet is simulated by white electric field streamline. This streamline was empirically found by precisely matching its beginning to the jet-ejection point, and observing where this streamline arrives to the substrate, thus simulating the deflection length. This streamline shows the trajectory which a point charge would follow if introduced at the tip of the Taylor cone.

It is important to note that the real jet trajectory may be different due to many other parameters which are not accounted for in shown simulation. For example, real jet has a mass, and thus inertial forces, so that the jet deflection is expected to depend on the deflection frequency, which is also not presented by this static simulation. Furthermore, real jet is continuously generated and propelled to the substrate, while solvent evaporation from the jet causes the change in its viscoelastic properties. Mechanical interaction between the jet and the substrate further complicates the matter, depending both on the ratio between the jet and deflection speeds, as well as on jet wetness upon deposition.

4.2.2. Experimental study of jet deflection angle

The effect of electrode configurations and deflection signal parameters were studied experimentally to reveal their action on the deflection angle. All experiments were conducted with a still substrate. Three electrode configurations were used in this study (Figure 2): Two are for 1D deflection using single electrode (or two opposing electrodes),

and a third configuration (#3) for 2D jet deflection. Figure 3 showcases those electrode configurations and the setup used.

Parametric analysis was performed for all configurations, where the effect of signal amplitude and frequency on the deflection angle was studied by performing minimum 5 repetitions for each set of parameters. In a typical experiment, Taylor cone was established emitting continuous liquid jet, while the XY stage was kept still. Then, the set of bias, amplitude and frequency was applied. For each experiment one parameter was varied, while all others were fixed. Parameter to be studied was varied between extreme values with a fixed step. For example, frequency was varied from 100 Hz to 1000 Hz with 100 Hz step, giving 10 data points during the same experiment.

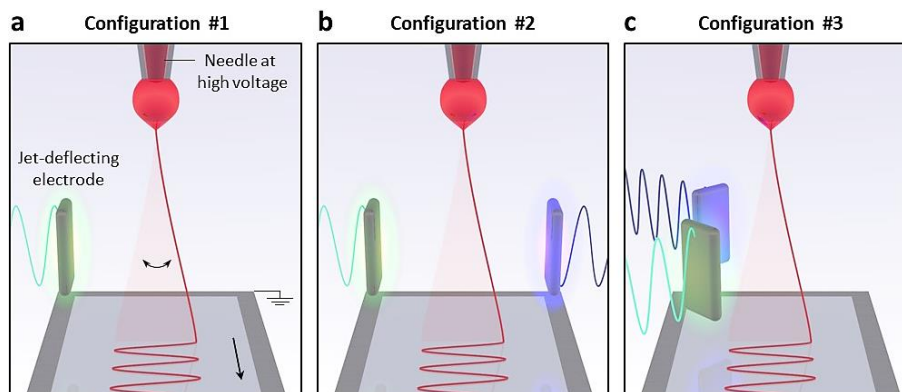


Figure 2. Schematics of electrode configurations used to experimentally study jet deflection: a Single electrode configuration; **b** two opposite electrodes deflecting the jet in one plane, while opposite signals are applied to electrodes, thus one electrode attracting and another repelling the jet in any instant; and **c** extension of the first configuration, where two electrodes are positioned perpendicularly to each other and can deflect the jet in 2D.

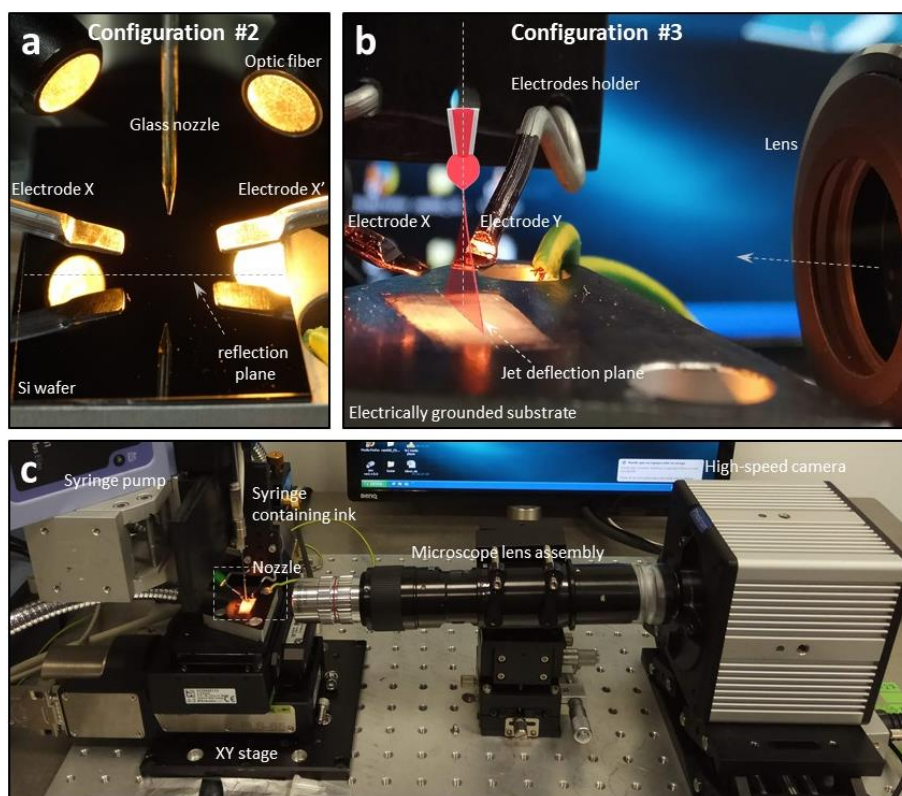


Figure 3. Experimental setup for parametric analysis of jet deflection. a-b show electrode configurations, corresponding to Fig. 2b-c, while c shows the setup for high-speed video imaging, highlighting the optical microscope system (Navitar 1-50486) and high-speed camera (Photron FASTCAM-1024PCI). Configuration #1 is not shown, but was obtained by removing one electrode from configuration #2 (a). For all arrangements, optical axis was perpendicular to the jet deflection plane, while nozzle-to-substrate separation was 5 mm, and electrodes were positioned at 3.5 mm away from both the substrate and the default jet trajectory. Dark-field light setting was used for video recording, with high-intensity light source (AmScope HL-250-A) positioned as on panel (a) to render thin EHD jet visible. Recorded videos were analyzed to reveal the dependence of jet deflection angle on various parameters, as summarized on Figure 7.

4.2.3. High-speed imaging and analysis

Jet-deflection behavior was recorded using high-speed camera (Photron FASTCAM-1024PCI) for each data point. Total of 10 data points were typically filmed in only 15-20 seconds. Short time between filming each data point (set of parameters) helped to minimize undesirable effects by other factors, such as changes in drying and ink composition, thus minimizing experimental error if jetting was not in steady state. Then, recorded videos were analyzed, and deflection angles manually measured. At least 5 measurements were conducted for a single set of variables, and then were averaged and corrected to the nearest neighbor to represent the clean signal on the graphs. Jet was linear (almost straight jet trajectory) at smaller deflection angles ($<15^\circ$), and non-linearity was present at higher angles. Such non-linearity was reducing the accuracy of measuring deflection angle. While measuring small angles could be done with precision of up to $\pm 1^\circ$,

high angles led to higher errors. On the other side, high deflection angles causing such nonlinearity were not typically required for printing.

The optical microscope consisted of a 12X lens with adjustable zoom and focus (Navitar 1-50486), a 2x lens adaptor (Navitar 1-62136) and a 5X microscope lens (Mitutoyo 1-60226). A high-intensity light source (AmScope HL-250-A) was positioned behind the observed object under ca. 5° angle from the camera optical axis, thus that direct light did not reach the camera sensor (dark-field setting). High-speed imaging was performed with a high-speed camera (Photron FASTCAM-1024PCI) mounted on the microscope and recording at rate at 1000 fps (and 90000 fps for determining the jet acceleration speed).

4.2.4. Acceleration of the deflecting jet

The lateral speed and acceleration reached by the jet under electrostatic deflection were estimated from high-speed video captures of the jet while it was oscillated at 10000 Hz with a triangular wave signal. Two jet-deflecting electrodes were positioned on the same deflection axis and 3 mm away from the default jet trajectory (nozzle axis), as shown on Fig. 5a. Nozzle-to-substrate separation was 5 mm. The same voltage amplitudes (max. ± 1000 V) of opposite signs were applied to the electrodes. The electrified jet was produced from an ink containing 5% PEO (300 kDa) in water:ethanol (1:3) and it was sustained by applying 1500 V between the nozzle and the substrate. A high-speed camera (Photron FASTCAM-1024PCI, Fig. 5c) was used to capture jet deflection at its maximum rate, 90000 frames per second, and maximum available frame resolution at such high rate (256 pixels wide and 16 pixels high). This captured video strip was obtained 400 μm below the jet-ejection point to observe the jet oscillation. Video captures showed the jet oscillating side to side at 10000 Hz. Through the calibration of microscope and camera, the side-to-side length of this oscillation was determined to be 40 μm .

4.2.5. Signal generation and amplification

A LabVIEW software was specifically developed to define and generate the voltage at the different jet-deflecting electrodes from parameters such as the pattern geometry, the number of printed layers, the layer printing frequency and the signal amplitude. A data acquisition card (National Instruments, USB-6259) was used to generate the synchronized analog signals (max. ± 10 V), which were amplified (max. ± 2000 V, Matsusada AMJ-2B10 and Trek 677B) and applied to the jet-deflecting electrodes. The amplitude of the signals applied to the electrodes defined the size of the printed pattern and typically ranged about 200-400 V for 3 mm nozzle-to-electrodes separation (configuration used for parametric study). We used frequencies as high as 5000 Hz to study the jet deflection angle, and 10000 Hz for determining the acceleration of electrostatic jet deflection.

4.3. Parametric studies of jet deflection

We deliberately separate the printing setup and method into two subsystems. The first one is essentially a conventional EHD jet printing (often referred to as near-field electrospinning) (see Chapter 1.5.5). This system does not contain deflecting electrodes. The second subsystem is the setup and method for electrostatic jet deflection, which can be conveniently decoupled from the basic printer design and described independently. Our parametric analysis studies the influence of the auxiliary electrostatic field, as well as other setup and printing parameters, on the jet deflection. By auxiliary electrostatic field we mean an additional electric field created by one of two electrodes, and used to deflect the jet from its default vertical trajectory.

4.3.1. Finite element study

Finite element analysis was used to reveal main printing parameters affecting electrostatic jet deflection. Deflection length is the distance between right-most and left-most jet positions (at specified deflection signal) and defines the size of the pattern to be printed. For a symmetrical electrode configuration (Figure 4a), arbitrary bias of 50 V was set, while an amplitude of ± 88 V was chosen to deflect the jet for 1 mm. Note that the amplitude is defined as the difference between the maximum or minimum potential relative to the bias potential. Step-wise change in amplitude was studied via multiple simulations and resulted in varying jet deflections, revealing a linear dependence plotted on Figure 4b.

Another simulation (Figure 4c) featuring a single deflection electrode and, thus, asymmetric electric field, is performed for the sake of comparison. First, bias voltage of 70 V was found, keeping the jet in its vertical position. Then, the amplitude of ± 126 V was empirically found to attract the jet for 1 mm toward the electrode. As would be expected, single electrode results in asymmetric attraction and repulsion due to the changing distance between the jet and the electrode. For the same amplitude, jet is attracted for 1 mm, while repelled only for 0.35 mm. Such asymmetric deflection would result in printing deformed pattern, where relative pattern size is nonlinearly dependent on the signal amplitude (Figure 4d). Furthermore, while not shown here, such deformation would have another important consequence: jet deposition point onto substrate would move faster

when the jet is attracted, and slower when repelled. Such a variance in the speed of the contact point makes it impossible to match the deflection speed to the speed of the jet and would manifest itself in portions of pattern having buckled fiber, and other portions of pattern which could not be printed because of the shortage in jet length.

Overcoming such pattern deformation is a critical step toward printing when single electrode is used for each deflection axis. The mechanism for correcting such deformation involves nonlinear scaling of the deflection signal, such as to compensate for the excessive jet attraction toward the electrode and disproportionately small repulsion. Such algorithm was developed and integrated into the printing software and is described by the end of this Chapter.

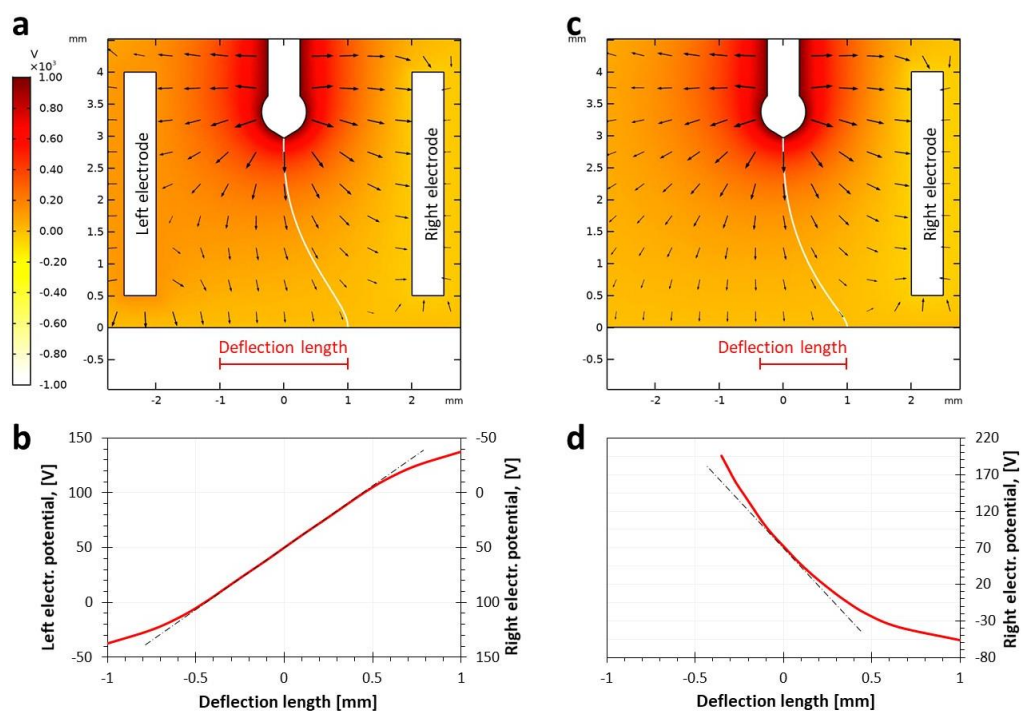


Figure 4. Simulation of the deflection length for symmetric (a-b) and asymmetric (c-d) electrode configurations. **a** jet deflection simulation at the right-most jet position, resulting in 1 mm jet displacement relative to the default (vertical) jet trajectory and total deflection length of 2 mm. **b** jet arrival position obtained with 15 simulations, similar to (a), revealing its linear dependence on electrodes potential. While linear dependence breaks when jet is strongly attracted toward one electrode, at medium deflection lengths attractive and repelling forces are balanced due to symmetrical positioning of two electrodes. Applied to printing, linear dependence means that preset signal should result in printing same pattern. **c-d** show similar simulation results for the case of asymmetric configuration featuring single electrode. Note that bias voltage of 70 V is necessary to maintain the jet in vertical position, rendering the electrode effectively “invisible” to the jet. Amplitude of ± 126 V was chosen to mimic same deflection length of 1 mm when the jet is attracted toward the electrode. Note that the jet is repelled only for 0.35 mm, showing nonlinear deflection dependence

due to the asymmetric electric field. Such nonlinear dependence should result in a deformation of the printed pattern relative to the preset pattern. Mechanism employed to compensate for such deformation is discussed in Chapter 4.4.2.

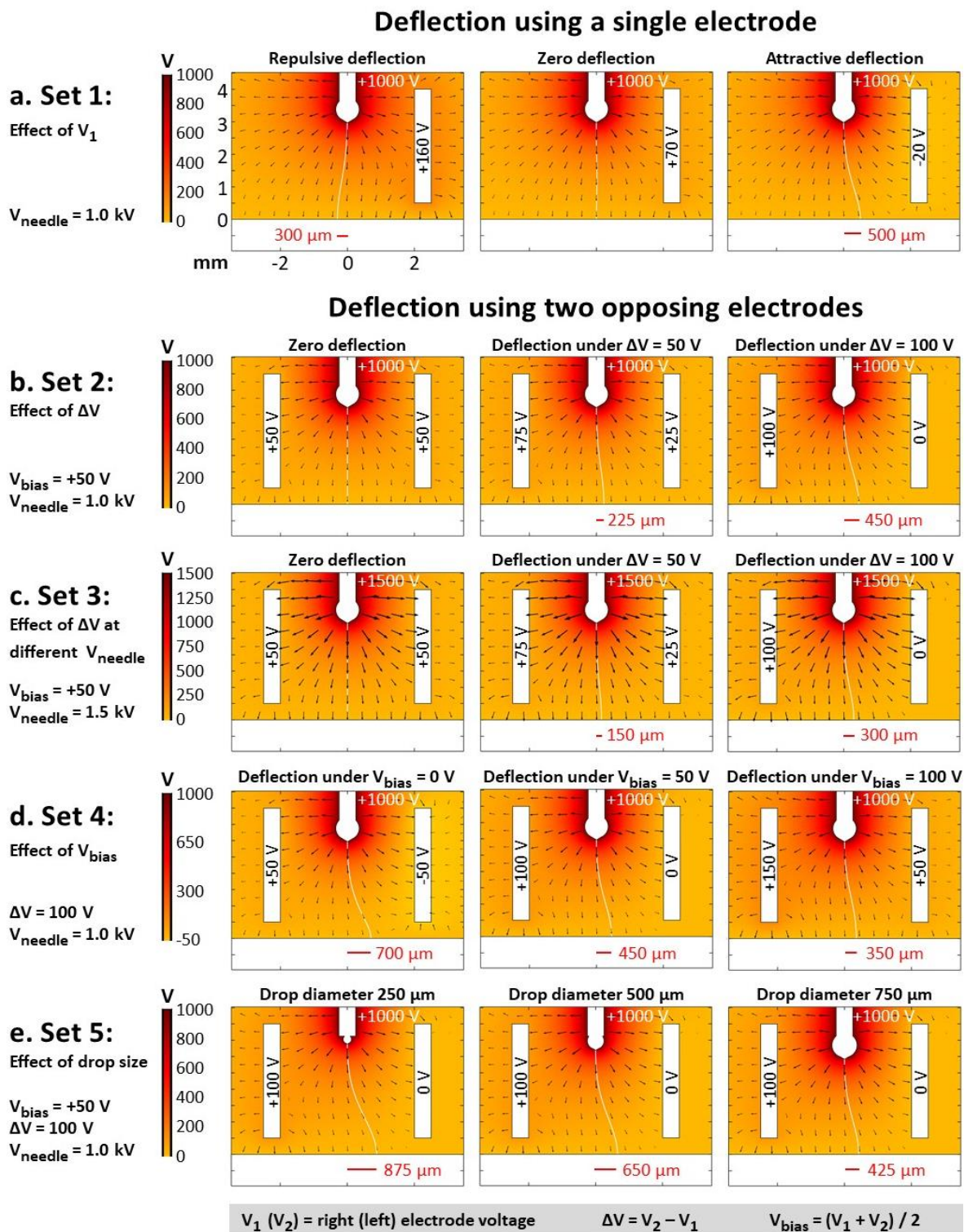


Figure 5. Jet deflection simulations at different parameters. Simulation of the electric potential and field around the jet in the presence of one (a) and two jet-deflecting electrodes (b-e). The nozzle (at the center), the ink drop (hanging at the tip of the nozzle),

and the deflecting electrode are shown in white for clarity but are at the specified potentials. The electric field "streamline" (also in white) starting at the tip of Taylor cone (ink drop conical end) represents the theoretical trajectory of a massless jet. The positions of deflected jet arrival point to the substrate is highlighted with red bar and corresponding length from vertical jet (nozzle axis).

Role of jet-deflection signal

We next wanted to establish the relationship between the electric field around the Taylor cone and the jet deflection distance from its default vertical trajectory. To do this, we used one or two electrodes, varied the voltages applied to those electrodes, and then studied the effect of the nozzle voltage. Figure 5 displays this series of simulations. Within each set a different parameter was studied:

Set 1 (Figure 5a) shows jet deflection using single electrode. Voltage bias (+70 V in this case) is required to keep the jet in vertical position. Jet is attracted and repelled from the electrode by applying signal amplitude of ± 90 V relative to the bias voltage. The jet deflection distance is greater when the jet is attracted than when it is repelled, 500 μm compared to 300 μm . To correct for this effect and avoid distortion in the printing of predefined objects, our software is designed to dynamically decrease the amplitude when the jet is attracted, and increase when it is repelled (see section 4.4.2.).

Set 2 (Figure 5b) shows configuration with 2 electrodes. As deflection signal amplitude is increased to $\Delta V=50$ V and $\Delta V=100$ V, jet deflection distance is linearly increased. This simulation result is supported by experimental results, also showing linear increase of the printed fiber track as the signal amplitude is increased (see Fig. 3a-b from Chapter 3 and Figure 5 from Chapter 5).

Set 3 (Figure 5c) shows the effect of needle voltage by comparing to **Set 2**. As would be expected, the deflection distance is reduced proportionally to the increase in needle

$$\text{voltage: } \frac{1500 \text{ V}}{1000 \text{ V}} = \frac{450 \mu\text{m}}{300 \mu\text{m}} = 1.5$$

For example, this observation means that if EHD jet becomes unstable and higher nozzle voltage is applied to stabilize it, then the deflection distance is expected to decrease at same deflection signal.

Set 4 (Figure 5d) shows how in 2-electrode configuration voltage bias influences the jet deflection. While the amplitude of the deflection voltage is the same ($\Delta V=100$ V) for all pictures in the set, the jet is deflected less as the bias increases. Stated differently, increasing the bias has a “focusing effect”, which decreases jet deflection angle. This result is supported by experimentally observing the jet deflection angle, and the bias effect is schematically depicted in Figure 9.

Role of drop size

Set 5 (Figure 5e) shows that large drops substantially decrease the jet deflection distance. This result is explained considering two dependences: i) For small droplets, the vertical electric field strength decays faster as the jet moves away from the drop. As the vertical component of the electric field becomes weaker, the jet-deflecting field (horizontal field component) becomes relatively stronger, thus resulting in larger horizontal deflection of the jet. ii) While the nozzle elevation is kept constant, the jet ejection point is lower for larger drops. Thus, even at equal deflection angle, the jet contact point at the substrate will be moved a shorter horizontal distance.

Beyond finite element analysis of drop size effect on the jet deflection, here we also highlight other important observations on how the drop size affects EHD jet printing, both in direct and indirect ways. We experimentally found that smaller drops required smaller voltage applied to the needle to initiate the jet. This experimental observation can be rationalized considering that, at equal applied voltage, a higher electric field and a higher field gradient are generated on the surface and at the surrounding of smaller drops. Results of finite element analysis of the electric field with different drop sizes support this view (Figure 5e).

On the other hand, smaller drops lead to slower solvent evaporation rates, which resulted in a lower polymer concentration at the site of jet ejection than for larger drops. The main consequence of this is that smaller drops lead to a more easily deformable (less viscous) ink at the jet, thus a faster EHD jet (for the same electric field strength, despite a lower voltage is used). Due to the difference in the solvent evaporation rate and jet speed, drop size thus also influences the viscoelastic properties of the jet on its arrival to the substrate. Larger drops result in a more viscous jet arriving to the substrate and thus produce a more

porous final 3D solid structure since different layers do not fuse together. The results obtained from the deposition of jets with variable dryness is displayed in Fig. 9-10 from Chapter 3. Additionally, solute enrichment at the interface of the drop can cause changes in the surface tension. A reduction in surface tension will result in a reduction in the required voltage needed to sustain the jet. In this case, the same deflection will be obtained with a lower deflection signal amplitude (ΔV).

4.3.2. Experimental study

The goal of this section is to empirically study the dependence of jet deflection angle on deflection signal parameters, as well as on electrode configurations. This study was conducted through high-speed imaging of the Taylor cone and the deflected jet, with subsequent analysis aimed to reveal mathematical relation between control parameters and jet deflection.

Figure 6 shows a rare case of jet deflection, recorded during this study. Sometimes small shiny particles were observed in the jet, probably due to small impurities or polymer aggregates trapped into a jet. Conveniently, such particles could be used to shed light on the peculiar dynamics of the deflected jet. For example, instantaneous speed/acceleration of the jet deflection and the speed of the jet (vertical component of the velocity vector) could be computed. Video snapshots on Figure 6a show deflection between jet utmost positions at 20 Hz. Figure 6b plots the position of one shiny particle as it moves from the Taylor cone toward the substrate (not shown). Particle position was measured from 30 frames during which the jet oscillated more than 3 periods, forming a zigzag trajectory. Instantaneous jet trajectories are depicted as grey lines, highlighting that jet trajectory at any moment is nearly straight, so that the whole jet is proportionally deflected by electric field perturbation. Interestingly, the EHD jet does not develop waves like those observed when a rope is shaken from one side. The difference could be due to the simultaneous action of electric field on each part of the jet, while in case of rope mechanical perturbation is supplied only to one end and subsequently propagates through rope' length as a wave.

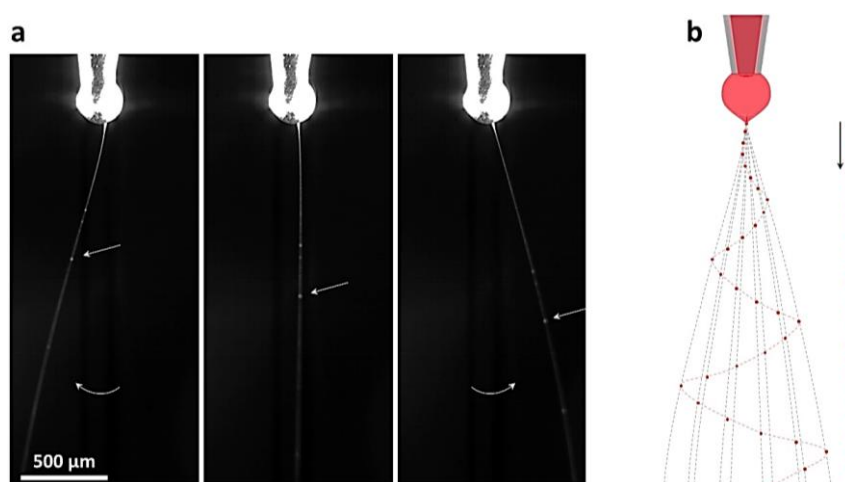


Figure 6. Mechanics of jet deflection and particle tracking. **a** Frames from high-speed video showing the jet being deflected in configuration #2 with sawtooth wave of 20 Hz, ± 400 V amplitude and 500 V bias, while nozzle was kept at 1060 V. Standard PEO-based solution was used as ink (5wt% PEO Mw=300,000 kDa in ethanol:water=3:1), supplied with flow rate of 0.1 $\mu\text{l}/\text{min}$. Curiously, sometimes parts of the jet were brighter (as shown on selected images with arrow), probably due to a small polymer aggregate or impurity trapped into the jet. This allowed to perform particle tracking to reveal real trajectory of the jet. **b** plots particle positions (red points) measured from video frames taken with equal time intervals, tracking one particle from the jet ejection point till its arrival to the bottom of the field of view.

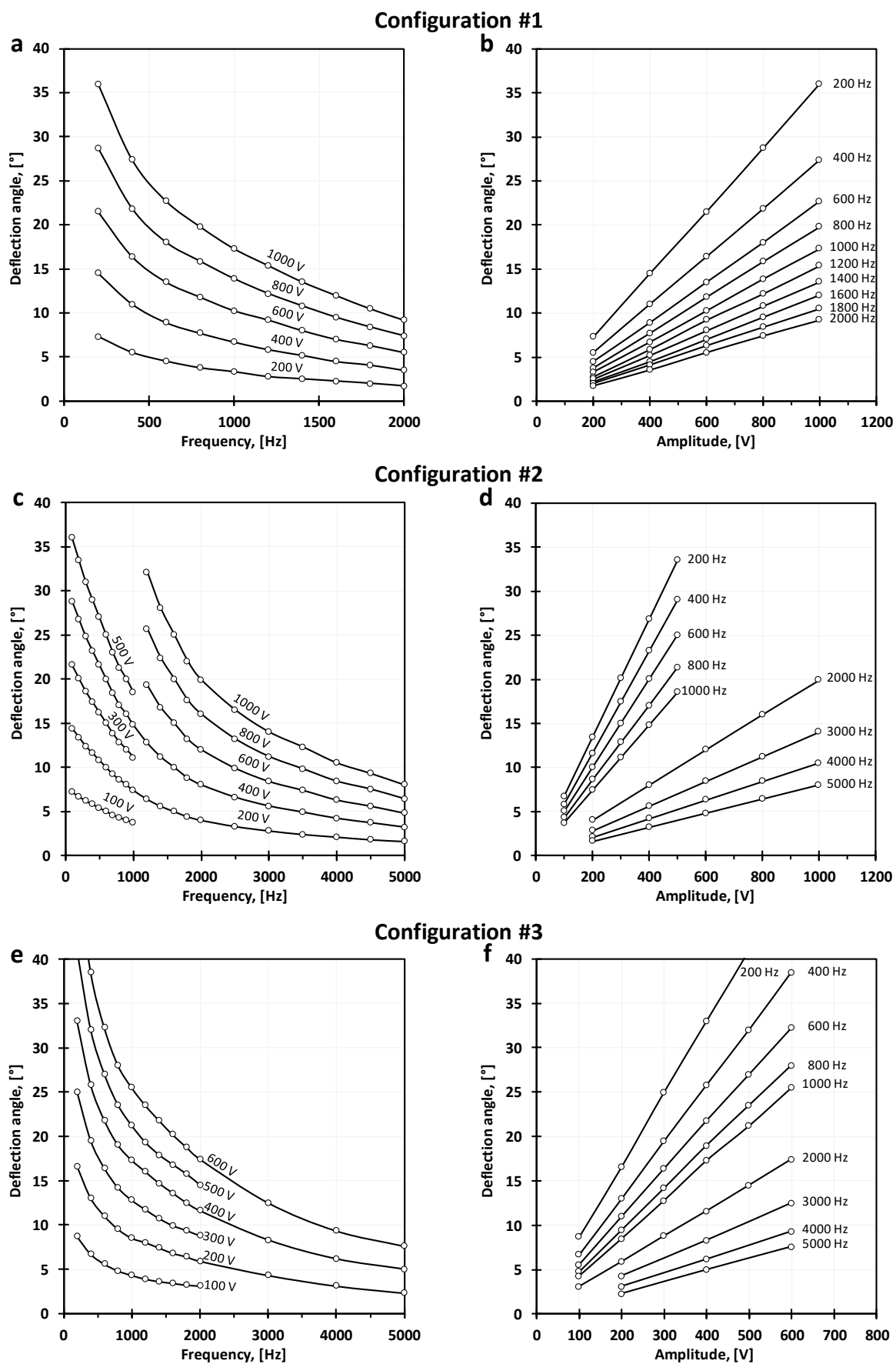


Figure 7. Deflection angle as a function of signal amplitude and frequency, experimentally measured for 3 electrode configurations, as per Figures 2-3. Each set of data (a-b, c-d, e-f)

exists in 3D parametric space and is presented both versus Frequency and Amplitude, revealing non-linear and linear dependence on those parameters. Deflection angle is linearly dependent on signal amplitude and degenerates at zero amplitude. Graphs **d** and **f** were simplified by not plotting all frequency lines, shown on **c** and **e**. For each set of parameters jet deflection was recorded on high-speed video, from which deflection angle was measured, giving at least 5 data points, which were averaged and corrected to the nearest neighbor. 10 parametric sets were recorded during each experiment to decrease experimental error. Nozzle and bias voltages were: 1500 V and 100 V for conf. #1, 2000 V and 500 V for conf. #2, and 1500 V and 300 V for conf. #3. Ink composition was 5wt% PEO Mw=300,000 kDa in ethanol:water=3:1 solvent system.

Figure 7 shows how jet deflection angle is dependent on signal frequency and amplitude. For each configuration experimental data is plotted both versus frequency and amplitude. Such graphs are used for determining signal parameters for printing a preset pattern with desired size, and this methodology is detailed later in this Chapter. As seen from these graphs, higher frequency results in non-linear decrease of deflection angle. On the other hand, deflection angle is linearly increased by increasing amplitude. For zero amplitude no deflection is observed, which is expected. Both observations are confirmed by EHD jet printing, shown in Chapters 3 and 5. Graphs also show that the strength of auxiliary electric field and resulting jet deflection strongly depends on electrode configuration.

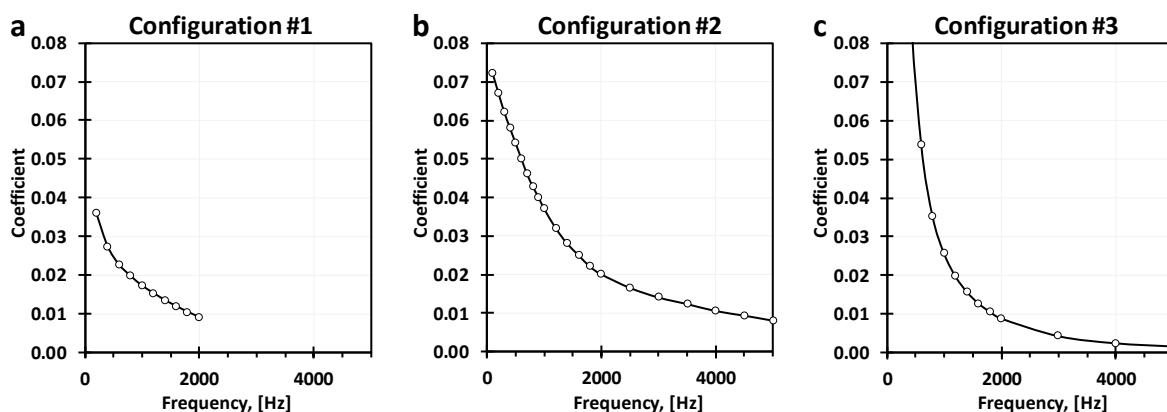


Figure 8. Coefficients linking deflection angle to signal amplitude, obtained from the linear graphs shown on Figure 7, where $\text{Coefficient} = \frac{\text{Deflection angle } [^\circ]}{\text{Amplitude [V]}}$. Trendlines show the continuity of trend, allowing to interpolate jet-deflection behavior for other frequencies.

Linear trends from Figures 7b,d,f also allow extracting the coefficient which links the deflection angle to the signal amplitude, as shown on Figure 8. Those coefficients provide further comparison between electrode configurations (Figure 2) and can be used to interpolate and determine jet deflection angles for intermediate frequencies, which were not measured. Such functionality could be integrated into a printing software, so that signal parameters could be automatically computed from other printing parameters (pattern geometry and size, jet speed, etc.).

Role of Voltage Bias

The effect of voltage bias on jet deflection is summarized in Figure 9. A single electrode positioned near the EHD jet affects the electrostatic field around the jet, thus perturbing its trajectory. In order to bring the jet to its normal vertical position, a voltage bias can be applied to the electrodes equal to the voltage that would be present at its location if the electrodes were not present. In other words, voltage bias makes the jet-deflection electrode electrostatically invisible to the EHD jet, and such bias is easily found experimentally by observing the jet trajectory. One consequence of a non-vertical jet is that when it is deflected, deflection length (and thus its deflection speed at substrate) will be higher when it is attracted toward the electrode, and smaller when repelled. To avoid this, it is favorable to apply voltage bias before printing via jet deflection approach.

Contrary to the case of single electrode, locating two opposing electrodes symmetrically relative to the jet does not perturb its trajectory (Figure 9d-f), which is due to the balanced force exerted by the electrodes. On the other hand, voltage bias applied to the electrodes affects the jet deflection angle. Note that in this case voltage bias has a “focusing effect” on jet deflection, similar to the signal amplitude. For example, for positively charged jet, higher voltage bias reduces the deflection angle. Too small bias is not desirable as non-linear deflection occurs when the jet approaches each electrode, causing a deformation of the printed pattern. Furthermore, too low bias may result in jet landing on one of the electrodes, from which point this electrode starts acting as a substrate. While this situation is prevented, voltage bias can be adjusted in a wide range, as shown on Figure 10.

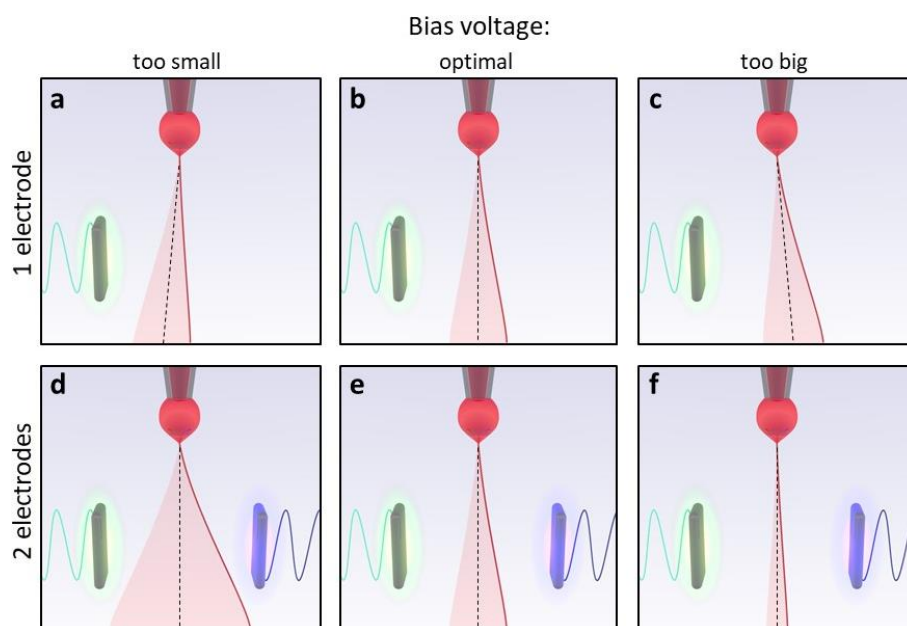


Figure 9. Schematic of voltage bias effect on jet deflection. a-c show how bias affects the verticality of the default jet trajectory in case of asymmetric electric field, as in configuration #1. In the presence of a single electrode proper bias must be applied to keep the jet in vertical position. d-f shows “focusing” effect on jet deflection angle in case of symmetric electric field, as in configuration #2. Note that the verticality of the jet is not affected due to the symmetric and opposing action of the electrodes. Too small bias may result in jet jumping on the deflection electrode, while excessive bias minimizes jet deflection angle and requires applying higher amplitudes, which may be not practical.

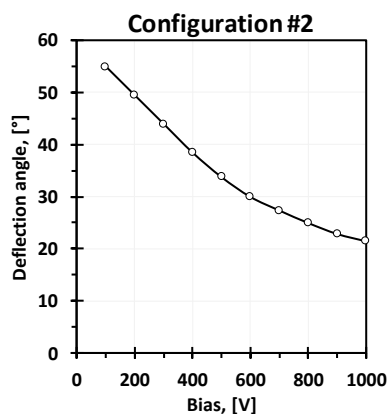


Figure 10. Bias effect on deflection angle for symmetric electric field. Bias voltage was varied while other parameters were kept constant: nozzle voltage 1500 V, signal frequency 100 Hz and amplitude 400 V. 5wt% PEO Mw=300,000 kDa in ethanol:water=3:1 was used as ink. Deflection angle decreases nonlinearly as bias voltage increased, resulting in a “focusing effect”, as schematically depicted in Figure 9d-f.

Lateral acceleration of the jet under electrostatic deflection

We estimated the lateral speed and acceleration reached by the jet under electrostatic deflection from high-speed video captures of the jet while it was oscillated at 10000 Hz with a triangular wave signal. The average lateral jet speed ($v_{L\text{ aver}}$) was calculated from the video as a product of the full length travelled by the jet in one oscillation period ($40\ \mu\text{m} \times 2$) times the frequency 10000 Hz, giving 0.8 m/s.

The minimum lateral jet acceleration allowing such an average lateral speed was calculated considering that the jet lateral speed was zero at the extreme side positions, and that the maximum lateral speed (v_{LM}) was reached at the jet's vertical position. Considering a constant lateral jet acceleration (a_L), the maximum lateral speed equals twice the average lateral speed, and the constant acceleration of the jet can be computed as: $a_{LM} = \frac{v_{LM}}{T/4}$ where T is the signal period. This equation results in a lateral jet acceleration of 64,000 m/s². Considering that the jet is straight at small jet-deflection angles, this calculation was extrapolated to the jet oscillation just above the substrate, 5 mm below the jet-ejection point. In this case, the average jet speed and the minimum required jet acceleration were 12.5 m/s and 800,000 m/s², respectively. Considering non-constant accelerations, higher lateral acceleration values would be obtained. Furthermore, much higher accelerations are potentially obtainable by applying larger voltages to the electrodes, increasing their size, or by positioning them closer to the jet, etc.

Thus, from the conservative calculation presented here we conclude that jet lateral acceleration caused by electrostatic deflection could be significantly higher than 500,000 m/s², the value provided in the thesis for the sake of comparison to the accelerations typically reached by mechanical stages.

4.4. Control of jet deflection

In jet-deflection printing, the main printing parameters are the amplitude and frequency of the signals applied to the jet-deflection electrodes. Amplitude defines the width of the printed pattern in X and Y dimensions, and frequency presets how many times the motif is printed per second. Any set of printing parameters with predefined motif geometry, motif size and printing frequency results in corresponding intended printing speed (length of printed motif * frequency = intended printing speed). This speed must match the speed of jet by selecting appropriate signal parameters for any given motif geometry. Figure 11a shows how printing speed can be computed from simple geometrical considerations and can be expressed as exemplified by Figure 11b, which is used (combined with plots on Figure 7) to select appropriate printing. This algorithm can be potentially made more user-friendly by automatic calculation of jet-deflection parameters from the pattern geometry, size, and jet speed.

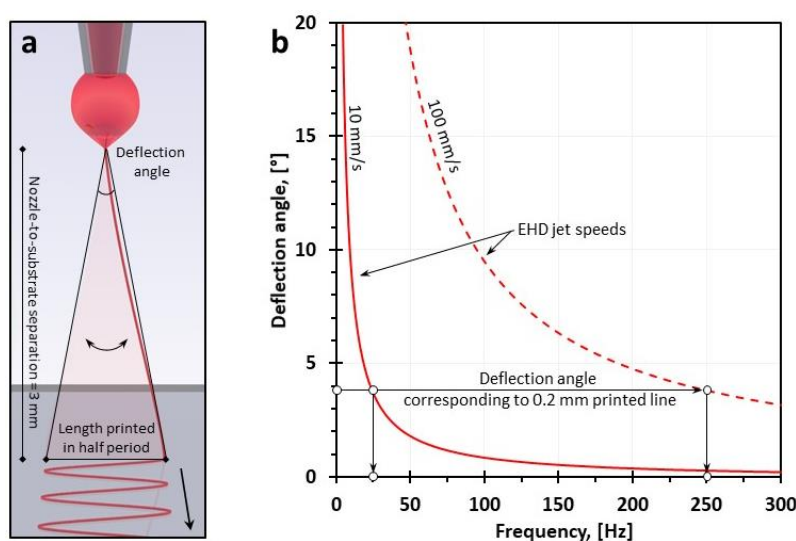


Figure 11. Selection of appropriate jet deflection parameters based on EHD jet speed. Schematic (a) shows how jet speed can be computed from isosceles triangle formed by extreme jet positions and length printed in half period of a sawtooth signal. Graph (b) plots two jet speeds of 10 and 100 mm/s, which were computed for such triangle with 3 mm height (nozzle-to-substrate separation). To match deflection speed to the jet speed, desired printed length must be selected, here exemplified by 0.2 mm and corresponding to 3.81° deflection angle. Signal frequency is found by intersecting the jet speed to be matched. Those deflection angle and frequency are used to determine appropriate signal amplitude for any electrode configuration from Figure 7a,c,e.

4.4.1. Software for controlling jet-deflection printing

A LabVIEW software was specifically developed to define and generate the voltage at the different jet-deflecting electrodes from parameters such as the pattern geometry, the number of printed layers, the layer printing frequency and the signal amplitude.

Below we describe the strategy which allows simple conversion between preset pattern geometry and jet-deflection parameters into jet-deflection signals. The signals applied to the jet-deflection electrodes are computed by the developed software. First, a pattern geometry (also referred to as motif) is described as a multitude of points with coordinates in the XY plane, where the first and last points have the same coordinates (Figure 12a-b). In terms of jet-deflection signals, one pattern/motif describes one period of jet-deflection signals both in the X and Y directions. Period duration is the inverse of the frequency of the signal (controlled independently from the motif geometry), i.e. the rate of motif repetition.

Independent digital signals are computed by software and are applied as an input to the DAQ card (signal generator). Synchronized digital signals encode the pattern geometry and other parameters (signal amplitude, frequency, etc.), and are represented as X and Y waveforms (Figure 12g). A waveform is defined as a series of "waypoints", which are specific voltage targets occurring at specific times along the waveform. Signal generator converts those digital signals into analog signals, which are then amplified and applied to the electrodes.

It must be noted that to generate continuous analog signal needed for jet deflection along a desired motif, digital input signals must have high temporal resolution. For example, for the printing frequency of 1000 Hz, the waveform should have a high enough sampling rate (100-1000 samples per period) to appropriately represent the desired printing motif within a single period of 0.001 seconds. Such temporal resolution of jet-deflection signal sets requirements on signal generator and amplifiers regarding sample rate (samples per second) and slew rate (volts per second), which is the maximum rate at which an amplifier can respond to an abrupt change of input voltage.

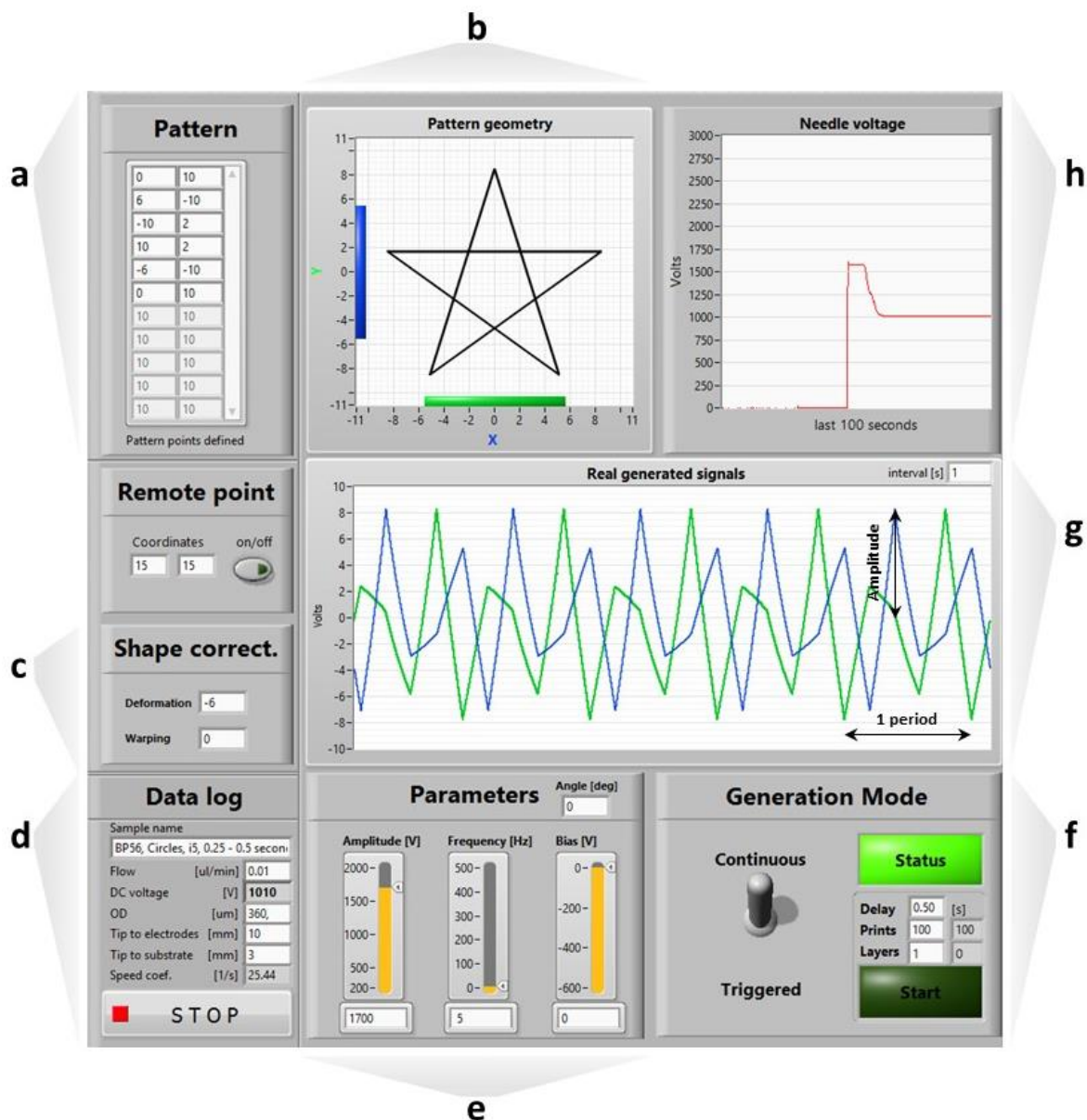


Figure 12. User interface of LabView software for jet deflection 3D printing. Desired pattern is preset in (a) as coordinate points in XY space (limited by the maximum output of control signal ± 10 V). The pattern is preset either manually or is imported from a text file, and is depicted in panel (b), where relative orientation of deflection electrodes is schematically shown. Shape correction parameters compensating for asymmetric electric field are set in (c). Printing parameters are logged in (d) and saved in a separate file for each printing session. Signal amplitude, bias and frequency are set in (e), while (f) controls printing mode (continuous vs. triggered signal generation). Analog signals for both electrodes (blue and green) are generated and then measured by DAQ card, and continuously updated in (g). Finally, nozzle voltage is monitored in (h), in this case showing voltage increase up to 1600 V for jet initiation and then lowering it to 1000 V for stable jetting. The screen was typically recorded while printing, including LabView interface and video inspection of the drop/jet, so that the effect of printing parameters on printed sample could be subsequently analyzed.

4.4.2. Deformation correction

A 2-electrode configuration used in our printer results in a printed pattern which is deformed compared to the predefined design. This happens because of the asymmetry of the jet-deflection electrode arrangement, which generates an asymmetric electrostatic field in the XY plane (as discussed in the beginning of this Chapter). A 4-electrode configuration would provide a more symmetric electrostatic field with respect to the 2-electrode configuration, although not expected to be radially homogeneous in the XY plane. Such symmetric configuration was not used in our work due to availability of only 2 signal channels. Far from a disadvantage, achieving precise printing with a simpler printer has clear relevance for future technology commercialization, which was an additional motivation behind developing such a correction algorithm.

To correct for motif deformation, a mathematical algorithm integrated into the software is used. This algorithm applies modified signals to signal generators, which are then amplified and applied to the jet-deflection electrodes. This method permits to preventively eliminate the deformation, allowing to print a predefined design without deformation.

In principle, for developing such mathematical algorithm, the deformation occurring because of unsymmetrical electrostatic field could be theoretically modeled. However, due to complex physics and often questionable assumptions built into any simulation, a more practical approach is to correct the deformation empirically by first printing a test motif and observing the resultant deformation relative to the preset design. Then, the mathematical function is determined, which expresses the coordinates of the resultant motif as a function of the coordinates of the preset design (a transformation between the preset pattern, red, to the printed deformed pattern, blue; Figure 13a). The inverse of this mathematical function is used in the software to preventively correct the deformation.

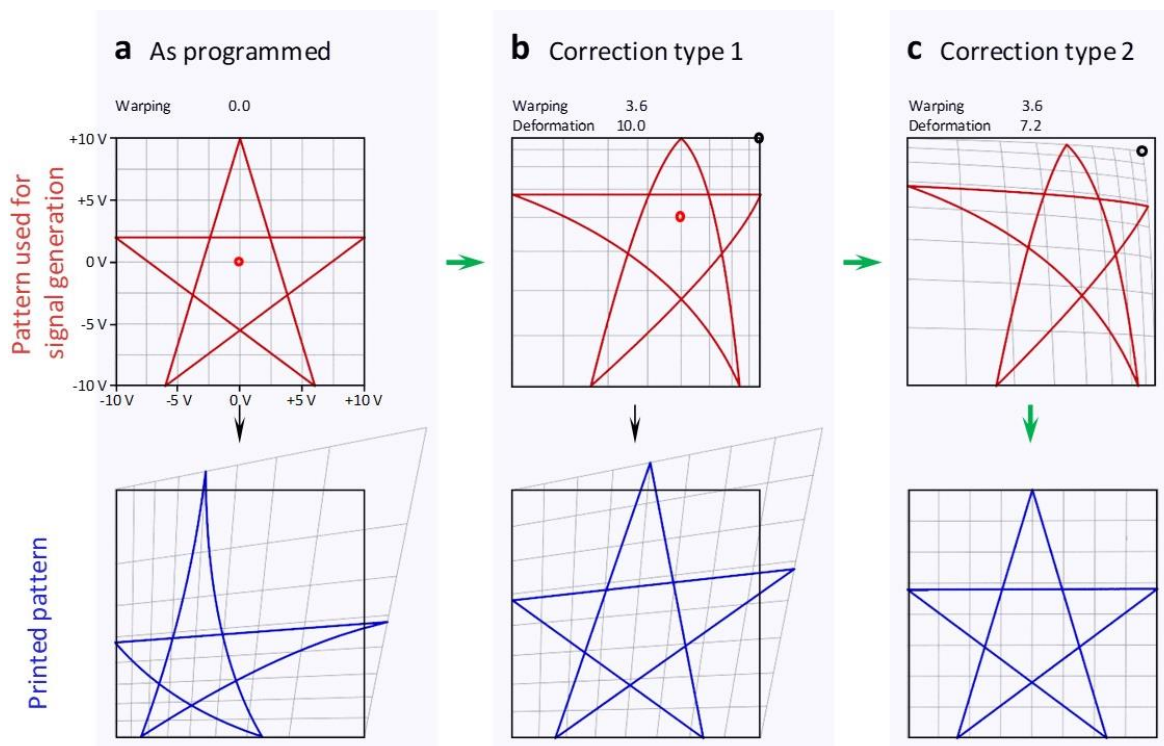


Figure 13. Printed pattern deformation and developed correction algorithm. **a** shows how as-programmed pattern (red), used to generate jet-deflection signals, results in deformed printed pattern (blue) due to the asymmetric electric field (configuration #3, electrodes positioned from top and right relative to printed pattern). Printed pattern deformation was observed experimentally and used to develop mathematical model describing such deformation. **b** shows the first type of correction applied (“warping”), which compensates for uneven distances between checkboard lines for printed pattern. To achieve this, the center of the checkboard (red point) is shifted by 3.6 V, while the edges of checkboard are kept in place. **c** shows the effect of the second type of correction applied (“deformation”), which shifts the top-right corner (black point) of the checkboard from its default position of 10 V to 7.2 V. Second signal transformation results in square printed field. Both correction coefficients are found experimentally and are (conveniently) constant for any given electrode configuration. Green arrows highlight the order of applying two transformations for obtaining desired printed pattern.

Figure 13 summarizes the deformation empirically observed for printing a star pattern and the developed algorithm for correcting such deformation. Such deformation and correction coefficients were found specifically for Configuration #3 (Figure 3b). Curiously, the deformation manifests itself in two different ways:

- (i) First one is that the distance between parallel lines on the “checkboard” is altered. This can be explained by non-linear dependence of the deflection length on signal amplitude, previously simulated in Figure 4d. To compensate for this deformation, “correction type 1”

is applied, warping the checkboard space while its edges are not perturbed. For shown deformation, “warping” coefficient of 3.6 V was found empirically, effectively correcting uneven distribution of checkboard mesh (Figure 13b). The value of warping coefficient represents the shift of the center of the checkboard (marked as red point) from its original coordinates [0 V; 0 V] to new position [3.6 V; 3.6 V] in both X and Y. For any other electrode size and position this coefficient must be adjusted. However, higher nozzle-to-electrodes separation of 10 mm resulted in only minor deformation, which could be ignored.

(ii) Second manifestation of deformation was, surprisingly, in shifting one of the corner points of the checkboard, and particularly the one which was positioned between X and Y electrodes (electrodes would be from top and right sides relative to printed patterns, highlighted in blue). “Correction type 2” required finding a more complex transformation allowing to manipulate one corner of the checkboard (marked as black point). The responsible “deformation” coefficient is +10 V when the checkboard corner is located on its normal position. By decreasing this coefficient to +7.2 V, the corner is moved from its original coordinates [10 V; 10 V] to new position [7.2 V; 7.2 V] in both X and Y. By applying both correction coefficients, the printed pattern now corresponds to the designed one and the deformation is corrected. Finally, it must be noted that two correction types must be applied in the strict order (shown by green arrows), otherwise the deformation cannot be corrected.

Described correction mechanism allows using only 2 electrodes which deflect the jet in plane normal to the default jet trajectory thus controlling the EHD jet positioning within the printing zone. It is advantageous to have only 2 jet-deflecting electrodes (compared to 4) because only 2 control signals have to be computed, generated, and amplified. Having fewer independent channels for control signal generation significantly reduces the cost for DAQ card and amplifiers, while reduced power consumption and simplification of printing device are other benefits.

An additional advantage is that having 2 jet-deflection electrodes around the nozzle leaves more free space around the nozzle to potentially locate additional elements, such as a gutter electrode for interrupting material deposition when needed, for example. Concluding, configuration with only 2 electrode allows extended functionality and is more convenient for practical use of the printing device.

4.5. Conclusions

This Chapter was devoted to performing a parametric analysis of jet deflection and developing means to control 3D printing based on electrostatic jet deflection. The concept of electrostatic jet deflection was proposed multiple times during last decade, and various attempts were made in fields of electrospinning and EHD jet printing. Despite previous research has demonstrated the feasibility of jet deflection, it was limited in two major ways, which were addressed in this chapter:

1. The effect of parameters on electrostatic jet deflection was only sparsely reported, leaving big gaps in knowledge about setup configuration and jet dynamics. To address this shortcoming and expand fundamental understanding of electrostatic jet deflection, we performed rigorous parametric analysis via both finite element analysis and experimental data obtained with high-speed imaging. As a result, the effect of relevant printing parameters on jet deflection is reported for various setup configurations. Jet deflection angle was found to increase linearly with increasing signal amplitude, and to decrease non-linearly with increasing the frequency of the control signal. Revealed dependencies are essential for determining appropriate signal parameters for controlling jet-deflection printing. Furthermore, high-speed imaging showed that the jet is surprisingly resilient and can be deflected up to 10000 Hz while maintaining its stable operation. Fast switching of electrostatic field allowed to reach deflection speeds above 10 m/s and accelerations well in excess of 500 km/s^2 , for the first time providing an estimation of amazing dynamic characteristics attainable by jet deflection approach. Such excellent accelerations allow using much slower and cheaper XY stages, which is a significant advantage compared to the stage-driven EHD jet printing.

2. In prior art, the control of jet-deflection printing was based on primitive configurations where control signal was obtained either by manual switching of DC potentials or by using elementary wavefunctions built into off-the-shelf voltage generators. Thus, all previous attempts lacked the capability to generate complex wavefunctions at high temporal resolution, which is an essential requirement for 3D printing of complex patterns using EHD jets. In most cases printed patterns were limited to 1D deflection and very little attempt was made to extend jet deflection printing into 2D and 3D. In this work we addressed this

“control challenge” by developing a software allowing to direct EHD jet in 3D space, thus precisely controlling its deposition speed and location onto the substrate. Developed software was essential for studying jet deflection and was a critical stepping stone for obtaining printing results at the base of this doctoral thesis. We described the software fundamentals, one of which is the deformation correction algorithm, which allowed us to correct the detrimental action of asymmetric electric field when only 2 deflecting electrodes are used. This enables printing as-desired patterns while using fewer independent channels for signal generation, thus making the setup simpler and cheaper, which will aid in future commercialization of this technology.

4.6. References

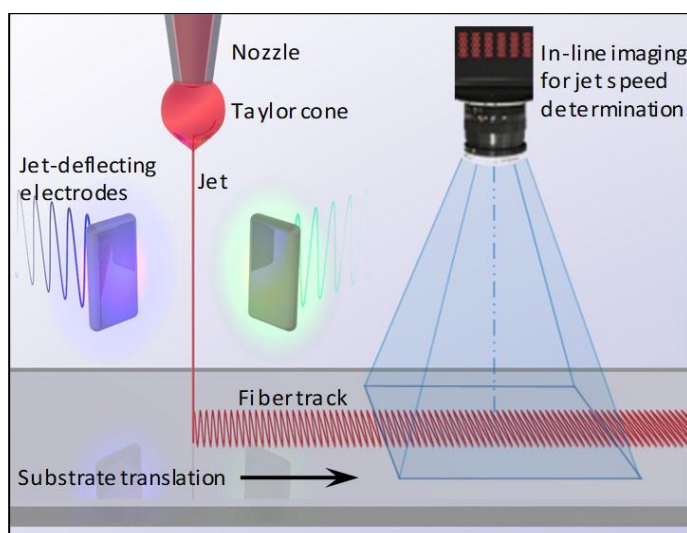
1. Kim, H. Y., Lee, M., Park, K. J., Kim, S. & Mahadevan, L. Nanopottery: coiling of electrospun polymer nanofibers. *Nano Lett.* 10, 2138–2140 (2010).
2. Lee, M. & Kim, H. Toward nanoscale three-dimensional printing: nanowalls built of electrospun nano-fibers. *Langmuir* 30, 1210–1214 (2014).
3. Brown, T. D. et al. Melt electrospinning of poly(ϵ -caprolactone) scaffolds: Phenomenological observations associated with collection and direct writing. *Mater. Sci. Eng. C.* 45, 698–708 (2014).
4. Cai, X., Zhu, P., Lu, X., Liu, Y., Lei, T., & Sun, D. (2017). Electrospinning of very long and highly aligned fibers. *Journal of Materials Science*, 52(24), 14004–14010.
5. Dalton, P. D., Klee, D., & Möller, M. (2005). Electrospinning with dual collection rings. *Polymer*, 46(3), 611–614.
6. Bellan, L. M. & Craighead, H. G. Control of an electrospinning jet using electric focusing and jet-steering fields. *J. Vac. Sci. Technol. B* 24, 3179 (2006).
7. Martinez-Prieto, N. et al. Feasibility of fiber-deposition control by secondary electric fields in near-field electrospinning. *J. Micro Nanomanuf.* 3, 041005 (2016).
8. Fang, F. et al. Controllable direct-writing of serpentine micro/nano structures via low voltage electrospinning. *Polymers* 7, 1577–1586 (2015).
9. Zhu, Z. et al. Fabricated wavy micro/nanofiber via auxiliary electrodes in near-field electrospinning. *Mater. Manuf. Process* 31, 707–712 (2016).
10. Kyselica, R., Enikov, E. T. & Anton, R. One- and two-dimensional electrodynamic steering of electrospun polymer nanofibers. *Appl. Phys. Lett.* 113, 183705 (2018).
11. Soldate, P. & Fan, J. Controlled deposition of electrospun nanofibers by electrohydrodynamic deflection. *J. Appl. Phys.* 125, 054901 (2019).
12. Karatay, O., Dogan, M., Uyar, T., Cokeliler, D. & Kocum, I. C. An alternative electrospinning approach with varying electric field for 2-D-aligned nanofibers. *IEEE Trans. Nanotechnol.* 13, 101–108 (2014).
13. Grasl, C., Arras, M. M. L., Stoiber, M., Bergmeister, H. & Schima, H. Electrodynamic control of the nanofiber alignment during electrospinning. *Appl. Phys. Lett.* 102, 053111 (2013).
14. Rasel, S. M. An Advanced Electrospinning Method of Fabricating Nanofibrous Patterned Architectures with Controlled Deposition and Desired Alignment. (University of Ontario Institute of Technology, 2015).
15. Arras, M. M. L., Grasl, C., Bergmeister, H. & Schima, H. Electrospinning of aligned fibers with adjustable orientation using auxiliary electrodes. *Sci. Technol. Adv. Mater.* 13, 035008 (2012).

Chapter 5

In-line fiber speed control for EHD jet-deflection printing

Abstract

Additive micro-manufacturing using EHD jets is based on the continuous deposition of a polymeric nanofiber on a substrate. Owing to the small fiber size and high fibers speeds that can be achieved, this method is capable of high resolution combined with high printing speed, well beyond the state of the art. Printing with high fidelity critically depends on controlling the fiber speed, which must be closely matched by the desired printing speed. However, current methods to determine the fiber speed are either cumbersome, suffer from imprecision or can't be performed in-situ as they are based on laborious high-resolution imaging of individual fibers. Here we propose a facile method using electrostatic jet deflection, where the speed and the length of printed fiber are readily computed through the width of a printed pattern, attainable in-line through optical inspection. This approach allows determination of the speed and the length of the printed fiber without the need to resolve individual fiber, and thus requires only inexpensive optical equipment. We demonstrate the feasibility to determine the fiber speed in situ during printing, which can be provided as a feedback to control the printing process. This method will not only assist in studying fundamental relation between the fiber speed and other printing parameters, but also enable reproducible printing of fibers in rapidly expanding area of applications.



5.1. Introduction

The improvement of printing resolution and speed is an ongoing focus in AM methods. Nozzle-based AM entails the ejection of inks or melts through a nozzle which are then deposited layer-by-layer on a substrate, forming 3D structures¹⁻³. For extrusion-based AM systems the smallest achievable voxel size is typically above 100 micrometers. By contrast, electrostatic acceleration of liquid inks after they exit the nozzle allows reducing voxel size by many orders of magnitude⁴⁻⁸. Such electrohydrodynamic (EHD) jets are typically printed as continuous lines, by using viscoelastic inks containing polymers. At high charging levels, the liquid at the nozzle exit adopts a pointed shape, often called “Taylor cone”, which ejects a thin liquid thread or jet whose size can be much thinner than the width of the nozzle opening (Figure 1a). Viscous and elastic stresses stabilize the jet against the development of Rayleigh jet breakup. Lines in the micrometric and submicrometric range can easily be printed in this way⁹⁻¹⁰ (Figure 1a). We here refer to this AM approach as Electrohydrodynamic Jet Printing, but it has also been referred to as Near-Field Electrospinning (NFES) for its connection to electrospinning¹¹.

Determining jet speed is critical in controlling EHD jet printing, as this speed controls the contact point between the jet and the substrate, while the jet speed may further vary with time. Unfortunately, because jet speed depends on the electrical field and fluid properties in a complex way, its prediction from the process parameters is an enormous challenge. It must, therefore, be determined empirically by inspection of the printed pattern. Table 1 shows the connections between jet speed and pattern quality for each mode of EHD jet printing, (i) the conventional *stage-driven* approach, versus (ii) the *jet-deflection* approach, recently introduced by us⁴. For each of the two EHD printing modes, three regimes are found depending on the speed of the jet. In stage-driven printing, the substrate or collection surface is displaced under the jet, driven by a mechanical stage. In this case, pattern fidelity (Table 1, top row, center panel) relies on matching the (horizontal) substrate speed U_s to the (vertical) jet arrival speed U_j , attained by the jet before it reaches the substrate. *Direct-writing*, namely, the direct transfer of the stage motion to a printed pattern, is only strictly possible when U_s matches U_j (or, in practice, U_j is set slightly above U_s). Such *matched speed* regime (Table 1) has been used extensively with melts of biocompatible polymers for tissue engineering applications, and is referred to as *melt*

*electrowriting*¹²⁻¹³. At substrate speeds exceeding the jet speed, stage-driven printing enters the *stretched jet regime*, in which the jet is under tension while stretching slightly (rather than under compression). Here, the printed pattern deteriorates, although it can still be used to print lines and walls with a large curvature radius (compared with the fiber diameter)¹². Stage-driven printing with U_s set below U_j ($U_s < U_j$) leads to the *compressed jet regime* (Table 1). Here, the EHD jet is under compression next to the substrate, undergoing buckling instabilities¹⁴⁻¹⁷. These can result in different printed patterns depending on the ratio U_s/U_j : sinuous folding, zigzag folding, helical coiling, meandering/serpentine, etc^{16,18}. As the amplitude and wavelength of the printed coils can be quite small (from a few to several tens of microns)¹⁹, this regime of printing has been proposed for printing flexible electronics²⁰⁻²¹. However, only a few patterns are available as permitted by the physics of the buckling. In addition, precise fiber positioning is not, strictly speaking, achieved, because of the spontaneous nature of jet buckling as it approaches the substrate. Furthermore, although the printed patterns are usually periodic, chaotic printing may set in. To the best of our knowledge, however, the parametric conditions that lead to chaotic behavior have not been investigated.

Table 1. Classification of printing regimes of EHD jet printing (also known as NFES).

Speeds ratio Printing mode	Jet speed > Printing speed Compressed jet regime <i>Jet buckles under compression</i>	Jet speed ≈ Printing speed Matched speed regime <i>Best printing fidelity</i>	Jet speed < Printing speed Stretched jet regime <i>Cutting corners due to jet lag</i>
Stage-driven printing (conventional)			
Jet-deflection printing (Liashenko et al. 2020)			

The methods for determining the jet speed in stage-drive printing are complex and are not robust. One is (i) the *speed matching method*, in which the jet speed is determined by inspection of printed lines taken at different speeds. This method involves collecting various patterns at the three different regimes (Table 1) and inspecting the sample to identify the moment when the wavy printed pattern becomes a straight line, corresponding to the matched-speed condition at which the stage speed equals the jet speed¹². This approach relies on resolving the amplitude of the wavy pattern to ensure the straight-line condition, which involves the use of a microscope able to resolve the jet's small size (in the micrometer to submicrometer ranges). Even when the fibers are large enough to be visible to the naked eye, such as in MEW²² this method requires iterations before the jet speed can be determined and can be hardly implemented in situ. (ii) In the *fiber length method*, a printed pattern is analyzed to extract the printed fiber length within a given travel of the collection surface, thus in a known time²³. The jet speed is then computed as the length divided by the time. Here also, a powerful microscope is needed to resolve the individual fiber defining the fiber pattern. This method only works for absent or sufficiently infrequent fiber overlap. In sum, these methods are laborious and require high resolution imaging equipment; therefore, simpler methods are needed which can be used *in situ* during printing of very small fibers. Ideally, such methods should be interfaceable with fast pattern-recognition software, so they can be implemented in commercial products and industrial settings.

In the present work, we propose the use of electrostatic jet deflection to overcome the difficulties with these jet-speed determination methods. In *EHD jet deflection printing* (Table 1, bottom), additional electrodes are used for electrostatically stirring the EHD jet. The trajectory and point of arrival of the jet to the substrate are controlled by the voltages applied to these electrodes, allowing jet stirring at very high accelerations (e.g. 500 km/s²). Therefore, printing speed can be much higher than in stage-driven printing, where it is constrained by the limitations of mechanical stages⁴. The jet deflecting parameters are programmed to ensure matching between the jet speed and the desired *printing speed* (the intended speed of the contact point over the substrate). At this condition, the jet is neither under compression nor under tension. Unlike in stage-driven printing, the position

of the contact point where the fiber meets the substrate is controlled *independently from* the motion of the substrate, which can even remain still.

Determining EHD jet speed by jet deflection is demonstrated for two approaches. (1) In the first one, the EHD jet is continuously deposited on a moving collector while it is electrostatically deflected periodically in the transverse direction (as shown in Table 1). The width of the printed track with a repeating motif is used to compute the jet speed from knowledge of the printed pattern and the frequency of the jet deflection signal. A key advantage of this method is that the printed fiber track is much wider than the fiber; therefore, it can be observed and quantified easily using standard optical inspection equipment (as opposed to microscopy). (2) Our second strategy is based on building a 3D structure layer by layer over a motionless substrate, wide enough to be accurately sized by standard optical equipment. In this case, the jet speed is obtained from the signal frequency and the width of the object of known shape. In both cases, the speed is obtained from a measurement of pattern width, which is easily done in situ, while printing, and a frequency which is preset in the software. For convenience, we focus here on inks, but the method could in principle be translated to the case of melts, as well.

5.2. Methods

5.2.1. Printing setup description

Our EHD printer comprises a thin tube as nozzle (described below), a glass syringe into which inks were loaded (Hamilton #81320, 1 ml), a syringe pump (Harvard apparatus, Pump 11 Pico Plus Elite 70-4506) to supply the ink from the syringe to the nozzle at a known rate, a printing substrate mounted on a XY translation mechanical stage (PI miCos linear stages PLS-85 with 10 mm range in both X and Y with RS422 encoders), and a high voltage power supply (Matsusada AU-20P15) providing (in our case) positive high voltage to the nozzle (Figure 1b). The printing substrate is attached atop an electrically-grounded aluminum plate, which is mounted on the XY translation stage. The separation between the nozzle and the printing substrate is 3 mm except where noted. Stainless needles with blunt ends (Hamilton N726S, 26s gauge, 127 μm ID, 474 μm OD) or borosilicate glass tips (c.a. 150-200 μm OD) were used as nozzles. No surface treatment was applied to the tips before their use. Glass tips were manufactured from borosilicate capillaries (Sutter Instruments, B100-50-15) by a Pipette puller (Sutter Instruments P-97) and the tips were manually broken by scratching two tips against each other. Glass tips were glued atop of a stainless-steel needle with blunt end (B Braun Sterican, 27 gauge).

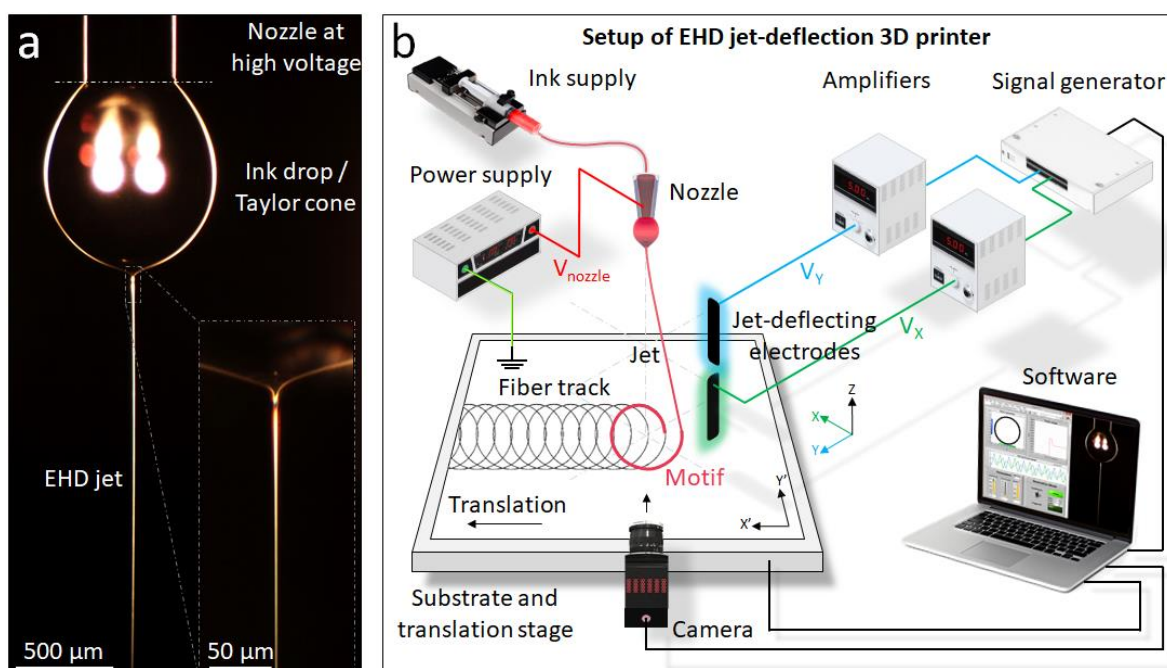


Figure 1. EHD jet deflection printing. **a** EHD jetting from the pendant drop of ink. **b** Schematic of an EHD 3D printer with jet-deflecting electrodes.

In addition to these standard elements, our printer has two extra electrodes around the jet (Figure 1b) for modifying the electric field in the vicinity of the jet, to deflect it from its otherwise vertical trajectory (Figure 1a). Except where noted, the electrodes were placed at 90 degrees from one another (as in Figure 1b), and kept 10 mm away from the nozzle-

axis. In this configuration, they were glued to a plastic holder made with an SLA 3D printer (Formlabs Form 2) using FLGPCL04 clear resin.

As in conventional 3D printing, printing process was controlled through the parameterization of the layer-by-layer deposition to print an object with predefined geometry, size and even microstructure. The custom-made software (see Chapter 4.4), developed in LabVIEW, and a data acquisition card (National Instruments, USB-6259) generated the jet deflection voltages, defined as a function of the pattern geometry, the layer printing frequency and the signal amplitude. Synchronized analog signals (max. ± 10 V) provided by the DAQ card were amplified (max. ± 2000 V, using Matsusada AMJ-2B10 and Trek 677B amplifiers) and applied to the jet-deflecting electrodes typically within 1000-2000 V for 10 mm nozzle-to-electrodes separation. The nozzle voltage was also monitored through the LabView software, while camera imaging and the XY stage motion were controlled through standard software supplied by the manufacturer.

5.2.2. Materials and inks preparation

Polyethylene oxide (PEO) of various molecular weights was purchased from Sigma-Aldrich (#182001, viscosity-average molecular weight 300 kDa; #372781, 1000 kDa; #189472, 5000 kDa). Poly(3,4-ethylenedioxythiophene) polystyrene sulfonate (PEDOT:PSS) dispersion was purchased from Sigma-Aldrich (#655201, 3-4% in water). Ethanol and ethylene glycol were reagent grade from different sources. All chemicals were used as received without further purification. Ag nanoparticles of diameter ca. 50 nm were synthesized using PVP as ligand²⁴. After synthesis, the nanoparticles were thoroughly washed by multiple precipitation and redispersion cycles using ethanol as solvent and acetone as antisolvent, and finally, were precipitated for posterior use. Obtained Ag nanoparticles could be dispersed in polar solvents such as water and ethanol.

For inks formulation, deionized water was the main solvent, to which some amounts of ethanol or ethylene glycol were added to lower surface tension and evaporation rate during printing. PEO inks were prepared by dissolving PEO (typically 2-10 wt%) in the solvent mixture during 24 hours under magnetic stirring. PEDOT:PSS inks were prepared by adding the proper amount of PEDOT:PSS dispersion into the-PEO ink and homogenizing the mixture by magnetic stirring. Ag nanoparticle inks were prepared by adding the PEO ink into a flask containing precipitated Ag nanoparticles and dispersing them using ultrasonication and magnetic stirring. All inks were kept in sealed vials, where they could be stored for months and even years without showing signs of degradation. Inks containing PEDOT:PSS were stored at 4 °C.

5.2.3. Printing protocol and in situ inspection

Inks were loaded into the glass syringe and supplied to the nozzle with a typical flow rate of 0.05-0.07 $\mu\text{l}/\text{min}$. The pendant drop formed at the nozzle aperture. Silicon wafers (University Wafers #452, p-type, <100>) were used as substrates. Silicon was cleaned with isopropanol to remove organic contamination prior to printing. The substrate was either translated continuously to print 2D fiber tracks, or only moved in steps between which the

substrate remained motionless while 3D structures were printed by electrostatic jet deflection.

Upon application of a high voltage to the nozzle, the ink drop forming at the exit of the nozzle expels a charged jet toward the substrate (Figure 1a). Electrohydrodynamic (EHD) jetting was initiated by slowly increasing the nozzle voltage up to 1800-3000 V, until the pendant ink drop forming at the exit of the nozzle elongated and fell on the printing substrate, establishing a jet. This voltage was then lowered to 400-1500 V and the jet was stabilized for 2 minutes before initiating the printing. The jet thickness is independent of the size of the nozzle aperture and it can be below ~ 100 nm depending on the ink properties, the supply rate and the applied voltage²⁵. The printing process was carried out under ambient temperature in the range 18-20 °C. Where noted, dry nitrogen gas was supplied around the jet from a side tube to ensure predictable solvent evaporation rate.

The printing process was monitored with a CMOS camera (Basler acA2040-25gc) mounted on an optical microscope, which consisted of a 12X lens with adjustable zoom and focus (Navitar 1-50486), a 2x lens adaptor (Navitar 1-62136), and a 5X microscope lens (Mitutoyo 1-60226). The optical axis was set horizontal. A fiber optic illuminator (AmScope HL-250-A) on the other side of the observed object aimed at it at ca. 5° angle from the microscope optical axis, so that direct light did not reach the camera sensor for dark-field setting (as on Figures 1a and 2b). For real-time monitoring of the liquid drop during the printing process (as on Figure 8c,d), a paper sheet was placed between the light source and the observed object for bright-field setting.

5.2.4. Post-printing fiber inspection

In jet-deflection printing, either fiber tracks were printed as the substrate is moved, or 3D structures were printed with the still substrate. These tracks and 3D structures were inspected after printing by scanning electron microscopy (SEM), confocal microscopy (CM), and by macro-photography based on the in-situ inspection optical system to simulate in situ machine-inspection. SEM micrographs were obtained at 1-2 kV electrons acceleration voltage on AURIGA (FIB-FESEM) from Carl Zeiss using either an inlens detector or a secondary electrons (SE2) detector. Prior to imaging any samples by SEM, they were sputter-coated with silver to a several nm using a DC magnetron sputter (Emitech K575X, 80 mA, argon, 90 seconds) while the sample was slowly rotated to obtain uniform thickness. This improved the quality of SEM images and protected the PEO fiber from degradation/shrinkage caused by the electron beam. Optical images were taken using a Sensofar confocal microscope with polarized light to improve the contrast between printed fibers and substrate. Images larger than 0.6 mm were obtained by stitching multiple images having smaller field of view, which was done within original Sensofar software.

To simulate in-situ imaging of printed fiber tracks (as on Figure 9), PEO fiber tracks were imaged after printing using the CMOS camera and microscope assembly described earlier, while the substrate was moved in front of the microscope at the same speed as had been used during printing.

5.2.5. Electric field simulation

The simulation of the electric potential and field around the jet in the presence of a single jet-deflecting electrode (Figure 2a) was done in COMSOL Multiphysics® 5.2a using the following parameters: nozzle potential at +1000 V; substrate was kept at 0 V (Earth-grounded) and jet-deflecting electrode at -50 V; nozzle-to-substrate separation of 3.6 mm; and nozzle-to-electrode separation at 2 mm.

5.3. Results and Discussion

5.3.1 Jet-deflecting electrodes configurations to control jet position

In EHD jet deflection printing, the time-varying deflection of the EHD jet is accomplished by off-axis distortion in the electric field. Deflection of the jet along a fixed direction can be accomplished by one jet deflecting electrode or by two electrodes. Figure 2a shows the electric field distortion created by a single electrode. In this simulation, a massless jet is shown as an electric field "streamline" (in white) starting at the tip of Taylor cone, along with the electric potential and the electric field (arrows) around the jet. Color gradient represents the electric equipotential lines and black arrows represent the electric-field vectors, of length proportional to field strength. The deflecting electrode, nozzle and ink drop were plotted in white for clarity, but are at the specified potentials.

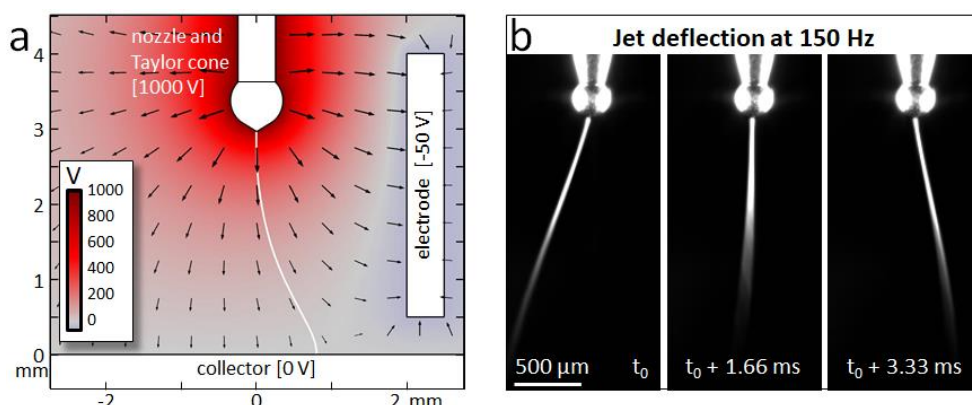


Figure 2. Electrostatic jet deflection. **a** Simulation of the electric potential and field around the jet in the presence of a jet-deflecting electrode. **b** High-speed video captures of a jet at leftmost, central, and rightmost positions being deflected at 150 Hz using two opposing jet-deflecting electrodes (not shown) positioned 3 mm away from the needle axis, with a needle-to-substrate distance of 5 mm.

Jet deflection along a fixed direction can also be accomplished by a pair of jet deflecting electrodes positioned on opposite sides of the jet. Symmetrically alternating signals applied to those electrodes translate to periodic jet deflection. Figure 2b shows high-speed video captures of the thin jet for this configuration. Triangular signals of opposite polarity (symmetrically alternating) were applied to the jet deflecting electrodes (at a given moment one electrode was attracting the jet, while another repelled it). To achieve a

periodic and symmetric motion of the jet as in this figure, the voltages on the two electrodes follow a function of the kind: $V_1=V_b+U(\omega t)$ and $V_2=V_b+U(\omega t+\pi)$, where V_b is a constant bias voltage. The function U is a periodic function of the argument (*e. g.* triangular or sinus) with frequency $\nu=\omega/2\pi$, so its value inverts every half period $T/2$ ($=\pi/\omega$), the voltage difference V_2-V_1 varies periodically ($=2U(\omega t)$) and the time averaged voltage is constant: $(V_2+V_1)/2 = V_b$.

To control the jet motion along two directions one could expand the two-electrode configuration with another electrodes pair in the orthogonal direction. However, this requires the use of two additional high voltage amplifiers, to a total of four. Therefore, we have proposed expanding the single-electrode configuration instead, by adding only one electrode, resulting in two electrodes positioned at 90 degrees to each other⁴ as shown in Figure 1b. In this case, the time signals are still periodic but symmetric jet motions cannot be obtained with symmetric signals, and the necessary corrections are made by the software (see Chapter 4.4.). Our LabView software is designed to preventively compensate for such asymmetric electric field when generating the jet-deflection signals, allowing us to obtain an as-designed printed pattern. This compensation mechanism is developed by first observing and mathematically describing the difference between the deformed printed pattern relative to as-designed pattern, and then applying an opposite function to the signals to be generated. Such simple correction is automatically applied to any new pattern, given that the electrodes configuration (and thus the action due to the asymmetric electric field) is not changed.

5.3.2 Jet speed from 2D patterns

Jet speed can be determined from analysis of printed patterns obtained while moving the substrate at constant speed while deflecting the jet in the orthogonal direction. Figure 3 compares how jet speed is obtained conventionally (left panels) and by the proposed jet-deflecting method (right panels). In the conventional method, Figure 3a, the stage is translated at increasing speeds, from a value which is lower than the jet speed. At low speeds the jet buckles on arrival to the substrate, resulting in printed loops. The amplitude of the loops reduces as the stage speed increases, eventually giving way to meanders in a serpentine pattern. The amplitude of such meanders decreases as the stage speed

increases, eventually leading to a straight fiber (bottom panel). At this condition, the stage speed matches the jet speed. In this method, the jet speed is determined by searching for the condition at which the jet becomes straight. However, exceeding the jet speed value with the stage also results in a straight jet; so it is critical to reach the straight jet condition incrementally. In addition: (i) a fast (and fast-accelerating) stage is needed (at least as fast as the jet), where this could be a challenge because EHD jets can attain speeds well in excess of 1 m/s; and (ii) a powerful microscope is needed to resolve a single fiber on the printed substrate, so the condition of a perfectly straight jet can be distinguished from a meander of low amplitude. As a result of these, an online determination of jet speed by this method would seem complex.

In the jet deflection method (Figure 3b) the jet is periodically oscillated in a direction which is orthogonal to the stage motion, so a repeating pattern, or motif, is printed (sawtooth shaped in the figure). Speed is measured by dividing the length of fiber L printed in one period of jet deflection divided by the period duration T . As the substrate speed increases, the pattern's wavelength increases while its amplitude decreases (Figure 3b, panels A through F). When the substrate speed exceeds the jet speed, the fiber becomes straight (panel G) due to stretching caused by tension from the contact point of the jet with the substrate (just as in the conventional method). The key advantage of this method lies in the fact that all of the images, A through F, can be used to compute the jet speed from the (known) geometry of the printed pattern. In the example of Figure 3b, a triangular wave was created, so $U_j = L / T = 2 * [W^2 + (U_s * T/2)^2]^{1/2} / T$, where W is the width of the fiber motif track, U_s is the stage speed, and T is the inverse of the frequency ν of the jet deflection signals. The computed speeds for all of the panels are shown in Figure 3c. The constancy of the speed data shown in Figure 3c proves that the stage motion did not impart speed to the fiber, as assumed in the calculation. A more sophisticated formula could be used to decrease error, to factor in for the smallest fiber curvature radius.

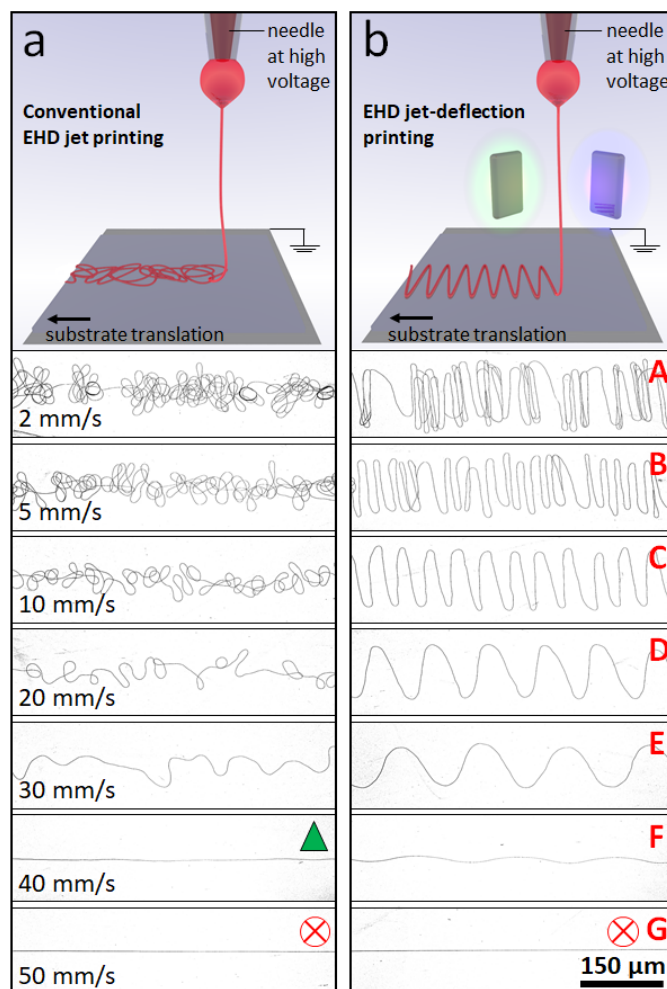


Figure 3. Comparison of conventional and jet-deflection methods for determining the fiber speed. **a** Conventional method: Schematic and scanning electron microscopy images of a PEO fiber collected on a Si substrate for different substrate. Buckling of the jet arriving to the substrate left a disorganized printed fiber when the jet speed was higher than the translation stage speed moving the substrate. The jet speed is found to equal that of the stage when a fiber is printed straight. **b** Jet-deflecting method: the jet is electrostatically

deflected periodically in the direction perpendicular to the substrate translation using a 200 Hz signal frequency and 1200 V signal amplitude. **c** Jet speed determined by the conventional method (green triangle) and jet-deflection method (red circles). The latter are computed as explained in the text. Error bars represent the standard deviation, which was computed from 3 to 5 data points for each translation speed. SEM used an inlens detector.

The proposed jet deflection method clearly overcomes the above-mentioned difficulties of the conventional method, as it does neither require matching any speeds, nor resolving individual fibers. Nor is a fast-moving stage needed. In fact, the proposed method works better at low stage speeds, as the measurement accuracy on the track's width will improve as the width increases. In addition, a single pass suffices in this method, in contrast to the conventional one. Finally, the space requirements are much smaller in our method. Using the conventional method with high jet speeds (hundreds of mm/s and greater) requires significant space on the substrate for the substrate to be able to accelerate to the required high speed, and then decelerate back to zero. For instance, for an acceleration of 20-30 m/s^2 typical of a high performance stage, reaching 0.5 m/s would require acceleration/deceleration lengths of at least 4-6 mm, giving a total line length of at least 20 mm. Note also that the precision of the method depends on the step of translation speed change, where typically a dozen speeds or more have to be tested to provide acceptable precision.

Finally, note that while on Figure 3b, panel B the fiber is straight and regularly distributed, in panel A, at a lower substrate speed, the density of fibers becomes inhomogeneous. This happens by the tendency of some fibers to fall on top of a previously deposited fiber by electrostatic attraction, after these have discharged and then recharged with charge of opposite polarity by electrostatic induction^{4,26}. This phenomenon has no impact on the determination of speed, because the width of the track is not affected.

5.3.3 Jet deflection method based on 3D structures

The idea for obtaining jet speed from a printing track onto a slow-moving substrate can be extended to the case where the substrate is stationary and 3D structures are printed. A 3D geometry is printed by periodically stacking layers of fibers, as shown in Figure 4. Electrostatic charge dissipation and charge reversal here become key in promoting the

precise self-assembly of the fibers⁴. The XY translation stage isn't moving during the printing (only just before and after the printing). Figure 4 shows straight walls made with PEO fiber (a-c), and cylinders made of a PEO-Ag nanoparticles composite (d-f), as well as other more complex 3D structures. The optical images are sufficient to resolve the size of even the smallest printed structures (Figure 4d-e), while SEM micrographs (Figure 4b,c,f) are just provided here to reveal the accurate layer-on-layer fiber assembly this technique is capable of.

As for 2D printed patterns and 3D structures, the jet speed is now computed as the product of fiber length L in a single period times the frequency ν of the jet-deflecting signal: $U_j = L/T = L\nu$. For the case of the straight walls (Figure 4a,b), two layers of fiber are deposited per period (20 ms). Therefore, the jet speed equals twice the wall length (≈ 0.6 mm) times the frequency of the jet-deflecting signal (50 Hz), namely 60 mm/s. For the case of the cylinder on Figure 4e, the jet speed is equal to the cylinder diameter (≈ 0.029 mm) times π and times the jet deflecting signal frequency (100 Hz), namely 9.1 mm/s. Similarly, the cylinder on Figure 4f has the diameter of 0.008 mm and was printed at 100 Hz, from which the jet speed of 2.5 mm/s was computed. Note that the height or the number of layers making up the object (up to 150 in the case of the walls) are not used in the computation, yet there must be enough layers so the object becomes visible to the inspection system.

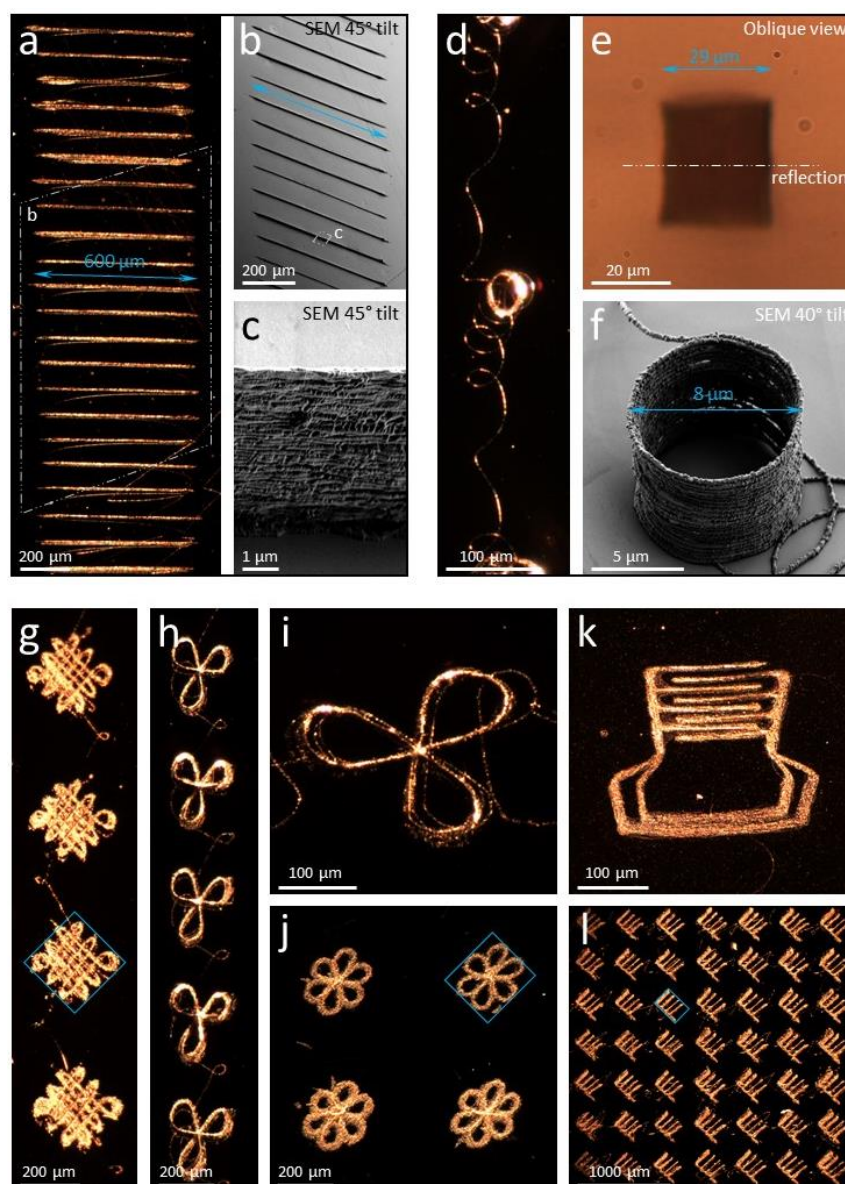


Figure 4. Jet speed determination from analysis of 3D printed structures. Optical images and SEM micrographs of PEO structures built by layer-by-layer assembly. **a-c** Straight walls printed by oscillating a 60 mm/s jet at 50 Hz using triangular signal, depositing two fiber layers per period. The XY translation stage was moved in between the printing of consecutive walls. **d-f** PEO-Ag cylindrical structures containing 50 nm Ag nanoparticles. The cylindrical structure on **(f)** was printed by jet deflecting at 100 Hz while the stage was stopped for 0.25 s, which resulted in a cylinder containing 25 layers. The jet speed of 2.5 mm/s was computed as described in the text. **g-l** show more complex patterns from which size the jet speed can be determined in a similar fashion, such as **(g)** boxed scaffolds, **(h-i)** triplets, **(j)** flowers, **(k)** interdigitated electrodes and **(l)** separate electrodes. Secondary electrons (SE2) detector was used for SEM imaging.

5.3.4 Operating regimes for the jet deflection method

To practice the jet deflection method, it is necessary to understand the role played by the jet deflection parameters^{4,27-29}. A key to collecting unbuckled fiber is using a jet deflection signal $U(\omega t)$ with large enough amplitude (U_0) and frequency (ν). The moment of disappearance of the buckling can be observed as the signal amplitude and frequency vary. Figure 5a shows the effect of the signal amplitude on the 2D track's width, for constant frequency, on a EHD jet moving at 140 mm/s towards the collection substrate. At low speeds, when the jet buckles over the collector, the width of the fiber track, shown in Figure 5b, increases linearly with signal amplitude (cases A through F). At a critical condition, represented on this graph as α , the printed fiber is aligned, and remains aligned beyond the critical amplitude, while track's width remains constant (cases G and H). This probably happens because, beyond condition α , the fiber opposes stretching by building mechanical tension which is transferred along its length from its contact point at the substrate. The electrical force component due to the jet deflection signal (U) acts orthogonally to this tension, and is therefore unable to stretch the jet. Conceivably, an ink could be soft enough to yield under this force, in which case the track's width *would* increase after point α . The critical condition would still be detectable in the track's width versus amplitude function by a change (decrease) in slope at α . Figure 5c illustrates how, at this signal frequency, pattern width is expected to vary with signal amplitude for different jet speeds. The buckled part of the curves is the same up to the critical point, which is attained at larger amplitudes for larger jet speeds.

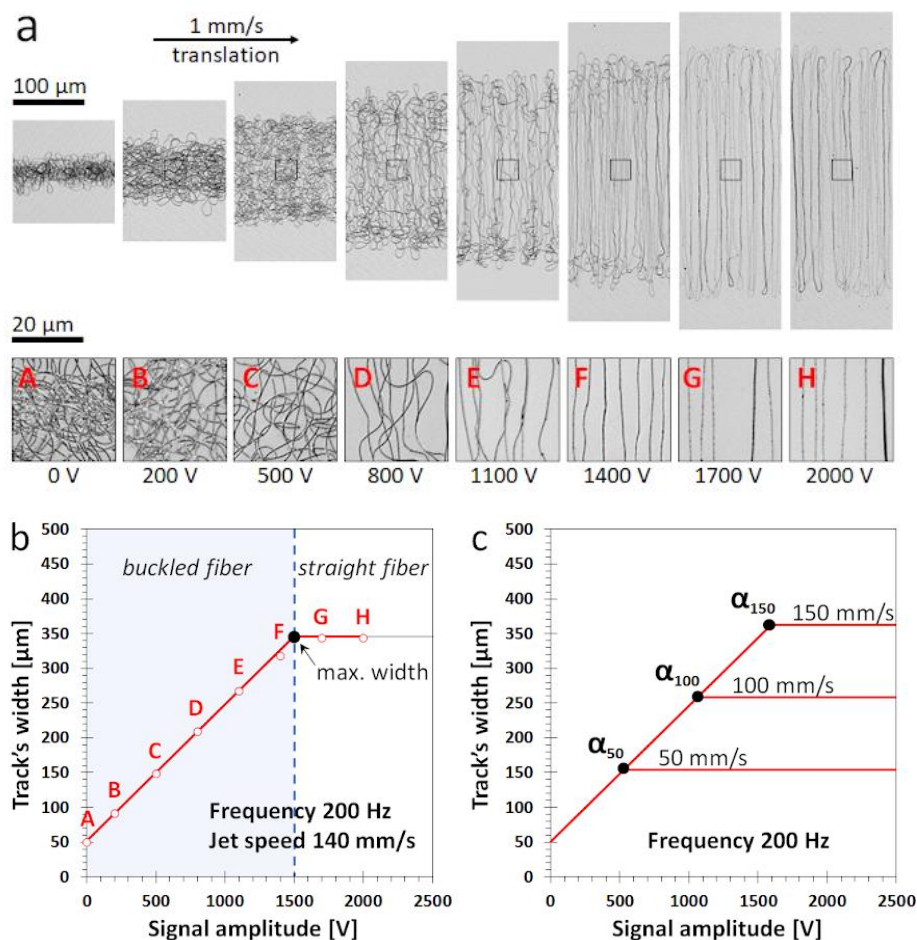


Figure 5. Effect of the amplitude of the jet-deflecting signal on the width of a printed pattern while moving the substrate at low speeds. The jet deflecting electrodes are positioned at 90 degrees, and the substrate translation is oriented as shown in Figure 1b. **a** Optical photographs of PEO fiber collected as the substrate moves at 1 mm/s and the jet is deflected in the perpendicular direction with a triangular wave at a frequency of 200 Hz, for different amplitudes of the jet-deflecting signal (shown in volts). **b** Dependence of the width of the printed fiber track on the signal amplitude at a fixed frequency (200 Hz). Shaded in blue is the amplitude range where buckled fiber is collected and, thus, the fiber speed cannot be determined by the proposed method. **c** Extrapolation of printed width versus signal amplitude from (b) at different fiber speeds. Similarly to (b), the graph predicts the evolution of printed widths for different jet speeds. Dry nitrogen gas was supplied around the jet.

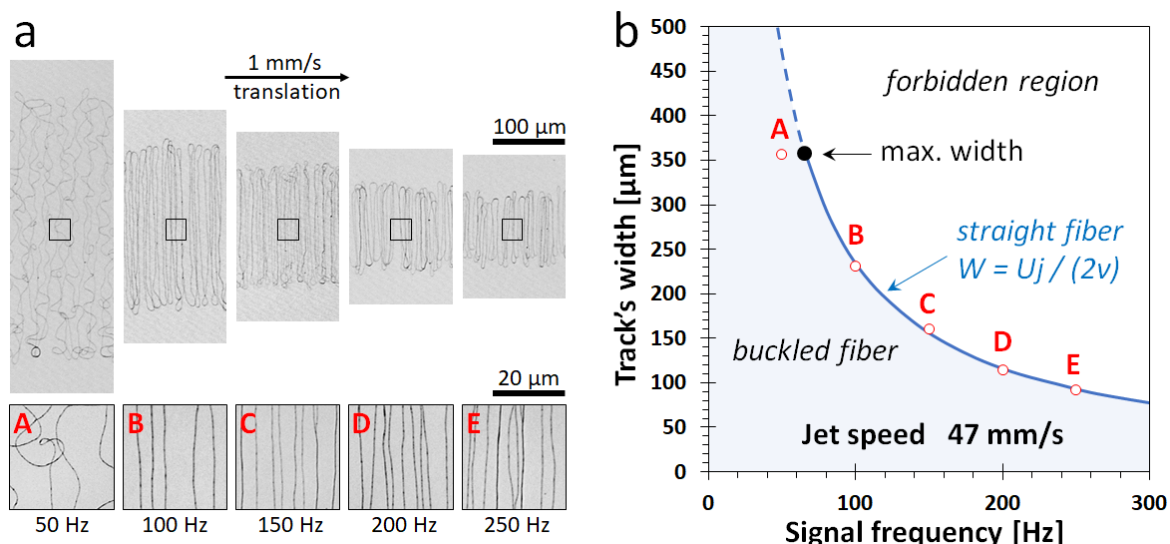


Figure 6. Effect of the frequency (ν) of the jet-deflecting signal on the width of a printed pattern while moving the substrate at low speeds. **a** Optical photographs of the PEO fiber collected as the substrate is moved at 1 mm/s and the jet is deflected in perpendicular direction by a triangular wave for different frequencies of the jet-deflecting signal (shown in hertz) at fixed amplitude of 1100 volts. **b** Width of the printed fiber track versus frequency. The blue shaded area displays the region where the same jet would buckle (if the amplitude or the frequency were decreased compared to the straight fiber case, like in point A). Dry nitrogen gas was supplied around the jet.

Figure 6 shows the role played by the frequency of the jet-deflecting signal. If the frequency is low enough, the jet undergoes buckling (at condition A). By raising the frequency at constant amplitude, the buckling is reduced but the track's width stays constant (set by the signal amplitude). Eventually buckling disappears as the fiber becomes straight at the critical condition α , which was reached between conditions A and B (Figure 6b). Beyond this point, the track's width decreases with increasing frequency (conditions B-E), as imposed by mass conservation. Indeed, assuming a constant diameter fiber, the simple inverse dependence $W=Uj/(2\nu)$ fits the data very well. The good agreement between theory and experiment in Figure 6b proves that the jet deflection did not cause fiber stretching (as concluded from Figure 5b by a different argument). Also note that only one condition (one fiber track) represented in these graphs is needed to determine the jet speed.

5.3.5. Case study: Jet speed dependence on nozzle voltage

Figure 7 displays the jet speed dependence on nozzle voltage³⁰. The jet speed was measured using the described method to demonstrate the ease of its implementation. Jet was deflected while the substrate was continuously moved to print fiber tracks, and nozzle voltage was updated for each pass. Importantly, jet speed evolution as a function of nozzle voltage was determined continuously, in a single experiment, thus reducing experimental error associated with conducting multiple experiments. The advantage of performing multiple measurements in one experiment and also much lower requirement as for the substrate space, is an essential improvement over the state of the art.

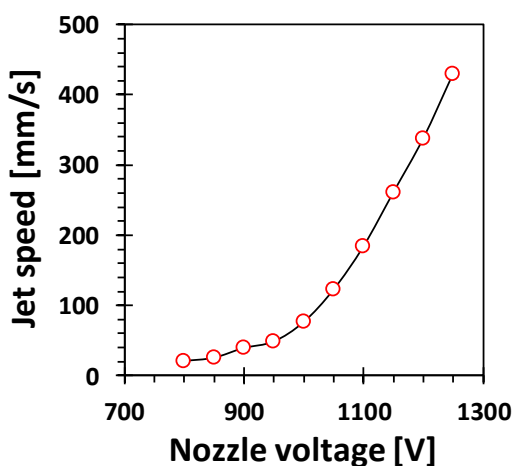


Figure 7. Dependence of the jet speed on nozzle voltage. The substrate was translated at 1 mm/s while the jet was deflected in the perpendicular direction using a triangular signal with 500 Hz frequency and 2000 V amplitude, ensuring straight fiber collection. Glass nozzle was c.a. 200 μm OD while the electrodes were located at 10 mm from the default jet trajectory and needle-to-substrate distance was 5 mm. Dry nitrogen gas was supplied around the jet.

5.3.6. Case study: Jet speed determination in presence of jet instabilities

In this case study, the method based on 2D tracks was used to detect instabilities in the EHD jetting causing jet speed pulsing³¹ or movement of jet ejection point. These situations are presented in Figure 8. In Figure 8a, the width of the track has a modulation which reflects a beating in the jet speed (of about 1.2 Hz), while the jet is oscillated at a much faster frequency (500 Hz). Figure 8b shows how the modulation in the track's width is synchronized with a non-symmetrical displacement of the jet. In both cases, the track's width can be easily converted to jet speed, as twice the width times the jet deflection

frequency ($U_j=2W_v$). Figure 8c,d show that in one case (panel c) the jet-ejection point is stable, while in the other (panel d) it moved around the pending ink drop and thus affects the centerline of the deposited fiber track. Two images of the EHD jet were taken with c.a. 2 second interval.

The process of detecting the two types of jet instability shown in Figure 8 can also be automated using in situ inspection equipment and image recognition software, and then be used for ensuring stable jetting conditions while printing.

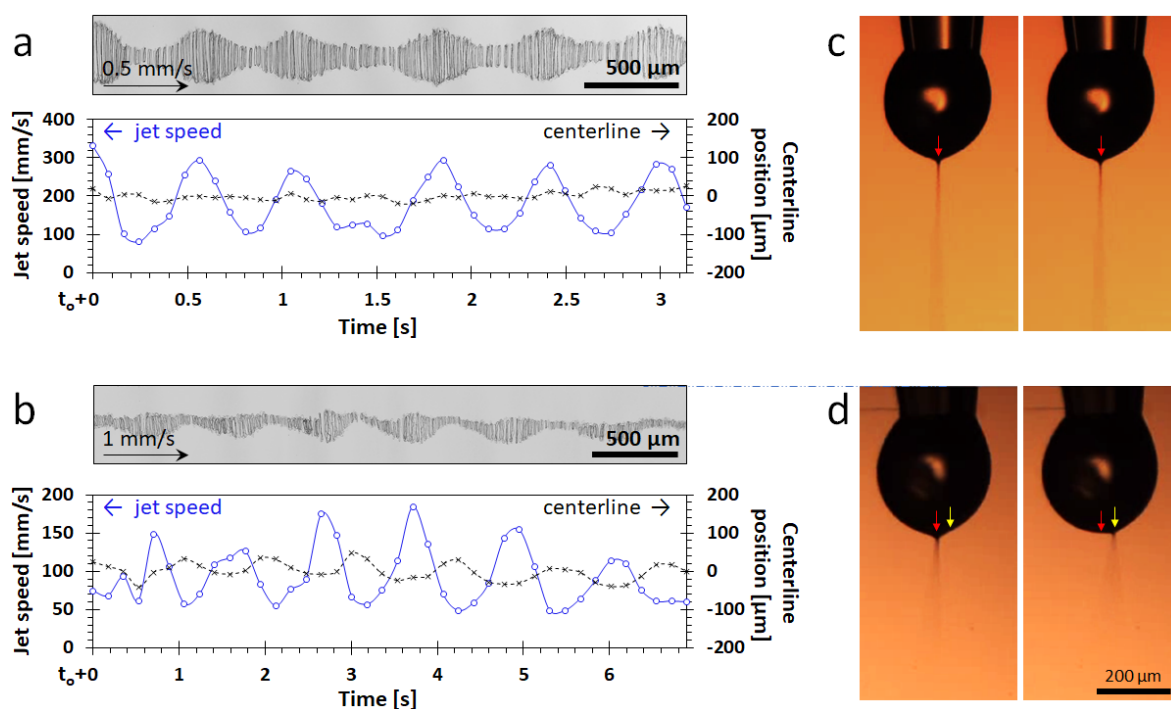


Figure 8. Detection of jet speed instabilities. The images on (a-b) were obtained after printing by confocal microscopy. The PEO fiber was collected on the substrate moving at 0.5 mm/s (a) and 1 mm/s (b) horizontally, while the jet was deflected in the perpendicular direction, with a triangular signal with 2000 V amplitude at 500 Hz. **a** Jet with pulsating speed, as reflected in the width of the fiber track. **b** Jet pulsation with displacement of the jet on the pendant drop. Printed fibers are photographed by confocal microscopy. Underneath these, we show the jet speed obtained by our method (valid as the fiber is straight) and the centerline position. For (b) centerline position and jet speed are correlated. **c-d** show optical images of the pendant drop with EHD jet during printing corresponding to cases shown on (a-b). While the jet-ejection point is stable on (c), it moved around the drop on (d), resulting in period oscillations of the fiber track centerline (as seen on b). Dry nitrogen gas was supplied around the jet.

5.3.7. Simulation of in situ inspection system

Although the images shown thus far were obtained with confocal or electron microscopes, the method can be used with standard machine inspection optics, and can be automated by image recognition software to detect the edges of the fiber tracks or widths of the 3D structures. Figure 9 illustrates this approach where the printed fiber tracks are readily visible with a standard CMOS camera coupled to a microscope of modest magnification and standard LED illumination (see Methods section). For convenience this experiment was carried out a posteriori (schematically presented on Figure 9a), but using the same substrate speed as used during printing. Computed jet speeds are: (b) 42 mm/s, (c) 37.5 mm/s, and (d) 37 mm/s. The jet was electrostatically deflected along a plane perpendicular to the direction of stage motion. The stage moved much slower than the fiber was generated, so the fiber is laid down nearly perpendicularly to the direction of substrate motion. Because the fiber is deposited without buckling, it is straight and perfectly aligned. In this case, the jet speed is computed as the product of twice the width of the track times the frequency of the jet-deflecting signal. As the track's width is visible "macroscopically", this method does not rely on resolving individual fibers and does not require expensive microscopy nor laborious analysis. Figure 9b uses 10 mm/s, producing a blurred image, while Figures 9c-d use a lower speed of 1 mm/s, resolving individual fiber tracks. The shiny (golden) lines visible in this case result from stronger scattering from multiple fibers stacked on top of each other by self-assembly (as explained earlier). The track's width in these figures, however, is independent of the extent of self-assembled fiber.

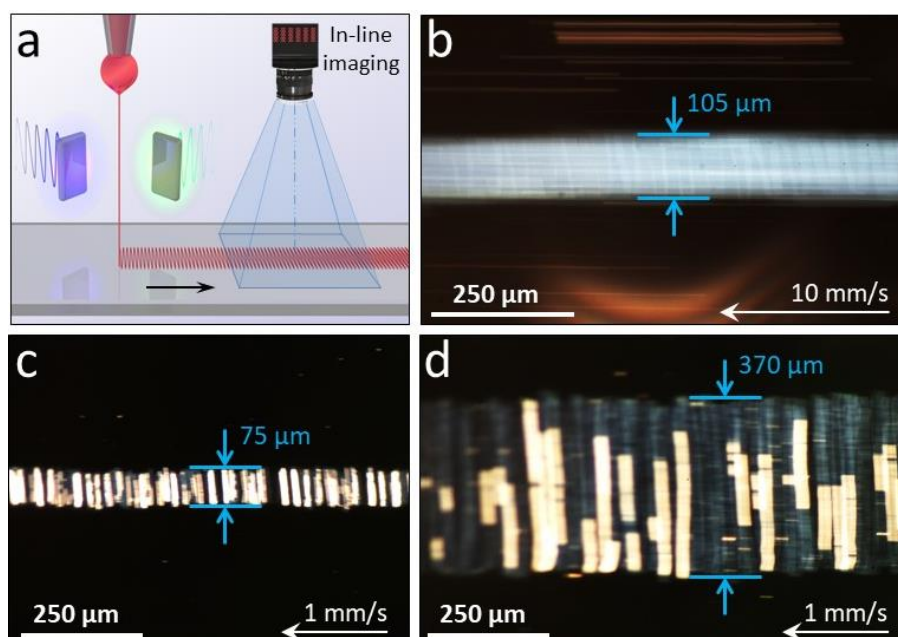


Figure 9. In situ jet speed determination. Schematic (a) and top-view optical photographs (b-d) of PEO fiber tracks collected as the substrate is moved sideways, and the jet is deflected in the perpendicular direction with a triangular signal, with frequencies and amplitudes of: (b) 200 Hz and 1200 V, (c) 250 Hz and 1100 V, and (d) 50 Hz and 1100 V. Photographs b-d are top views taken with CMOS camera (see methods). Exposure times: (b) 50 ms, (c) 10 ms and (d) 25 ms. For convenience the images were taken after collection using the same substrate speed as while printing. The track's width in these figures, however, is independent of the extent of fiber self-assembly. Case (b) is the same as for Fig. 3b panel C, (c) is Fig. 6a panel E, (d) is close to Fig. 6a panel A, but with straight fibers instead of buckled (see Figure 6). Note that in (b) the substrate travels 500 μm during exposure time, so the illusion of individual fibers is an artifact possibly caused by the fact that the printing frequency (200 Hz) is a multiple of the light source frequency (50 Hz). The computed jet speeds (mm/s) are: (b) 42, (c) 37.5, and (d) 37. Dry nitrogen gas was supplied around the jet.

5.4. Conclusions

Matching the jet speed by the printing speed entails that the jet speed must be stable and precisely measured. Current methods of determining jet speed are cumbersome, involve high-resolution microscope, and can be hardly automated. Here we proposed a novel method based on electrostatic jet deflection, which does not require resolving individual fibers and can be used with standard optical imaging to determine the jet speed. We suggest that this method can be applied in-situ, even when the substrate is moving, to monitor EHD jet speed. Additional advantage of this approach is that it is able of detect jet speed instabilities as they arise and could provide a feedback control capability to the printer. We believe this tool will be useful for studying and controlling printing parameters and may aid in bringing this nascent and fascinating field of EHD jet printing to further technology readiness level and toward future applications.

5.5. References

1. Gibson, I., Rosen, D. & Stucker, B. Additive manufacturing technologies. 3D Printing, Rapid Prototyping, and Direct Digital Manufacturing. (Springer, 2013).
2. Pei, E., Monzón, M. & Bernard, A. Additive Manufacturing - Developments in Training and Education. (Springer, 2018).
3. Srivatsan, T. S. & Sudarshan, T. S. Additive manufacturing: Innovations, Advances, and Applications. (CRC Press, 2015).
4. Liashenko, I., Rosell-Llompart, J. & Cabot, A. Ultrafast 3D printing with submicrometer features using electrostatic jet deflection. *Nat Commun* 11, 753 (2020).
5. Zhang, B., He, J., Li, X., Xu, F., & Li, D. (2016). Micro/nanoscale electrohydrodynamic printing: from 2D to 3D. *Nanoscale*, 8(34), 15376–15388.
6. Zheng, G., Li, W., Wang, X., Wu, D., Sun, D., & Lin, L. (2010). Precision deposition of a nanofibre by near-field electrospinning. *Journal of Physics D: Applied Physics*, 43(41), 415501.
7. Onses, M. S., Sutanto, E., Ferreira, P. M., Alleyne, A. G., & Rogers, J. A. (2015). Mechanisms, Capabilities, and Applications of High-Resolution Electrohydrodynamic Jet Printing. *Small*, Vol. 11, pp. 4237–4266.
8. Kiselev, P. & Rosell-Llompart, J. Highly Aligned Electrospun Nanofibers by Elimination of the Whipping Motion. *J. Appl. Polym. Sci.* 125, 2433–2441 (2012).
9. He, X. X., Zheng, J., Yu, G. F., You, M. H., Yu, M., Ning, X., & Long, Y. Z. (2017). Near-Field Electrospinning: Progress and Applications. *Journal of Physical Chemistry C*, 121(16), 8663–8678.
10. Huang, S., Bu, N., Duan, Y., Pan, Y., Liu, H., Yin, Z., & Xiong, Y. (2013). Electrohydrodynamic direct-writing. *Nanoscale*, 5(24), 12007–12017.
11. Sun, D., Chang, C., Li, S., & Lin, L. (2006). Near-Field Electrospinning. *Nano Letters*, 6(4), 839–842.
12. Robinson, T. M., Hutmacher, D. W., & Dalton, P. D. (2019). The Next Frontier in Melt Electrospinning: Taming the Jet. *Advanced Functional Materials*, 29(44), 1904664.
13. Wunner, F. M., Wille, M.-L., Noonan, T. G., Bas, O., Dalton, P. D., De-Juan-Pardo, E. M., & Hutmacher, D. W. (2018). Melt Electrospinning Writing of Highly Ordered Large Volume Scaffold Architectures. *Advanced Materials*, 30(20), 1706570.
14. Reneker, D. H., Yarin, A. L., Fong, H., & Koombhongse, S. (2000). Bending instability of electrically charged liquid jets of polymer solutions in electrospinning. *Journal of Applied Physics*, 87(9), 4531–4547.
15. Ribe, N. M., Habibi, M., & Bonn, D. (2011). Liquid Rope Coiling. *Annual Review of Fluid Mechanics*, 44(1), 249–266.

16. Han, T., Reneker, D. H., & Yarin, A. L. (2007). Buckling of jets in electrospinning. *Polymer*, 48(20), 6064–6076.
17. Duan, Y., Ding, Y., Xu, Z., Huang, Y., & Yin, Z. (2017). Helix Electrohydrodynamic Printing of Highly Aligned Serpentine Micro/Nanofibers. *Polymers*, 9, 434.
18. Chiu-Webster, S., & Lister, J. R. (2006). The fall of a viscous thread onto a moving surface: a 'fluid-mechanical sewing machine.' *Journal of Fluid Mechanics*, 569, 89–111.
19. Shin, D., Kim, J., Choi, S., Lee, Y. B. & Chang, J. Droplet-jet mode near-field electrospinning for controlled helix patterns with sub-10 μm coiling diameter. *Journal of Micromechanics and Microengineering* 29, (2019).
20. D. Ye, Y. Ding, Y. Duan, J. Su, Z. Yin, Y.A. Huang, Large-Scale Direct-Writing of Aligned Nanofibers for Flexible Electronics, *Small*. 14 (2018) 1703521.
21. Yin, Z., Huang, Y., Duan, Y., & Zhang, H. (2018). Electrohydrodynamic Direct-Writing for Flexible Electronic Manufacturing. Springer Nature. (Chapter 3. Helix Electrohydrodynamic Printing (HE-Printing); Pages 67-88)
22. Liashenko, I., Hrynevich, A., Dalton, P. D., Designing Outside the Box: Unlocking the Geometric Freedom of Melt Electrowriting using Microscale Layer Shifting. *Adv. Mater.* 2020, 2001874.
23. Kim, J., Shin, D., Han, K.-B. & Chang, J. A Quantification of Jet Speed and Nanofiber Deposition Rate in Near-Field Electrospinning Through Novel Image Processing. *J. Micro Nano-Manufacturing* 6, 031002 (2018).
24. Bastús, N. G., Merkoçi, F., Piella, J. & Puntès, V. Synthesis of highly monodisperse citrate-stabilized silver nanoparticles of up to 200 nm: Kinetic control and catalytic properties. *Chem. Mater.* 26, 2836–2846 (2014).
25. Bisht, G. S. et al. Controlled continuous patterning of polymeric nanofibers on three-dimensional substrates using low-voltage near-field electrospinning. *Nano Lett.* 11, 1831–1837 (2011).
26. Galliker, P. et al. Direct printing of nanostructures by electrostatic autofocussing of ink nanodroplets. *Nat. Commun.* 3, 890–899 (2012).
27. Zhu, Z., Chen, X., Du, Z., Huang, S., Peng, D., Zheng, J., & Wang, H. (2016). Fabricated Wavy Micro/Nanofiber via Auxiliary Electrodes in Near-Field Electrospinning. *Materials and Manufacturing Processes*, 31(6), 707–712.
28. Fang, F., Chen, X., Du, Z., Zhu, Z., Chen, X., Wang, H., & Wu, P. (2015). Controllable Direct-Writing of Serpentine Micro/Nano Structures via Low Voltage Electrospinning. *Polymers*, 7, 1577–1586.
29. Grasl, C., Arras, M. M. L., Stoiber, M., Bergmeister, H., & Schima, H. (2013). Electrodynamic control of the nanofiber alignment during electrospinning. *Applied Physics Letters*, 102(5), 7–11.

- 30.** Shin, D., Kim, J. & Chang, J. Experimental study on jet impact speed in near-field electrospinning for precise patterning of nanofiber. *J. Manuf. Process.* 36, 231–237 (2018).
- 31.** Hochleitner, G., Youssef, A., Hrynevich, A., Haigh, J. N., Jungst, T., Groll, J., & Dalton, P. D. (2016). Fibre pulsing during melt electrospinning writing. *BioNanoMaterials*, 17(3–4), 159–171.

Chapter 6

Unlocking the geometric freedom of melt electrowriting using microscale layer shifting

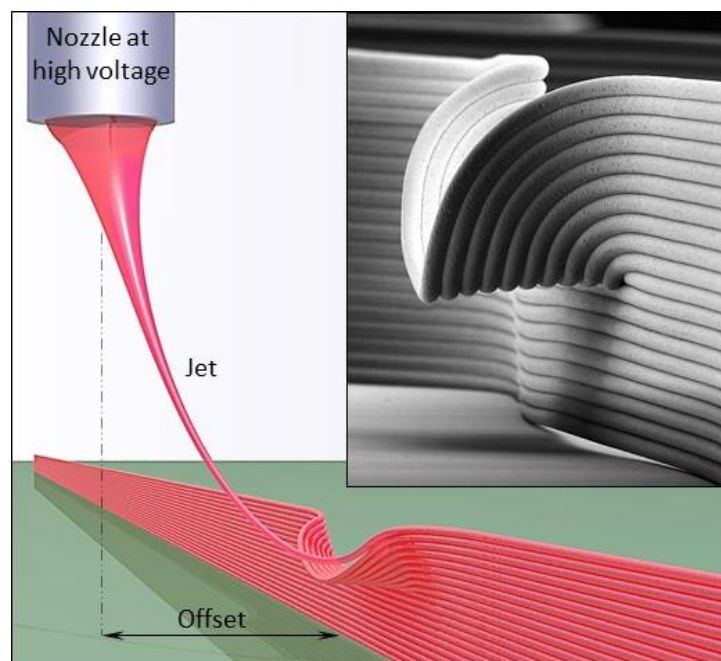
This chapter is based on the results published in

Liashenko, I., Hrynevich, A., Dalton, P. D., Designing Outside the Box: Unlocking the Geometric Freedom of Melt Electrowriting using Microscale Layer Shifting. *Advanced Materials*. 2020, 2001874.

* - equal contribution

Abstract

Melt electrowriting, a high-resolution additive manufacturing technology, has so far been developed with vertical stacking of fiber layers with a printing trajectory that is constant for each layer. In this work, microscale layer shifting is introduced through deliberately offsetting printing trajectory for each printed layer. Inaccuracies during the printing of sinusoidal walls are corrected via layer shifting, resulting in accurate control of their geometry and mechanical properties. Furthermore, more substantial layer shifting allowed stacking of fiber layers in a horizontal manner, overcoming the electrostatic autofocusing effect that favors vertical layer stacking. Novel non-linear geometries, such as overhangs, wall texturing and branching, smooth and abrupt changes in printing trajectory are presented, demonstrating the flexibility of layer shifting approach beyond the state-of-the-art. The practice of microscale layer shifting for melt electrowriting enables more complex geometries that promise to have a profound impact on the development of products in broad range of applications.



*"There are no straight lines or sharp corners in nature.
Therefore, buildings must have no straight lines or sharp corners."*

- Antoni Gaudi

6.1. Introduction

Melt electrowriting (MEW) is a high-resolution additive manufacturing technology with potential use in several areas including optics, electronics, textiles and biomedical applications¹. It is based on a melt-extrusion 3D printing concept, however the nozzle is raised above the collector, while the application of a high voltage maintains a thin molten jet between the two². MEW also has a substantially lower flow rate to the nozzle (typically 0.5 to 20 $\mu\text{L/h}$) which typically results in fiber diameters from 2 to 50 μm ³; notably smaller than conventional melt-extruded fibers. The smallest diameter MEW fibers reported to date are 0.8 μm ⁴.

Reinforcing frames made from MEW prints also have a substantial effect on the mechanical properties of hydrogels⁵. MEW prints with a sinusoidal laydown pattern can render weak hydrogels into tough, flexible materials even though the overall volume fraction occupied by the reinforcing frame is low⁶. The MEW fiber placement in particular greatly impacts the flexural properties for such soft network composites⁷, and mechanically complex tissues such as heart valves are being designed and fabricated based on such principles⁸.

To date, MEW research has involved the repeated stacking of individual fibers vertically upon each other^{1,9}, or deliberately misaligning each layer to induce a more porous morphology through fiber suspension¹⁰. Figure 1a and Video S1 shows that when printing above the critical translation speed (CTS), the electrified MEW jet lands on the collector/sample a slight distance behind the nozzle position. Due to this “*jet lag*”, fiber placement is substantially affected when the translation direction is changing while following non-linear printing path (Figure 1b), as it is in this study¹¹. Similar degradation is observed when printing sinusoidal pattern (Figure 2a, top) and result in additional tilting when printing a sinusoidal wall composed of 20 fiber layers (Figure 2a, bottom). Figure 2b shows a poly(ϵ -caprolactone) (PCL) fiber “wall” sinusoidally printed with identical printing path for each layer at the CTS (180 mm/min) so that jet lag is minimal. Artifacts can be seen at a certain fiber layer height⁹, and the black arrow in Figure 2b indicates this transition from ideal to non-ideal manufacturing conditions.

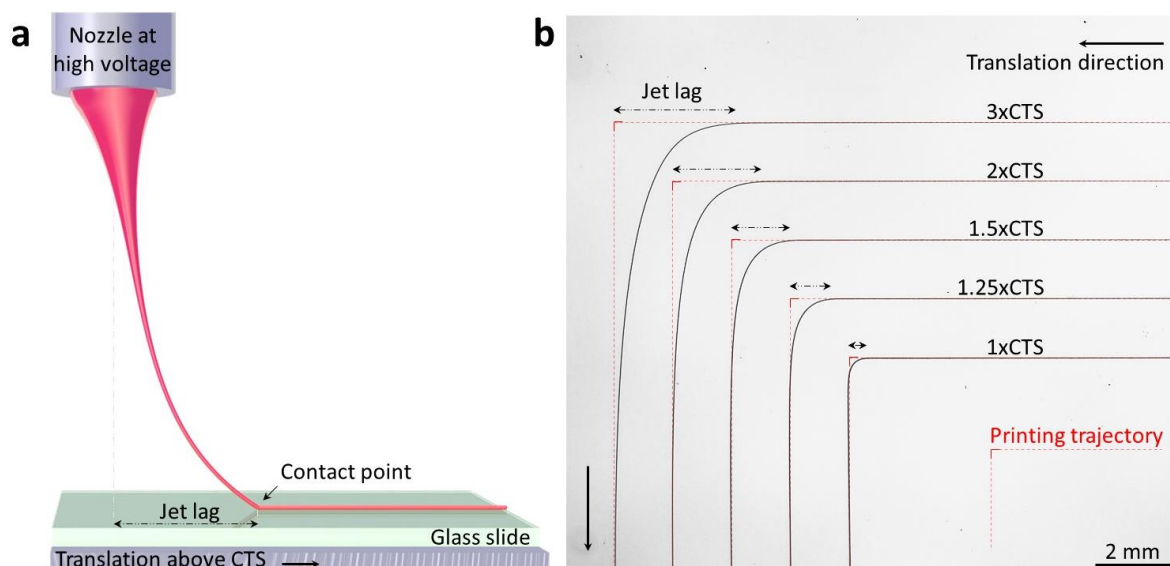


Figure 1: Jet lag and printed pattern degradation. **a** Schematic of the electrified molten jet while printing above CTS, highlighting the jet lag. **b** Printed path degradation due to the jet lag when printing direction is changed. Simple corners printed at increasing speeds demonstrate how the increase of the jet lag results in printed pattern degradation.

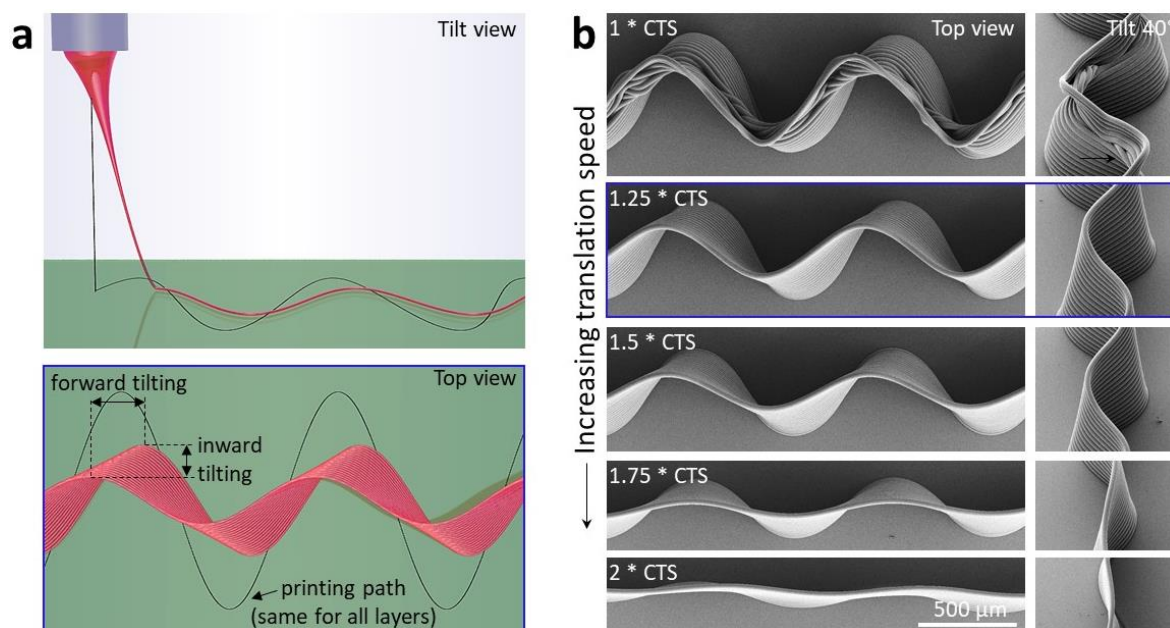


Figure 2. Sinusoidal walls printed with various speeds. **a** Schematics of printing a sinusoidal pattern when printing speed is slightly above the CTS (simulating the case of 1.25xCTS shown on **b**). Even though the printing path (black line) is same for all 20 layers, resulting wall is tilted. **b** SEM images of fiber walls fabricated with identical printing paths and different collector speeds.

Normally, this printing defect at the CTS is accounted for by performing MEW at higher collector speeds¹², as exemplified in Figure 2b. Increasing the collector speed, however, increases the jet lag and results in greater deviation in printed pattern compared to the intended pattern, to the extent that at 2xCTS (360 mm/min), the fiber wall has a significantly reduced sinusoidal form (Figure 2b; Video S2-S3). An important observation for collector speeds above the CTS, is the *inward tilting* of the fiber wall towards the centerline of the printed structure.

Based on collection speeds used in previous papers^{6,12}, Figure 2b (1.25xCTS) is most representative of this situation and is adopted here, and a rendering of this effect is presented in Figure 2a and Video S2. For the remainder of the study, all printing parameters were fixed with only the printing path altered.

6.2. Methods

6.2.1. Printer set-up and printing process

A custom-built MEW printer, used for several other studies was used in this study. All printing parameters are stable throughout, once a translation speed of 1.25xCTS was established. Pellets of PURAC PC-12 Corbion PCL were purchased and used as received after appropriate storage. A heating temperature of 87°C was used to melt the PCL, while an applied pressure of 1.2 bar forced the melt to a flat-tipped stainless-steel nozzle of 22 gauge protruded approximately 0.7 mm from the printhead. The collector distance was set to 3.5 mm, a high voltage of +5.75 kV was applied to the nozzle, while -1.5 kV was applied to the metal collector.

MEW fibers were deposited onto glass slides (1 mm thick) positioned atop the metal collector. These parameters resulted in a CTS (i.e. jetting speed) of 180-230 mm/min, which is variable due to daily changes in both the polymer and environmental conditions (ranging 19-22°C and 35-42% RH). Before each printing session, the jet was established/stabilized for more than 5 minutes to reach a steady state, after which CTS was measured and used to define the translation speed (1.25xCTS), resulting in fiber diameters of approximately 25 µm. This approach of setting translation speed as a function of CTS allowed to decouple the effect of microscale layer shifting from small variations of CTS. The microscale layer shifting approach was repeatable and stable, given that all other printing parameters are constant (CTS, fiber diameter, collector distance, etc.). Circular pore scaffolds required the most care as slight changes in the CTS caused a jet lag change, that required recalibration of the G-code.

Printing geometries were controlled solely by the definition of the translation trajectory performed by the XY stage, while other printing parameters were fixed. Translation trajectory and speed were preset through the G-code. Translation trajectory typically varied as a function of layer number and was used to deliberately offset arriving fiber placement onto previously-deposited one, and allowed printing non-vertical features. Unless indicated, a total of 20 fiber layers were printed into a fiber wall. The printing paths used for all experiments shown in this study are given in Table 1 in the ANNEX.

6.2.2. SEM Imaging

MEW structures were sputter-coated with approximately 4 nm of Pt using a Leica EM ACE600 system to improve imaging resolution. SEM images were taken with a Zeiss Crossbeam 340 with a secondary electron detector and acceleration voltages of 5-15 kV. Most samples were imaged directly on the glass collector, while the scaffold with circular pores was manually detached and imaged both from top and bottom for better showcasing its complex geometry (Figures 15-16). Similarly, circular domes (Figure 12) were detached using tweezers and positioned on sticky carbon tape for imaging. Cross-section of walls (Figure 9c) were obtained by carefully cutting the sample with scissors and fixing on adhesive tape so that no deformation of printed structures was observed.

6.2.3. Mechanical Testing

MEW samples for tensile testing were fabricated using the design shown in Figure 7b and with the printing paths provided in Table 1 in the ANNEX. "Chain-like" tensile testing samples were required over standard clamp-based testing, as the small diameter MEW fibers are difficult to grip/glue in the mechanical testing equipment without generating artifacts. Samples were detached from the glass slide after printing, and manually hooked over loops in the tensile tester (ElectroForce 5500, TA Instruments, USA). The length of sinusoidal wall was 12 mm and total displacement reached was 7.5 mm (a fixed limit of the micromechanical tester). Variations in sample mounting were corrected by shifting the strain axis while the measured force takes into account both sinusoidal walls in each test sample. Data is presented as force versus strain, due to difficulties in calculating the cross-sectional area (and hence stress) of the sinusoidal and tilting fiber walls.

6.3. Results and Discussion

6.3.1. Microscale layer shifting

A layer-by-layer offset for the printing path amplitude can be used to affect the inwards tilting of the MEW fiber wall. When the printing path amplitude is increased by 2% of the first layer amplitude (15 μm per layer), the MEW walls were more vertical (Figure 3a). Figure 4 and Video S6 show similar effect of 2% layer-on-layer increase for sinusoidal walls with different amplitudes. When increasing the amplitude of the printing path by 4% or 6% on the previous layer, the fiber wall tilts outwards (Figure 3a; Video S4). As would be expected, the reduction in amplitude resulted in more inwards tilting for -4% and -2% layer-on-layer samples.

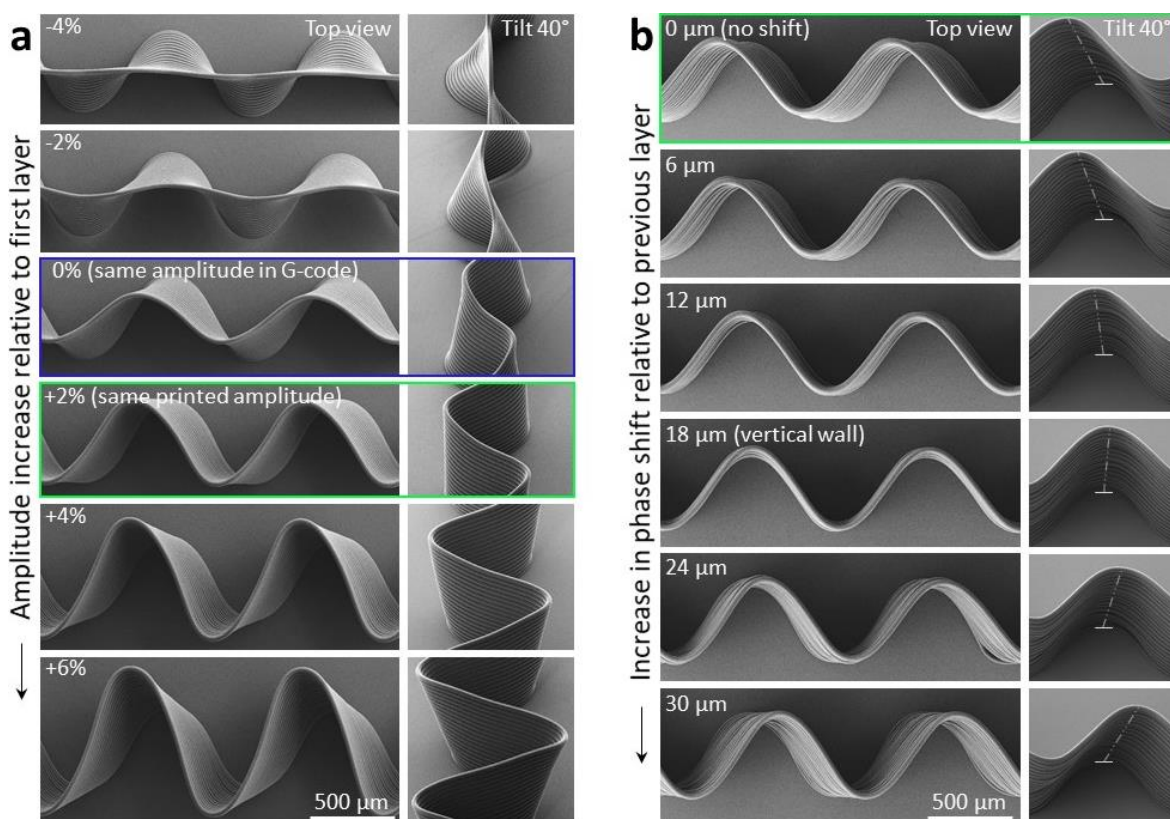


Figure 3. Effect of microscale layer shifting on tilting of the MEW fiber wall. SEM images of fiber walls fabricated with identical printing paths and an identical collector speed of 1.25xCTS but with: **a** an increase/decrease in amplitude layer-on-layer; **b** identical 2% layer-on-layer increase in amplitude as well as various phase shifts of the printing path. Videos S3-S6 visualize these alterations. Additional figures show the effect of amplitude (Figure 4), and how smooth change in collector speed, amplitude, and layer-on-layer offset affects the tilting and overall geometry of sinusoidal walls (Figure 5).

A sinusoidal fiber wall was also found to tilt forward (i.e. in the direction of the direct-writing), shown in Figures 2-3. However, it is possible to shift the phase of the sinusoidal printing path for each subsequent layer backward to correct this imperfection. Video S5 and Figure 3b shows a series of different phase shifts for the printing path, ranging from no shifting to 30 μm per layer. **Forward tilting** of the sinusoid could be corrected to a near-vertical wall using 12 μm to 18 μm phase shifts in the printing path for each subsequent layer. Similarly, backwards tilting of the sinusoid wall can be induced by shifting the phase of the sinusoidal printing path above 18 μm per layer (Figure 3b).

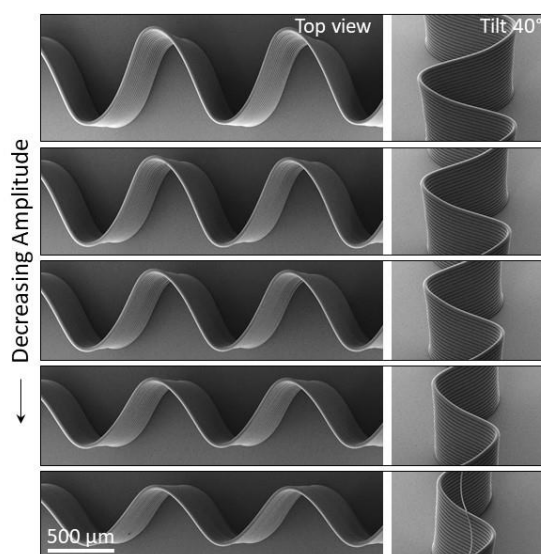


Figure 4. Sinusoidal walls with decreasing amplitude.

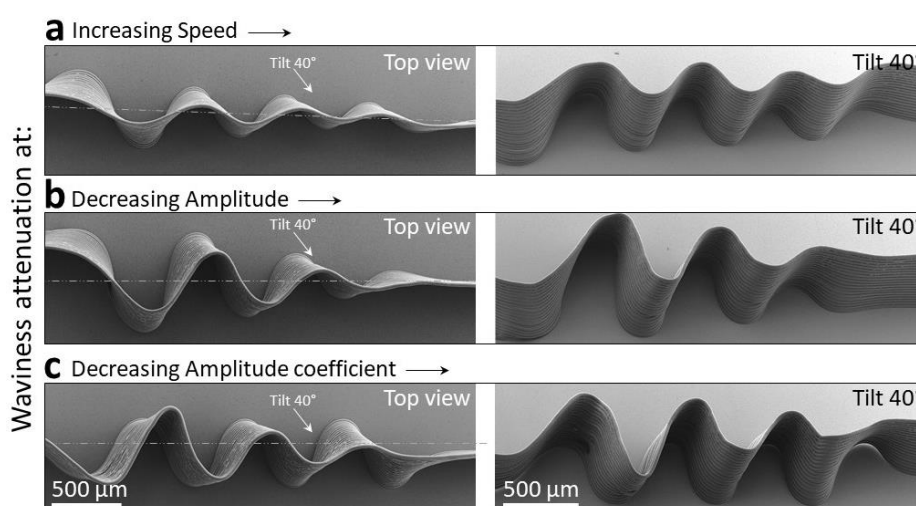


Figure 5. Sinusoidal walls attenuation as one parameter is linearly varied along printing direction. Three walls demonstrate **a** speed increase, **b** amplitude decrease, and **c** amplitude coefficient decrease. While Figures 2b and 3 show each wall discrete values, here those parameters are varied smoothly along the wall.

6.3.2. Adjustable mechanical properties

Such adjustment to each fiber layer path (i.e. microscale layer shifting) allows to arbitrarily control the tilt of sinusoidal walls (as shown on Figure 6), and would be expected to impact the mechanical properties of the printed structure. Since there is variance in the inwards/outwards tilting, each fiber would experience a different force depending on its position within the fiber wall. Mechanical testing (Figure 7) used samples where the first layer had the same pattern, and subsequent layers had different magnitudes of amplitude increase. Sinusoidally-printed walls all had toe and heel regions in their tensile responses, however shape of this curve greatly depended on the microscale shifting and whether it was inwards or outwards tilting.

For inwards tilting, the upper fiber is initially loaded while for outwards tilting the lower fiber has the initial load. However, for a 2% layer-on-layer increase for each printing path amplitude, the sinusoidal wall is near-vertical. When this sample (pink-color indicated) is stretched, the tensile load is nearly equally distributed across the wall, and there is substantial deformation before the resistance to strain starts growing with its maximal rate. For this sample, a linear zone (pink arrowed) is observed, and corresponds to an elastic modulus of 115 MPa that is lower than the straight MEW fiber control (190 MPa) and the values found previously for this medical-grade PCL (154 ± 23 MPa)¹³. As an indicator, the standard approach to MEW for sinusoidal fibers results in a force-strain curve shown in light blue. Under these printing circumstances, there are fibers within the sinusoidal wall that are loaded differently depending on their height in the fiber wall.

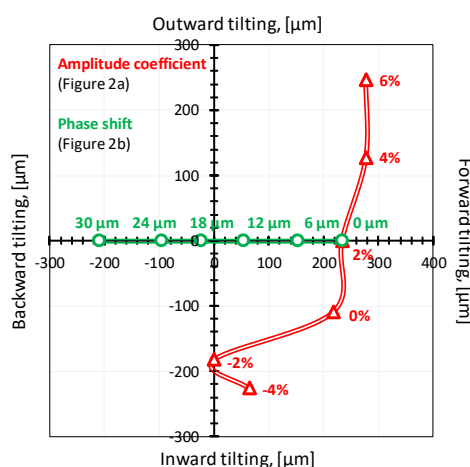


Figure 6. Adjustable tilting of sinusoidal walls. Plot demonstrates ultimate tailorability of sinusoidal walls in terms of their tilt direction, enabled by microscale layer shifting.

Forward/Backward and Inward/Outward tilting of sinusoidal walls presented on Figure 2a (amplitude coefficient, red) and Figure 2b (phase shift, green).

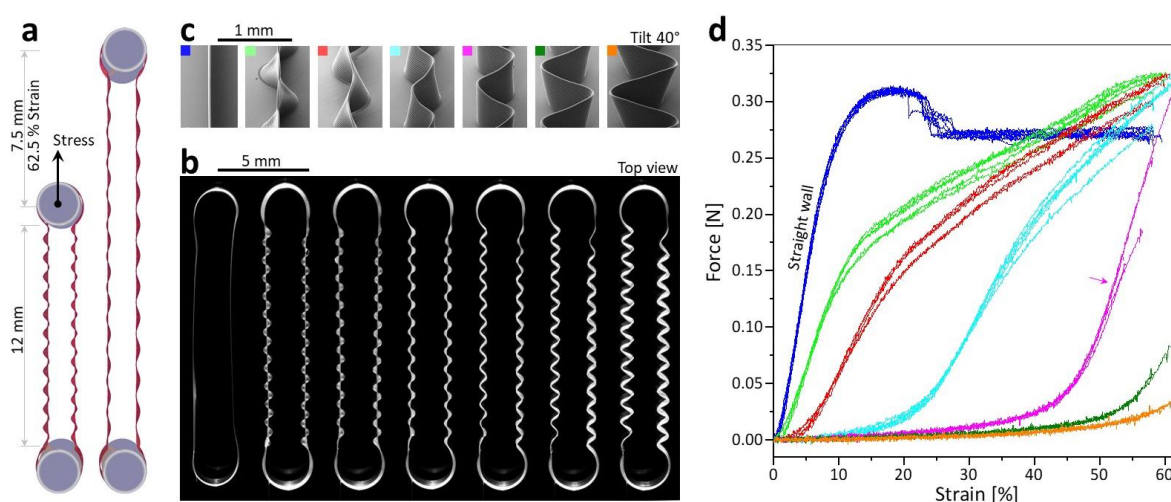


Figure 7. Tensile testing of sinusoidal fiber walls with controlled inwards/outwards tilting. **a** is a schematic of the “chain” style tensile testing approach that avoids sample slippage. **b** stereomicroscope photograph and **c** SEM of the sinusoidal fiber walls used for tensile testing. Each sinusoidal wall comprised 20 fiber layers, thus the difference in tensile properties across samples is solely attributed to the deliberate placement of fiber layers. Force-strain curves **d** are presented for these samples shown on **b-c**. Notably, the (pink-arrowed) sample with the most vertical walls had a similar linear slope to the straight fiber control. The 62.5% strain corresponds to the maximum limit of 7.5 mm in displacement.

6.3.3. Complex geometries enabled by layer shifting approach

The capability to non-vertically stack MEW layers using microscale shifting increases the geometric freedom for the fabrication of structures, as it addresses an inherent feature of additive manufacturing. For example, walls of stacked MEW fibers can be tilted to varying degrees, by offsetting each layer with changes in the printing path. Notably, horizontal MEW fiber stacking is possible (Figure 8), allowing the fabrication of overhanging MEW structures without using supports. In this instance, ten straight fibers were first printed, and the next ten printing paths shifted away from the centerline, resulting in a fiber depositing towards the side of the previous one. The degree of shifting allowed to precisely control the tilt angle of top 10 layers (shift values are detailed in Table 1 in ANNEX). In the instance of 90° overhangs, it is important to note that a substantial offset is required (625 μm) to overcome the electrostatic attraction of the jet to the top of the previously deposited fiber.

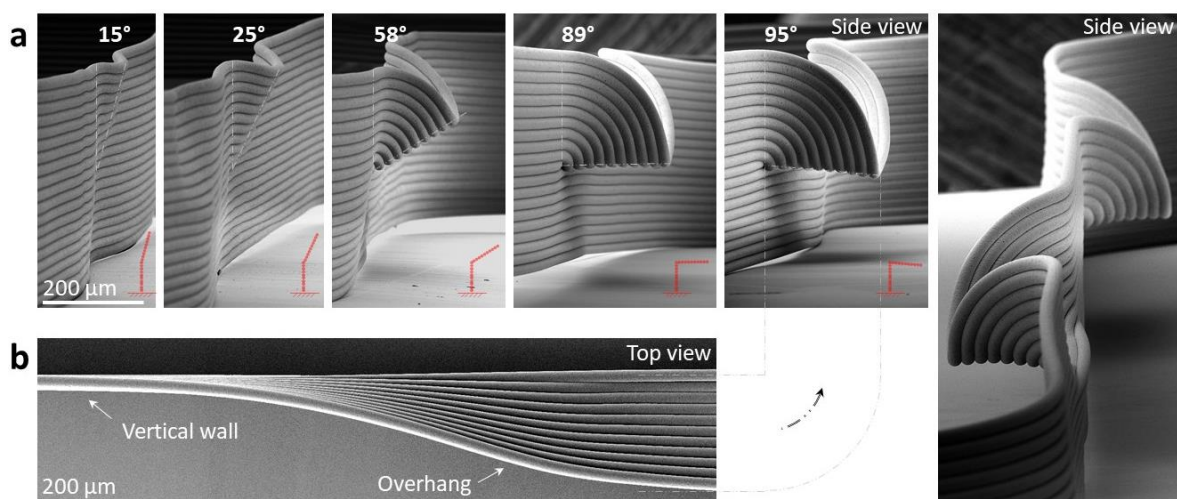


Figure 8. Overhangs with increasing tilt ultimately allow horizontal printing without supporting/sacrificial structure. **a** SEM images showing the side view of overhangs with variable tilting angle controlled by the offsets in printing path (exact offsets are detailed in Table 1 in ANNEX). **b** Top view of the overhang with the biggest tilt achieved.

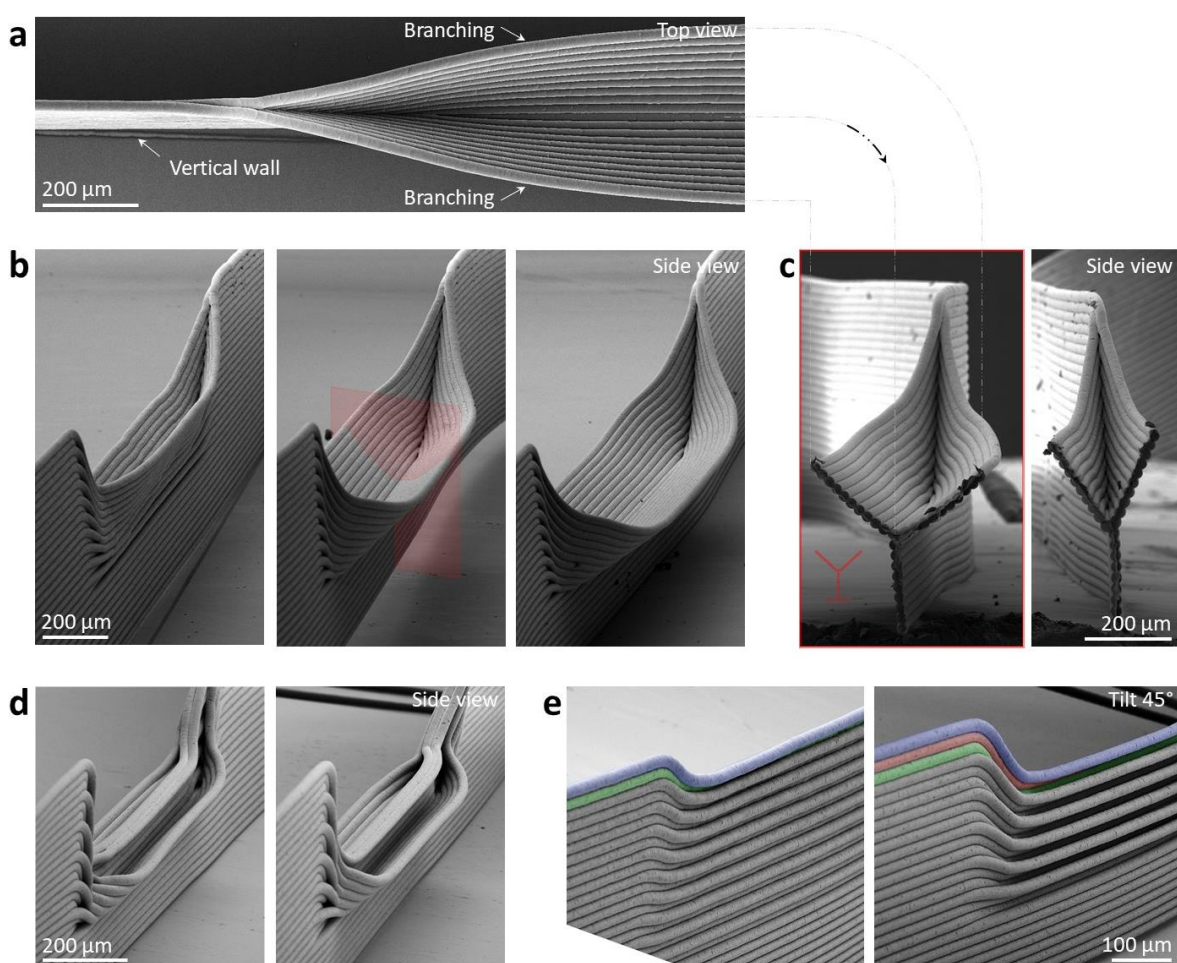


Figure 9. Branching and texturing obtained by alternating printing path offsets. **a** SEM image of the top of a vertical wall branching into two overhangs, similar to those shown in

Figure 8. **b** shows side views of branching walls with various tilting angles and resembling “boats”. **c** Cross-sections of branching walls. **d** Similarly to the double-branching (**a-c**), triple-branching is also possible. We envision such branched walls could potentially find application as i) vessels for “nesting” biomaterials, ii) for increasing its resistance to bending, or for iii) printing boxed scaffolds with variable pore size, where each pore could split into 2 or 4 smaller ones. **e** Demonstrates the case when offsets were insufficient to split the wall into separate branches, resulting in wall texturing. Such microscale texturing allows fabricating grooves and local control of the wall height.

Similarly, branching walls were printed by alternating the offset in printing path in opposite directions relative to the fiber wall centerline. The wall is composed of 10 straight layers and top 20 tilted layers, thus making 10 layers per branch (Figure 9a-c). Importantly, tilted layers were alternated between branches to ensure equal height growth (and thus electrical field gradient), during printing. Similar to overhangs, by presetting varying shift values it was possible to control the angle between branches (Figure 9b-d). Triple-branched walls are also possible (Figure 9d).

Furthermore, the same approach used for printing double- and triple-branched walls can be employed for wall texturing (Figure 9e) by presetting small shift values, thus not reaching the separation of alternating fibers into “branches”. Such texturing of the MEW wall could be used for i) wall reinforcement (against bending), ii) guiding cell growth with the grooves, or iii) to compensate for the local increase in heights when two walls cross (the textured wall is lower compared to normal one, even though the same number of layers are used).

Figure 10 shows SEM images of complex MEW fiber walls inspired by nature (e.g. leaves, seaweed, liana) and composed of 20 fibers layers. To highlight the geometrical flexibility provided by layer shifting, three types of geometries depict how straight and sinusoidal layers can be smoothly morphed into a single fiber wall.

Expanding on the previous samples, Figure 11a shows an abrupt change in translation trajectory fabricating a “multiphasic fiber wall”, where a straight wall was printed atop of a sinusoidal vertical wall. This also extends to the printing of several different MEW structures, including a multiphasic wall comprising two sinusoids with different amplitudes (Figures 11b-d). Multiphasic walls could be used for achieving “step-function” mechanical properties, thus allowing to fine-tune the force-strain curve of the wall beyond what is

already demonstrated in Figure 7d. This is particularly pertinent for soft network composites that are attempting to replicate the mechanical properties of soft tissue such as heart valves⁸ or ligaments/tendons⁶. In such a “reverse engineering” approach, the desired mechanical properties are defined by the tissue of interest and the appropriate combination of fiber placement is then established.

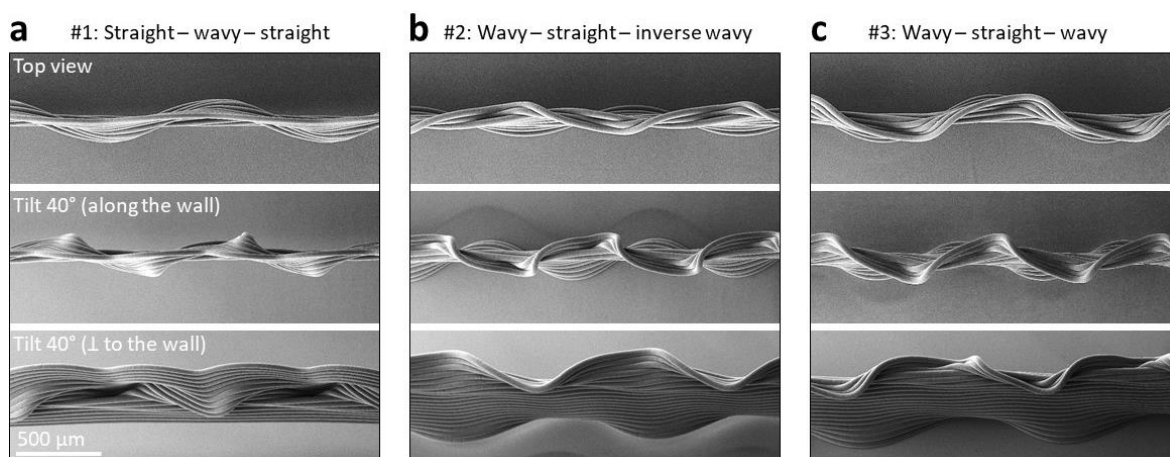


Figure 10. Nature-inspired walls where sinusoidal and straight fiber layers are smoothly morphed producing three wall designs. Smooth transitions between straight and wavy layers produced complex geometries, which are highlighted by the SEM images of the same walls (a-c) taken at different angles.

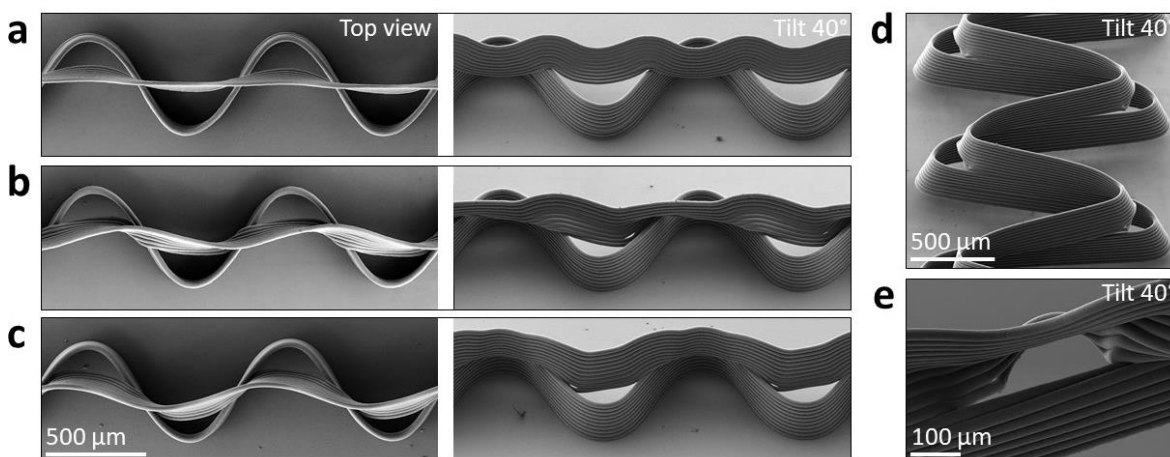


Figure 11. Multiphasic walls created by an abrupt change in printing trajectory (a-d), to enable highly tunable “step-function” mechanical properties, beyond those presented in Figure 7. a-c show top and tilt views on multiphasic walls, where 10 bottom layers assemble into a vertical sinusoid wall, and top 10 layers are laid in straight line (a) or sinusoid of smaller amplitude (b-c). d Similar multiphasic wall with two sinusoids of larger amplitudes. e Demonstrates a possibility of introducing openings/pores into the straight fiber wall so that the wall is less of a physical barrier, which could be useful in the scaffolds design.

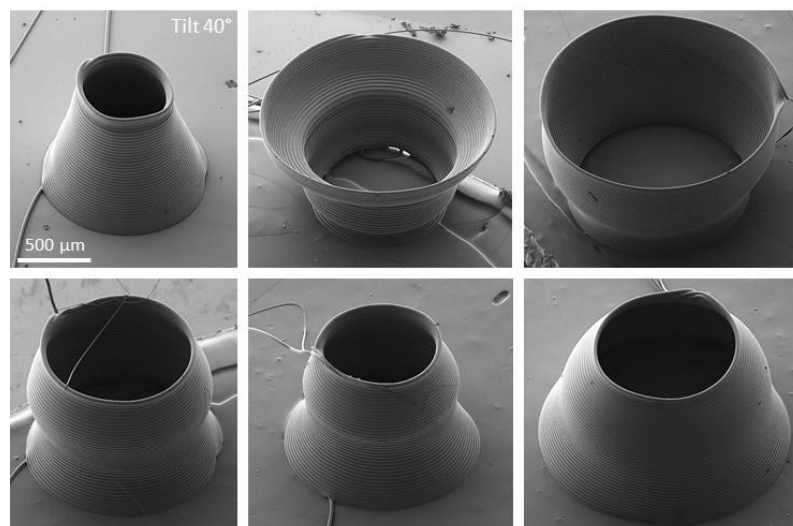


Figure 12. Microscopic domes (“micro-pottery”) fabricated with different taper using layer shifting principles.

To demonstrate how microscale layer shifting can facilitate fabrication of microstructures, small domes, shown in Figure 12, were printed with 40 layers at 1.25xCTS. The top-left structure was printed using 0.5 mm constant radius trajectory but resulted into a truncated cone due to the shape change associated with jet lag. Dome structures can be fabricated with various degrees of taper by continuously updating the trajectory radius as a function of layer number. As a demonstration, radius was varied both linearly and periodically (sinusoidally) to obtain different wall inclinations and “vase-like” geometries (Figure 12, top and bottom, correspondingly).

6.3.4. Novel scaffold designs

The implications of this new geometric design capability for MEW include the ability to fabricate new biomedical materials such as scaffolds for tissue engineering. Such MEW designs to date are almost exclusively based on straight fibers made in square “box-shaped” MEW scaffolds. The majority of MEW is also performed with linear movement between the nozzle and collector, resulting in straight fibers. Exceptions to both of these points are those MEW prints intended for use in the heart tissue engineering, since they have to undergo cyclic and complex mechanical loading¹⁴. Auxetic MEW prints and injectable scaffolds with hexagonal microstructure have been developed as heart patches, whereas soft network composites are being investigated for heart valve replacement⁸.

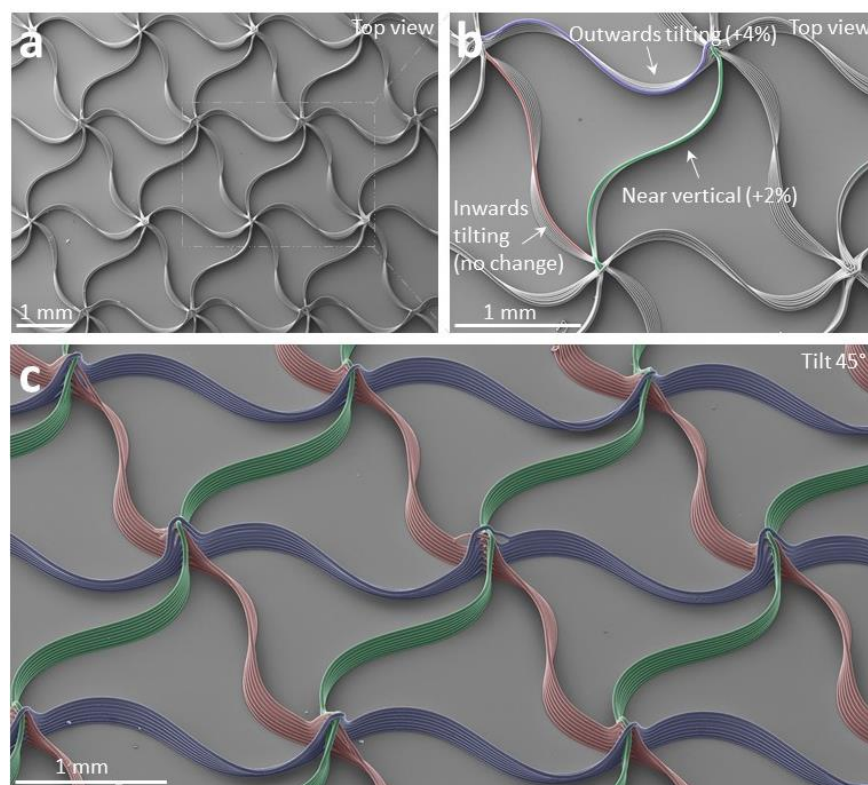


Figure 13. MEW scaffold with triangle-shaped pore. **a** SEM image of MEW scaffold, with the magnified view **b** showing that each edge of the triangle-shaped pore is printed with either 0%, 2% or 4% increase in amplitude. This accordingly affects the tilting of the wall from inwards, near vertical and outwards, indicated by false-coloring red, green and blue respectively. **c** shows the tilted view on the same scaffold, where walls with different tilts are false-colored correspondingly to **b**.

Building on such complex sinusoidal geometries, it is now possible that different MEW fiber walls can be tilted, as exemplified with a triangle-pore scaffold (Figure 13). Each side of this triangle pore has 1) vertical (indicated green), 2) inward tilting (red) and 3) outward tilting (blue) fiber walls. Triangle-pore scaffolds have been previously reported⁶, although in this instance the fiber wall tilting should alter the mechanical properties when the material is stretched in different directions, similar to Figure 7. For applications involving repetitive cyclic loading, however, a more elastomeric polymer would take advantage of wall tilting. A small but growing number of chemically- and physically-crosslinked polymers have been developed for MEW^{15,16}. The primary challenge in processing such polymers is reducing thermal crosslinking so that the printing conditions remain stable with time¹⁶.

The concept of straight fiber wall tilting (shown in Figure 8) was also exploited for fabricating box-shaped structures. These are the most common MEW geometrical

structures reported^{3,16} and, up until now, are fabricated with straight, vertical walls. Figure 14 shows how the morphology is altered when the fiber walls are tilted, where variable pore sizes result from crossing tilted walls.

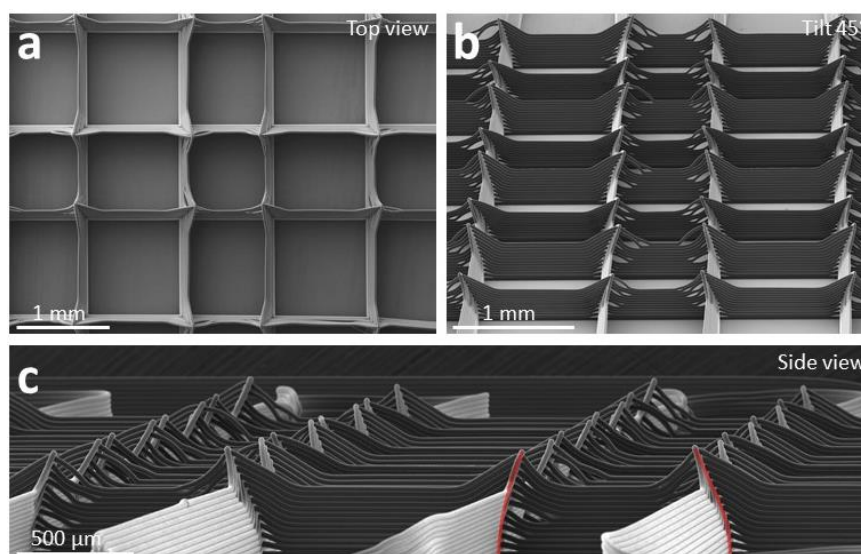


Figure 14. MEW box scaffold with wall tilting. **a** Top view of the scaffold, showing pore closing and opening as a function of layer number. **b-c** tilted views on MEW box scaffolds designed with variable wall tilting, false colored red lines indicating the tilting of two fiber intersection points.

The sinusoidal patterns shown in Figures 3 can also be used to fabricate circular pore MEW prints when opposite sinusoidal peaks are aligned and crossing points are precisely controlled. Figure 15 shows three views of the circular pore scaffold design (made of 20 layers), that combines the sinusoidal fiber walls into a uniform and reproducible circular pore scaffold. Figure 16 further highlights its geometrical complexity, showing all views of the same scaffold. While circular pore design is clearly visible from tilted view taken from the bottom of the scaffold (Figure 15a), top view emphasizes the rapidly-growing peaks at the four locations where the circular pores intersect with each other (Figure 15c, white arrow, and Figure 16b-c). All printed structures can be readily handled, with an example shown in Video S7. Such circular scaffolds have particular utility for spheroid bioassembly, improving on box-pore MEW scaffolds previously reported¹⁸.

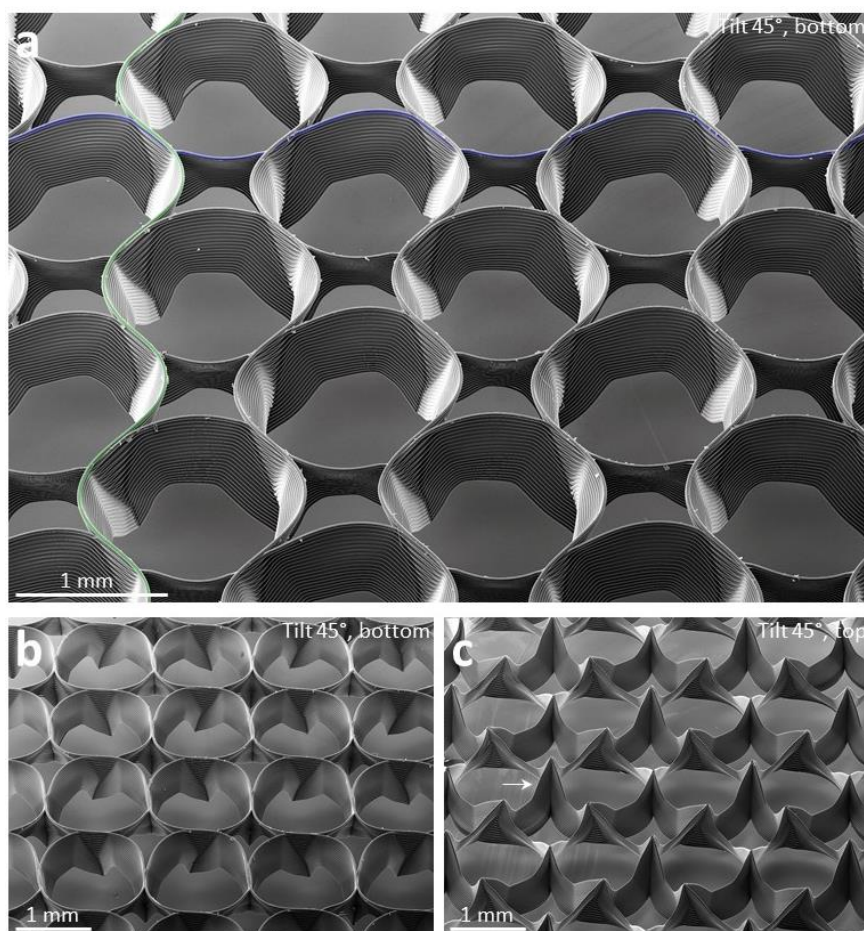


Figure 15. MEW scaffold with circular pore design. **a** SEM image of underneath a MEW scaffold with circular pores made by combining sinusoidally deposited fibers (two are exemplified with blue and green false-coloring). **b** Another tilt view from underneath of the same scaffold. There are four parts of the circular pore which have double the quantity of fibers, and make a corresponding four fiber “peaks” on the upper side (**c**). Other views of the same scaffold are available in Figure 16, highlighting its geometrical complexity.

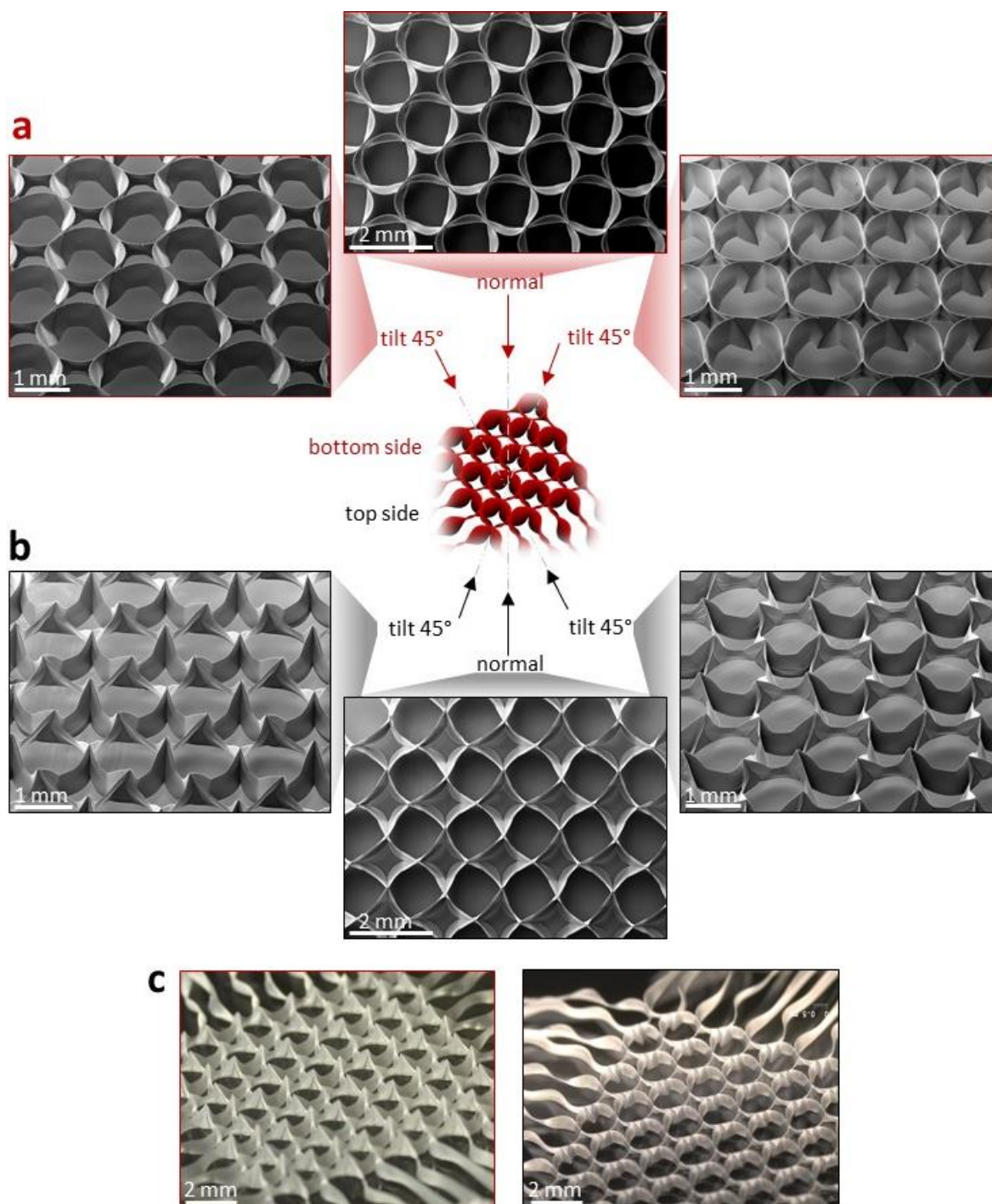


Figure 16. Geometric complexity of MEW scaffold with circular pores made by combining sinusoidal patterns. SEM images on **a-b** and optical photographs on **c** show the same MEW scaffold revealing its geometrical complexity. SEM images include **a** 3 images of the bottom side of the print (detached from the collector) and **b** 3 images of the top side, revealing the peaks where sinusoidal fibers cross. From either side of the scaffold, normal views are presented together with tilted views of 45 degrees. Optical images on **c** show the whole scaffold with 10 mm side, where perpendicular sinusoidal walls composing it are visible.

6.4. Conclusions

In summary, we demonstrate how layer positioning inaccuracies that occur within MEW due to jet lag can be corrected by updating the printing path for each deposited layer. Such microscale layer shifting can be used to layer fibers in a non-vertical manner, for example, to create overhangs without support structures, wall branching and texturing, as well as nature-inspired designs. As sinusoidal MEW printing substantially affects the mechanical properties of soft network composites, microscale layer shifting can substantially alter their mechanical properties. "Primitive" lines and boxed-shaped structures have generally been used in MEW since it was not previously known how to deliberately tilt walls to obtain more complex features. The electrostatic attraction of fibers to previously deposited ones also results in an autofocusing effect that tends to result in vertical MEW fiber walls. Overcoming this with microscale layer shifting is therefore an extra and powerful design approach for the fabrication of highly resolved and tailor-designed MEW products that have utility in a spectrum of value-added applications.



6.5. References

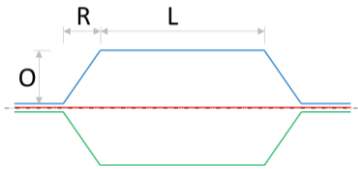
1. T. M. Robinson, D. W. Hutmacher, P. D. Dalton, *Advanced Functional Materials* 2019, 29, 1904664.
2. A. G. Marin, D. Lohse, *Physics of Fluids* 2010, 22.
3. A. Hrynevich, B. S. Elci, J. N. Haigh, R. McMaster, A. Youssef, C. Blum, T. Blunk, G. Hochleitner, J. Groll, P. D. Dalton, *Small* 2018, 14, e1800232.
4. G. Hochleitner, T. Jungst, T. D. Brown, K. Hahn, C. Moseke, F. Jakob, P. D. Dalton, J. Groll, *Biofabrication* 2015, 7, 035002.
5. J. Visser, F. P. W. Melchels, J. E. Jeon, E. M. van Bussel, L. S. Kimpton, H. M. Byrne, W. J. A. Dhert, P. D. Dalton, D. W. Hutmacher, J. Malda, *Nature Communications* 2015, 6, 6933.
6. O. Bas, D. D'Angella, J. G. Baldwin, N. J. Castro, F. M. Wunner, N. T. Saidy, S. Kollmannsberger, A. Reali, E. Rank, E. M. De-Juan-Pardo, D. W. Hutmacher, *ACS Appl Mater Interfaces* 2017, 9, 29430.
7. O. Bas, E. M. De-Juan-Pardo, I. Catelas, D. W. Hutmacher, *Adv Drug Deliv Rev* 2018.
8. N. T. Saidy, F. Wolf, O. Bas, H. Keijndener, D. W. Hutmacher, P. Mela, E. M. De-Juan-Pardo, *Small* 2019, 15, 1900873.
9. F. M. Wunner, M. L. Wille, T. G. Noonan, O. Bas, P. D. Dalton, E. M. De-Juan-Pardo, D. W. Hutmacher, *Adv Mater* 2018, 30, e1706570.
10. B. L. Farrugia, T. D. Brown, Z. Upton, D. W. Hutmacher, P. D. Dalton, T. R. Dargaville, *Biofabrication* 2013, 5, 025001.
11. G. Hochleitner, A. Youssef, A. Hrynevich, J. N. Haigh, T. Jungst, J. Groll, P. D. Dalton, *BioNanoMaterials* 2016, 17, 159.
12. F. Tournomousis, C. Jia, T. Karydis, A. Mershin, H. Wang, D. M. Kalyon, R. C. Chang, *Microsystems & Nanoengineering* 2019, 5, 15.
13. G. Hochleitner, PhD Thesis. University of Würzburg, 2018, p156. <https://nbn-resolving.org/urn:nbn:de:bvb:20-opus-162197>
14. S. Mori, J. T. Tretter, D. E. Spicer, D. L. Bolender, R. H. Anderson, *Clinical Anatomy* 2019, 32, 288.
15. F. Chen, G. Hochleitner, T. Woodfield, J. Groll, P. D. Dalton, B. G. Amsden, *Biomacromolecules* 2016, 17, 208; G. Hochleitner, E. Fursattel, R. Giesa, J. Groll, H. W. Schmidt, P. D. Dalton, *Macromol Rapid Commun* 2018, 39, e1800055.
16. D. Nahm, F. Weigl, N. Schaefer, A. Sancho, A. Frank, J. Groll, C. Villmann, H.-W. Schmidt, P. D. Dalton, R. Luxenhofer, *Materials Horizons* 2020.
17. K. F. Eichholz, D. A. Hoey, *Acta Biomater* 2018, 75, 140.



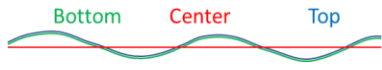
- 18.** R. McMaster, C. Hoefner, A. Hrynevich, C. Blum, M. Wiesner, K. Wittmann, T. R. Dargaville, P. Bauer-Kreisel, J. Groll, P. D. Dalton, T. Blunk, *Advanced Healthcare Materials* 2019, 8, 1801326.

6.6. ANNEX

Table 1. Printing path trajectories for the various MEW structures from Figures 2-16.

Figure # / Structure description	G-code trajectory formula ^{a)}	Constants ^{a)}
Figure 2b Translation speed V	$Y = A * \sin(X)$	V = [1, 1.125, 1.25, 1.5, 2] * CTS A = 0.75 mm (peak-to-peak amplitude) W = 1 mm wavelength
Figures 3a and 7 Amplitude coefficient K	$Y = A * \sin(X) * K * N$	K = [-4, -2, 0, 2, 4, 6] % increase from the first layer A = 0.75 mm W = 1 mm wavelength V = 1.25 * CTS
Figure 3b Phase shift S	$Y = A * \sin(X + S * N) * K * N$	S = [0, 6, 12, 18, 24, 30] μm shift from previous layer K = 2% A = 0.75 mm W = 1 mm wavelength V = 1.25 * CTS
Figure 4 Amplitude A	$Y = A * \sin(X) * K * N$	A = [0.5, 0.75, 1, 1.25, 1.5] mm K = 2 % increase from previous layer W = 1 mm wavelength V = 1.25 * CTS
Figure 8 Overhangs	Layers 1-10: Straight lines Layers 11-20: 	O = [125, 250, 375, 500, 625] $\mu\text{m} + N * 25 \mu\text{m}$ N = 10 layers of overhangs R = 0.2 mm L = 1 mm V = 1.25 * CTS
Figure 9a-c,e Double branching / Texture	Layers 1-10: Straight lines Layers 11-30: 	O = $(-1 * N) * ([100 - \text{texturing}, 200, 300, 400, 500, 600] \mu\text{m} + N * 25 \mu\text{m})$ N = 20 layers of double branching R = 0.2 mm L = 4 mm V = 1.25 * CTS

		- blue highlight - this component switches the path from blue to green, thus alternating each layer to build both branches.
Figure 9d-e Triple branching / Texture	Layers 1-7: Straight lines Layers 8-28: 	$O = (-1 * N) * ([100 - \text{texturing}, 200, 300, 400, 500, 600] \mu\text{m} + N * 25 \mu\text{m})$ $N = 21$ layers of triple branching (7 per branch) $R = 0.2 \text{ mm}$ $L = 4 \text{ mm}$ $V = 1.25 * \text{CTS}$
Figure 11a-b Bridges/windows	Layers 1-10: $Y = A * \sin(X + S * N) * K * N$ Layers 11-20: Straight line	$A = 0.75 \text{ mm}$ $T = 87^\circ\text{C}$ for 10 bottom layers; 80°C (Fig. S5B) and 75°C (Fig. S5A) for top 10 layers $S = 15 \mu\text{m}$ shift from previous layer $K = 2 \%$ increase from previous layer $W = 1 \text{ mm}$ wavelength $V = 1.25 * \text{CTS}$
Figure 11c Bridges/windows	Layers 1-10: $Y = A * \sin(X + S * N) * K * N$ Layers 11-20: $Y = (A / 2) * \sin(X) * K * N$	$A = 0.75 \text{ mm}$ $T = 87^\circ\text{C}$ for 10 bottom layers; 75°C for 10 top layers $S = 15 \mu\text{m}$ shift from previous layer $K = 2 \%$ increase from previous layer $W = 1 \text{ mm}$ wavelength $V = 1.25 * \text{CTS}$
Figure 11d Bridges/windows	Layers 1-10: $Y = A * \sin(X) * K * N$ Layers 11-20: $Y = (A / 1.3) * \sin(X)$	$A = 2 \text{ mm}$ $T = 87^\circ\text{C}$ for 10 bottom layers; 75°C for 10 top layers $K = 2 \%$ increase from previous layer $W = 1 \text{ mm}$ wavelength $V = 1.25 * \text{CTS}$
Figure 10a Liana #1: straight-wavy-straight	$Y = A * \sin(X)$, where A is linearly interpolated between Bottom, Center and Top values	$A_{\text{Bottom}} = 0 \text{ mm}$ $A_{\text{Center}} = 0.625 \text{ mm}$ $A_{\text{Top}} = 0 \text{ mm}$ $W = 1 \text{ mm}$ wavelength

		$V = 1.25 * CTS$
Figure 10b Liana #2: wavy-straight-inverse wavy	$Y = A * \sin(X)$, where A is linearly interpolated between Bottom, Center and Top values 	$A_{Bottom} = 0.4 \text{ mm}$ $A_{Center} = 0.2 \text{ mm}$ $A_{Top} = -0.78 \text{ mm}$ $W = 1 \text{ mm wavelength}$ $V = 1.25 * CTS$
Figure 10c Liana #3: wavy-straight-wavy	$Y = A * \sin(X)$, where A is linearly interpolated between Bottom, Center and Top values 	$A_{Bottom} = 0.345 \text{ mm}$ $A_{Center} = 0.288 \text{ mm}$ $A_{Top} = 0.805 \text{ mm}$ $W = 1 \text{ mm wavelength}$ $V = 1.25 * CTS$
Figure 12 Dome structures	$X = D * \sin(2\pi * N)$ $Y = D * \cos(2\pi * N)$, where $D_{variable} = D_{bottom} + (\Delta D * N) + \sin(2\pi * N/40)$	$N = 40 \text{ layers}$ $(\Delta D * N)$ – linear increase of diameter toward top layers, controlling wall inclination $\sin(2\pi * N/40)$ – periodic oscillation of diameter, controlling “vase-like” taper
Figure 5a Attenuation: Speed V	$Y = A * \sin(X)$ Linear increase in speed V	$V = [\text{from } 1 * CTS \text{ to } 3 * CTS] \text{ mm/min}$ when $X = [\text{from } 0 \text{ to } 3] \text{ mm}$ $A = 1.125 \text{ mm}$ $W = 1 \text{ mm wavelength}$
Figure 5b Attenuation: Amplitude A	$Y = A * \sin(X)$ Linear decrease in amplitude A	$A = [\text{from } 1.5 \text{ to } 0] \text{ mm}$, when $X = [\text{from } 0 \text{ to } 3] \text{ mm}$ $W = 1 \text{ mm wavelength}$ $V = 1.25 * CTS$
Figure 5c Attenuation: Amplitude Coefficient K	$Y = A * \sin(X) * K * N$ Linear decrease in amplitude coefficient K	$K = [\text{from } +6\% \text{ to } -4\%]$, when $X = [\text{from } 0 \text{ to } 3] \text{ mm}$ $A = 0.75 \text{ mm}$ $W = 1 \text{ mm wavelength}$ $V = 1.25 * CTS$
Figure 13 Triangular sinusoidal scaffold	$Y = A * \sin(X) * K * N$ Sinusoidal lines were shifted to create a triangular pore,	$K = [0, 2, 4] \%$ increase from previous layer $A = 0.5 \text{ mm}$ $W = 2 \text{ mm wavelength}$

	where pore size equals the wavelength of sinusoidal wave.	$V = 1.25 * CTS$
Figure 14 Boxed tilted scaffold	Layers 1-8: Straight line Layers 9-16: Straight line with Offset O Bottom fibers were placed with equal separation of 1 mm, while top side of the walls were tilted in opposite directions.	$O = 250 \mu\text{m} + (25 \mu\text{m} * N)$ $V = 1.25 * CTS$
Figure 15-16 Boxed sinusoidal scaffold	$Y = A * \sin(X)$ Sinusoidal walls were shifted in phase to align opposite peaks. Additionally, perpendicular sinusoidal walls were shifted to cross in desired locations, creating the pattern comprising circular and rhomboidal pores.	$A = 0.5 \text{ mm}$ $W = 2 \text{ mm wavelength}$ $V = 1.25 * CTS$

a) **List of variables, as used in Table 1:**

- A – amplitude (peak-to-peak), [mm]
- CTS – critical translation speed, [mm/min]
- D – diameter, [mm]
- K – amplitude coefficient, increase from previous layer, [%]
- L – length, [mm]
- N – layer number
- O – offset, [μm]
- R – ramp, [mm]
- S – phase shift, [μm]
- T – heating temperature, [C]
- V – translation speed, [$_ * CTS$]
- W – wavelength, [mm]
- X – direction along trajectory centerline
- Y – direction perpendicular to trajectory centerline

Supporting videos

Video S1. Animation of printing of one sinusoid layer. Printing path degradation (actual fiber placement relative to the XY stage trajectory) occurs due to jet lag.

Video S2. Animation of printing of a sinusoidal wall composed of 20 layers, where the printing path for each layer is the same (black sinusoidal line), representing the common printing approach. Resulting sinusoidal wall has a geometry similar to that shown in Figure 2b, printed at 1.25xCTS. Inward tilting together with forward tilting, naturally occurring due to presence of jet lag, are shown.

Video S3. Animation showing the effect of translation speed (varied from 1xCTS to 2xCTS) on the sinusoidal walls printing, where each later has the same trajectory. Frames are taken from Figure 2b. Amplitude decrease, Inward tilting and forward tilting is observed for all sinusoidal walls. Additionally, a printing instability occurs while printing at 1xCTS.

Video S4. Animation showing the effect of Amplitude coefficient on the sinusoidal walls. Frames are taken from Figure 2c.

Video S5. Animation showing the effect of layer-to-layer phase shift on the sinusoidal walls. Frames are taken from Figure 3b.

Video S6. Animation showing the effect of Amplitude on the sinusoidal walls. Frames for the video file are taken from Figure 4.

Video S7. Video showing the stability of melt electrowritten scaffolds under handling.

Supporting videos can be found at:

<https://onlinelibrary.wiley.com/doi/10.1002/adma.202001874>

General Conclusions

The aim of this thesis was to address the fundamental challenges of accurately positioning fast submicrometer EHD jets to print high resolution 2D and 3D patterns, which requires that the speed of EHD jet must be narrowly matched by the printing speed.

Currently, EHD jet printing is done using mechanical stages to locate the material on the printing substrate. In **Chapter 2** we conducted a detailed study of the performance of a top-notch mechanical stage and revealed its limitations for the printing with fast EHD jets (with speeds $\gg 10$ mm/s). First, we established that the acceleration of the best XY stages is about 1000X smaller than required for the fast EHD jet printing with micron resolution. Fast EHD jets lead to fiber buckling and pattern degradation when the stage is moving at lower speed than the jet, while the minimum radius of curvature that can be printed is limited to around 0.5 mm due to limitations in the stage acceleration. Experimental results confirmed this, showing that the average stage speed is limited to only few mm/s when executing complex trajectories, which is due to the insufficient stage acceleration. Furthermore, the stage speed varied in a wide range, leading to both fiber buckling/accumulation and cutting corners at different segments of the printed path. At the same time, the positioning error was as high as 30 μm demonstrating that even at such low average speeds positioning precision is unacceptable for high-resolution printing. We argue that to reach full potential of EHD jet printing, the kinetic limitations (for speed and acceleration) of XY mechanical stages must be overcome by developing another, radically different, means of material positioning – which was the core objective of this thesis.

In **Chapter 3** we presented a new strategy to control the material positioning in the EHD jet printing process, which is based on tuning the trajectory of EHD jet by controlling the surrounding electrostatic field. *Electrostatic deflection of electrified EHD jets* enabled us to control the location of the EHD jet collection in 2D and to print 3D structures of varying degree of complexity, including cross overs and bridges. We report high printing frequencies up to 2000 layers per second, allowing to print microscopic 3D structures layer-by-layer by precise electrostatically-driven self-assembly. We demonstrated printing speeds up to 500 mm/s in-plane and 0.4 mm/s in the vertical direction, three to four orders of magnitude faster than other additive manufacturing techniques providing equivalent

feature sizes. In this study we used inks containing polyethylene oxide (PEO), which is a golden standard in solvent-based EHD jet printing for a wide range of applications. EHD jetting of such inks produced fibers with diameters of about 200 nm from much thicker nozzles, and allowed us to adjust the jet speed in a wide range from 3 to 500 mm/s. We also dispersed silver nanoparticles and electrically conductive polymer PEDOT:PSS to merely demonstrate the material versatility of possible ink formulations. Besides, controlling the ink viscosity and composition permits adjusting the microstructure of the printed objects in nanoscale, resulting in either porous or dense fiber walls. To sum up, we believe that the unique advantages of the EHD jet-deflection printing will represent a significant step forward toward ultrafast additive micromanufacturing of 3D objects with virtually any composition and adjusted microstructure and functionality.

The concept of electrostatic jet deflection of EHD jet was proposed multiple times during the last decade. Despite previous research has demonstrated the feasibility of jet deflection in simple configurations, the previous attempts were limited in two major ways, which were addressed in **Chapter 4**: (i) the effect of printing parameters on electrostatic jet deflection had only been sparsely reported and was poorly understood, which did not allow reaching optimal control over printing conditions and (ii) signal generation was limited to primitive wavefunctions available in power generators and to manual voltage switching, which did not allow printing preset 2D patterns while controlling the printing speed. To address the first limitation, here we performed a rigorous parametric study via both finite element analysis and experimental data obtained with high-speed imaging. Simulations revealed the effect of the ink drop size, electrode configurations and applied voltages on the jet deflection angle. Furthermore, using high-speed imaging, we showed that EHD jet is surprisingly resilient and can be deflected up to 10000 Hz while maintaining its stable operation. Fast switching of electrostatic field allowed us to reach deflection speeds above 10 m/s and accelerations well in excess of $5 \cdot 10^5 \text{ m/s}^2$, which are essential for the printing with fast jets. Furthermore, we studied the effect of signal parameters for various electrode arrangements and found that the deflection angle is linearly proportional to the signal amplitude, and decreases non-linearly with increasing signal frequency. To address the second limitation in the prior studies, we developed a software to control jet-deflection printing. This custom-made software was indispensable for studying the jet deflection

phenomenon and was a critical stepping stone for obtaining printing results presented in this thesis. Based on the parametric study, we could match the speed of EHD jet by the deflection speed, while printing an arbitrary 2D pattern – the capability which allowed us to bring the old jet-deflection idea to the new level of implementation. One of functions employed in the software is the “deformation correction algorithm”, which allows to correct for the detrimental action of asymmetric electric field when only 2 deflecting electrodes are used to print in 2D and 3D. Having fewer deflecting electrodes and easing the dynamic requirements to the XY stage allows to use simpler and substantially cheaper setup, which may help in future commercialization of this technology.

Matching the jet speed with the printing speed in EHD jet printing entails that the jet speed must be stable and precisely measured. However, current methods of determining jet speed are cumbersome, involve high-resolution microscopy, and can hardly be automated. In **Chapter 5** we proposed a novel method based on electrostatic jet deflection, which does not require resolving individual fibers with powerful microscopes, but instead uses standard optical imaging to determine the jet speed from the large features of predefined geometries printed using EHD jet deflection and the deflection signal frequency. We argue that this method can be applied in-situ, even when the substrate is moving, to monitor EHD jet speed. An additional advantage of this approach is that it is able to detect jet speed instabilities as they arise and could provide a feedback control capability to the printer. We believe this tool will be useful for studying and controlling printing parameters and may aid in bringing this nascent and fascinating field of EHD jet printing to further technology readiness level and toward future applications.

Additional to the core scope of this thesis, in **Chapter 6** we contributed to the stage-driven EHD jet printing of polymer melts, also known as melt electrowriting or MEW, where much thicker and slower jets (than are typical of solution-based EHD jet printing, with speeds <10 mm/s) are collected into 3D structures. First, we report how layer positioning inaccuracies that occur within MEW due to the *jet lag* can be corrected by updating the printing path for each deposited layer. We tinkered with such *microscale layer shifting* to layer fibers in a non-vertical manner and produced prints with complex geometries, such as overhangs without support structures, wall branching and texturing, as well as nature-inspired designs. We also explored how the mechanical properties of sinusoidal walls can be tailored

through such microscale layers shifting, which can be potentially used in tissue engineering applications. In previous work, MEW prints were generally limited to "primitive" lines and boxed-shaped structures since it was not known how to deliberately tilt walls to obtain more complex features. The electrostatic attraction of fibers to previously deposited ones also results in an autofocusing effect that tends to stack MEW fiber into vertical walls. Here we demonstrated that microscale layer shifting can overcome this difficulty, and is therefore an extra and powerful design approach for the fabrication of complex, highly-resolved, and tailor-designed MEW 3D structures that have utility in a spectrum of value-added applications.

Future aims and Outlook

The motivation behind this thesis can be loosely generalized as “problem-driven” rather than “application-driven” research. Here we focused on overcoming some fundamental challenges of EHD jet printing via developing novel methodology, which we believe will enable new possibilities toward potential applications and have a lasting impact. While the concept of electrostatic jet deflection proved to be surprisingly capable in overcoming some persistent limitations in the field of EHD jet printing, we acknowledge that the field is still in its infancy and much has to be done before it can become an established microfabrication technique. Next we suggest a few critical areas which will need to be improved:

- **Setup.** Overall, for future commercialization and better reproducibility, the setup must be refined, simplified, made cheaper and preferably be designed into a desktop printer. A more affordable XY stage can be used together with off-the-shelf solution for signal generation/amplification. Our use of two jet deflecting electrodes with the same theoretical functionality as four electrodes is a possible step in this direction. Furthermore, we suggest redesigning the printhead assembly to fix the nozzle relative to the deflecting electrodes. This should improve the reproducibility of printing non-deformed patterns. Additionally, it would be beneficial to develop robust, small and affordable pump technology for low flow rates which can provide steady flow without drying at the reservoir.
- **Software.** Similar to other extrusion-based techniques, slicing may be implemented in the software, which will potentially enable more complex 3D prints. Additionally, the software must control both jet deflection and XY stage movement. Image recognition of the drop size and measuring the electrical current carried by the jet to the printing substrate could help in monitoring the stability of the jet. The jet speed could be measured in-situ by our method (Chapter 5) and be used to automatically adjust printing parameters (Chapter 4).
- **Materials.** It is critical to develop inks with diverse formulations (tailored to specific applications) and to find optimal printing parameters for stable EHD jetting. Post-

processing steps, such as polymer cross-linking or carbonization, must be developed, and the range of possible substrates for printing must be expanded.

- **Applicability.** Translating the jet-deflection concept to the melt-based EHD printing would be an interesting opportunity for properly positioning fast jets.



IEVGENII LIASHENKO



evgenii.liashenko@gmail.com
linkedin.com/in/ievgeniiliashenko



EDUCATION

- **Ph.D. Candidate in Ultra-Fast EHD 3D Printing with Submicron Resolution** Jun 2015 - **Present**
University Rovira i Virgili
Catalonia Institute for Energy Research (IREC)
Tarragona, Spain
Barcelona, Spain
- **InnoEnergy Ph.D. Fellow in Business, Innovation and Startups** Dec 2017 - **Present**
European Institute of Innovation and Technology (EIT)
innoenergy.com
- **Erasmus Mundus Masters in Engineering Rheology** eurheo.eu
Thesis "Impact of SBS modification on rheological properties of bituminous mastics".
Completed M.Sc. studies with the overall grade A and obtained multiple Degrees:
- **European M.Sc. in Engineering Rheology** Jan - Aug 2014
University of Huelva
Huelva, Spain
- **European M.Sc. in Engineering Rheology** Sep - Dec 2013
University of Minho
Guimaraes, Portugal
- **European M.Sc. in Mechanical Engineering** Sep 2012 - Jul 2013
University of Ljubljana
Ljubljana, Slovenia
- **M.Sc. (with honors) in Refrigeration Machines and Systems** Sep 2011 - Jul 2012
Odessa State Academy of Refrigeration
Thesis "Fluid dynamics and heat transfer of ice slurry in refrigeration and AC apparatuses".
Odessa, Ukraine
- **B.Sc. (with honors) in Power-Plant Engineering** Sep 2007 - Jul 2011
Odessa State Academy of Refrigeration
Odessa, Ukraine



EXPERIENCE, ACHIEVEMENTS AND SKILLS

- **Research assistant** at Complex Fluid Engineering Lab. (M.Sc. thesis), Huelva, Spain Jan - Aug 2014
- **Research assistant** at Institute for Sustainable and Innovative Technologies, Slovenia Jun - Aug 2013
- **HVAC technician** at Odessa Port Plant, Ukraine Jun - Aug 2011
- **Courses:**
 - "International Workshop on Innovating 2018" Massachusetts Institute of Technology, USA
 - "Becoming an Entrepreneur" Massachusetts Institute of Technology, USA
 - "Managing Innovation and Entrepreneurship" ESADE Business School, Spain
 - "Communication and Leadership" AGH University, Poland
 - "IP strategy / Law for Academic Innovator" Uppsala University, Sweden
 - "Energy Solution Design for eco-districts" Grenoble School of Management, France
 - "Energy Economics" Grenoble School of Management, France
- **Awards:**
 - First prizes at 14th & 15th Doctoral Days, University Rovira i Virgili May 2017/2018
 - Best poster award at EUROMAT 2017 conference Sep 2017
 - Scholarship from InnoEnergy Ph.D. School Dec 2017
 - Catalan government scholarship for Ph.D. studies (FI 2017) Mar 2017
 - EU scholarship for Erasmus Mundus M.Sc. programme Sep 2012
 - Ukrainian state scholarships for excellence in B.Sc. and M.Sc. studies Sep 2007, Sep 2011
 - Awards for student competitions in Physics, Math and Thermodynamics 2008 - 2011
- **Patents filed:**
 - "Printing device and method"
 - "Device and method for determining the speed of printing of a fiber and the length of a printed fiber"
- **Languages:** English ●●●●● Spanish ●●●●● Russian ●●●●● Ukrainian ●●●●●

